

**Thermoelectrics by Design: Improved Properties of Chalcogenides
through Metavalent Bonding**

Von der Fakultät für Georessourcen und Materialtechnik der
Rheinisch-Westfälischen Technischen Hochschule Aachen

zur Erlangung des akademischen Grades einer

Doktorin der Naturwissenschaften

genehmigte Dissertation

vorgelegt von

Nan Lin, M. Eng.

Berichtende: **Univ.-Prof. Dr.rer. nat. Joachim Mayer**
Univ.-Prof. Dr.rer. nat. Matthias Wuttig

Tag der mündlichen Prüfung: 12. Juli, 2024

Diese Dissertation ist auf den Internetseiten der Universitätsbibliothek online verfügbar

Thermoelectrics by Design: Improved Properties of Chalcogenides through Metavalent Bonding

from the Faculty of Georesources and Materials Engineering of the RWTH Aachen
University

to obtain the academic degree of

Doctor of Natural Science

approved thesis

submitted by

Nan Lin, M. Eng.

from Shangqiu, China

Advisors: Univ.-Prof. Dr. rer. nat. Joachim Mayer

Univ.-Prof. Dr. rer. nat. Matthias Wuttig

Day of the oral examination: *12 July 2024*

This dissertation is available on the website of the University Library.

Abstract

Thermoelectric (TE) materials offer a solution to address energy consumption challenges by solid-state refrigeration and waste heat recovery. Chalcogenides are attracting research interest due to their diverse structures and high TE performance. Bi_2Te_3 (near-room temperature) and SnSe/Pb-based compounds (mid- to high-temperature) exemplify this potential. The dimensionless figure of merit (zT) quantifies TE performance: $zT = S^2\sigma T/\kappa_{\text{tot}}$, where S is the Seebeck coefficient, σ the electrical conductivity, κ_{tot} the total thermal conductivity, and T the absolute temperature. zT enhancement strategies target both electrical and thermal properties. Electrical properties are optimized by decoupling S and σ through energy band engineering (band convergence, density-of-states resonance, band anisotropy) and interface engineering (energy filtering, modulation doping). In terms of thermal properties, the minimization of the lattice thermal conductivity (κ_{lat}) is achieved by decreasing the phonon relaxation time or phonon group velocity, including the introduction of lattice defects and lattice softening. Besides, research on novel materials with intrinsically high TE properties is a burgeoning topic.

Metavalent bonding (MVB), distinct from classical covalent, ionic, and metallic bonding, is crucial for high-performance TE chalcogenides. MVB exhibits a unique combination of properties: large Born effective charges, high optical dielectric constants, low Debye temperatures, and near-metallic electrical conductivity. Quantum-chemical calculations unveil MVB's unique nature, visualized via an electron transferred-electron shared (ET-ES) map. This map reveals MVB materials occupying a unique region with moderate electron transfer and nearly one electron shared between the nearest neighbors.

Bi_2Te_3 and Sb_2Te_3 , classic MVB compounds, are commonly alloyed for *p*-type TE materials at room temperature. However, the impact of alloying on MVB and its effect on TE properties remain unclear. To minimize the impact of defects on TE properties, high-quality $\text{Bi}_x\text{Sb}_{2-x}\text{Te}_3$ ($x = 0.5, 0.6$, and 0.7) single crystals were synthesized using the vertical Bridgman method. Characterization techniques (Fourier-transform infrared spectroscopy for optical properties and atom probe tomography for bond analysis) validated the MVB character of the alloys. Their favorable transport properties arise from the interplay between MVB and the electronic band structure, featuring high valley degeneracy, low band effective mass, and strong phonon anharmonicity – key factors for high TE performance.

Building on the MVB-performance link in Bi-Te alloys, this study explores novel MVB-based materials for enhanced TE efficiency. SnSe, a material with abundant elements, shows high TE performance only in its high-symmetry phase, especially in polycrystalline forms. This work addresses this challenge by stabilizing the desired rock-salt SnSe phase at lower temperatures through $\text{Ag}VI_2$ ($V = \text{Sb}, \text{Bi}$; $VI = \text{Se}, \text{Te}$) doping. Cubic SnSe exhibits MVB character, while the *Pnma* phase is covalently bonded. This work demonstrates that alloying-induced transition from covalent bonding to MVB stabilizes the desired cubic phase at lower temperatures. Consequently, zT near room temperature is significantly enhanced by over tenfold in $Fm\bar{3}m$ SnSe alloys compared to pristine *Pnma* SnSe.

The reported structural transformation in SnSe could also be potentially linked to the high-entropy effect. To elucidate the interplay between MVB bonding and the high-entropy effect, *n*-type polycrystalline $\text{BiPbAg}Q$ ($Q = \text{S}_3, \text{Se}_3, \text{Te}_3$, and TeSeS) alloys were fabricated. Atom probe tomography confirmed abnormal bond-breaking behavior, indicative of the MVB character of these alloys. Interestingly, the maximum optical absorption decreased ($\text{BiPbAgTe}_3 > \text{BiPbAgSe}_3 > \text{BiPbAgS}_3$) with increasing charge transfer, suggesting a weakening of MVB. This correlates with a decline in TE performance as the chalcogen element changes from Te to S. These results emphasize the potential of controlled charge transfer in designing MVB-based high-entropy thermoelectrics.

This study establishes the link between MVB and high zT in Bi-Te alloys. Then we leverage MVB principles to design cubic SnSe alloys with significantly improved average zT across a wide temperature range. Finally, we explore high-entropy MVB alloys, promoting solid solution formation and increasing configurational entropy. This approach offers a promising avenue for optimizing TE properties through controlled charge transfer within the high-entropy framework.

Kurzfassung

Thermoelektrische (TE) Materialien bieten eine Lösung für die Herausforderungen des Energieverbrauchs durch Festkörperkühlung und Abwärmerückgewinnung. Chalkogenide ziehen aufgrund ihrer vielfältigen Strukturen und ihrer hohen TE-Leistung das Interesse der Forschung auf sich. Bi_2Te_3 (nahe Raumtemperatur) und SnSe/Pb-basierte Verbindungen (mittlere bis hohe Temperaturen) sind Beispiele für dieses Potenzial. Die dimensionslose Gütezahl (zT) quantifiziert die TE-Leistung: $zT = S^2\sigma T/\kappa_{\text{tot}}$, wobei S der Seebeck-Koeffizient, σ die elektrische Leitfähigkeit, κ_{tot} die Gesamtwärmeleitfähigkeit und T die absolute Temperatur ist. zT -Verbesserungsstrategien zielen sowohl auf elektrische als auch auf thermische Eigenschaften ab. Die elektrischen Eigenschaften werden durch Entkopplung von S und σ mittels Energiebandtechnik (Bandkonvergenz, Zustandsdichte-Resonanz, Bandanisotropie) und Grenzflächentechnik (Energiefilterung, Modulationsdotierung) optimiert. Im Hinblick auf die thermischen Eigenschaften wird die Minimierung der Wärmeleitfähigkeit des Gitters (κ_{lat}) durch die Verringerung der Phononenrelaxationszeit oder der Phononengruppengeschwindigkeit erreicht, einschließlich der Einführung von Gitterdefekten und der Erweichung des Gitters. Darüber hinaus ist die Erforschung neuartiger Materialien mit intrinsisch hohen TE-Eigenschaften ein aufkeimendes Thema.

Metavalente Bindungen (MVB), die sich von den klassischen kovalenten, ionischen und metallischen Bindungen unterscheiden, sind entscheidend für leistungsstarke TE-Chalkogenide. MVB weist eine einzigartige Kombination von Eigenschaften auf: große effektive Born-Ladungen, hohe optische Dielektrizitätskonstanten, niedrige Debye-Temperaturen und nahezu metallische elektrische Leitfähigkeit. Quantenchemische Berechnungen enthüllen die einzigartige Natur von MVB, die durch eine ET-ES-Karte (Electrons Transferred – Electrons Shared) visualisiert wird. Diese Karte zeigt, dass MVB-Materialien einen einzigartigen Bereich mit moderatem Elektronentransfer und fast einem gemeinsamen Elektron zwischen den nächsten Nachbarn einnehmen.

Bi_2Te_3 and Sb_2Te_3 , klassische MVB-Verbindungen, werden üblicherweise für p -Typ TE-Materialien bei Raumtemperatur legiert. Die Auswirkungen der Legierung auf MVB und ihre Auswirkungen auf die TE-Eigenschaften sind jedoch nach wie vor unklar. Um die Auswirkungen von Defekten auf die TE-Eigenschaften zu minimieren, wurden hochwertige $\text{Bi}_x\text{Sb}_{2-x}\text{Te}_3$ ($x = 0.5, 0.6$, und 0.7) Einkristalle nach der vertikalen Bridgman-Methode synthetisiert. Charakterisierungstechniken (Fourier-Transform-Infrarotspektroskopie für optische Eigenschaften und Atomsondertomographie für die

Bindungsanalyse) bestätigten den MVB-Charakter der Legierungen. Ihre Transporteigenschaften ergeben sich aus dem Zusammenspiel zwischen MVB und der elektronischen Bandstruktur, die eine hohe Entartung, eine niedrige effektive Masse und eine starke Phononen-Anharmonizität aufweist - Schlüsselfaktoren für eine hohe TE-Leistung.

Aufbauend auf dem MVB-Leistungszusammenhang in Bi-Te-Legierungen werden in dieser Studie neuartige MVB-basierte Materialien für eine verbesserte TE-Effizienz untersucht. Insbesondere in polykristallinen Form zeigt SnSe eine hohe TE-Leistung, allerdings nur in der hochsymmetrischen Phase. Diese Arbeit befasst sich mit der Herausforderung die gewünschte Steinsalz-SnSe-Phase bei niedrigeren Temperaturen durch AgVI_2 ($V = \text{Sb, Bi}$; $VI = \text{Se, Te}$) Dotierung zu stabilisiert. Kubisches SnSe weist MVB-Charakter auf, während die $Pnma$ -Phase kovalent gebunden ist. Diese Arbeit zeigt, dass der legierungsbedingte Übergang von kovalenter Bindung zu MVB die gewünschte kubische Phase bei niedrigeren Temperaturen stabilisiert. Folglich ist zT bei Raumtemperatur in $Fm\bar{3}m$ SnSe-Legierungen im Vergleich zu reinem $Pnma$ SnSe um mehr als das Zehnfache erhöht.

Die berichtete strukturelle Umwandlung in SnSe könnte möglicherweise auch mit dem Hochentropie-Effekt zusammenhängen. Um das Zusammenspiel zwischen MVB-Bindung und dem Hochentropieeffekt zu ergründen, wurden n -leitende polykristalline $\text{BiPbAg}Q$ -Legierungen ($Q = \text{S}_3, \text{Se}_3, \text{Te}_3$, und TeSeS) hergestellt. Die Atomsondertomographie bestätigte ein abnormales Bindungsbruchverhalten, das auf den MVB-Charakter dieser Legierungen hinweist. Interessanterweise nahm die maximale optische Absorption mit zunehmendem Ladungstransfer ab ($\text{BiPbAgTe}_3 > \text{BiPbAgSe}_3 > \text{BiPbAgS}_3$), was auf eine Schwächung der MVB hindeutet. Dies korreliert mit einer Abnahme der TE-Leistung, wenn das Chalkogen-Element von Te zu S wechselt. Diese Ergebnisse unterstreichen das Potenzial eines kontrollierten Ladungstransfers bei der Entwicklung von MVB-basierten hochentropischen Thermoelektrika.

Diese Studie stellt die Verbindung zwischen MVB und hoher zT in Bi-Te-Legierungen her. Dann nutzen wir die MVB-Prinzipien, um kubische SnSe-Legierungen mit deutlich verbesserter durchschnittlicher zT über einen breiten Temperaturbereich zu entwickeln. Schließlich untersuchen wir hochentropische MVB-Legierungen, die die Bildung von Mischkristallen fördern und die Konfigurationsentropie erhöhen. Dieser Ansatz bietet einen vielversprechenden Weg zur Optimierung der TE-Eigenschaften durch kontrollierten Ladungstransfer im Rahmen einer hohen Entropie.

Contents

Thermoelectrics by Design: Improved Properties of Chalcogenides through Metavalent Bonding	
NAN LIN, M. ENG.....	
Abstract.....	I
Kurzfassung	III
Contents.....	V
1 Introduction	1
1.1 RESEARCH BACKGROUND	1
1.2 STRUCTURE AND GOALS OF THIS WORK	3
2 Fundamentals of Thermoelectrics and Metavalent Bonding.....	5
2.1 THERMOELECTRIC PRINCIPLES	5
2.1.1 Thermoelectric Effects	5
2.1.2 Figure of Merit.....	8
2.1.3 Strategies to Optimize zT	10
2.2 A NOVEL CHEMICAL BONDING MECHANISM	17
2.3 CORRELATIONS BETWEEN THERMOELECTRICS AND METAVALENT BONDING ...	22
2.3.1 Bonding Origin of Low Lattice Thermal Conductivity	22
2.3.2 Bonding Origin of Intrinsically High and Tunable Carrier Concentration ...	23
2.3.3 Bonding Origin of Complex Electronic Band Structure	25
2.3.4 Fermi Surface Complexity Factor	27
3 Methodologies	29
3.1 CRYSTAL GROWTH.....	29
3.1.1 Different Preparation Methods for Thermoelectric Materials	29
3.1.2 Single Crystals Grown by Bridgman Oven.....	29
3.1.3 Bulk Polycrystalline by Spark Plasma Sintering	33
3.2 STRUCTURAL AND CHEMICAL BONDING CHARACTERIZATIONS	34
3.2.1 Phase Composition and Crystal Orientation.....	34
3.2.2 Chemical Composition.....	37
3.2.3 Chemical Bond Breaking in Atom Probe Tomography.....	41

3.2.4 <i>Optical Properties</i>	42
3.3 THERMOELECTRIC PROPERTY MEASUREMENTS	46
3.3.1 <i>Seebeck Coefficient Measurement</i>	46
3.3.2 <i>Electrical Conductivity</i>	47
3.3.3 <i>Hall Measurement</i>	48
3.3.4 <i>Thermal Transport Measurements</i>	49
3.4 STRUCTURAL CALCULATIONS	53
3.4.1 <i>Density Functional Theory (DFT) Calculations</i>	53
3.4.2 <i>Defect Formation Energy Calculation</i>	53
4 Outstanding Thermoelectric Performance of Bismuth Telluride: A Chemical Bonding Perspective	55
4.1 OVERVIEW OF BISMUTH TELLURIDE	55
4.1.1 <i>Crystal Structure of Bi_2Te_3</i>	55
4.1.2 <i>Importance of Bi_2Te_3 in the Room Temperature Region</i>	58
4.1.3 <i>Improvement of Thermoelectric Performance of Bi_2Te_3</i>	58
4.2 COMPOSITION AND STRUCTURE OF THE BISMUTH TELLURIDE SINGLE CRYSTAL	62
4.2.1 <i>Composition of Bismuth Telluride</i>	62
4.2.2 <i>Structure of Bismuth Telluride</i>	64
4.3 OPTICAL PROPERTIES AND UNCONVENTIONAL BOND BREAKING	66
4.3.1 <i>Optical Reflection and Absorption of Bismuth Telluride</i>	66
4.3.2 <i>Bond Breaking in Atom Probe Tomography of Bismuth Telluride</i>	69
4.4 METAVALENT BONDING EMPOWERS THE HIGH THERMOELECTRIC PERFORMANCE	73
4.4.1 <i>Electric Transport Properties of Bismuth Telluride</i>	73
4.4.2 <i>Thermal Transport Properties of Bismuth Telluride</i>	79
4.5 CONCLUSIONS	82
5 Doping by Design: Enhanced Thermoelectric Performance of SnSe Alloys over a Broad Temperature Range through Metavalent Bonding	83
5.1 OVERVIEW OF THERMOELECTRIC SnSe	83
5.2 OBTAINING METAVALENTLY BONDED SnSe	86
5.2.1 <i>Motivation to Obtain High-symmetry SnSe</i>	86

5.2.2 Content of this Chapter.....	87
5.2.3 Confirmation of Metavalent Bonding in the As-synthesized Alloys.....	87
5.2.4 Homogeneity in Various Scales of Cubic SnSe	92
5.3 THERMOELECTRIC PROPERTIES AND THEIR CHEMICAL BONDING ORIGINS	96
5.3.1 Thermoelectric Properties of Cubic SnSe.....	96
5.3.2 Chemical Bonding Origins of Improved Thermoelectric Performance.....	100
5.4 IMPROVED MECHANICAL PROPERTIES OF SnSe-AGVVI_2 ALLOYS.....	104
5.5 CONCLUSIONS	105
6 High-entropy Thermoelectrics: The Role of Metavalent Bonding	107
6.1 INTRODUCTION OF HIGH-ENTROPY THERMOELECTRICS.....	107
6.2 THE FORMATION OF SOLID SOLUTION.....	113
6.2.1 Homogeneity in Macro Scale of the Solid Solution	113
6.2.2 Atomic Homogeneity of the Solid Solution	117
6.3 CHEMICAL BONDING MECHANISM OF THE SOLID SOLUTION	119
6.3.1 Confirmation of Metavalently Bonded Solid Solution	119
6.3.2 Optical Properties of the Solid Solution	120
6.4 THERMOELECTRIC PROPERTIES OF BiPbAgQ_3.....	121
6.4.1 Electrical Transport and Band Structures of BiPbAg Q_3	121
6.4.2 Thermal Conductivity and zT of BiPbAg Q_3	125
6.5 VICKERS HARDNESS OF BiPbAgQ_3	130
6.6 CONCLUSIONS	130
7 Conclusions and Outlooks	133
References	135
Acknowledgments	169
Personal Details	171
List of Publications during Doctoral Studies.....	171
Declaration of Authorship.....	173

1 Introduction

1.1 Research Background

The rapid pace of global industrialization has led to an increasing energy demand for social and industrial development. Natural fossil fuels can contribute positively to human civilization and industrialization, while their current low utilization rate results in energy loss and waste. Moreover, the utilization of fossil energy invariably results in environmental degradation. Hence, there is an urgent need to prioritize the development of new renewable energy sources and transition towards an energy structure aimed at mitigating carbon emissions. Environmentally friendly energy like wind, solar, and biomass, alongside the clean and efficient utilization of coal, dominate the current energy development landscape. Additionally, there is a growing demand for power supplies tailored for the aerospace sector.

Currently, wind power generation and solar photovoltaics play a crucial role in green energy development. Furthermore, thermoelectric materials facilitate direct conversion between thermal and electric energy, serving as vital tools in reducing environmental pollution.¹ At the microscopic level, carriers in the solid move directionally due to temperature gradients, leading to variations in carrier concentration between the ends of a material or across interfaces between different conductors, thereby generating a potential difference. This process realizes power generation from waste heat. Thermal energy is abundant and originates from diverse sources, including vehicle exhaust, geothermal heat, industrial waste heat, solar energy, and even human bodies. Conversely, since the second industrial revolution, electricity has emerged as the most versatile and highest-quality form of energy. Thermoelectric devices with compact size and lightweight design facilitate heat-electricity conversion without any moving parts, enabling the direct conversion of waste heat energy into usable electric energy.²⁻⁵

Given the diverse benefits of thermoelectric materials, they find extensive applications in specialized power sources, industrial waste heat recovery, precise local temperature control, etc. However, the energy conversion efficiency of thermoelectric materials

remains relatively low, significantly below that of traditional heat engines. Consequently, they are presently unable to efficiently convert large quantities of industrial waste heat into electrical energy, which hampers their commercial viability. Concerning thermoelectric refrigeration, micro components crafted from thermoelectric materials can be utilized to cool computers, infrared detectors, optical communication laser diodes, and temperature adjustment systems for various electronic and optoelectronic devices. Nonetheless, the development of thermoelectric models for large-scale refrigeration systems currently has encountered challenges, with the progress toward mass production being slow.²

Thermoelectric materials are critical in both power generation and thermoelectric refrigeration, with considerable potential for future advancement. Thus, it is of practical and long-term significance to develop environmentally friendly thermoelectric materials characterized by abundant resources, low costs, and superior performance.

Bi_2Te_3 alloys have been the predominant thermoelectric materials widely utilized in recent years.⁶ However, there is a noticeable shift in research towards investigating alternative materials like SnSe ⁷ and high-entropy thermoelectric materials,⁸ which have gained heightened attention owing to their promising properties. The continuous pursuit of enhancing performance and improving energy conversion efficiency remains a prominent and active research field. Researchers are motivated to discover innovative strategies, optimize material composition, and explore novel fabrication techniques to advance thermoelectric technology toward greater efficiency and practical application.

The thermoelectric performance is closely tied to their chemical bonds and structural features. The type of chemical bonding in a material strongly affects its electrical and thermal conductivity, thereby influencing its thermoelectric efficiency. By regulating and manipulating the chemical bonds in a material, researchers can potentially unlock new avenues for optimizing thermoelectric performance.

Chemical bond engineering presents a promising avenue for tailoring the electronic structure, carrier transport characteristics, and phonon scattering behavior of thermoelectric materials.⁹ By modifying the chemical composition, crystal structure, and bonding configurations, it is feasible to manipulate the band structure, improve carrier mobility, optimize carrier concentration, and reduce phonon thermal conductivity.¹⁰ These adjustments can ultimately lead to improvements in the thermoelectric

characteristics, such as the Seebeck coefficient, electrical conductivity, thermal conductivity, and figure of merit (zT).

Therefore, comprehending the chemical bond mechanism holds immense significance, not only for expanding the knowledge of thermoelectric materials but also for facilitating material design. Consequently, elucidating the bonding mechanisms in thermoelectric materials such as Bi_2Te_3 , SnSe , and high-entropy thermoelectrics, and extrapolating this understanding to other material families, constitute the primary focus of this thesis.

1.2 Structure and Goals of This Work

Understanding the chemical bonding mechanism is crucial for improving thermoelectric material performance, as it is one of the most fundamental factors influencing material properties. This study focuses on chalcogenides such as Bi_2Te_3 , utilized in real-world applications; SnSe , abundant in elemental sources and low in toxicity; and high-entropy thermoelectrics, gaining significant attention. The main studies are as follows:

First, the fundamental principles of thermoelectric materials are discussed, and the features of metavalent bonding are identified. Metavalent materials lie between covalently and ionically bonded materials as well as metals, but are distinct from all.

The following [Chapter 3](#) presents all experimental methods, encompassing sample preparation, as well as optical and electrical characterization. Atom Probe Tomography, a crucial characterization technique in this thesis, will also be introduced.

Then in the fourth chapter, three *p*-type bismuth telluride materials doped with Sb at varying compositions were prepared to examine the chemical bonding origin of superior thermoelectric properties near room temperature. Taking bismuth telluride, a classic compound renowned for its excellent thermoelectric properties, as a case study, the concept of metavalent bonding is introduced from the perspective of several physically observable features.

Subsequently, leveraging the theory that metavalent bonds crucially enhance thermoelectric properties, and utilizing the ET-ES map, which categorizes various chemical bonding mechanisms, it is found that the AgVVI_2 solids exhibit metavalent bond characteristics. Consequently, in [Chapter 5](#), attempts are made to heavily dope AgVVI_2 into SnSe , aiming to augment the thermoelectric properties of SnSe alloys across a wide

temperature range through metavalent bonding.

Lastly, high-entropy thermoelectrics comprising PbVI and AgVVI_2 were examined to explore the role of metavalent bonding by adjusting the degree of charge transfer.

[Chapter 7](#) provides a summary of conclusions and discusses future outlooks.

These studies offer valuable insights into the bonding mechanism in thermoelectric materials and present a new opportunity for nanoscale analysis and material optimization through doping. Researchers then can develop innovative strategies to enhance the performance and efficiency of thermoelectric materials, unlocking their full potential for practical applications.

2 Fundamentals of Thermoelectrics and Metavalent Bonding

2.1 Thermoelectric Principles

Thermoelectric materials, as clean energy sources, facilitate direct conversion between thermal and electrical energy.^{2,11} The thermoelectric effect, discovered in the early 19th century, involves the directional movement of carriers within a material due to a temperature gradient, encompassing the Seebeck, Peltier, and Thomson effects.^{3,5}

2.1.1 Thermoelectric Effects

Seebeck effect

In 1821, the German scientist Thomas Johann Seebeck discovered that when two different conductors or semiconductors (A and B) are connected, a temperature difference at the contact point (represented as T_h and T_c for the hot and cold ends, respectively) results in an accumulation of charge in the circuit they form.^{3,5,12,13} The quantity of accumulated charge depends on the material's intrinsic properties.¹³ Upon reaching a certain threshold, this accumulated charge induces a built-in electric field, facilitating further charge diffusion to establish a dynamic equilibrium within the material, as illustrated in Figure 2.1 (a). Then at the open circuit position of material B, a weak thermoelectromotive force ΔV can be measured, which is defined as:

$$\Delta V = S_{AB} \cdot (T_h - T_c) \quad (2.1)$$

where S_{AB} is the relative Seebeck coefficient of the two conductor materials A and B. If the temperature difference (ΔT) between T_h and T_c is relatively small, this relationship is linear, and S_{AB} can be considered constant. The unit thermoelectromotive force is called the Seebeck coefficient (unit: V K^{-1}) and is defined as:

$$S_{AB} = \lim_{\Delta T \rightarrow 0} \frac{\Delta V}{\Delta T} \quad (2.2)$$

Depending on the temperature gradient and the characteristics of A and B materials, the Seebeck coefficient is positive when current flows from A to B at the hot junction, and negative otherwise.

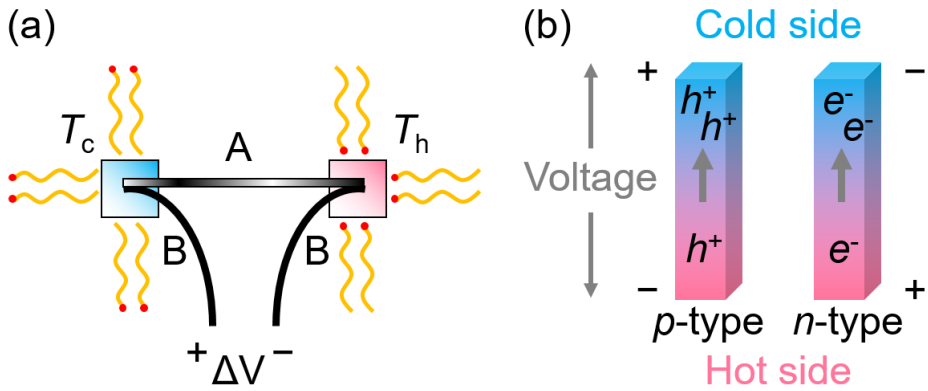


Figure 2.1 | (a) A model of the Seebeck effect circuit. The voltage difference, ΔV , produced across the terminals of an open circuit made from a pair of dissimilar materials, A and B. (b) Schematic illustrations of power generation (Seebeck effect). An applied temperature difference causes charge carriers in the material (electrons or holes) to diffuse from the hot side to the cold side, resulting in a flow of current through the circuit.

The thermoelectric power generation process via the Seebeck effect is depicted in Figure 2.1 (b). *p*-type and *n*-type semiconductors are interconnected in series through electrodes to create a closed circuit. A temperature gradient is established at the upper and lower ends of the semiconductors, leading to carrier migration from the hot end to the cold end. This migration results in charge accumulation at the latter, followed by the flow of accumulated charges through the wire to the load, inducing a voltage across the load and enabling thermoelectric power generation.

Peltier effect

In 1834, the French physicist Jean Charles Athanase Peltier discovered the converse of the Seebeck effect.^{3,5,13,14} When two dissimilar conductors or semiconductors, A and B, are connected into a closed loop, an external current through the junctions at the ends causes heat absorption and release. The rate of heat absorption and release is directly proportional to the current I_{input} passing through the circuit, and this phenomenon of heat absorption and release caused by an applied external voltage is called the Peltier effect, as depicted in Figure 2.2 (a). The heat absorption or release (q) at the junction between A and B is termed Peltier heat and can be expressed as

$$q = \pi_{AB} I_{\text{input}} \quad (2.3)$$

where π_{AB} is the Peltier coefficient, with units of W A^{-1} .

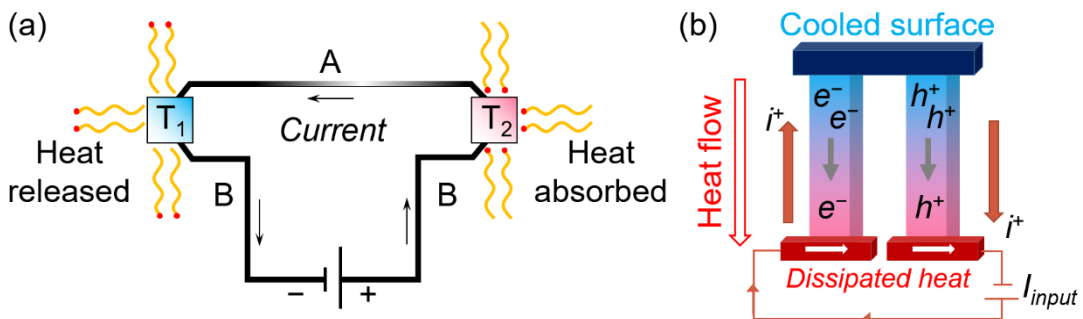


Figure 2.2 | Illustrations of (a) a Peltier effect circuit, and (b) a thermoelectric module for active refrigeration (Peltier effect). Heat evolves at the upper junction and is absorbed in the lower junction when a current is made to flow through the circuit.

The Peltier effect can be applied to solid-state temperature difference refrigeration, and its working principle is shown in Figure 2.2 (b). A direct current flowing through a series-connected circuit of *p*-type and *n*-type semiconductors induces heat transport due to carrier movement. This results in heat absorption at one end (cold side) and heat release at the other (hot side) of the *p*-*n* junction. The direction of heat flow (cooling or heating) depends on the current direction.

Thomson effect

In the 1850s, as thermodynamic theory gradually matured, William Thomson analyzed the aforementioned two effects and observed a temperature difference phenomenon within the same homogeneous conductor, rather than between two different materials.^{3,5,14} Specifically, when a temperature gradient (ΔT) existed between the two ends of a homogeneous material and an electric current I was applied, the material not only generated Joule heat but also experienced additional heat absorption or release, known as the Thomson effect. The corresponding rate of heat absorption and release shown in Figure 2.3 is:

$$Q = \beta I \Delta T \quad (2.4)$$

Among them, β is defined as the Thomson coefficient with a unit of V K^{-1} . When I flows in the same direction as ΔT , β is positive if the conductor absorbs heat, i.e. gets cold, and negative if the conductor releases heat, i.e. gets warm. William Thomson approximated the relationship between the above three thermoelectric effects based on the theory of thermodynamic equilibrium, that is, the Kelvin relationship:^{5,14}

$$S_{AB} = \pi_{AB}/T \quad (2.5)$$

$$\beta_A - \beta_B = T \frac{dS_{AB}}{dT} \quad (2.6)$$

By deriving Equation (2.6), the absolute Seebeck coefficient for a single material can be obtained:

$$S = \int_0^T \frac{\beta}{T} dT \quad (2.7)$$

Therefore, when measuring the absolute Seebeck coefficient of an unknown material in practice, it can be obtained by connecting it in series with a material of known Seebeck coefficient and measuring the loop Seebeck coefficient.

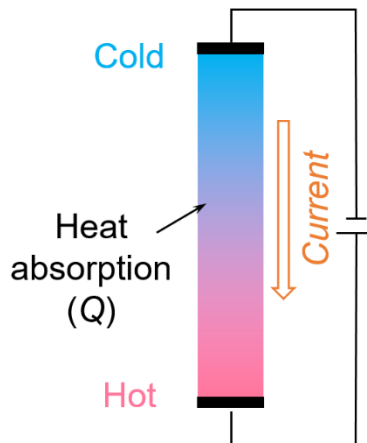


Figure 2.3 | Schematic diagram of Thomson effect.

2.1.2 Figure of Merit

To compare thermoelectric materials, the thermoelectric properties are usually characterized by a dimensionless thermoelectric figure of merit,¹⁴ zT , which can be expressed as

$$zT = \frac{S^2 \sigma}{\kappa_{\text{tot}}} T \quad (2.8)$$

where S is the Seebeck coefficient, and σ is the electrical conductivity, κ_{tot} is the total thermal conductivity, and T stands for absolute temperature. $S^2 \sigma$ is known as the power factor (PF) with the unit of $\mu\text{W cm}^{-1} \text{K}^{-2}$. It represents the electrical transport capability. A high zT value is crucial for optimizing thermoelectric device efficiency, which requires

a high Seebeck coefficient, high electrical conductivity, and low thermal conductivity. For thermoelectric devices, the maximum power generation efficiency (η_{\max}) and cooling efficiency (ϕ_{\max}) can be expressed by the following equations, respectively:

$$\eta_{\max} = \frac{T_h - T_c}{T_h} \cdot \frac{(1+z\bar{T})^{1/2} - 1}{(1+z\bar{T})^{1/2} + \frac{T_c}{T_h}} \quad (2.9)$$

$$\phi_{\max} = \frac{T_c}{T_h - T_c} \cdot \frac{(1+z\bar{T})^{1/2} - \frac{T_h}{T_c}}{(1+z\bar{T})^{1/2} + 1} \quad (2.10)$$

where $\frac{T_h - T_c}{T_h}$ is the Carnot cycle limit efficiency, and \bar{T} is the average temperature of the cold and the hot end. The equations show that the maximum achievable efficiency is related to the temperature difference between the hot and cold ends and zT within the Carnot cycle efficiency range.¹⁵ While zT will not be higher than the Carnot cycle efficiency, as shown in Figure 2.4, illustrating the dependence of the maximum power generation efficiency on both hot-end temperature and zT . For medium and high-temperature power generation, materials with zT of 1 exhibit a maximum conversion efficiency near 15%, considered practical for certain applications. At $zT=2$, the efficiency reaches around 20%, making it suitable for waste heat recovery. Notably, when zT reaches 3, the efficiency approaches 20-30%, comparable to traditional compressors.

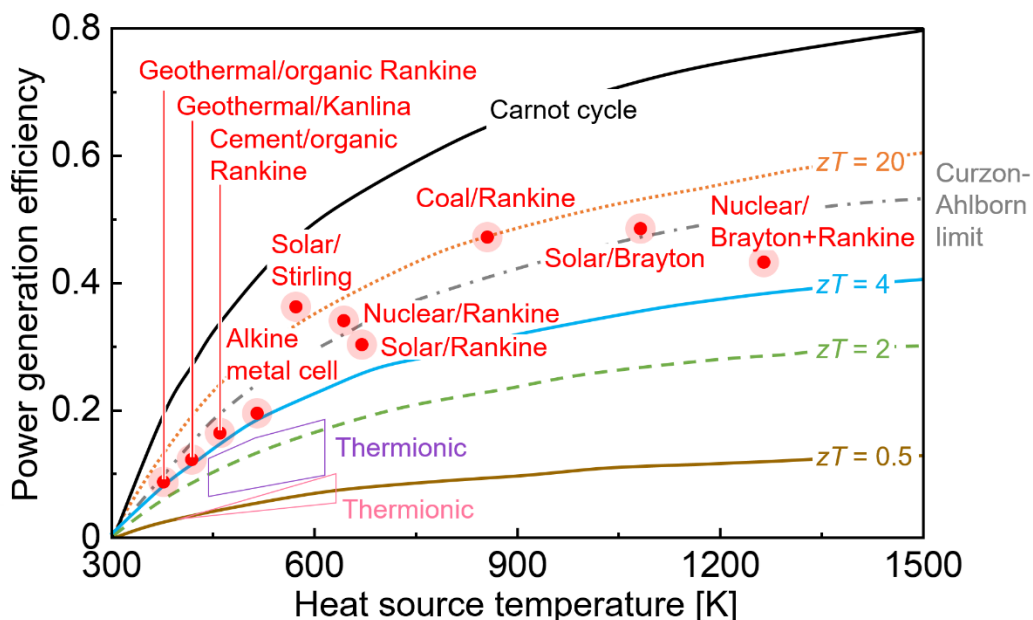


Figure 2.4 | Dependence of power generation efficiency of the thermoelectric generator on zT and hot end temperature (cold end temperature is 300 K).^{16,17}

2.1.3 Strategies to Optimize zT

The zT value reflects the interaction between charge carriers and phonons, as well as electrical and heat transport properties involved, accompanied in three crucial parameters: Seebeck coefficient, electrical conductivity, and thermal conductivity. These parameters are often inherently coupled, making the independent optimization of properties challenging. A thorough understanding of the transport mechanisms of electricity (charge carriers) and heat (phonons) is essential for developing high-performance thermoelectric materials.

Optimization of electrical transport properties

The electrical conductivity (σ) can be estimated from the concentration of charge carriers and their mobility. In semiconductors, the Drude-Sommerfeld model (free electron model)¹⁸ provides a foundation for deriving the equation for σ :

$$\sigma = -ne\mu \quad (2.11)$$

Where n is the carrier concentration (m^{-3}), e is the electron charge, μ is the carrier mobility ($\text{m}^2 \text{V}^{-1} \text{s}^{-1}$). The carrier concentration can be calculated from the Fermi-Dirac distribution function,^{19,20} describing the probability of occupation of energy states by electrons at thermal equilibrium. It calculates the number of electrons in the conduction band.

$$n = N_c \cdot \exp\left(\frac{E_F - E_c}{k_B T}\right) \quad (2.12)$$

where n is the electron (or hole) concentration, N_c is the effective density of states in the conduction band, E_F is the Fermi level, E_c is the energy of the conduction band edge, k_B is Boltzmann's constant, T is the temperature. The carrier concentration depends on the temperature and the energy difference between the conduction band edge and the Fermi level. Higher temperatures or closer Fermi levels to the conduction band edge increase carrier concentration.

The mobility of charge carriers describes the ease of movement for charge carriers under an electric field in a semiconductor. It is related to the relaxation time (τ) between scattering events (phonon-electron, electron-electron, and ionized-impurity, etc.) and conductivity effective mass (m_σ^*)²¹⁻²⁴

$$\mu \propto \tau \frac{e}{m_\sigma^*} \quad (2.13)$$

Carrier mobility is inversely proportional to their effective mass, meaning heavier carriers have lower mobility,²⁵ while longer relaxation times lead to higher mobility.

The Single Parabolic Band (SPB) model is an effective tool for analyzing the carrier transport and simulating physical quantities like the Lorenz constant, which quantifies the ratio of electrical conductivity to thermal conductivity.²⁶ The Seebeck coefficient, the Fermi integrals (F_i), and the reduced Fermi energy level (η_F) are denoted as

$$S = \mp \frac{k_B}{e} \left[\eta - \frac{\left(r_s + \frac{5}{2}\right) F_{r_s + \frac{3}{2}}(\eta)}{\left(r_s + \frac{3}{2}\right) F_{r_s + \frac{1}{2}}(\eta)} \right] \quad (2.14)$$

$$F_i(\eta) = \int_0^\infty \frac{\varepsilon^i d\varepsilon}{1 + \exp(\varepsilon - \eta)} \quad (2.15)$$

$$\eta_F = \frac{E_F}{k_B T} \quad (2.16)$$

where r_s is the scattering factor, and ε is the reduced carrier energy ($\varepsilon = \frac{E}{k_B T}$). At temperatures exceeding Debye temperature (Θ_D), acoustic phonon scattering ($r_s = -0.5$) dominates the carrier transport mechanism, leading to a simplified expression for S :

$$S = \frac{8\pi^2}{3} \cdot \frac{k_B^2 T}{e h^2} m_d^* \left(\frac{\pi}{3n}\right)^{\frac{2}{3}} \quad (2.17)$$

For degenerate semiconductors, the carrier concentration, density of states (DOS) effective mass (m_d^*), relaxation time (τ), Fermi level, and r_s significantly influence S and σ . A high Seebeck coefficient can be obtained with low carrier concentration and large effective mass, while large electrical conductivity benefits from high carrier concentration and mobility. Thus optimizing thermoelectric properties requires balancing these two competing factors. Figure 2.5 (a) illustrates the trade-off between optimal carrier concentration (n_{opt}) and electrical conductivity for maximizing zT . In effective thermoelectrics (typically heavily doped semiconductors, $n_{\text{opt}}: 10^{19} \sim 10^{20} \text{ cm}^{-3}$), the PF peaks at a higher carrier concentration compared to zT .²⁷ However, most materials exhibit intrinsic carrier concentrations outside the optimal range, necessitating optimization through doping or other methods.²⁸⁻³⁰ For instance, *p*-type materials require decreased carrier concentration achievable by donor doping, while the opposite applies to *n*-type ones. Self-doping, which regulates intrinsic point defects, offers an effective strategy for carrier concentration optimization, as exemplified in Bi_2Te_3 -based thermoelectrics.^{6,31,32}

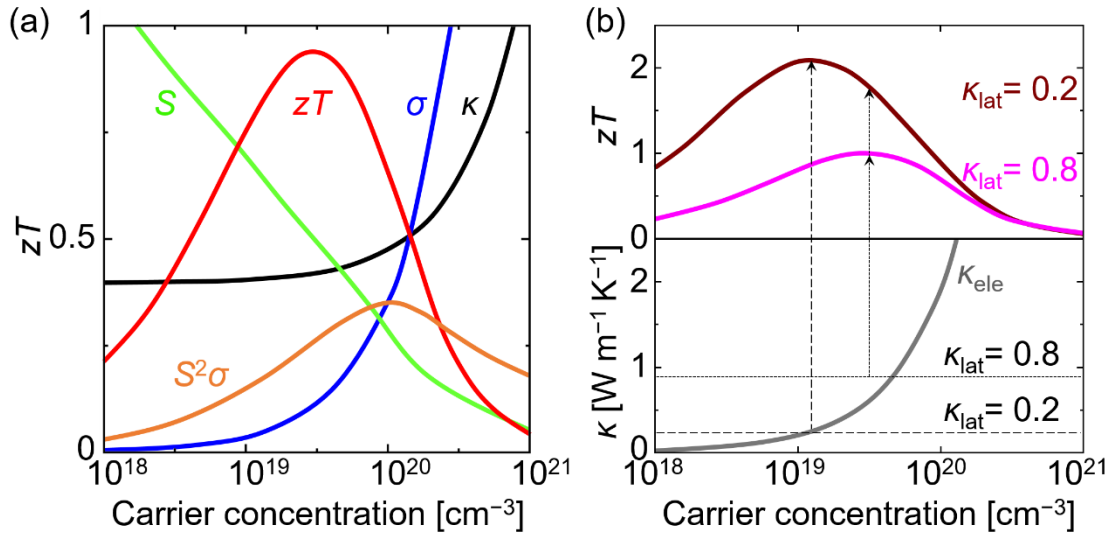


Figure 2.5 | (a) zT optimization involves balancing κ (0 to $10 \text{ W m}^{-1} \text{ K}^{-1}$) with S (0 to $500 \mu\text{V K}^{-1}$) and σ (0 to $5000 \Omega^{-1} \text{ cm}^{-1}$).^{27,33} Typically, effective compounds are heavily doped semiconductors with carrier concentrations between 10^{19} and 10^{21} cm^{-3} . $S^2\sigma$ reaches its peak at a higher carrier concentration than zT . This difference is more pronounced in newer lower- κ_{lat} materials. The trends are modeled using Bi_2Te_3 based on empirical data.^{27,34} (b) Reducing κ_{lat} offers a two-fold benefit for zT .²⁷ A model system (Bi_2Te_3) with κ_{lat} of $0.8 \text{ W m}^{-1} \text{ K}^{-1}$ and carrier-dependent κ_{ele} (gray curve) achieves an optimized zT of 0.8. Lowering κ_{lat} to $0.2 \text{ W m}^{-1} \text{ K}^{-1}$ directly increases zT . Furthermore, this reduction allows for reoptimization of the carrier concentration (reduction), leading to a reoptimized zT via lower κ_{ele} and higher S .

The optimal electronic performance is heavily influenced by several effective masses, i.e., DOS effective mass (m_d^*), the band effective mass (m_b^*), and the conductivity effective mass (m_σ^*) of electrons, relevant for describing charge transport within the parabolic band approximation.^{26,35} m_b^* is a fundamental quantity describing the curvature of the E-k dispersion relation near band extrema (minima for conduction band, maxima for valence band) compared to a perfect parabola.^{36,37} A steeper curvature corresponds to a smaller effective mass relative to the free electron mass (m_e).^{38,39} m_b^* can be derived from the energy band (E) with respect to the wave vector (\mathbf{k}):²²

$$m_b^* = \frac{\hbar^2}{\frac{d^2E}{d^2k}} \quad (2.18)$$

where \hbar is the reduced Planck constant.

m_d^* is crucial for calculating the DOS within a band.⁴⁰⁻⁴³ A higher m_d^* signifies a larger DOS at a specific energy level. Band degeneracy (N_v), where multiple electronic states

occupy the same energy level, also affects the DOS.⁴⁴⁻⁴⁷ As many high-performance semiconductors are heavily doped with optimal carrier concentration (n_{opt}) varies with $(m_{\text{d}}^* T)^{\frac{2}{3}}$, a high Seebeck coefficient can be achieved by adjusting the effective mass.^{35,38,40}

In a single-carrier system under classical statistics, n_{opt} scales with $(m_{\text{d}}^* T)^{\frac{2}{3}}$, suggesting that a high m_{d}^* benefits both the Seebeck coefficient and n_{opt} .^{33,48} High m_{d}^* can be achieved through high band degeneracy, but flat bands, while also increasing m_{d}^* , negatively impact carrier mobility, limiting thermoelectric performance.³³ In isotropic materials, the following relationship holds:^{33,49}

$$m_{\text{d}}^* = N_{\text{v}}^{\frac{2}{3}} m_{\text{b}}^* \quad (2.19)$$

$$m_{\text{b}}^* = [(m_{\perp}^*)^2 m_{\parallel}^*]^{\frac{1}{3}} \quad (2.20)$$

$$m_{\sigma}^* = 3\left(\frac{2}{m_{\perp}^*} + \frac{1}{m_{\parallel}^*}\right)^{-1} \quad (2.21)$$

where N_{v} , m_{\parallel}^* and m_{\perp}^* are the band degeneracy, the transverse effective mass and the longitudinal effective mass, respectively. m_{b}^* play a decisive role for m_{d}^* : in most cases, the increase in m_{d}^* is due to the increase in m_{b}^* . Higher m_{b}^* generally reduces carrier mobility and electrical conductivity.^{38,50}

The equations illustrate how electronic properties are influenced by the effective mass tensor, band degeneracy, and carrier relaxation time. m_{σ}^* refers to the effective mass of charge carriers that contribute to σ .⁵¹ High m_{σ}^* signifies low carrier mobility, impeding the charge carrier movement, thus reducing σ .⁵¹ A larger $m_{\text{b}}^*/m_{\sigma}^*$ results in a higher PF .²² A large N_{v} is desirable because it can significantly enhance m_{d}^* resulting in a pronounced S without compromising carrier mobility.⁴⁴ m_{d}^* together with mobility and electron mass (m_{e}) constitute weighted mobility (μ_{w}), predicting the electrical properties:⁵²⁻⁵⁴

$$\mu_{\text{w}} = \mu \frac{m_{\text{d}}^*}{m_{\text{e}}} \quad (2.22)$$

However, μ is usually low in bands with a high m_{b}^* . For materials with dominant acoustic phonon scattering (common in excellent thermoelectrics) and isotropic band structure:⁵³

$$\mu \propto (m_{\text{b}}^*)^{\frac{5}{2}} \quad (2.23)$$

Thus using Equations (2.12), (2.20) and (2.24), μ_W can be derived as below:

$$\mu_W \propto \frac{N_v}{m_b^*} \quad (2.24)$$

This suggests that increasing m_b^* would negatively impact PF , while greater band degeneracy leads to higher PF . N_v is closely related to the symmetry of the crystal structure.⁵⁵ High-symmetry crystal structures and symmetry-related multi-valley carrier structures are common features of superior thermoelectric materials.⁵⁶⁻⁵⁹ The layered crystal structure of SnSe leads to an anisotropic m_b^* , resulting in a dependence of zT on the measurement direction.^{41,60-63} Constructing cubic highly-symmetric crystal structures is a promising strategy to achieve high Seebeck coefficient due to the large N_v .^{22,64} Another strategy to enhance N_v is band engineering through multiple band convergence within the Brillouin zone (BZ) within a few $k_B T$ energy range near the Fermi level.^{65,66} Section 2.3.3 will elaborate on the influence of band degeneracy on electrical properties from the perspective of the chemical bonding origin.

Numerous studies have explored enhancing the Seebeck coefficient by manipulating the effective mass via band engineering.^{55,67} However, this approach often comes at the expense of decreased carrier mobility. Thus, separately improving the effective mass is not necessarily conducive to improving the zT value, and it is even believed that reducing the effective mass of the energy band can increase the zT value in some systems. Therefore, balancing the relationship between effective mass and carrier mobility to achieve the maximum zT value still needs further research and verification.

Reduction of thermal conductivity

Electrons transport heat as well as charge, thus contributing to the thermal conductivity, which in turn decreases zT . The total thermal conductivity (κ_{tot}) of a semiconductor can be approximated as the sum of the contributions from free electrons (or holes), denoted as κ_{ele} , and the lattice thermal conductivity (κ_{lat}) arising from phonons (atomic vibrations).

$$\kappa_{\text{tot}} = \kappa_{\text{ele}} + \kappa_{\text{lat}} \quad (2.25)$$

The electronic thermal conductivity is determined by the same transport function σ_E that governs the Seebeck coefficient and electrical resistivity. For a system with only one type of charge carrier (either electrons or holes), κ_{ele} is generated by the random thermal movement of carriers in the crystal, which follows the Wiedemann-Franz law, namely:

$$\kappa_{\text{ele}} = L\sigma T \quad (2.26)$$

where T is the absolute temperature, and L is the Lorenz number. Similar to the Seebeck coefficient, the Lorenz number primarily relies on the position of the Fermi level in a single-band system. Thus, a reliable estimation of L (at any temperature) can be derived solely from the measured thermopower ($|S|$).⁶⁸

$$\frac{L}{10^{-8} \text{ W } \Omega \text{ K}^{-2}} = 1.5 + \exp\left(\frac{-|S|}{16 \mu\text{V K}^{-1}}\right) \quad (2.27)$$

where L is expressed in unit of $10^{-8} \text{ W } \Omega \text{ K}^{-2}$ and S in $\mu\text{V K}^{-1}$. Hence, the most common method for expressing phonon thermal conductivity is by computing

$$\kappa_{\text{lat}} = \kappa_{\text{tot}} - L\sigma T \quad (2.28)$$

where κ_{tot} represents the experimentally measured value, and L is estimated based on the measured value of $|S|$.

In cases where a significant number of both electrons and holes contribute to charge transport (bipolar charge transport), the thermoelectric properties experience significant influence. This situation arises when electrons are excited across the band gap, generating minority charge carriers (e.g., holes in an n -type material) alongside majority charge carriers (e.g., electrons in an n -type material). Bipolar effects manifest in materials with small band gaps at high temperatures $k_B T \approx E_{\text{gap}}$ and intrinsic (undoped) semiconductors where $n_{\text{ele}} \approx n_{\text{hole}}$.⁶⁹ The total thermal conductivity (κ_{tot}) can be expressed if κ_{lat} exhibits a rise at high temperatures due to the bipolar effect, then $(\kappa_{\text{tot}} - L\sigma T)$ can be more appropriately referred to as $\kappa_{\text{lat}} + \kappa_{\text{bip}}$. Phonon transport in crystals, similar to carrier transport, is influenced by various scattering mechanisms.^{2,70} This analogy between phonon and molecular motion allows leveraging concepts from molecular dynamics theory to describe κ_{lat} in solids:

$$\kappa_{\text{lat}} = \frac{1}{3} C_V v_g^2 \tau_p \quad (2.29)$$

where C_V is the heat capacity at constant volume, v_g is the phonon group velocity, and τ_p is the phonon relaxation time. v_g can be described by the spring-ball model:

$$v_g \approx \sqrt{\frac{F}{M}} \quad (2.30)$$

where F represents the force constant between atoms, quantifying the strength of the

chemical bond, and M is the reduced atomic mass. Soft chemical bonds, yielding a low F value, are advantageous for achieving low κ_{lat} . Introducing phonon scattering centers reduces τ_p . This, in turn, shortens the phonon mean free path \bar{l}_p based on the relationship:

$$\bar{l}_p = v_g \tau_p \quad (2.31)$$

\bar{l}_p typically ranges from a few angstroms to hundreds of nanometers. For the Debye model approximation, a certain wave vector k can correspond to one longitudinal wave and two independent shear waves. These waves have distinct velocities: v_l for the longitudinal wave and v_t for the transverse wave, which can be related to the shear (G) and bulk moduli (B) by the Navier's equations⁷¹

$$\begin{aligned} v_l &= \left(\frac{3B + 4G}{3\rho} \right)^{\frac{1}{2}} \\ v_t &= \left(\frac{G}{\rho} \right)^{\frac{1}{2}} \end{aligned} \quad (2.32)$$

Then the average sound velocity (v_s) in a polycrystalline system is evaluated by⁷²

$$v_s = \left[\frac{1}{3} \left(\frac{1}{v_l^3} + \frac{2}{v_t^3} \right) \right]^{\frac{1}{3}} \quad (2.33)$$

The Debye temperature can be estimated using v_s , with V_a denotes the atomic volume:⁷³

$$\Theta_D = \frac{\hbar}{k_B} \left(\frac{3}{4\pi V_a} \right)^{\frac{1}{3}} v_s \quad (2.34)$$

The phonon contribution to the heat capacity at constant volume (C_V) exhibits two limiting behaviors: a constant value at temperature much higher than Θ_D (Dulong-Petit Limit) and a T^3 dependence at lower temperatures (Debye's T^3 law).⁷⁴

$$C_V(x) dx = \frac{3k_B}{2\pi^2 v_s^3} \left(\frac{k_B T}{\hbar} \right)^2 \int_0^{\Theta_D/T} \frac{x^4 e^x}{(e^x - 1)^2} dx \quad (2.35)$$

where $x = \frac{\hbar\omega}{k_B T}$, is the reduced phonon frequency. Similarly, according to the Debye-Callaway model, the expression for the lattice thermal conductivity can be defined as:^{75,76}

$$\kappa_{\text{lat}} = \frac{k_B}{2\pi^2 v_s} \left(\frac{k_B T}{\hbar} \right)^2 \int_0^{\Theta_D/T} \tau_{\text{tot}}(x) \frac{x^4 e^x}{(e^x - 1)^2} dx \quad (2.36)$$

where τ_{tot} is the total relaxation time, and $k_B \Theta_D = \hbar v_s (6\pi^2 N)^{1/3}$. Phonon relaxation times in solid-state semiconductors depend on various scattering mechanisms (phonon-

phonon, crystal defect, carrier) with distinct relaxation time expressions. The total relaxation time is determined by these combined mechanisms using Matthiessen's rule:

$$\frac{1}{\tau_{\text{tot}}} = \frac{1}{\tau_U} + \frac{1}{\tau_N} + \frac{1}{\tau_{\text{GB}}} + \frac{1}{\tau_{\text{PD}}} + \frac{1}{\tau_C} + \dots \quad (2.37)$$

where τ_U , τ_N , τ_{GB} , τ_{PD} and τ_C are relaxation time for phonon-phonon Umklapp scattering (U process), phonon-phonon normal scattering (N process), grain boundary scattering, point defect scattering and carrier scattering, respectively. Lowering κ_{lat} through phonon scattering at different length scales directly enhance zT , while requires the further re-optimization of carrier concentration for additional zT boost (Figure 2.5 (b)).

Equations (2.33) and (2.36) indicate that specific heat, phonon group velocity, Debye temperature, and phonon relaxation time all influence lattice thermal conductivity. Tailoring these parameters offers a route for κ_{lat} optimization. However, manipulating specific heat and Debye temperature often proves challenging. Instead, incorporating heavy elements and materials with soft chemical bonds to achieve lower sound velocity and introducing phonon scattering centers to reduce the relaxation time are considered more effective. This approach necessitates a thorough understanding of the relationship between material properties, crystal structure, and chemical bonding.

2.2 A Novel Chemical Bonding Mechanism

In solid-state physics, the bonding type between atoms in a crystal lattice determines its physical and chemical properties.^{9,10,77,78} Typically, materials consist of atoms interacting via valence electrons, close to the nuclei and primarily influenced by the positive charges of the nuclei. Inner electrons, however, are shielded by outer electrons and do not participate in bonding due to a lack of interaction with other atoms. Valence electrons, influenced by orbital spatial distribution, facilitate the formation of chemical bonds between atoms. Electron spatial distribution varies based on the atom types involved and their relative positions. Bonding types, simplified models of valence electron interactions, are characterized by electron localization/delocalization.⁷⁹

For decades, it has been established that bonds in solids fall into five types: three "primary bonds" (covalent, ionic, and metallic) and two weaker bonds (hydrogen and van der Waals).⁸⁰ In the three primary bonding types, valence charges are either localized as an electron pair (covalent), reside on the ionic core due to significant charge transfer (ionic),

or form a rather delocalized electron cloud (metallic). Various chemical bonds offer straightforward and convenient performance predictions. The rather delocalized nature of conducting electrons in metals results in high electrical conductivities, as demonstrated by Drude-Sommerfeld theory.¹⁸ The strong electrostatic attraction between cations and anions, stemming from charge transfer in ionic compounds and localized additional electrons, accounts for their large band gap and very low conductivity. In covalent materials, band gaps and conductivities typically fall between those of metals and ionic compounds, given that the shared electron pair is localized and jointly owned by the involved nuclei.

Crystalline chalcogenides like GeTe or PbTe exhibit a unique combination of properties stemming from a bonding type, which significantly differs from metallic, ionic, and covalent bondings.^{22,81-83} This unconventional combination of properties is also present in other chalcogenides such as SnTe, PbTe, PbSe, and PbS.²² Specifically, this bonding type identified in thermoelectric materials, notably in chalcogenides, *metavalent bonding* (MVB), will be extensively investigated. This is because most materials used in this thesis may potentially demonstrate MVB, a concept that is still relatively new.⁸⁴ To identify bonding mechanisms, Wuttig et al. proposed using five measurable parameters as bond indicators,⁷⁷ summarized in Table 2.1.

Table 2.1 | Five properties, i.e., electronic conductivity (σ), ECoN, optical dielectric constant (ϵ_2^{\max}), Born effective charge (Z^*), and Grüneisen parameter (γ), that distinguish chemical bonding mechanisms.⁷⁸

Bonding identifier	Ionic (e.g., NaCl)	Covalent (e.g., Si)	Metavalent (e.g., GeTe)	Metallic (e.g., Cu)
σ	Very low ($< 10^{-8} \text{ S cm}^{-1}$)	Low to moderate ($10^{-8}\text{--}10^2 \text{ S cm}^{-1}$)	Moderate ($10^1\text{--}10^4 \text{ S cm}^{-1}$)	High ($> 10^5 \text{ S cm}^{-1}$)
ECoN ^a	4 (ZnS), 6 (NaCl), 8 (CsCl)	8-N rule satisfied	8-N rule not satisfied	8 (BCC) 12 (FCC/HCP)
ϵ_2^{\max}	Low ($\approx 2\text{--}3$)	Moderate ($\approx 5\text{--}15$)	High (> 15)	— ^b
Z^*	Low (1-2)	Moderate (2-3)	High (4-6)	Vanishes (0)
γ	Moderate (2-3)	Low (0-2)	High (> 3)	Low (0-2)

a) The provided structure types for ionic and metallic systems are representative.

b) This indicator is typically not applicable to metallic systems.

Electrical conductivity is directly proportional to the degree of electron delocalization and is assessable via methods like the van der Pauw setup⁸⁵ or the 4-point probe method,⁸⁶ detailed in [Section 3.3](#). Effective Coordination Number (ECoN) is a structural identifier that indicates the number of neighbors. Metallic bonding involves atoms with numerous neighbors, facilitating the existence of half-filled orbitals. Conversely, covalent bonds satisfy the octet rule, resulting in filled bands. Metavalent bonding exhibits a high ECoN of 8 for BCC and 12 for FCC and HCP structures. ECoN can be estimated by X-ray diffraction (XRD) measurement or a more precise technique, extended X-ray absorption fine structure (EXAFS).

The dielectric constant (ϵ_{∞}) represents the electronic polarizability of a material, detectable via Fourier transform infrared spectroscopy (FTIR), as explained in [Section 3.2.4](#). MVB has large optical dielectric constants ϵ_{∞} compared to conventional chemical bonding. IR-active phonon measurements from FTIR can determine the Born effective charge (Z^*), quantifying the change in polarization (P) due to an atomic displacement (u):

$$Z^* = \frac{dP(u)}{du} \quad (2.38)$$

The Peierls distortion (PD) was initially utilized to elucidate the formation of bandgaps, and metavalent materials tend to exhibit a weak PD value owing to the alignment of the p -orbitals of adjacent atoms. Increased Peierls distortions result in decreased bonding polarization, leading to lower Z^* values. While metals lack localized bonds and instead possess a free electron gas, rendering the Born effective charge inapplicable.

The Grüneisen parameter (γ_i) characterizes the degree of anharmonicity in a material, which quantifies how a crystal's volume(V) change relates to its phonon frequencies (ω_i):

$$\gamma_i = \frac{V}{\omega_i} \frac{\partial \omega_i}{\partial V} \quad (2.39)$$

A larger γ_i generally indicates a stronger degree of anharmonicity in the lattice vibrations, translating to a lower lattice thermal conductivity due to increased phonon-phonon scattering. The detail will be extended in [Section 2.3.1](#). MVB demonstrates a notably high γ_i , where increased anharmonicity leads to a more pronounced change in mode frequency during volume change.²² The Equation (2.40) below can be employed to calculate the Grüneisen parameter if the thermal expansion coefficient (α), elastic bulk modulus (B), and isochoric heat capacity (C_V) are known:⁸⁷

$$\gamma_i = \frac{\alpha B V}{C_V} \quad (2.40)$$

Several characteristics of MVB can be summarized as follows:

- I. Half-filled σ -bonds: MVB primarily involves p-electrons, with negligible participation from s-electrons due to the significant energy separation between the orbitals. This results in an octahedral atomic arrangement and, on average, only one p-electron (half an electron pair) per bond, unlike the electron pair in covalent bonds.
- II. Weak distortion: Half-filled bands are susceptible to Peierls-type periodic lattice distortion, causing MVB compounds to deviate slightly from the perfect rocksalt structure. Severe distortion can lead to the breakdown of MVB.
- III. Weak sp-hybridization and electron transfer: The large energy gap between s- and p-orbitals leads to weak orbital hybridization, consistent with minimal structural distortion. Additionally, electron transfer from the cation to the anion is weak due to similar electronegativities or the constituting elements.
- IV. Medium-range interaction: Interatomic interactions extend beyond the first nearest neighbors, characteristic of MVB occurring in crystalline solids sustaining medium-range interactions.
- V. Intermediate between localization and delocalization: MVB lies between electronic localization (covalent) and delocalization (metallic) but is distinct from both, potentially contributing to its "metal-like" electrical conductivity.

Besides these indicators, a map (illustrated in [Figure 2.6](#) below) based on quantum mechanical calculations for the number of electrons being transferred (ET) and shared (ES) between two adjacent atoms aids in quantifying chemical bonding from an alternative perspective. Ionic, covalent, and metallic bonds occupy distinct regions in this map. Notably, MVB materials cluster in the central region, with shared electrons nearing 1 and limited transferred electrons. The notably high values of σ_∞ , Z^* , and γ distinguish MVB from traditional bonding materials, suggesting it cannot be merely a combination of existing mechanisms. Metavalent bonding is a relatively novel type of chemical bonding that involves atoms with an average of three p-orbitals each.^{9,10,22,77,78,80,83,88} When bonded with their six neighbors, these atoms form three σ -orbitals, resulting in an octahedral arrangement. Each σ -orbital is occupied by one electron, leading to a half-filled orbital. For instance, in a perfect cubic crystal arrangement of a single atom type,

such as cubic antimony, electrons can move quite freely within the half-filled orbitals, and this results in a metallic energy band structure.

By identifying the mode of bond breaking, the approach of indicating MVB was later expanded with the probability of multiple events (PME) measured by Atom Probe Tomography (APT).^{22,22,78,78,82,83,89} During APT, a high voltage on a sub-100 nm tip and a laser pulse eject charged ions from the tip surface. Typically, a single ion ("single event") is ejected per laser pulse. However, occasionally, multiple ions ("multiple events") can be ejected. While a low PME is usual, MVB exhibits an extraordinarily high PME, which highlights the "correlative" nature of atoms within MVB compounds. Further details will be provided in Section 3.2.3. PME serves as experimental evidence for chemical bonding indicators, which can assist in designing various materials and is also highly beneficial for thermoelectric applications, as indicated by the ET-ES map.

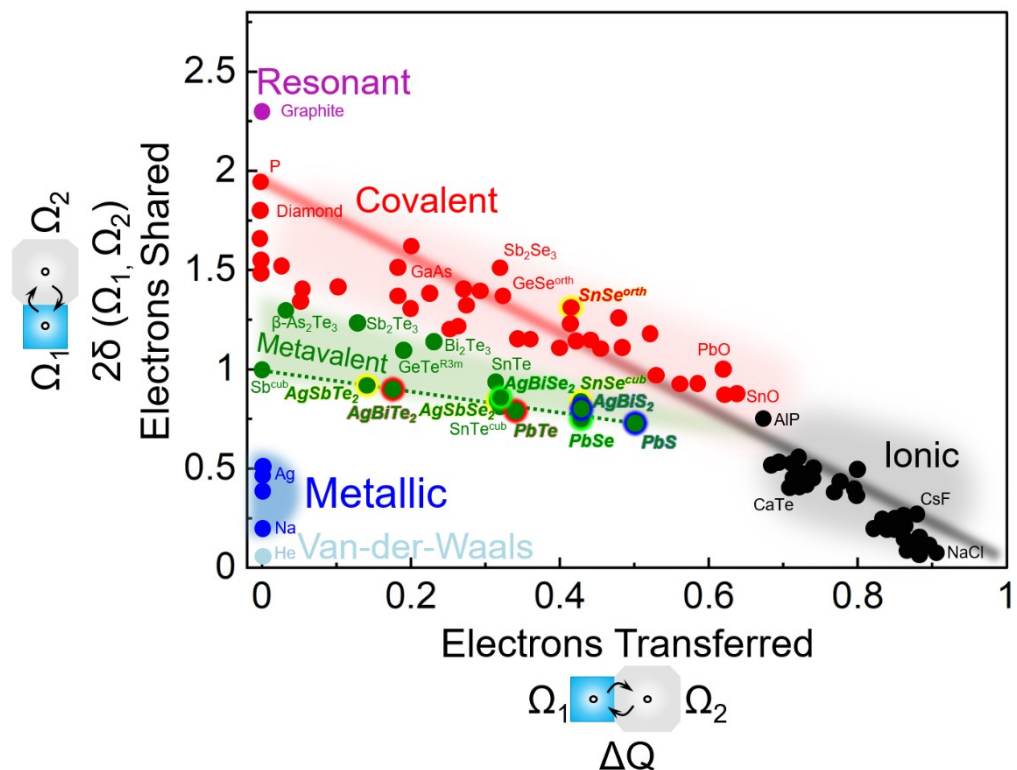


Figure 2.6 | A visualization of a 2D graph that represents electron interactions and bonding in various materials.²² Using a quantum topological approach, the graph shows the amount of electrons transferred (x -axis) and shared (y -axis) between adjacent atoms. A linear trend is observed, with materials possessing ideal rocksalt structure and half-filled p-bonds (e.g., Sb to PbS) lying below those with distorted octahedral coordination and a higher degree of electron sharing. This graph has the potential to identify novel thermoelectric materials.

2.3 Correlations between Thermoelectrics and Metavalent Bonding

As previously demonstrated, chemical bonding correlates with material properties and heavily relies on the spatial distribution of electrons. The thermoelectric properties closely correlate with their electronic structures. Recently, the concept of metavalent bonding offers a new framework for comprehending bonding in complex materials, including those used in thermoelectrics. Charge transfer in metavalent bonding generates polarizable atoms and partially charged species, significantly influencing the electronic structure. The correlation between metavalent bonding and thermoelectric properties has significant implications for designing efficient thermoelectric materials. The following will illustrate the relationship between metavalent bonding and various thermoelectric characteristics from the aspects of carrier concentration, lattice anharmonicity (lattice thermal conductivity), effective mass of charge carriers (electronic band structure), and Fermi surface complexity factor (detailed in [Section 2.3.4](#)).

2.3.1 Bonding Origin of Low Lattice Thermal Conductivity

The bond strength is closely related to the bulk modulus, coordination number, electron density, and bond length. [Figures 2.7 \(a\) and \(b\)](#) show that the metavalently bonded materials in the green region exhibit relatively small bulk modulus and Debye temperature values compared to the materials with covalent (red) and ionic (black) bonds, suggesting a softer chemical bond.^{22,81} This is further supported by phonon mode softening upon crystallization (e.g., $\text{Ge}_2\text{Sb}_2\text{Te}_5$),⁹⁰ which is consistent with the increased bond lengths between nearest neighbors.⁹¹ Utilizing bond length—bond strength correlations, commonly effective in describing solids, offers additional evidence for the presence of soft bonds in the octahedrally coordinated chalcogenides under discussion. One might argue that the presence of a single bonding electron (approximately one electron shared) between adjacent atoms corresponds to a lower bond order compared to the expected electron pair for a true covalent bond. Despite a perfect crystal lacking defects, finite lattice thermal conductivity persists due to anharmonic phonon scattering via Umklapp processes. In the harmonic spring-ball model, phonon interactions are negligible. Real crystals exhibit anharmonic behavior, where atomic displacements alter the spring constant (force not proportional to displacement). This leads to phonon-phonon interactions that reduce their propagation velocity, hindering the overall phonon and

entropy transport, ultimately lowering the lattice thermal conductivity.⁹² Stronger anharmonicity, characterized by the Grüneisen parameter (γ_i), reduces intrinsic lattice thermal conductivity. When acoustic phonons dominate scattering, lattice thermal conductivity can be estimated by⁹³

$$\kappa_{\text{lat}} = A \frac{\bar{M} \Theta_D^3 \bar{V}^3}{\gamma_i^2 n_a^3 T} \quad (2.41)$$

where A represents a collection of physical constants, \bar{M} denotes the average mass of the atoms, Θ_D signifies the Debye temperature, \bar{V} represents the volume per atom, n_a stands for the number of atoms in the primitive unit cell, and T is the temperature. Two crucial factors in reducing thermal conductivity are the Debye temperature and the Grüneisen parameter. Figure 2.7 (c) depicts the γ_i^{-2} dependence of lattice thermal conductivity for certain covalent and ionic compounds with zincblende structure and metavalent compounds with rock-salt structure. The significant anharmonicity (large γ_i) contributes to the inherently low lattice thermal conductivity of MVB materials.

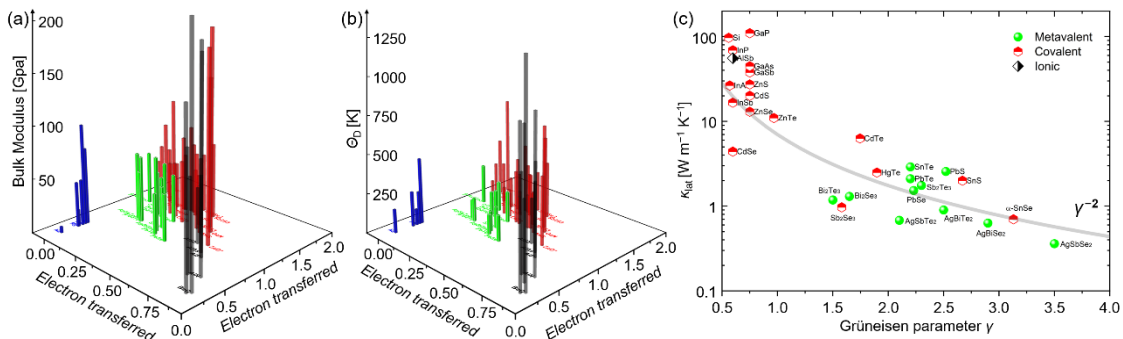


Figure 2.7 | 3D maps showing (a) bulk modulus and (b) Debye temperature of compounds with different bonding mechanisms.^{22,94} Green, red, black, and blue colors represent metavalent, covalent, ionic, and metallic bonding, respectively. (c) Map showing dependence of lattice thermal conductivity average Grüneisen parameter γ for materials adapting covalent, ionic, and metavalent bonding. Compounds which utilize metavalent bonding are characterized by particularly high Grüneisen parameters and hence low lattice thermal conductivities.

2.3.2 Bonding Origin of Intrinsically High and Tunable Carrier Concentration

The position of the Fermi energy level significantly impacts thermoelectric

performance.⁷⁰ Figure 2.8 (a) reveals an optimal Fermi level (E_f) corresponding to a specific carrier concentration that maximizes the power factor. Typically, the ideal carrier concentration for thermoelectric materials lies within the range of 10^{18} to 10^{21} cm^{-3} ,^{27,33,49} as illustrated in Figure 2.5. Figure 2.8 (b) presents key integrands for electrical conductivity: the density of states ($D(E)$) and the derivative of the Fermi integration function ($\partial f_0 / \partial E$). The term $v^2 D(\partial f_0 / \partial E)$ characterizes the differential electrical conductivity (normalized to the relaxation time), and the red area of the integral is proportional to the conductivity, demonstrating that only a minority of carriers near E_f contribute significantly to electrical conductivity due to the non-zero value of $\partial f_0 / \partial E$ of $\sim 3k_B T$ around E_f . Figure 2.8 (b) also presents the integrand for the Seebeck coefficient: $v^2(E_f - E_c)D(\partial f_0 / \partial E)$. This reveals that carriers below the Fermi level contribute positive entropy, while those above contribute negative entropy, despite all contributing to electrical conduction. The net value of the pink area of these two-part integral is related to the Seebeck coefficient. In a parabolic band, the slow rise of $D(E)$ near E_c signifies a limited number of carriers in that region. While deeper Fermi level placement enhances electrical conductivity, it also allows carriers below E_f to counteract the entropy contribution of those above, ultimately reducing the Seebeck coefficient (a measure of average entropy per charge carrier).⁹⁵

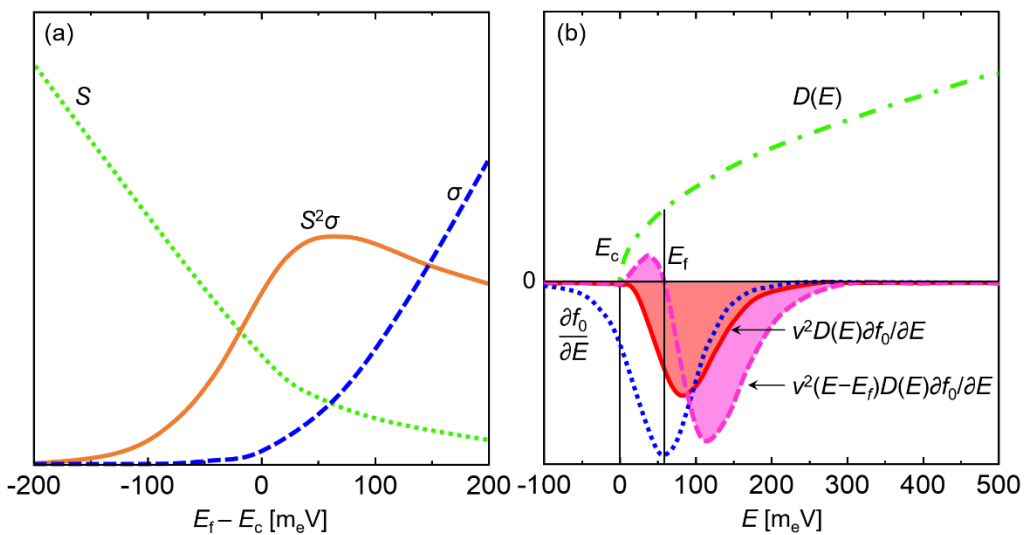


Figure 2.8 | (a) Dependence of S , σ , and PF on the Fermi level (E_f) position relative to the conduction band minimum (E_c).⁷⁰ The axes ranges are: $0\sim 10^{-3}$ V K^{-1} for S , $0\sim 10^7$ $\Omega^{-1} \text{m}^{-1}$ for σ and $0\sim 0.05$ $\text{J m}^{-2} \text{K}^{-1}$ for PF . (b) Plot of electron density of states ($D(E)$), $\partial f_0 / \partial E$, $v^2 D(\partial f_0 / \partial E)$ and $v^2(E_f - E_c)D(\partial f_0 / \partial E)$ versus electron energy (E), based on single parabolic band and constant relaxation time ($\tau = 10^{-12}$ s) with $m^* = 0.33 m_e$.

Undoped chalcogenides exhibiting good thermoelectric performance often possess a high intrinsic carrier concentration due to cation vacancies, which are energetically favorable to form.²² p-states near the Fermi level form σ -bonds, leading to an octahedral-like atomic arrangement. These half-filled p-orbitals (three electrons per site)^{96,97} suggest a metallic ground state in the absence of charge transfer or atomic distortion. A Peierls distortion or a minor charge transfer induces a small bandgap. Soft metavalent bonds promote vacancy formation, enhancing carrier concentration. The MVB transition further reduces cation vacancy formation energy due to the bond softness. Cation vacancies introduce delocalized holes with low effective mass, enhancing conductivity. Thermoelectric performance depends not only on carrier concentration, but also on their mobility and effective mass.

2.3.3 Bonding Origin of Complex Electronic Band Structure

Band Degeneracy

Equations (2.13) and (2.19) suggest that band degeneracy can independently modify the DOS effective mass without impacting carrier mobility (assuming negligible intervalley scattering). Band degeneracy increases when multiple bands exhibit similar energy within a few $k_B T$ near the Fermi energy level. Materials with high crystallographic symmetry (with carrier pockets situated at low-symmetry points of the Brillouin zone)⁶⁵ or those engineered through composition or temperature to achieve band convergence symmetry exhibit this effect.^{66,98}

As a first approximation, local atomic arrangement and orbital character define the energy dispersion relation within the Brillouin zone, resulting in bands reflect crystal symmetry.²² In cubic *IV-VI* compounds, three valence electrons per site and an octahedral atomic arrangement lead to half-filled p-bands due to σ -bonding between neighboring valence p-electrons.^{99,100} The valence band maximum (VBM) and conduction band minimum (CBM) at the L point primarily comprise group *VI* p and group *IV* p character, respectively. These states play a crucial role in charge transport and possess a band degeneracy of 4, attributed to the lower symmetry of the L point compared to the point-group symmetry of the crystal. This results in high valley degeneracy in octahedral-like group *IV* and *V* chalcogenides. For instance, N_v is 4 for PbTe⁶⁶ and PbSe,¹⁰¹ while Bi₂Te₃⁵³ exhibits an N_v of 6.

Octahedral chalcogenides exhibit an additional highly degenerate valley near the valence band maximum. Doping/alloying or temperature changes can further enhance orbital degeneracy. The widening bandgap with temperature in PbTe, PbSe, and PbS suppresses minority carrier excitation, favoring high-temperature thermoelectric performance.^{102–104} One explanation for band convergence in Pb chalcogenides is that thermal expansion can lead to increased bond lengths and reduced orbital overlap between atoms within the crystal structure. This decreased overlap weakens the s-p hybridization, lowering the energy of the valence band at the L point. Consequently, the valence band approaches the Σ -band, resulting in an enlarged bandgap.¹⁰⁵ The temperature of band convergence can be revealed by Hall coefficient, as indicated by the peak position.^{106–111} Temperature-induced band convergence cannot occur with large energy separations between top valence bands or a negative temperature coefficient. Doping/alloying can then be used to engineer the band structure and Fermi level for band convergence.^{106,109–114}

Band Anisotropy

Besides valley degeneracy, the significant contributions from p orbitals and minor contributions from s orbitals near Fermi level create a local hump in the DOS near the Fermi energy can enhance the Seebeck coefficient.^{115–119} However, while the Seebeck coefficient is enhanced by the increased m_d^* , carrier mobility is inevitably reduced due to heavier charge carriers and enhanced ionized impurity scattering.^{119,120} Band flattening offers an alternative approach to boost m_d^* . Indeed, the effective mass tensor m^* is dictated by the curvature of the energy dispersion relation at the band edge, as described in Equation (2.18). Heavier components lead to larger m_d^* , which benefits the power factor and ultimately, the zT value.^{121,122} The difference in the transverse (m_{\parallel}^*) and longitudinal effective masses (m_{\perp}^*), detailed in Equations (2.20) and (2.21), contributes to different m_d^* (proportional to Seebeck coefficient) and m_{σ}^* (inversely proportional to electrical conductivity). Consequently, the *PF* is ultimately governed by the electronic band structure through the ratio $\frac{m_d^*}{m_{\sigma}^*}$ as below.¹²³

$$\frac{m_d^*}{m_{\sigma}^*} = (N_V)^{\frac{2}{3}} \frac{2K+1}{3K^2} \quad (2.42)$$

Here, K signifies the band anisotropic factor, defined as the ratio of the longitudinal

effective mass to the transverse effective mass ($\frac{m_{\parallel}^*}{m_{\perp}^*}$). For a fixed valley degeneracy, a larger deviation of K from 1 signifies a more anisotropic band structure, leading to a larger ratio of m_d^*/m_{σ}^* , as depicted in Figure 2.9. This increased band anisotropy ultimately leads to a higher PF .

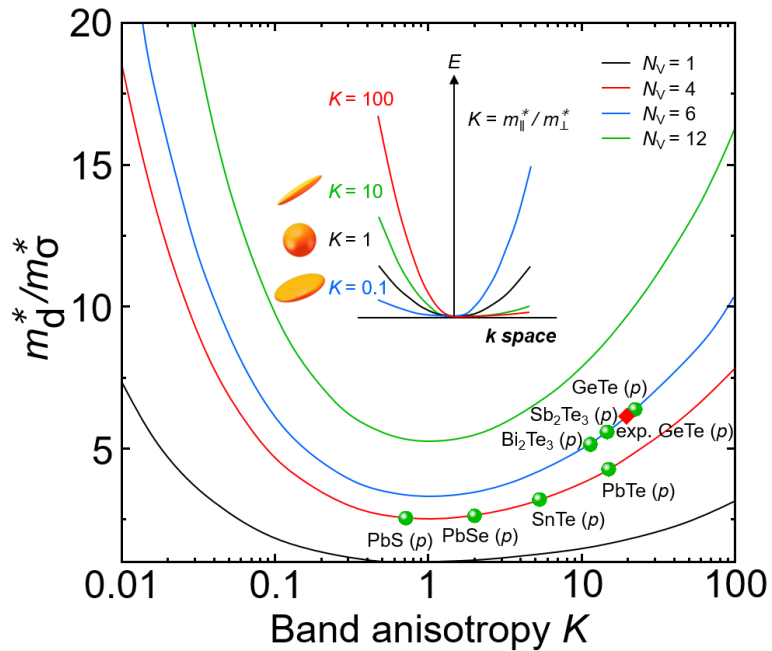


Figure 2.9 | Ratio of m_d^*/m_{σ}^* as a function of the band anisotropic factor K for various valley degeneracies of octahedral chalcogenides.²² The inset depicts valley anisotropy within the band structure: the orange ellipsoids illustrate the Fermi surfaces for various wave vectors (\mathbf{k}).¹²⁴

2.3.4 Fermi Surface Complexity Factor

Gibbs et al. investigated the effective mass and a parameter called the "Fermi surface complexity factor" for over 2,000 cubic compounds using ab initio band structure calculations, which is defined as⁴⁶

$$N_v^* K^* = \left(\frac{m_d^*}{m_{\sigma}^*} \right)^{\frac{3}{2}} \quad (2.43)$$

Figure 2.10 (a) depicts the calculated maximum power factor for various bonding types plotted against the Fermi surface complexity factor,^{22,46} demonstrating evidently that the metavalent compounds (green area) possess a relatively larger Fermi surface complexity

factor and higher maximum power factor than covalent and ionic compounds (red and black areas, respectively). This trend aligns perfectly with the visualization in Figure 2.10 (b), where $N_V^*K^*$ and power factor plotted on the basal plane of ET and ES. It confirms that high values of both $N_V^*K^*$ and power factor are concentrated in the metavalent bonding region.

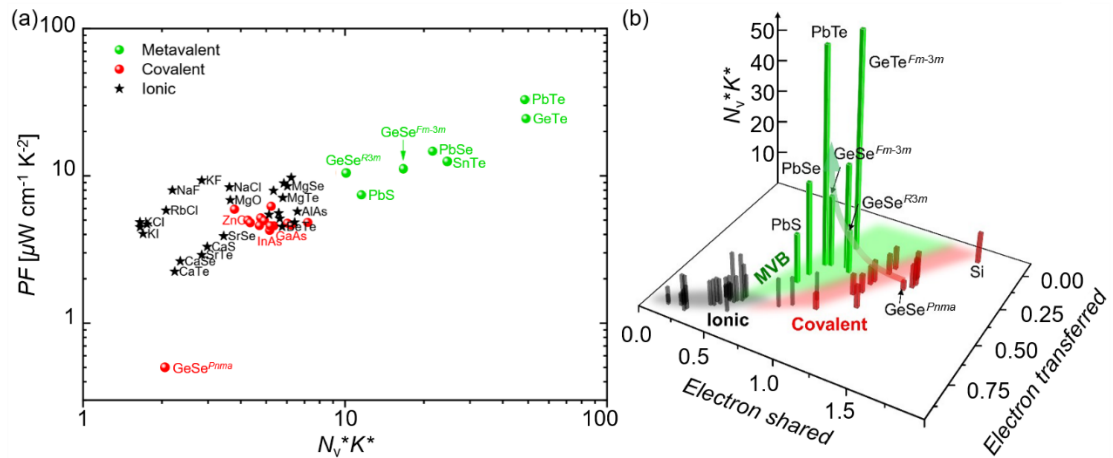


Figure 2.10 | (a) Influence of the Fermi surface complexity factor on the maximum achievable power factor in cubic compounds with different chemical bonding mechanisms.^{22,46} The MVB compounds show larger Fermi surface complexity and higher power factors than others. (b) The Fermi surface complexity factor of compounds with varying bonding mechanisms visualized on the ES-ET basal plane.^{22,46}

3 Methodologies

3.1 Crystal Growth

3.1.1 Different Preparation Methods for Thermoelectric Materials

The sample preparation process strongly influences the microstructure and thus resulting thermoelectric properties.¹²⁵ Numerous methods have been explored for their preparation, including melting methods,^{101,126–132} ball milling,^{133–138} solution synthesis,^{139–142} liquid exfoliation of layered thermoelectric materials,^{143,144} high-pressure synthesis techniques,^{145,146} electrodeposition,^{147–150} and chemical vapor deposition.^{151,152} The Bridgman-Stockbarger technique and SPS, enabling facile doping/alloying and precise structural control, are widely used to synthesize high-performance thermoelectric materials. This thesis employs the vertical Bridgman method for Sb-doped *p*-type Bi₂Te₃ (Chapter 4) and melt synthesis followed by SPS for SnSe and high-entropy samples (Chapters 5 and 6). High-purity starting materials are essential for achieving high-quality crystals. To prevent impurities in the crucible walls from causing polycrystalline or twinned grain growth, a careful cleaning protocol was employed for the quartz crucibles. This cleaning process involved: (i) removal of surface impurities using alcohol-dipped medical gauzes, (ii) ultrasonic cleaning in an alcohol bath at room temperature for 30 minutes, (iii) a high-velocity alcohol rinse, and finally, (iv) drying at 80 °C for 20 hours with the crucible positioned mouth-down.

3.1.2 Single Crystals Grown by Bridgman Oven

Bi_{*x*}Sb_{2-*x*}Te₃ (*x* = 0.5, 0.6, and 0.7) samples in this thesis have been grown by the vertical Bridgman method,^{153,154} using a seedless crystal growth method with a special-shaped high-quality quartz crucible. The nucleated crystals were formed upon supercooling, and then gradually transformed into a single crystal through geometric elimination. It can be seen from the phase diagram in Figure 3.1 (a) that when the reaction temperature is higher than 617 °C, a molten state is generated. Since the actual temperature distribution of the furnace is determined by the principle of heat transfer, the temperature distribution is

often not linear. In this study, the temperature gradient and distribution near the crystallization interface were obtained through the actual temperature measurement records of the system. The actual temperature curve used for the growth of bismuth telluride single crystals is shown in Figure 3.1 (b). It can be seen that the cooling rate is relatively uniform in the process of crystal growth, which indicates that the heat-insulating performance of the gradient zone of the furnace is effective, providing a more ideal temperature field. The uniformity of temperature distribution provides favorable conditions for the crystal growth.

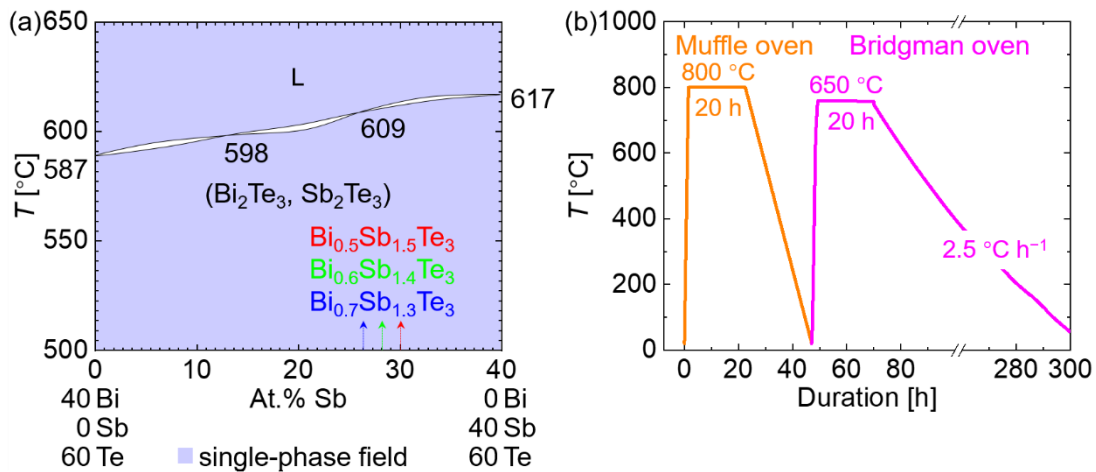


Figure 3.1 | (a) Phase diagram of Bi-Sb-Te. (b) Heat treatment specifications for the $\text{Bi}_x\text{Sb}_{2-x}\text{Te}_3$ samples.

As shown in Figure 3.2 (a), the vertical Bridgeman crystal growth furnace in this study adopts a tubular structure. The temperature field inside the furnace is divided into three zones, i.e., the hot zone, the gradient zone, and the cold zone. The temperature in the hot zone is set slightly higher than the melting point of the crystals, T_{melt} (~ 878 K), while the temperature in the cold zone is lower than T_{melt} , and the temperature in the gradient zone is in between, forming a unidirectional temperature gradient. Firstly, the starting material is loaded into the crucible, and then the crucible is placed in the hot zone and continuously heated for a period, which is 20 hours in this study so that it melts and converts sufficiently to obtain a homogeneous melt. Secondly, the crucible is slowly moved from the hot zone to the cold zone through the gradient zone. After entering the gradient zone, the bottom of the crucible starts to cool down and induces the crystallization of the melt when the temperature is below the melting point of the crystal. As the crucible moves continuously, the crystal interface moves in the opposite direction, thereby achieving

continuous crystal growth. Assuming simplified heat transfer in one dimension, the crystal growth rate can be modeled using the continuity equation of heat conduction

$$v = \frac{\Delta T (K_c - K_m)}{\rho_m \cdot L} \quad (3.1)$$

where ΔT is the temperature gradient at the solid-liquid interface; K_c and K_m are the thermal conductivities of the crystals and the melt, respectively; ρ_m is the density of the melt near the melting point; and L is the latent heat of the grain boundaries released from the growth of a unit mass of crystal. The growth rate of bismuth telluride single crystals in this study was derived to be about $3.5 \mu\text{m min}^{-1}$.

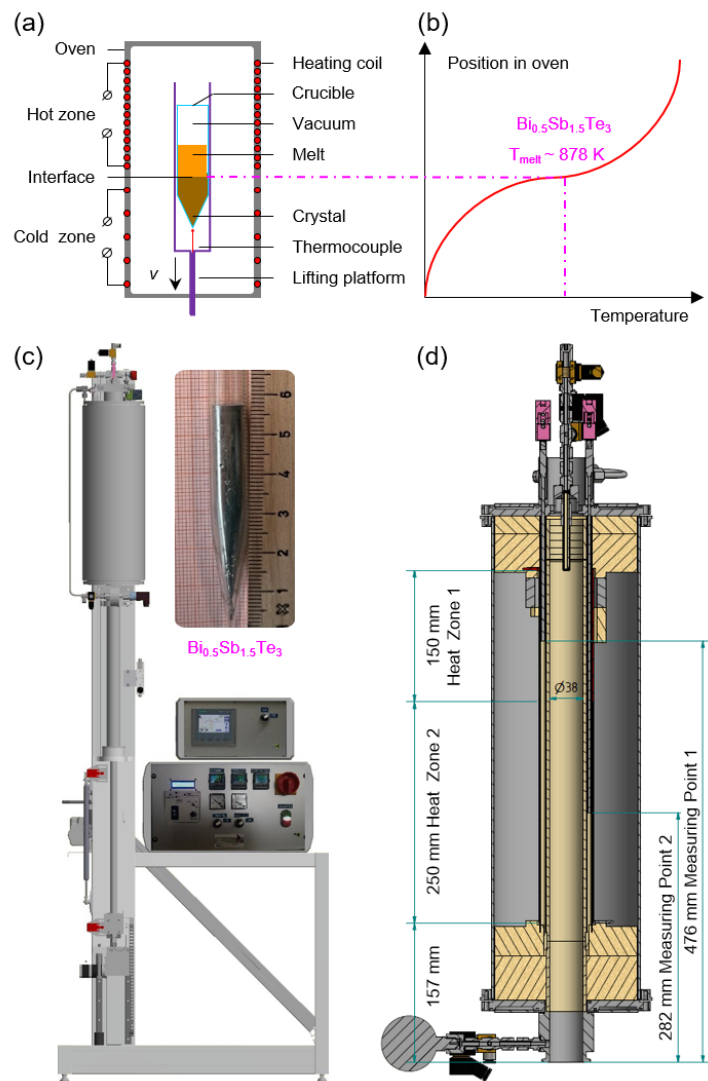


Figure 3.2 | Schematic diagram of (a) a vertical Bridgman furnace and (b) temperature profile for the as-synthesized Bi-Sb-Te samples. (c) Simulation diagram of Bridgman furnace (model 19-258 Bridgeman, HTM Reetz GmbH), with an inserted physical image of single-crystal $\text{Bi}_{0.5}\text{Sb}_{1.5}\text{Te}_3$ obtained in this thesis through the process in (b). (d) Schematic diagram of the furnace cavity's internal structure.

Figure 3.2 (c) shows the exterior structure of the Bridgman furnace in this study, and the insert shows the corresponding physical image of the $\text{Bi}_{0.5}\text{Sb}_{1.5}\text{Te}_3$ single crystal grown. The Bridgman technique offers two primary methods for single crystal growth: spontaneous nucleation by selective crystal method and directional growth with a seed crystal. The seed crystal method has higher requirements for the melting process, which not only requires long-term melting and overheating treatment of the material to fully homogenize the melt but also prevents the seed crystal from completely melting and losing its function as a seed. Therefore, in most cases, the seed crystal method is not used.

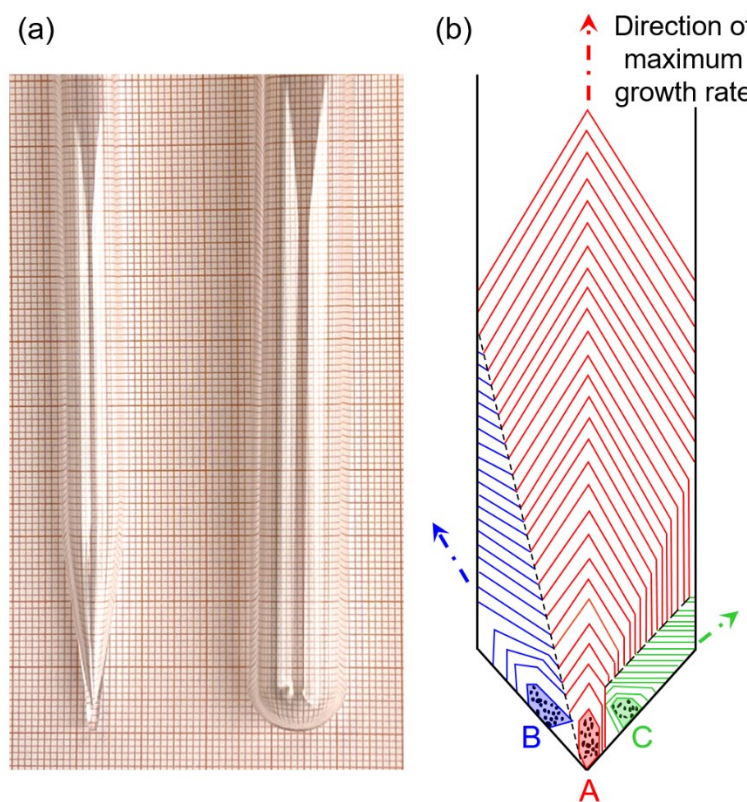


Figure 3.3 | (a) Physical drawing of the sharp-bottom quartz crucible and the corresponding anti-rupture crucible used in this research. (b) Schematic diagram of the geometric elimination law for a crystal.

The principle of the selective crystal method to obtain single crystals is based on the “geometric elimination law” in crystal growth. By optimizing the design of the initial growth section of the crucible, as shown in Figure 3.3 (a), the conical sharp corners at the bottom of the crucible allow only a small amount of melt to begin to crystallize at the bottom when the crucible drops through the gradient area. Due to the anisotropic nature

of crystals and the fact that the growth rate varies in different directions, it is reasonable to assume that the direction of the maximum growth rate of the A nucleus is parallel to the crucible wall, and that of the B and C nuclei is oblique to the crucible wall. From Figure 3.3 (b), it can be seen that during the growth process, the B and C nuclei shrink due to the continuous compression of the oriented fast-growing nucleus A, leaving only the well-oriented nucleus A occupying the entire melt and developing into a single crystal, following the geometric elimination rule. Considering factors such as thermal conductivity of bismuth telluride crystals, thermal shock resistance and selection of excellent crystal seeds, the crystal selection method was adopted in this experiment.

3.1.3 Bulk Polycrystalline by Spark Plasma Sintering

SPS utilizes pulsed direct current to generate a high-temperature spark plasma at particle contacts and Joule heating within the graphite die.¹⁵⁵ It offers numerous advantages: precise temperature control exceeding 2000 °C, rapid densification, excellent reproducibility, safety, and reliability. The initial spark plasma promotes rapid neck formation, enhances thermal diffusion, and cleans particle surfaces. The direct current (DC) electric field further accelerates diffusion. Consequently, SPS enables densification at lower temperatures and shorter times compared to conventional sintering.^{155,156}

In Chapter 5, the raw material shots (99.999%, Chempur GmbH) was sealed in quartz tubes under high vacuum ($\approx 10^{-5}$ mbar) and melted in a muffle furnace at 1223 K for 40 hours. The samples were furnace-quenched and ground to fine powders with a mortar and pestle in an Argon-filled glove box, then transferred to a graphite sintering mold with an inner diameter of 20 mm for sintering. The powders were then sintered at a maximum temperature of 873 K to 923 K for 5 min under an axial pressure of 50 MPa using spark plasma sintering (SPS, FCT Systeme GmbH) with the pyrometer temperature control mode. While for preparing high entropy compounds in Chapter 6, high-purity (99.999%, Aldrich) raw powders were weighed in appropriate molar ratios for synthesizing BiPbAgS_3 , BiPbAgSe_3 , BiPbAgTe_3 , and BiPbAgTeSeS . The stoichiometric mixtures for synthesizing the respective compounds was loaded into quartz tubes, evacuated to $\sim 10^{-5}$ mbar, and sealed. The tubes were then heated to ~ 1373 K in 15 hours, maintained at this temperature for 24 hours, and then quenched in air. Within an argon glovebox, the ingots were ground (< 5 mm) using a mortar and pestle followed by ball milling to achieve a particle size below 50 μm . Finally, SPS was conducted at ~ 873 K for 10 min under 40

MPa uniaxial pressure.

3.2 Structural and Chemical Bonding Characterizations

3.2.1 Phase Composition and Crystal Orientation

DSC

Differential scanning calorimetry (DSC) thermal analysis is a technique for measuring the relationship between physical properties and temperature. It can obtain thermodynamic and kinetic parameters such as the specific heat capacity, phase diagram, phase transition temperatures, and the reaction heat by measuring the rate of heat absorption and release of the sample. This study uses a DSC-Q20 thermal analyzer. The testing temperature range is from room temperature to ~ 750 K, with a heating rate of 5 K min^{-1} , and the atmosphere used is ammonia.

XRD

X-rays are electromagnetic waves, which will be diffracted in a crystal, according to Bragg's law:

$$2d_{hkl} \sin \theta_{hkl} = n\lambda \quad (3.2)$$

where n is the diffraction order, which is a positive integer; hkl is the index of the crystal plane; d_{hkl} is the distance between the corresponding crystal planes; θ_{hkl} is the angle between the incident angle and the crystal plane; λ is the wavelength of the X-rays. When the optical path difference between the two beams of X-rays is $n\lambda$, their intensities will have a maximum value and a sharp peak will appear in the spectrum. XRD analysis can be used to identify the phase of reaction products and determine the crystal structure and cell parameters. This thesis mainly compares the diffraction data of the sample measured with the standard phase to determine whether the reaction is complete and whether there is any impurity. By comparing the position and width of the diffraction peak, the effects of reaction temperature, reaction time, and concentration of dopant on the material are explored.

As depicted in Figure 3.5 (a), a powder X-ray diffractometer comprises several essential components, including an X-ray source, typically an X-ray tube, a sample stage, a detector, and a mechanism to vary the angle θ . X-ray beam is focused onto the sample at

a specific angle θ , and the detector, located opposite to the source, measures the intensity of the diffracted X-rays at 2θ from the source path. The incident angle is incrementally increased while the detector angle is maintained at 2θ above the source path.

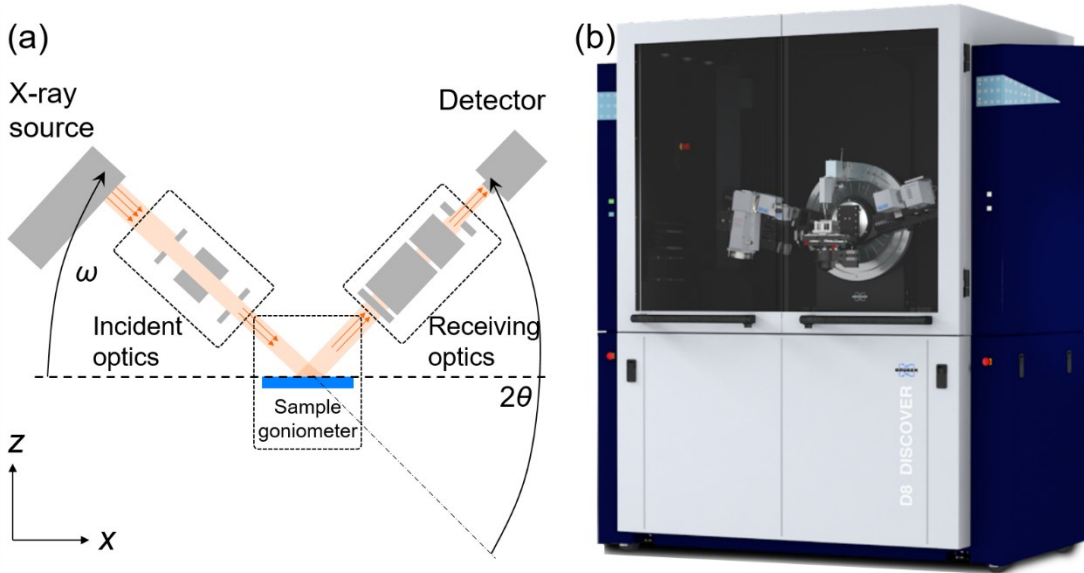


Figure 3.4 | (a) Schematic of XRD working principle. (b) Bruker D8 DISCOVER X-Ray Diffractometer in the RWTH Aachen University I. Institute of Physics (IA).

The samples were ground to a homogeneous powder in an agate mortar and then sieved through a 400 mesh sieve and flattened for powder XRD measurement. The D8 DISCOVER multifunctional automatic X-ray diffractometer from Bruker AXS Germany as shown in Figure 3.4 (b) was used. The diffraction parameters of the X-ray diffractometer were: Cu-K α rays, current 200 mA, scan voltage 40 kV, step scan, receiving slit 0.30 mm, scan speed 4° min^{-1} and scan angle $10 - 90^\circ$.

EBSD

Electron backscatter diffraction (EBSD), also known as backscatter Kikuchi diffraction, is a powerful technique for obtaining high-resolution (around 20 nm) crystallographic information from bulk materials.¹⁵⁷ EBSD measurements are performed within a scanning electron microscope (SEM) equipped with a dedicated detector shown in Figure 3.5. As illustrated in Figure 3.6 (a), this detector houses an electron-sensitive screen (phosphor or scintillator) positioned in front of the tilted specimen (typically at a 70° angle relative to the incident electron beam). A digital camera captures the diffraction

pattern generated by backscattered electrons striking the screen.^{157,158}

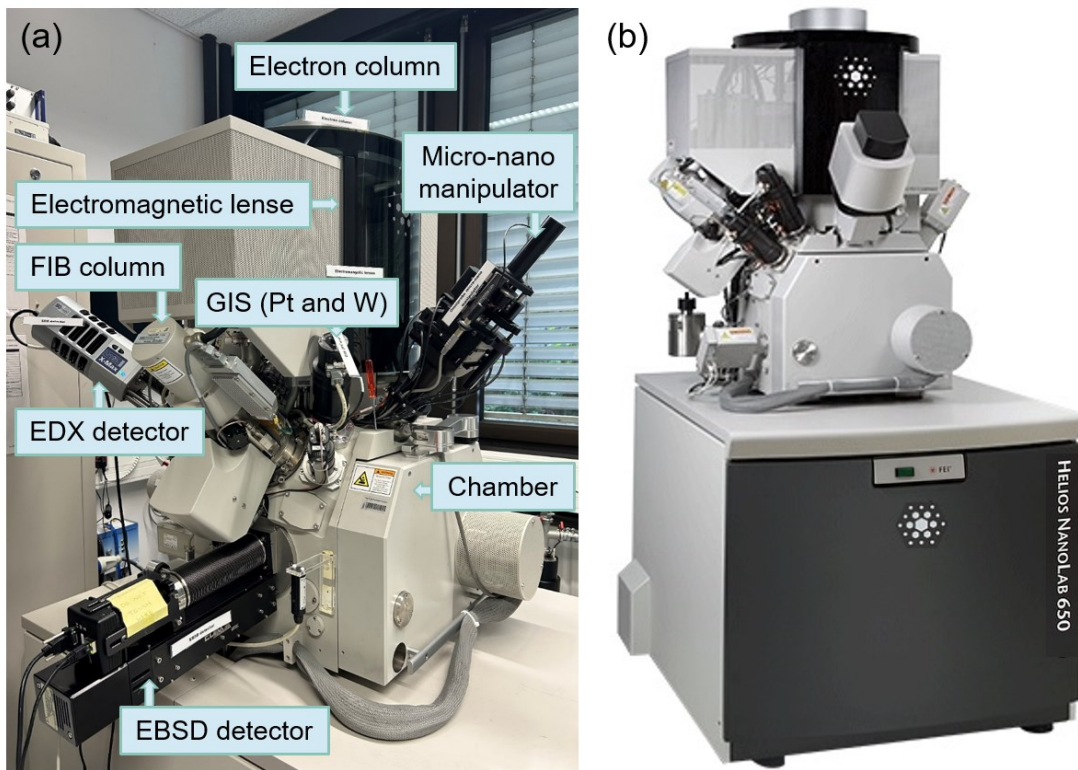


Figure 3.5 | (a) Main components and (b) physical diagram of the FEI's exclusive Dual-Beam Helios NanoLab™ 650 in the I. Institute of Physics (IA) at RWTH Aachen University.

Figure 3.6 (b) shows the working principle of EBSD analysis. The pattern geometry of an electron backscatter diffraction pattern (EBSP) can be understood by considering Bragg reflections. The incident electron beam interacts with the sample, undergoing elastic and inelastic scattering.^{157,159–165} Elastically scattered electrons can satisfy the Bragg condition as described in Equation 3.2 for specific lattice planes, leading to diffraction cones (Kossel cones). The intersection of these cones with the detector screen forms Kikuchi lines in a gnomonic projection (Figure 3.6 (a)) due to their shallow angles ($\theta \approx 1^\circ$). These lines appear on a background of inelastically scattered electrons. Importantly, each Kikuchi band (pair of Kikuchi lines) originates from a specific plane, allowing EBSD to directly measure sample orientation. Crystal rotations or tilts produce corresponding rotations or shifts in the EBSP pattern. By acquiring EBSPs from a grid of points on a sample, a map of crystallographic orientation variations can be generated as the results in Chapters 4~6.

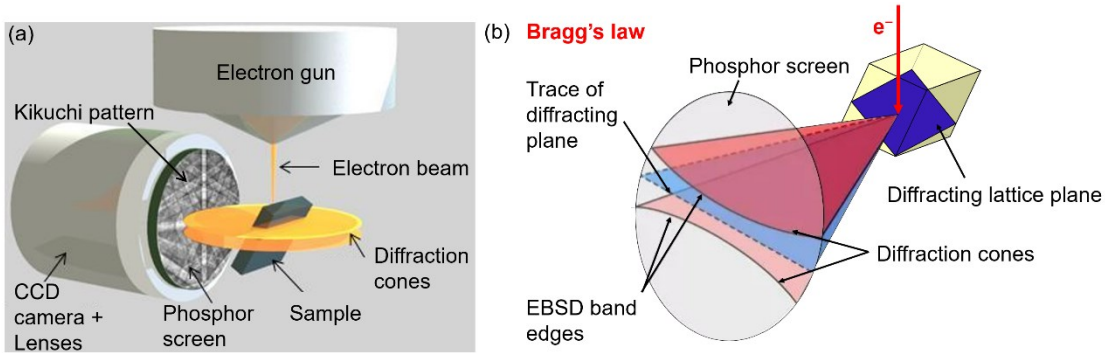


Figure 3.6 | (a) Illustration of the EBSD detection geometry. (b) Working principle of EBSD analysis.

FIB

Developed in 1990, focused ion beam (FIB) serves for preparing 3D atom probe and TEM samples of targeted materials, leveraging its micro/nano processing capabilities.^{166,167} Accurate APT data relies on meticulous FIB preparation, particularly for complex structures and nanoscale features in semiconductors. FIB's precise milling capability allows for targeted extraction of the desired analysis area at the needle tip. For semiconductors, the longitudinal FIB method reigns supreme. SEM identifies the target region on the sample surface. Then a protective Pt layer is deposited on the target region, followed by FIB milling of three sides to create a slender, triangular pillar. This pillar is then sculpted by the ion beam into a tapered tip with a top diameter of less than 100 nm.

3.2.2 Chemical Composition

EDX

In addition to EBSD, an Energy-Dispersive X-ray (EDX) spectrometer is integrated into the SEM system (Figure 3.5). EDX rapidly determines the elemental composition by analyzing the characteristic X-rays emitted from its atoms. The operating principle of EDX involves the electron beam exciting an inner-shell electron, causing its ejection and leaving a vacancy. An outer-shell electron fills this vacancy, releasing energy in the form of an X-ray. The X-ray energy is unique to the specific element and transition involved. The EDX detector collects these X-rays, and the measured signals are interpreted to identify the elements. These signals can be visualized as elemental maps and line scans. This thesis employed EDX for both qualitative and quantitative analysis. The SEM beam conditions included a 10 kV accelerating voltage and 0.8 nA beam current.

APT

3D Atom Probe Tomography (APT) is a technique for observing the arrangement of atoms in three dimensions with near-atomic resolution. This study utilized the CAMECA Local Electrode Atom Probe (LEAP) 5000XS instrument as shown in Figure 3.7 (a), which features two pulse modes, i.e., voltage mode and laser mode. All experiments in this study were performed in laser mode. This model has a linear flight path and a high detection efficiency of 80%, which makes it suitable for detecting low dopant concentrations in semiconductor samples. Experimental parameters in this thesis consist of a base temperature of 40 K, a laser pulse energy of 15 pJ, a laser pulse frequency of 200 kHz, a detection rate of 1%, and a flight path of 100 mm.

The APT measurement schematic in Figure 3.7 (b) depicts the sample stage, comprising the needle specimen, local electrode (LE), and multichannel detector. The sample stage with needle specimen, the local electrode (LE) and the multichannel detector are shown from left to right. The needle specimen is positively biased, and the reference voltage is carefully increased to approach the evaporation field. Additional pulses (either laser or voltage) are then applied to the needle-shaped specimen, leading to the evaporation of ions atom by atom from the tip surface. Subsequently, the charged ions are accelerated by an electric field between the specimen and the local electrode. After passing through the local electrode, the ions travel towards the detector at a constant velocity. Information on the evaporation sequence, flight time, and hit position is obtained, allowing the reconstruction of the distribution of atoms in 3D space through post-processing software of AP Suite 6.3 and Matlab.

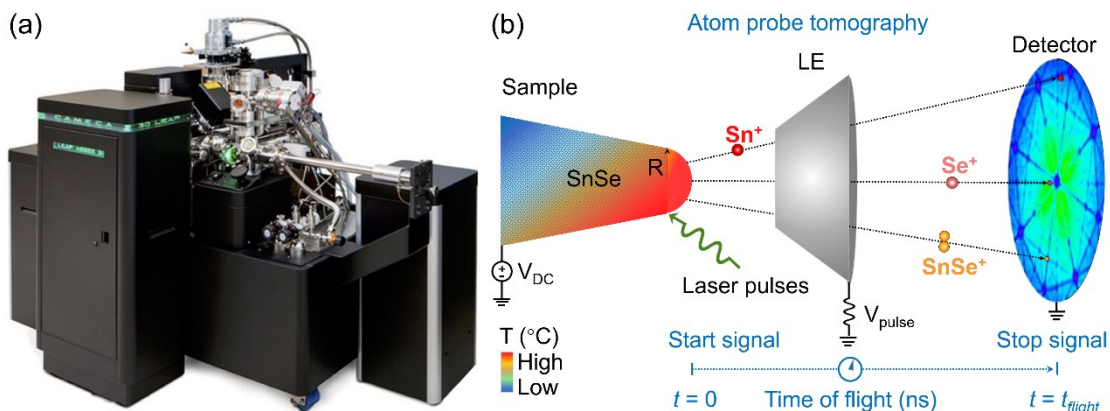


Figure 3.7 | (a) The CAMECA Local Electrode Atom Probe (LEAP) 5000 XS used in this study. (b) illustration of atom probe tomography.

When a laser pulse is applied, the temperature of the tip surface increases rapidly, while the voltage remains constant, enabling the evaporation process. Essentially, successful detection involves three primary steps: field evaporation, acceleration, and hit detection.

Field Evaporation

Field evaporation, a physical phenomenon, involves the removal of atoms from a material surface in ion form under a strong electric field. Field ion evaporation requires an electrostatic field of $\sim 10 \text{ V nm}^{-1}$ to selectively and sequentially remove surface atoms. To achieve this field, the sample is shaped into a sharp needle with an apex diameter around 100 nm as mentioned earlier. An analytical model related to the surface electrostatic field (F), i.e., Equation (3.3) can be derived from simple electrostatics.

$$F = \frac{V}{k \cdot r} \quad (3.3)$$

where V is the applied voltage, k denotes the constant of the electric field weakening caused by the tip geometry or field factor, ranging from 2 to 8, r is the end radius of the tip. To achieve the required electrostatic field, a moderate DC voltage (V_{DC}) of 3-8 kV can be applied. Photon-induced field evaporation generates ions on the surface irrespective of the path, which are then accelerated by the surrounding electric field.

Acceleration

When subjected to the electric field between the sample and local electrodes, atomic bonds break, leading to the evaporation of ions from the sample surface, followed by their acceleration toward the detector. The electric field accelerates ions based on their charge state, mass, and the length of the acceleration region. Given the relatively short acceleration distance compared to the tip-to-detector distance, ions can be assumed to fly to the detector at a constant speed following acceleration.

Detection

During data reconstruction, two primary sets of parameters are utilized: the (X , Y , Z) coordinates and the chemical identity of the evaporated ions. The hit position on the multi-channel detector is logged to establish the X and Y coordinates of the tip surface, while the evaporation sequence determines the Z coordinate following the projection law. After the ions are repelled by the sample surface, the electric field distribution and tip geometry affect the flight trajectory, resulting in a curved trajectory. Simultaneously, the

time-of-flight, t_{flight} , is also recorded to determine the mass-to-charge ratio ($\frac{m}{n_i}$) and chemical identities. Following the law of conservation of energy, the potential energy of a charged ion in an electrostatic field equals its kinetic energy:

$$\frac{1}{2}mv_i^2 = n_i eU \quad (3.4)$$

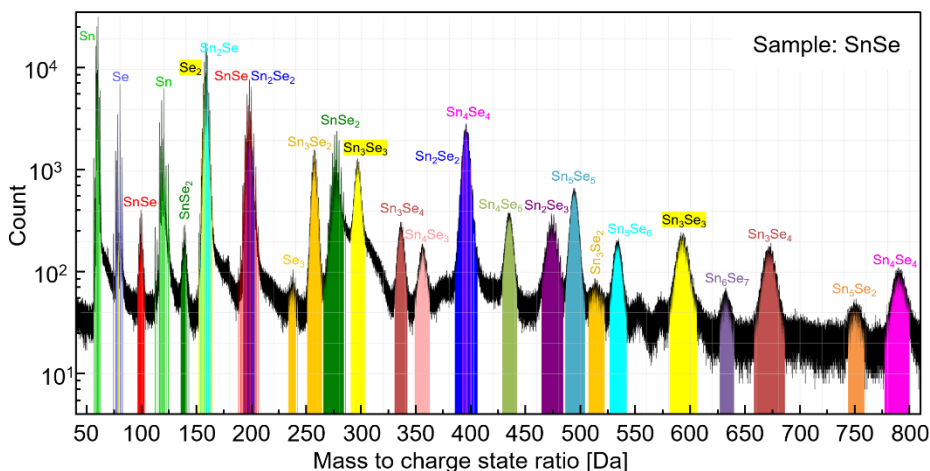
where m , v_i , and n_i are the mass, velocity, and charge of the ion. Given that the acceleration distance is significantly shorter than the flight path L ($L = 100$ mm in this thesis), assuming constant velocity is reasonable. Utilizing L and t_{flight} , it can be derived:

$$\frac{m}{n} = 2eU \frac{t_{\text{flight}}^2}{100^2} \quad (3.5)$$

Therefore, t_{flight} contains the combined information of chemical identity and charge state, yielding the so-called "mass spectrometry".

Mass Spectrometry Calibration

Equation (3.5) is applied to convert the ion data into a mass spectrometry, where each peak represents the mass-to-charge ratio of a detected ion. Due to a combination of local electromagnetic environment variations, instrumental calibration issues, ionization process dynamics, specimen effects, thermal variations, and data processing inaccuracies, the raw data of the mass-to-charge ratio is normally slightly shifted from the standard value.¹⁶⁸ The shift can be minimized by performing calibrations with reference materials, utilizing built-in calibration routines, and applying peak fitting/background subtraction techniques during data processing. So manual assignment of the correct mass-to-charge ratio to each peak is performed during calibration, as exemplified in Figure 3.8.



Calibration is vital for accurate mass determination, serving as the initial step in analyzing APT data and ensuring precise elemental distribution and concentration analysis.

3.2.3 Chemical Bond Breaking in Atom Probe Tomography

To dislodge ions from the sample surface, the chemical bonds must be disrupted, facilitating the investigation of bond-breaking mechanisms of various compounds. This thesis employs additional laser pulses beyond the base voltage to ultimately initiate the field evaporation process, thereby utilizing the principle of laser-assisted field evaporation. Due to the detection limitations of the multi-channel detector, only a small fraction of laser pulses induces the rupture of bonds, resulting in successful ion evaporation and consequently ion formation, as opposed to 'nulls,' wherein the majority of laser pulses fail to produce ions. The average number of ions detected by a single pulse is denoted as the "detection rate", calculated by integrating the evaporation rate over the pulse duration. The detection rate in this thesis is typically set at 1%. Generally, a successful laser pulse—meaning one that manages to remove fragments from the tip—typically yields only a single ion on the detector, termed a "*single event*" (Figure 3.9 (a)). A portion of laser pulses results in more than one ion, termed "*multiple events*," as depicted in Figure 3.9 (b). The ratio between the occurrence of multiple events and the total number of events is termed as "probability of multiple events" (PME). Nonetheless, a small yet non-zero PME is consistently observed.

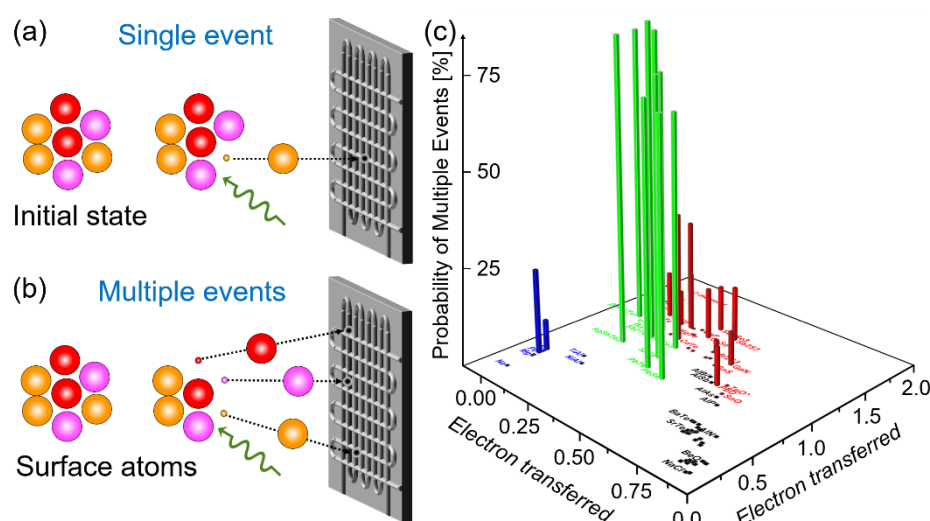


Figure 3.9 | Schematic diagrams illustrating (a) a single event and (b) multiple events for the evaporation of ions with one successful laser pulse. (c) A 3D map using the basal plane of electrons transferred and electrons shared showing the corresponding PME.

Figure 3.9 (c) illustrates that compounds with a high PME spanning from 60% to over 80% are situated within the green zone, i.e., MVB region, distinguished by unconventional physical properties as elaborated in Section 2.2. Under identical measurement parameters, PME for all covalent and metallic materials remains below 40%. The APT-measured PME are applicable for identifying new compounds with metavalent bonding. Notably, all chalcogenides with significant thermoelectric potential are categorized into the metavalent bond region. Thus, the correlations between thermoelectrics, bond breaking, and material properties emerges as stated in Section 2.3.

3.2.4 Optical Properties

Fourier-transform infrared spectroscopy

This study employed a Bruker VERTEX 80v FTIR spectrometer (Figure 3.10 (a)). Bulk crystals were polished to achieve a mirror-like finish, with the root-mean-square (RMS) surface roughness of ~ 5 nm as identified by atomic force microscopy. The working principle is illustrated in Figure 3.10 (b): FTIR works based on the principle of Fourier transform of the infrared light absorption by the sample. The source light is split into two beams by a beamsplitter: one beam transmits through the moving mirror, while the other reflects off the fixed mirror. The beams are then reflected by the fixed and moving mirrors, recombining at the beamsplitter. The moving mirror's constant linear motion creates a difference in light path length, resulting in interference. After converging in the beam splitter, the interfering light passes through the sample cell, and the sample information reaches the detector. Finally, Fourier transform processing yields the infrared absorption spectrum in terms of transmittance or absorbance with wave number or wavelength.

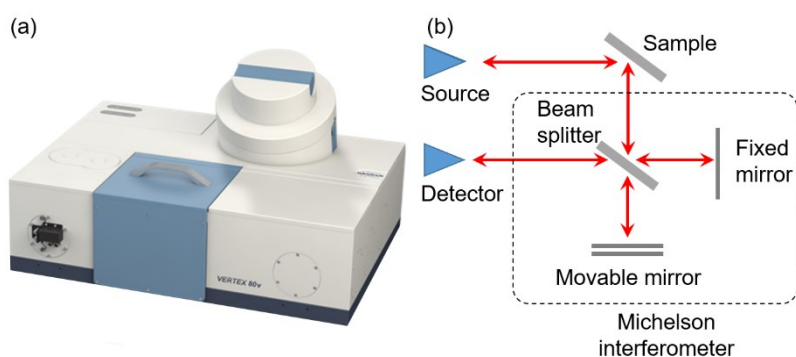


Figure 3.10 | (a) The Bruker VERTEX 80v FTIR Spectrometer, capable of measuring both in reflectance and transmittance modes. (b) The operational principle of FTIR measurement in reflectance mode.

FTIR measurements in our case are performed in reflectance mode spanning the 15-18000 cm⁻¹ spectral range. A 200 nm thick gold mirror served as the reference. Various light sources (Hg-arc, globar, and tungsten lamp), beam splitters (Mylar 50 μ m, multilayer, KBr, and CaF₂), and detectors (liquid He-cooled 4K silicon bolometer, DLaTGS with polyethylene and KBr windows, liquid nitrogen-cooled InSb, and room-temperature Si photodiode) were employed to cover the entire spectral range. Additionally, an Avantes AvaSpec-2048CL-EVO spectrometer and an aluminum reference mirror were used for reflectance measurements in the 9100-45000 cm⁻¹ spectral range.

Dielectric Function

The real and imaginary parts of the optical dielectric functions ($\varepsilon_1(E)$, $\varepsilon_2(E)$) were determined from the reflectivity data through Kramers-Kronig analysis and extrapolation using X-ray atomic scattering functions at high energy. From the FTIR reflectance measurements, extrapolations for the high-energy region can be performed using complex atomic scattering functions (f^j) and number densities (n_j) via the equations:¹⁶⁹

$$f^j = f_1^j + i \cdot f_2^j \quad (3.6)$$

$$\varepsilon = 1 - \sum_j \frac{4\pi n_j e^2}{m\omega^2} (f_1^j - f_2^j) \quad (3.7)$$

where the summation extends over all atoms (j) in the material. With the complex refractive index $N(\sqrt{\varepsilon})$, normal incidence reflectance $R\left(\left|\frac{1-N}{N+1}\right|^2\right)$, and extrapolations in both low and high-frequency limits, a full-spectrum reflectance ($R(\omega)$) is obtained. The amplitude reflectivity $r(\sqrt{R} \cdot e^{i\phi})$ allows for a simplified expression of the phase (ω):

$$\phi = -\frac{\omega}{\pi} \int_0^\infty d\omega' \frac{\ln[R(\omega')/R(\omega)]}{\omega'^2 - \omega^2} \quad (3.8)$$

The complex dielectric function ε can be calculated from the results above

$$\varepsilon = \left(\frac{1 - \sqrt{R} \cdot e^{i\phi}}{1 + \sqrt{R} \cdot e^{i\phi}} \right)^2 \quad (3.9)$$

The FTIR reflectance spectra are simultaneously fit using the CODE software (www.mtheiss.com). The dielectric function, $\varepsilon(\omega)$, is modeled by three components: (i) A constant background term, $\varepsilon_{BG}(\omega)$, accounting for high-energy polarizability. (ii) A Drude term, $\varepsilon_{Drude}(\omega)$, describing contributions from free carriers. (iii) A Tauc-Lorentz

term, ε_{TL} , representing inter-band transitions.^{170,171}

$$\varepsilon(\omega) = \varepsilon_{\text{TL}}(\omega) + \varepsilon_{\text{BG}}(\omega) + \varepsilon_{\text{Drude}}(\omega) \quad (3.10)$$

A model incorporating a Drude term and several Tauc-Lorentz oscillators is then fit to the obtained $\varepsilon(\omega)$. Subtracting the Drude contribution yields the spectra presented in Figure 4.9, Figure 5.5, and Figure 6.13.

Born Effective Charge

Dr. Tanmoy Ghosh conducted far infrared FTIR spectroscopy to calculate the Born effective charge in this study. The dielectric susceptibility $\chi(\omega, k)$ of polar phonons in the harmonic approximation is a Lorentzian oscillator with the following expression.

$$\chi(\omega, k) = \frac{\Omega_p^2}{\Omega_0^2 - \omega^2 - i\gamma\omega} \quad (3.11)$$

where ω represents the phonon frequency and γ denotes the damping. This Ω_p has the following relationship with the transverse effective charge q_T participating in the vibration.

$$\Omega_p^2 = \frac{q_T^2 N}{\varepsilon_0 \mu V} \quad (3.12)$$

where $\frac{N}{V}$ denotes the density of the oscillator, ε_0 is the vacuum dielectric constant, and μ represents the reduced mass. This plasma frequency can be obtained experimentally from the real part of the optical conductivity $\sigma_1(\omega)$ by

$$\Omega_p^2 = \frac{2}{\pi \varepsilon_0} \int_{\omega_1}^{\omega_2} \sigma_1(\omega) d\omega \quad (3.13)$$

The above equation covers only the region under the phonon response, and the contribution of free carriers must be removed from the optical conductivity. Born effective charge Z_k^* is related to the optical conductivity σ_ω as below:

$$\sum_k \frac{n_k Z_k^*}{m_k} = \frac{2V}{\pi} \int \sigma_1(\omega) d\omega \quad (3.14)$$

where V is the volume occupied by all the atoms on the left. Notice that the Born effective charge also obeys the charge neutralization law, which implies that

$$\sum_k n_k Z_k^* = 0 \quad (3.15)$$

Raman Spectroscopy Measurements

Raman spectroscopy is a non-destructive analytical technique that offers comprehensive insights into the crystal structure, crystallinity, and intermolecular interactions of a material. It works by irradiating a sample with monochromatic laser light. When the light interacts with the vibrational modes of the atoms within the solid, a small portion of the light scatters inelastically. This scattered light, called Raman scattered light, contains information about the vibrational frequencies of the bonds in the material. In this thesis, Raman spectroscopy measurements were performed using a commercial WITec system (alpha300) in backscattering geometry. A diode-pumped solid-state laser provided linearly polarized light at a wavelength of 532 nm (2.33 eV) via a single-mode optical fiber to excite the sample. Achieving a spot size of 400 - 500 nm involved a long working focusing lens with a numerical aperture of 0.70. By maintaining an excitation power of 500 μ W, significant heating effects were mitigated. Detection utilized reflected light transmitted through a single-mode optical fiber to a charge-coupled spectrometer with a 2400 lines per mm grating. All measurements were conducted at room temperature using a 50 \times objective (NA = 0.7) and were performed at various locations on the sample to assess the spatial variation of the Raman signal.

Femtosecond Pump-Probe Reflectivity Measurements

A two-color pump-probe experiment with anisotropic sampling was used in [Chapter 5](#) for ultrafast optical measurements. The setup employed a Ti: Sapphire regenerative femtosecond amplifier generating 800 nm, 60 fs pulses. The chopped (1500 Hz) pump beam (800 nm, 60 fs) was decoupled, delayed, and focused onto the sample (200 μ m spot). An optical parametric amplifier converted the probe pulses to 520 nm (70 fs) and focused them onto a 30 μ m spot on the sample. Two balanced Si-photodiodes connected to variable gain amplifiers and a data acquisition card detected the material response. All measurements used a pump fluence of \sim 1 mJ cm^{-2} with a probe fluence 10 times weaker. A polarizing beamsplitter cube separated the reflected probe beam into s and p-polarizations. Isotropic and anisotropic transient reflectance (ΔR) were normalized to steady-state reflectance (R_0 , measured with chopped pump). Isotropic ΔR combined s and p-polarized components.

$$\Delta R = \frac{\Delta(R_s + R_p)}{R_0} \quad (3.16)$$

The electro-optic detection scheme¹⁷² was used to calculate the anisotropic transient

reflectance (ΔR_{EO}) from the s and p-polarized components.

$$\Delta R_{\text{EO}} = \frac{\Delta(R_s - R_p)}{R_0} \quad (3.17)$$

Static reflectivity was monitored to verify the reversibility of the optical excitation.

3.3 Thermoelectric Property Measurements

Accurate characterization is vital for advancing high-performance materials, involving separate measurements of the Seebeck coefficient, electrical conductivity, and thermal conductivity, followed by zT value calculations. Measurement systems are categorized based on the parameters measured, such as Seebeck coefficient/resistance and thermal conductivity.

3.3.1 Seebeck Coefficient Measurement

The off-axis four-point method enables simultaneous measurement of the Seebeck coefficient and conductivity by placing the thermocouple in direct contact with the sample, eliminating contact resistance with the heater/irradiator. [Figures 3.11 \(a\) and \(b\)](#) depict corresponding measurements conducted in [Chapter 5](#) using the Linseis LSR-3 system, along with the associated schematic diagrams. The system directly obtains the relative Seebeck coefficient (S_{relative}) of the sample with respect to the thermocouple. The temperature difference ($\Delta T = T_B - T_A$) across a specimen under a temperature gradient is calculated from the temperatures at points A and B measured by two thermocouples. The sample temperature is taken by averaging the two thermocouple temperatures, i.e. $T_0 = (T_A + T_B)/2$, for accuracy. To plot the ΔV - ΔT curve, at least three pairs of ΔV and ΔT are collected. ΔV is normally not zero when $\Delta T = 0$ K, resulting in a voltage offset for S_{relative} , as [Figure 3.11 \(c\)](#) shows. Directly using $\Delta V/\Delta T$ to calculate S_{relative} may deviate from its true value, which is:

$$S_{\text{relative}} = \tan \theta - \frac{\Delta V_{\text{offset}}}{\Delta T} \quad (3.18)$$

The absolute Seebeck coefficient of the sample, S_{absolute} , is obtained by subtracting the thermocouple's Seebeck coefficient, S_{wire} , from the relative Seebeck coefficient:

$$S_{\text{absolute}} = S_{\text{relative}} - S_{\text{wire}} \quad (3.19)$$

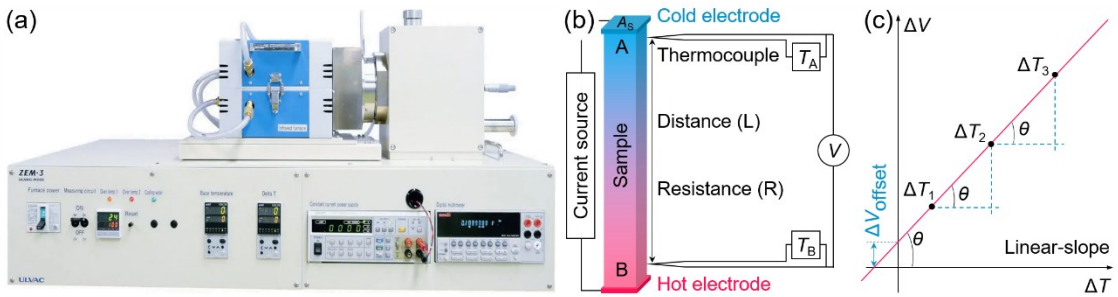


Figure 3.11 | (a) Linseis LSR-3 system utilized in Chapter 5 with assistance from Dr. Ran He's team from IFW Dresden Germany. The Analyzer ZEM-3 system from Dr. Dongwang Yang's team at Wuhan University of Technology China was employed in Chapter 6. (b) Schematic depiction of S and σ measurements. (c) Linear-slope processing method of Seebeck coefficient measurement.

3.3.2 Electrical Conductivity

Two primary methods are used to assess electrical conductivity: the van der Pauw method (Chapter 4, with physical property measurement system (PPMS) Dynacool from Quantum Design in Figure 3.12 (a)) and the more versatile four-point probe method (Chapters 5 & 6, Figure 3.11 (a)). As illustrated in Figure 3.11 (b), a specific current(I) is passed through the sample via outer probes. The potential difference (ΔV) between two inner probes separated by a known distance (L) is measured, allowing calculation of the sample's conductivity using the sample's cross-sectional area (A_s).

$$\sigma = \frac{IL}{\Delta V A_s} \quad (3.20)$$

Simultaneously measuring both Seebeck coefficient and electrical conductivity requires establishing a temperature difference (for Seebeck coefficient) and passing a current (for conductivity). However, the measured voltage includes both the Seebeck voltage and the Ohmic voltage. To isolate the Ohmic voltage, a common technique utilizes positive and negative currents of equal magnitude (V_1 and V_2 , respectively) passed through the sample in opposite directions. The final electrical conductivity is then obtained by averaging V_1 (>0) and V_2 (<0), effectively eliminating the Seebeck voltage contribution.

$$\sigma = \frac{L}{A_s} \left| \frac{2I}{V_1 - V_2} \right| = \frac{L}{A_s} \frac{I}{V_0} \quad (3.21)$$

To ensure accurate measurements, the difference between sample length and probe spacing should exceed twice the sample thickness. Accordingly, this study used samples with dimensions of $2 \times 2 \times 15 \text{ mm}^3$.

3.3.3 Hall Measurement

At a given temperature, the power factor $PF = S^2\sigma$ of a material can be maximized by adjusting the carrier concentration (n) to its optimal value, as the Seebeck coefficient and electrical conductivity vary inversely with n . Moreover, the carrier mobility, a crucial parameter for understanding scattering mechanisms, is not directly measurable but is typically inferred through post-processing measurements of σ and n . Hence, determining n , particularly at low temperatures, is crucial for selecting appropriate dopants and doping levels, analyzing scattering mechanisms, and optimizing overall thermoelectric performance. [Chapter 4](#) utilizes the Hall effect in a PPMS ([Figure 3.12 \(a\)](#)) to measure Hall concentration (n_H) and Hall mobility (μ_H), and its underlying principle is presented in [Figure 3.12 \(b\)](#). For a sample with given width (L) and thickness (A), a current (I_x) is applied to the sample along the x -axis with a current density of (j_x):

$$j_x = \frac{I_x}{dL} \quad (3.22)$$

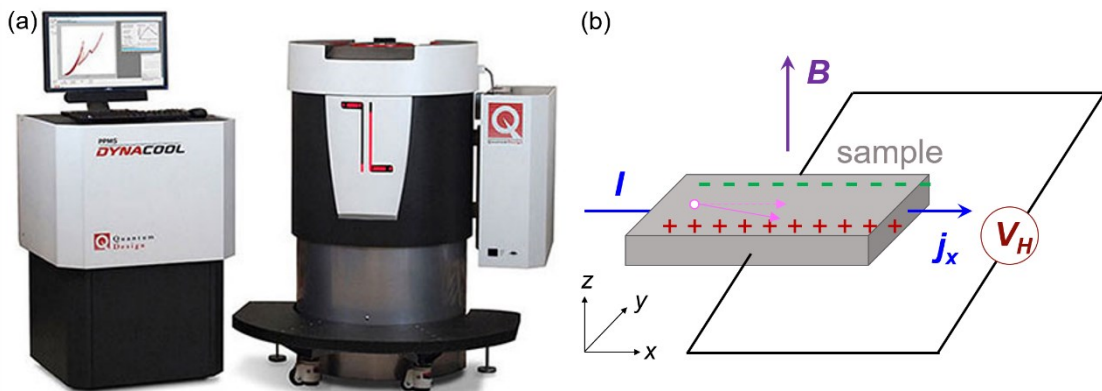


Figure 3.12 | (a) Quantum Design's PPMS DynaCool System. (b) Schematic diagram of Hall coefficient measurement for a *p*-type semiconductor.

A magnetic field (B) is introduced along the z -direction, and mobile charge carriers (holes in this case) are deflected along the y -direction by the Lorentz force. This deflection leads to charge accumulation on opposite sides of the sample, generating a transverse Hall electric field (E_H) across the sample width in the y -direction:

$$E_H = R_H j_x B \quad (3.23)$$

where, R_H is the Hall coefficient.

$$E_H = \frac{V_H}{L} \quad (3.24)$$

$$V_H = R_H \frac{I_x B}{d} \quad (3.25)$$

where V_H is the Hall voltage. For a cavity carrier moving at velocity (v_x), the drift current induced by E_H should precisely counteract the deflection current caused by the Lorentz force to achieve equilibrium that satisfies:

$$j_x = nq v_x \quad (3.26)$$

$$qE_H = qv_x B \quad (3.27)$$

where n is the charge carrier concentration and q is the charge of the carrier. Thus

$$V_H = \frac{1}{nq} \frac{I_x B}{d} \quad (3.28)$$

It can be derived that $R_H = \frac{1}{nq}$. For n -type semiconductors, it can be expressed as $R_H = \frac{1}{ne}$ (where e is the electron charge). Therefore, by measuring the Hall coefficient, both the Hall carrier concentration and the Hall mobility can be obtained as follows:

$$n_H = \frac{1}{e} R_H \quad (3.29)$$

$$\mu_H = \sigma R_H \quad (3.30)$$

3.3.4 Thermal Transport Measurements

Thermal Transport measurement at below room temperature

The PPMS DynaCool system also includes a thermal transport option (TTO, [Figure 3.13 \(a\)](#)), enabling thermal property measurement across a wide temperature range, down to 0.5 K. As illustrated in [Figure 3.13 \(b\)](#), the four-probe configuration utilizes four electrical contacts to the sample for simultaneous measuring the applied current (I), potential difference (ΔV), and temperature difference (ΔT) across a known distance (ΔL). These measurements enable calculation of the Seebeck coefficient, thermal conductivity, electrical conductivity, and ultimately, the zT value. The single measurement mode leverages the steady-state method to determine thermal conductivity via Equation (3.31), despite the time-consuming nature of establishing the measurement temperature.

$$\kappa = \frac{P}{\Delta T} \frac{\Delta L}{S} \quad (3.31)$$

Alternatively, this study utilizes the continuous measurement mode with the double τ model to derive the sample's thermal conductivity during temperature changes (Figure 3.15 (c)). This method analyzes the time-dependent variations in ΔT and ΔV during the heat pulse. Sample resistivity is obtained by averaging pre- and post-heat pulse AC resistivity measurements. To minimize thermal radiation errors, a high sample geometry factor ($A/\Delta L$) is preferred, ensuring the sample's thermal conductivity significantly exceeds the radiation thermal conductivity. Additionally, sample lengths are typically limited to 10 mm to avoid extended thermal diffusion times. Consequently, a sample size of $3 \times 3 \times 8 \text{ mm}^3$ was chosen for this study.

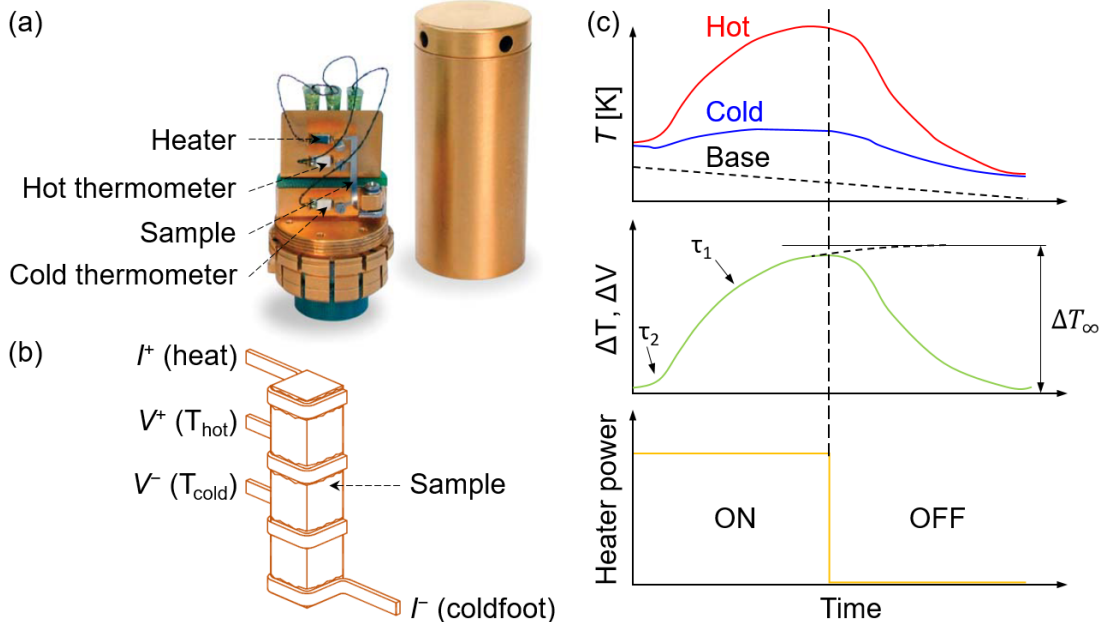


Figure 3.13 | (a) Sample puck with radiation shield in thermal transport sample station. (b) Illustration of leads mounted in a four-probe configuration. (c) Heat pulse (top panel) and temperature (middle panel) and voltage response (bottom panel) at the hot and cold thermometer contacts in an ideal sample.

Thermal conductivity of thermoelectric materials above room temperature is often calculated from separately measured thermal diffusivity (D), density (ρ), and specific heat at constant pressure (C_p) due to the challenges of direct measurement:

$$\kappa_{\text{tot}} = D \times \rho \times C_p \quad (3.32)$$

Density measurements were performed based on the Archimedes' method. Thermal diffusivity and specific heat capacity at elevated temperatures will be addressed.

Thermal diffusivity above Room Temperature

The laser flash method (widely used for measuring thermal diffusivity across varying temperatures) was employed in [Chapters 5](#) and [6](#) using laser thermal conductivity analyzers: Linseis LFA-1000 ([Figure 3.14 \(a\)](#)) and NETZSCH LFA 457. This technique ([Figure 3.14 \(b\)](#)) involves irradiating the sample's bottom surface with a short, high-energy laser pulse. This heat pulse diffuses through the sample and is detected by an infrared detector on the top surface. The resulting thermal signal typically shows a rapid rise to a peak, followed by a gradual decay as depicted in [Figure 3.14 \(c\)](#). Under assumptions of ideal one-dimensional heat diffusion, adiabatic external conditions, and negligible pulse width, the thermal diffusivity can be calculated using the Equation:

$$D = 0.1388 \times \frac{d^2}{\frac{t_1}{2}} \quad (3.33)$$

where d is the sample thickness and $\frac{t_1}{2}$ is the half-heating time, or the time required for the surface temperature to reach half the peak value, as shown in [Figure 3.16 \(d\)](#).

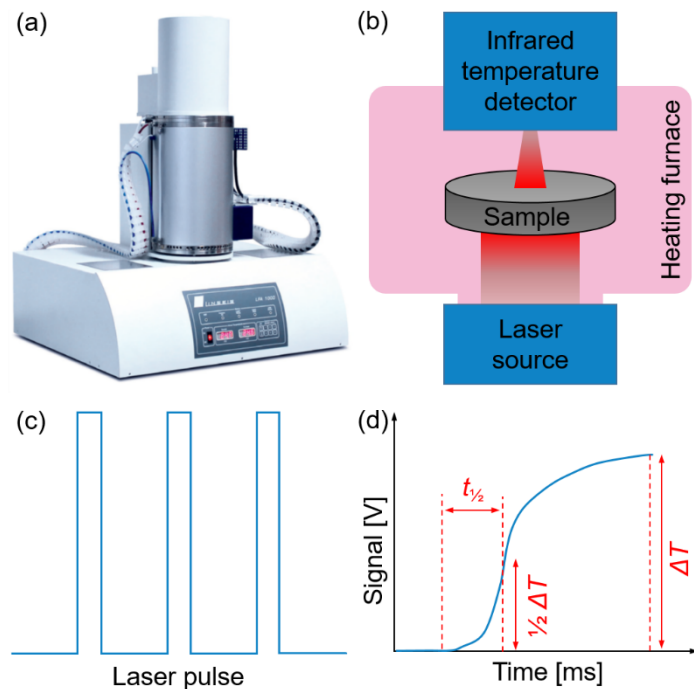


[Figure 3.14](#) | (a) The Linseis LFA 1000 Laser Flash instrument utilized in Chapter 5. Acknowledgments are extended to Dr. Ran He's team for conducting the related measurements in Chapter 5, and to Dr. Yang Dongwang's team at Wuhan University of Technology China for their contributions using the NETZSCH LFA 457 in Chapter 6. (b) Schematic diagram of the laser flash apparatus used for measuring thermal diffusivity. (c) The laser pulse changes over time. (d) The change of the detection signal over time.

For accurate measurements, the sample must be a flat disc with uniform thickness. Smaller samples deviate from this ideal, impacting accuracy. Sample thickness is chosen based on thermal conductivity: thicker for high conductivity materials to minimize insufficient data due to rapid heat transfer, and thinner for low conductivity materials to reduce heat loss and its associated effects on accuracy, such as signal drift and environmental influence. An 8 mm diameter, 2 mm thick disc was chosen for samples in this study.

In addition, while the laser thermal conductivity analyzer system is capable of determining the constant pressure heat capacity C_p of a sample by comparing signals between the test sample and a standard sample with known heat capacity, this study instead utilizes heat capacity data obtained by DSC, which will be elaborated upon in the following section.

Heat capacity at constant pressure

The tin selenide, lead telluride-based, and bismuth telluride-based thermoelectric materials studied in this paper have a constant pressure heat capacity C_p that hardly varies with temperature and, according to the Dulong-Petit law as below⁷⁴

$$C_p = \frac{3R}{\bar{M}} \quad (3.34)$$

where R is the gas constant, and \bar{M} is the average molar mass. Building on Boltzmann's equipartition theorem, Albert Einstein proposed a universal molar specific heat of $3R$.¹⁷³ From a classical perspective, assuming thermally excitable electrons in a continuous band, their expected specific heat capacity would be $3R$ per mole of electrons, i.e., $C_{m,p} \approx 3R = 3k_B N_A \approx 24.943 \text{ J mol}^{-1} \text{ K}^{-1}$.

Measurement of mass density (ρ)

Following cutting and polishing with sandpaper, the sample surfaces were cleaned. To prevent liquid penetration through pores during Archimedes' method density measurements, the samples were coated with wax. Dry weights were measured before (m_1) and after (m_2) wax-coated sample immersion. The density was subsequently calculated:

$$\rho = \frac{m_1}{m_1 - m_2} \rho_{\text{H}_2\text{O}} \quad (3.35)$$

where, $\rho_{\text{H}_2\text{O}}$ is the density of distilled water, which is taken as $0.998561 \text{ g cm}^{-3}$.

3.4 Structural calculations

3.4.1 Density Functional Theory (DFT) Calculations

Bond descriptors, including electrons shared and transferred, were computed using Projector Augmented Wave (PAW) potentials.¹⁷⁴ The DGRID and Critic2¹⁷⁵ codes were employed to determine ES and ET values based on Bader basin analysis.¹⁷⁶ Integration of electron density within a singular Bader basin yielded atomic electron populations. ES values were obtained through integration of the exchange-correlation hole over paired Bader basins, while ET was calculated by subtracting nominal charge from electron population and normalizing by formal oxidation state.

First-principles calculations were performed using the Vienna Ab initio Simulation Package (VASP).¹⁷⁷ Projector augmented wave (PAW) potentials¹⁷⁴ and the Perdew-Burke-Ernzerhof (PBE)¹⁷⁸ generalized gradient approximation (GGA)¹⁷⁹ were employed to describe ion-electron interactions and exchange-correlation effects, respectively. A plane-wave energy cutoff of 400 eV and convergence criteria of 10^{-4} eV/atom for energy and 0.01 eV/Å for force were adopted. Monkhorst-Pack K-point meshes of $6 \times 6 \times 2$ and $4 \times 4 \times 4$ were used for *Pnma* and *Fm* $\bar{3}$ *m* phases of SnSe, respectively. Spin-orbit coupling was incorporated for band structure calculations along high-symmetry paths of the Brillouin zone determined based on previous studies,¹⁸⁰ and band gaps were extracted using VASPKIT.¹⁸¹ Fermi surface visualizations were generated using XCrysDen.¹⁸²

3.4.2 Defect Formation Energy Calculation

Defect formation energies were calculated for $1 \times 3 \times 3$ and $2 \times 2 \times 2$ supercells containing 72 and 64 atoms of SnSe in *Pnma* and *Fm* $\bar{3}$ *m* phases, respectively. Plane-wave cutoff energy was set to 350 eV, with convergence criteria of 10^{-4} eV/atom for energy and 0.01 eV/Å for force. Monkhorst-Pack K-point meshes of $3 \times 3 \times 3$ and $2 \times 2 \times 2$ were used for the respective phases. Optimized lattice parameters ($a = 11.68$ Å, $b = 4.21$ Å, $c = 4.53$ Å for *Pnma* phase; $a = b = c = 6.06$ Å for *Fm* $\bar{3}$ *m* phase) agreed well with experimental data. To address finite-size effects in charged defect calculations, potential alignment and image charge corrections were applied [99].

The formation energy ($\Delta H_{D, q}$) of a defect (D) in charge state (q_c) is defined as:

$$\Delta H_{D,q}(E_F, \mu) = E_{D,q} - E_H - \sum n_\alpha \mu_\alpha + q(E_F + E_V + \Delta V) \quad (3.36)$$

where $E_{D,q}$ is the total energy of the supercell with the defect in q_c , E_H is the total energy of the perfect host supercell, n_α is the number of exchanged atoms (α) added ($n_\alpha > 0$) or removed ($n_\alpha < 0$) from the host to create the defect, μ_α is the corresponding chemical potential of α , E_F is the Fermi level, E_V is the valence band maximum, corrected by the ΔV method [100]. This equation reveals that defect formation energy depends on Fermi level and chemical potentials of constituent elements.

To calculate defect formation energies, we simulated two preparation conditions: Sn-rich (Se-poor) and Se-rich (Sn-poor). To prevent the formation of Sn or Se crystals, the chemical potential of Sn (μ_{Sn}) or Se (μ_{Se}) must be lower than that of their respective bulk phases (Equations 3.37 and 3.38).

$$\mu_{\text{Sn}} - \mu_{\text{Sn}}^0 < 0 \quad (3.37)$$

$$\mu_{\text{Se}} - \mu_{\text{Se}}^0 < 0 \quad (3.38)$$

Here, $\mu_{\text{Sn}}^0 = -3.82$ eV and $\mu_{\text{Se}}^0 = -3.31$ eV represent the reference energies of bulk Sn and Se, respectively. The growth of SnSe must adhere to the thermodynamic equilibrium condition expressed in Equation (3.39):

$$\mu_{\text{SnSe}} = \mu_{\text{Sn}} + \mu_{\text{Se}} = -8.24 \text{ eV} \quad (3.39)$$

However, under Se-rich growth conditions, SnSe_2 is prone to formation. To suppress SnSe_2 growth, the chemical potential of Se (μ_{Se}) must remain below its upper limit. The thermodynamic equilibrium for SnSe_2 is defined by Equation (3.40):

$$\mu_{\text{SnSe}_2} = \mu_{\text{Sn}} + 2\mu_{\text{Se}} = -11.84 \text{ eV} \quad (3.40)$$

By substituting the calculated supercell energies (with and without defects) into Equations (3.36) to (3.40), the defect formation energy can be determined.

4 Outstanding Thermoelectric Performance of Bismuth Telluride: A Chemical Bonding Perspective

Bismuth telluride remains the only commercially viable thermoelectric material despite ongoing research for superior alternatives.^{31,32,183,184} Early research prioritized materials with high average atomic mass for their low lattice thermal conductivity and favorable thermoelectric properties. Bismuth telluride, discovered in the 1950s, exemplifies this approach. The peak zT of bismuth telluride in the low-temperature range makes it ideal for low-temperature thermoelectric applications, including refrigeration. The relatively low melting point (around 500°C) facilitates the processing of bismuth telluride, a key factor in its commercial viability.

4.1 Overview of Bismuth Telluride

4.1.1 Crystal Structure of Bi_2Te_3

Bi_2Te_3 has a molecular weight of 800.76 g mol⁻¹ and a melting point of about 861.5 K and a theoretical density of 7.85 g cm⁻³.¹⁸⁵ Bi_2Te_3 is a narrow bandgap semiconductor with $E_{\text{gap}} = 0.13$ eV at room temperature and belongs to the rhombohedral tetradymite-type crystal system with a space group of $R\bar{3}m$ (D_{3d}^5) and a lattice constant of $a = 0.4384$ nm and $c = 3.045$ nm. The crystal structure in Figure 4.1 shows that Bi_2Te_3 is a typical hexagonal layered structure,^{186,187} consisting of alternating hexagonal single atomic crystal planes stacked in ABC order, and the layered arrangement in the c -axis direction is as follows

...Te-Bi-Te-Bi-Te...Te-Bi-Te-Bi-Te...

Te-Bi-Te-Bi-Te units form quintuple layers (QL): the strong covalent bonds within each QL involve metallic Bi and Te atoms, contributing to the stability and rigidity of the internal structure. However, due to the larger interlayer distance compared to typical covalent bonds, the interaction between adjacent QLs is mainly of the van der Waals-like type with relaxing weak bonding energy, which arises from induced dipoles in the atoms and molecules due to fluctuating electron clouds. Atoms at the surface of each QL have

reduced coordination numbers, leading to weak van der Waals interactions that minimize energy, enabling interlayer flexibility for its characteristic layered material. This allows the crystals to be easily cut along the inter-QL planes and so are prone to cleavage along the (001) plane (*ab* plane).

The hexagonal unit cell, characterized by a point group with a binary axis, a bisector axis, and a triangular axis, contains 3QLs (15 atoms). The translation vectors in the hexagonal system are

$$\mathbf{t}_1 = a \left(\frac{\sqrt{3}}{2}, -\frac{1}{2}, 0 \right), \mathbf{t}_2 = a(0, 1, 0), \mathbf{t}_3 = c(0, 0, 1) \quad (4.1)$$

where a and c are lattice constants of the hexagonal cell with $a = 4.38 \text{ \AA}$, and $c = 30.49 \text{ \AA}$. The corresponding reciprocal lattice vectors are

$$\mathbf{G}_1 = \frac{2\pi}{a} \left(\frac{2}{\sqrt{3}}, 0, 0 \right), \mathbf{G}_2 = \frac{2\pi}{a} \left(\frac{1}{\sqrt{3}}, 1, 0 \right), \mathbf{G}_3 = \frac{2\pi}{c} (0, 0, 1) \quad (4.2)$$

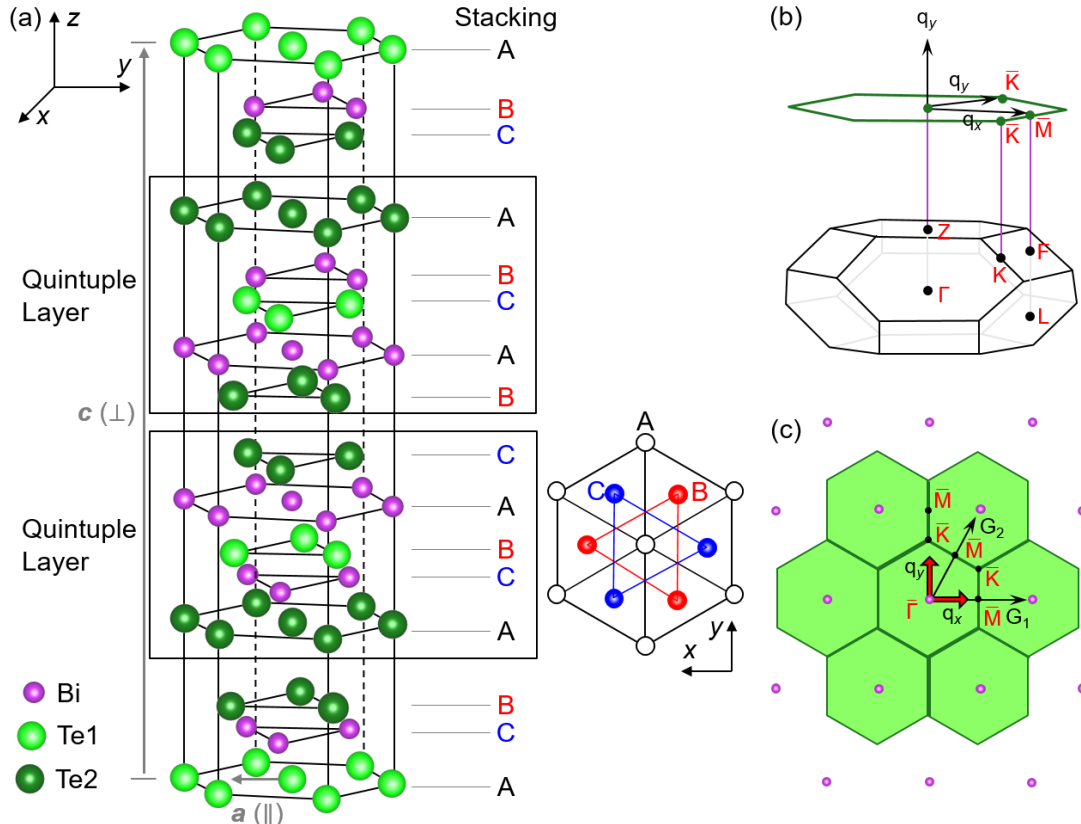


Figure 4.1 | Hexagonal unit cell of the Bi_2Te_3 crystal comprised of three QLs and belonging to the space group $R\bar{3}m$. Note that the Te_2 layer within each QL is a center of inversion symmetry. The bulk and surface reciprocal spatial structure of Bi_2Te_3 .

4 Outstanding Thermoelectric Performance of Bismuth Telluride: A Chemical Bonding Perspective

The reciprocal space structure of Bi_2Te_3 is shown in Figure 4.1 (b) and (c). The first BZ in Figure 4.1 (b) is shown for the rhombohedral unit cell, with 8 hexagonal and 6 rectangular faces. The surface reciprocal lattice (Figure 4.1 (c)) is a 2D hexagonal lattice obtained by projecting the block-like BZ along the q_z axis.

Like Bi_2Te_3 , Sb_2Te_3 and Bi_2Se_3 share the same crystal structure and form continuous solid solutions throughout their compositional range.¹⁸⁵ Bi_2Te_3 exhibits pronounced structural and property anisotropy, evident from the data in Table 4.1. Electrical and thermal conductivities along the cleavage plane (001) are 3-7 and 2-2.5 times higher, respectively, compared to the c -axis values. Conversely, the Seebeck coefficient shows minimal anisotropy.

Table 4.1 | Thermal properties and transport properties determined experimentally of Bi_2Te_3 .

Type	Parameters	Symbols	Value
Thermal properties	Debye Temperature	θ_D	155.5 K
	Latent heat energy		$1.21 \times 10^8 \text{ J} \cdot \text{kg}^{-1} \cdot \text{mol}^{-1}$
	Specific heat capacity	High temperature zone	$(1.507 \times 10^4 + 54.4 T - 0.130$
		Low temperature zone	$T^2) \text{ J} \cdot \text{K}^{-1} \cdot \text{kg}^{-1} \cdot \text{mol}^{-1}$
			$[(0.84 T + 2.33 \times 10^6 (T/\theta_D)^3)$
	Mobility	μ_n	$\text{J} \cdot \text{K}^{-1} \cdot \text{kg}^{-1} \cdot \text{mol}]^{-1}$
	($\perp c$ -axis)	μ_p	$0.120 \text{ m}^2 \cdot \text{V}^{-1} \cdot \text{s}^{-1}$ (293 K)
Transport properties	Mobility-Temperature relationship	Electron	$0.051 \text{ m}^2 \cdot \text{V}^{-1} \cdot \text{s}^{-1}$ (293 K)
		Hole	$\mu_n \propto T^{1.68}$
	Density-of-states effective mass	Electron	$\mu_p \propto T^{1.95}$
		Hole	0.37 m (77 K)
			0.58 m (273 K)
			0.51 m (77 K)
	Scattering factor	m_p^*	1.07 m (273 K)
	Lattice thermal conductivity	$\perp c$ -axis	$1.5 \text{ W} \cdot \text{m}^{-1} \cdot \text{K}^{-1}$ (300 K)
		$\parallel c$ -axis	$0.7 \text{ W} \cdot \text{m}^{-1} \cdot \text{K}^{-1}$ (300 K)

4.1.2 Importance of Bi_2Te_3 in the Room Temperature Region

Low-temperature TE materials have attracted widespread interest due to their ability to be used in low-grade heat harvesting and chip cooling. Bi-Te alloys are considered to be the most suitable materials for near-room temperature generators or cooling devices so far. The optimum compositions for thermoelectric cooling devices are typically composed of $\text{Bi}_2\text{Te}_{2.7}\text{Se}_{0.3}$ (*n*-type) and $\text{Bi}_{0.5}\text{Sb}_{1.5}\text{Te}_3$ (*p*-type) with zT near 1 at room temperature.¹⁸⁸ Figure 4.2 presents established bulk materials known for their high TE performance. Bi_2Te_3 and Sb_2Te_3 alloys are preferred for thermoelectric devices near room temperature (< 473 K) due to their excellent quality factors as *n*-type and *p*-type materials, respectively. Bi_2Te_3 (*n*-type) and Sb_2Te_3 (*p*-type) are doped with Se and Bi as $\text{Bi}_2\text{Te}_{3-x}\text{Se}_x$ and $\text{Bi}_{2-y}\text{Sb}_y\text{Te}_3$ respectively to enhance their TE performance.³⁶ They are widely known as BiTe-based systems.

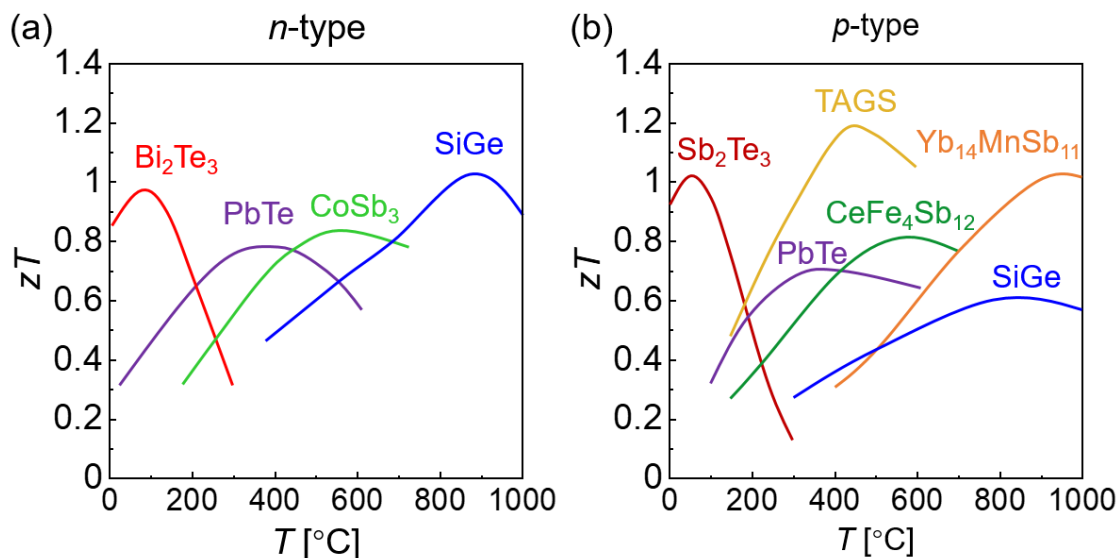


Figure 4.2 | A summary of established high- zT bulk thermoelectric materials: (a) *n*-type and (b) *p*-type materials.²⁷ Notably, the *p*-type material $(\text{GeTe})_x(\text{AgSbTe}_2)_y$ is also known as TAGS.

4.1.3 Improvement of Thermoelectric Performance of Bi_2Te_3

The research on the Bi_2Te_3 system began in the 1960s, with Goldsmid et al. pioneering studies on its thermal and electrical conductivity, and Seebeck coefficient in single crystals prepared via zone-fusion or Bridgman methods.^{189,190} Prior research focused on enhancing the temperature difference achievable by optimizing the Seebeck coefficients

4 Outstanding Thermoelectric Performance of Bismuth Telluride: A Chemical Bonding Perspective

of *p*-type and *n*-type thermoelectric materials¹⁸³. Some earlier works remain highly relevant, including the study of the anisotropy of the Seebeck coefficients by Dennis et al¹⁹¹ and the investigation of anisotropic transport properties and band structure in Bi_2Te_3 with varying carrier concentrations by Goldsmid et al.¹⁸⁴ Moreover, research has advanced beyond binary Bi_2Te_3 , focusing on manipulating carrier concentration and optimizing thermoelectric properties in ternary compounds: Se-doped Bi_2Te_3 solid solutions and halogen-doped Bi_2Te_3 variants.^{184,192,193} In 1965, the presence of anti-site defects in Bi_2Te_3 was first identified by Miller et al. using density measurements.¹⁹⁴ Horak et al. investigated the effect of external dopant atoms on the anti-site defects in Sb_2Te_3 and Bi_2Te_3 .¹⁹⁵ Subsequently, Navratil et al. proposed a "siderophore-like effect" associated with point defects, suggesting that excess electrons can be introduced by the powder metallurgy preparation process.¹⁹⁶ As experimental data accumulates, theoretical calculations are increasingly focused on understanding the band structure, effective mass, and carrier scattering of Bi_2Te_3 -based compounds.^{197,198} Zone melting traditionally yields ingots with superior properties due to their homogeneous composition and high crystal quality compared to powder-sintered polycrystalline samples. This technique enables mass production of commercially available Bi_2Te_3 -based *p*-type and *n*-type solid solutions, typically exhibiting zT around 1.⁵³

Innovation in the preparation process

Spark plasma sintering (SPS) and hot pressing (HP) have emerged as promising techniques to enhance zT by promoting grain size refinement and the introduction of nanostructures, leading to a significant reduction in thermal conductivity. Moreover, fine-grained bulk materials are increasingly favored for thermoelectric devices due to their superior machinability and durability. As discussed previously, the strategies to enhance zT encompass carrier concentration regulation, band optimization, microstructure tuning, and the incorporation of nanocomposites.

Carrier concentration in Bi_2Te_3 -based materials can be primarily tuned by incorporating Sb or Se via solid solution formation, yielding *p*-type $\text{Bi}_x\text{Sb}_{2-x}\text{Te}_3$ and *n*-type $\text{Bi}_2\text{Te}_{3-x}\text{Se}_x$, respectively, as achieved through zone melting.¹⁸⁵ However, point defects like anion vacancies and anti-site defects are prevalent in these materials, which can significantly impact carrier concentration, particularly when introduced by mechanical deformation during the preparation process.¹⁹⁴⁻¹⁹⁶ Numerous studies have reported the impact of point

defects on the carrier concentration and thermoelectric properties of *p*-type $(\text{Bi},\text{Sb})_2\text{Te}_3$ and *n*-type $\text{Bi}_2(\text{Te},\text{Se})_3$.^{81,199–205} Figure 4.3 demonstrates the dependence of point defect type and concentration on the dopant concentration, Sb and Se, in the system. Additionally, a comparison of single crystals with conventionally processed (sintered and hot-forged) samples highlights that mechanical deformation can also affect carrier concentration by altering the point defect concentration.²⁰¹

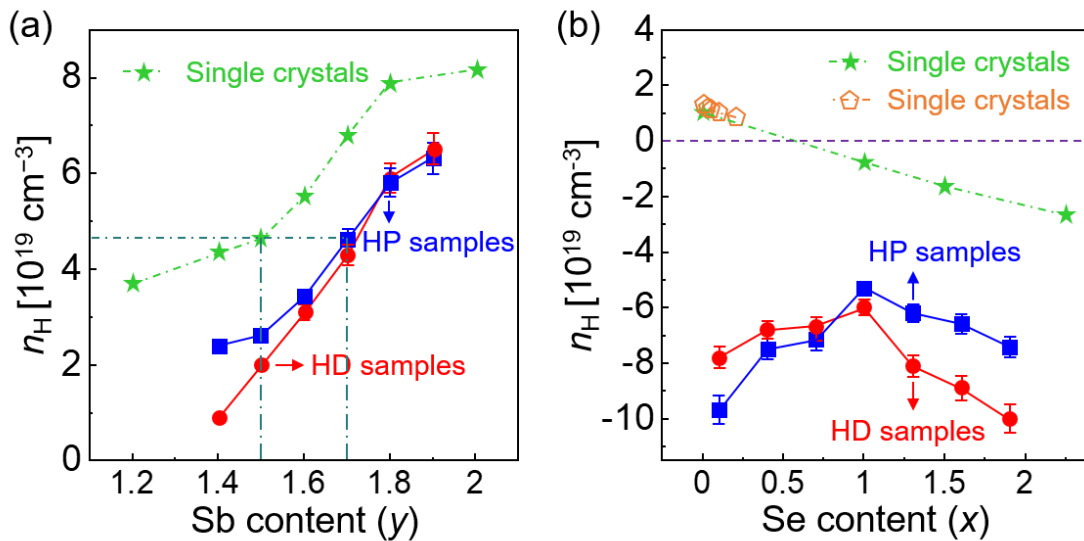


Figure 4.3 | The variation of point defect concentration caused by Sb and Se solid solution concentration and the influence of mechanical deformation on carrier concentration: (a) *p*-type $\text{Bi}_{2-x}\text{Sb}_x\text{Te}_3$, (b) *n*-type $\text{Bi}_2\text{Te}_{3-x}\text{Se}_x$.²⁰¹

The regulation of microstructure relies on novel synthesis methods, and can also be achieved through second-phase composites. A large number of nanostructures were found in the bulk upon ball-milling combined with hot-press sintering of zone-melting of $(\text{Bi},\text{Sb})_2\text{Te}_3$ crystals, which have a much lower thermal conductivity compared to the coarse-crystalline ingots, enhancing zT up to 1.4.¹³³ Liquid-phase sintering, through the introduction of grain boundary dislocations, effectively scatters intermediate-frequency phonons, leading to ultra-low thermal conductivity and a remarkable zT of 1.86.²⁰⁶ Grain refinement via a ‘dump banding’ method yields a zT of 1.2.²⁰⁷ For *n*-type $\text{Bi}_2(\text{Te},\text{Se})_3$, a zT of 1.18 was achieved through a combination of chemical nanosheet preparation and rapid sintering.⁸¹ Notably, texture engineering is particularly effective in enhancing the zT of *n*-type $\text{Bi}_2(\text{Te},\text{Se})_3$ due to its strong anisotropic properties.²⁰⁸

Various doping

Alongside advanced preparation methods, researchers explore reducing thermal conductivity using nanoscale secondary phases.^{82–90} Well-chosen composite materials can achieve this reduction while enabling energy filtering.^{209,210} For instance, SiC nanoparticle composites in $(\text{Bi},\text{Sb})_2\text{Te}_3$ enhance electrical properties without significantly raising thermal conductivity, leading to a higher zT value.²⁰⁹ Doping with Cd, Cu, and Ag achieves an average zT of 1.2 (373–573 K).²¹¹ Additionally, adjusting the Sb content in $(\text{Bi},\text{Sb})_2\text{Te}_3$ suppresses intrinsic excitation and increases the peak zT temperature.¹⁹⁹

Despite advancements in optimization strategies, the achievable zT for Bi_2Te_3 -based materials remain limited to a range of 1–1.5, hindering the application of high-efficiency thermoelectric devices. This suggests a potential bottleneck in current optimization approaches and theoretical understanding. Notably, studies of high-performing materials like PbTe and GeTe reveal a correlation between their superior thermoelectric properties and a specific chemical bonding mechanism.^{10,212,213} As summarized in Table 4.2, they exhibit high dielectric constants, large Born effective charges, large coordination numbers, relatively symmetric crystal structures, etc. Bismuth telluride shares these characteristics, suggesting similarities in chemical bonding to PbTe. Is the same chemical bonding a key factor that makes bismuth telluride a good thermoelectric material?

Table 4.2 | The average Born effective charges (Z^*_{avg}), ECoN, E_{gap} , ε_{∞} , electrical conductivities, and Debye temperatures of some V_2VI_3 materials.⁸⁹

Alloy	Type	σ [S cm ⁻¹]	Z^*_{avg}	ECoN	E_{gap}	ε_{∞}	Θ_D [K]
GeTe ^{cub*}	<i>p</i>	6.8×10^3	9.42	6.038	0.36	91.501	157
PbTe	<i>p</i>	2.9×10^3	5.758	6.038	0.34	26.822	130
Bi_2Te_3	<i>p</i>	6.6×10^2	6.19	5.79	0.53	(35.4; 35.4; 25.5)	155
Bi_2Se_3	<i>n</i>	1.0×10^3	4.98	5.66	0.54	(19.8; 19.8; 12.0)	182
Bi_2S_3	<i>n</i>	2.0×10^{-3}	4.88	4.76	1.36	(14.0; 14.1; 9.7)	284
Sb_2Te_3	<i>p</i>	2.3×10^3	5.93	5.84	0.29	(39.5; 39.5; 24.7)	162
Sb_2Se_3	<i>n</i>	4.0×10^{-7}	4.41	4.17	0.76	(19.1; 18.5; 9.7)	292
Sb_2S_3	-	1.0×10^{-8}	4.24	3.92	1.28	(14.2; 12.5; 7.34)	364
$\beta\text{-As}_2\text{Te}_3$	<i>p</i>	6.5×10^2	7.41	5.84	0.26	(65.7; 65.7; 42.6)	148

Understanding chemical bonding offers the potential to enhance the zT value through precise chemical bond tuning. In exploratory mechanistic research, single crystals can minimize the impact of grain boundaries and other defects on performance, addressing the structural defects complexity in polycrystalline materials fabricated using various processing techniques mentioned previously. In this chapter, the vertical Bridgman technique was selected to prepare single-crystal bismuth telluride, and the chemical bonding mechanism as well as its thermoelectric properties were systematically investigated in order to construct the relationship between TE and chemical bonding. Finally, some schemes will be proposed to further improve the TE performance by targeted modulating the chemical bonding.

4.2 Composition and Structure of the Bismuth Telluride Single Crystal

4.2.1 Composition of Bismuth Telluride

The powder XRD patterns of $\text{Bi}_x\text{Sb}_{2-x}\text{Te}_3$ ($x = 0.5, 0.6$ and 0.7) grown in the Bridgman furnace are illustrated in Figure 4.4 obtained by symmetric θ - 2θ scans. The diffraction peak positions of the $\text{Bi}_x\text{Sb}_{2-x}\text{Te}_3$ samples align with those of the standard card (ICSD_184246), confirming the formation of a single-phase rhombohedral structure with no detectable impurities. The strongest peak corresponds to the $(0\ 1\ 5)$ peak at $2\theta = 28^\circ$.

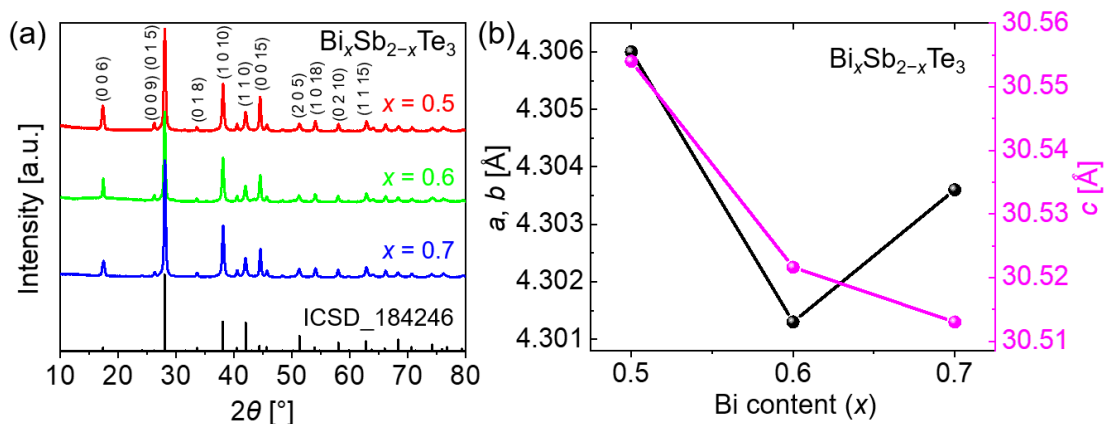
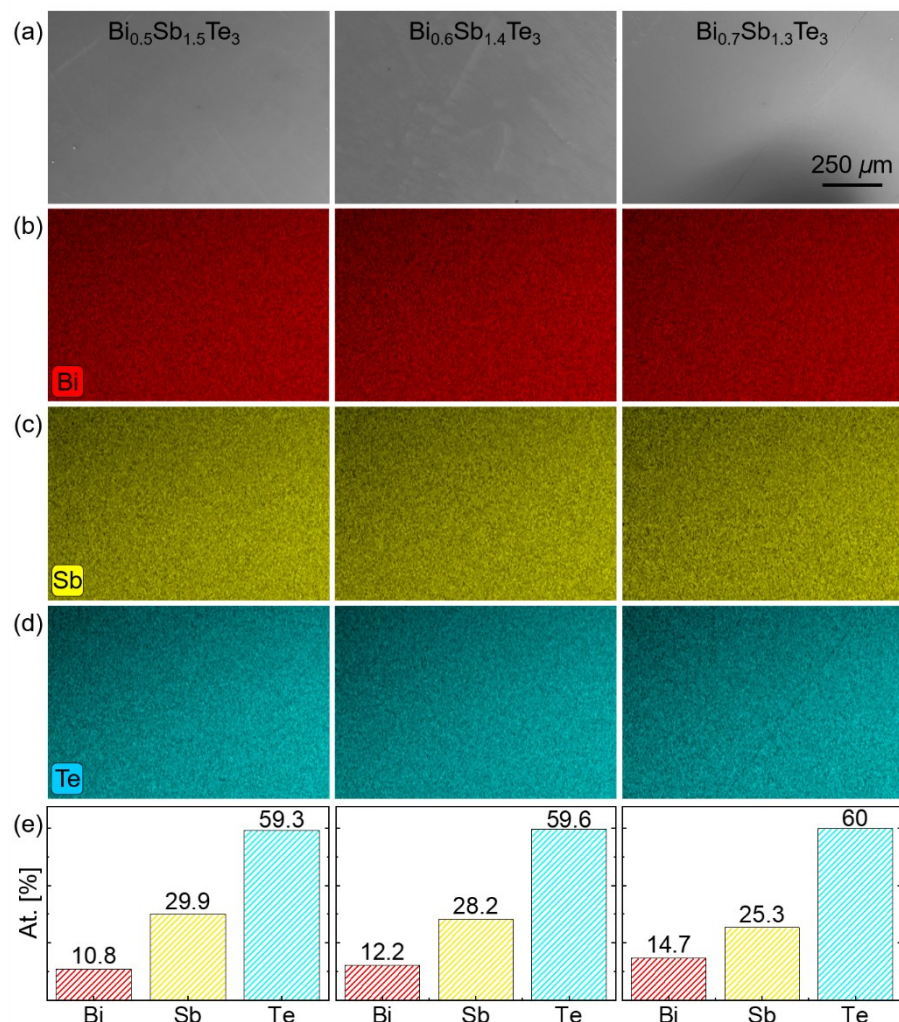


Figure 4.4 | (a) XRD of $\text{Bi}_x\text{Sb}_{2-x}\text{Te}_3$ ($x = 0.5, 0.6$ and 0.7). (b) Calculated lattice constants based on the data in (a).

4 Outstanding Thermoelectric Performance of Bismuth Telluride: A Chemical Bonding Perspective

The lattice constants determined by XRD Rietveld refinement are presented in [Figure 4.4 \(b\)](#). $\text{Bi}_{0.5}\text{Sb}_{1.5}\text{Te}_3$ exhibits the largest lattice constants ($a = b = 4.306(6)$ Å, $c = 30.554(24)$ Å) compared to $\text{Bi}_{0.6}\text{Sb}_{1.4}\text{Te}_3$ and $\text{Bi}_{0.7}\text{Sb}_{1.3}\text{Te}_3$. This increase in lattice constants with increasing Sb content can be attributed to the difference in the atomic radii of Bi (1.60 Å), Sb (1.28 Å) and Te (1.4 Å), causing the crystal lattice to expand. The variation in lattice constants leads to slight shifts in the peak positions of the XRD pattern.

EDX analysis of the single crystals in [Figure 4.5](#) reveals the uniform distribution of Bi, Sb, and Te within each crystal. The measured molar Bi:Sb:Te ratios (3:7:15, 7:13:30, and 1:3:6) closely match the nominal composition, indicating minimal elemental loss during processing and negligible sample contamination.



[Figure 4.5](#) | (a) SEM images acquired using secondary electrons. EDX mapping of the single-crystals confirming the homogeneous distribution of (b) Bi, (c) Sb, and (d) Te elements throughout the domain. (e) The atomic concentration (at. %) summarizing the composition of (a).

As explained in [Section 2.3](#), APT can be utilized to identify the 3D atomic distribution of compounds. [Figure 4.6](#) shows the atomic distributions for three samples, demonstrating that all atoms are uniformly distributed, and the atomic percentage content is consistent with the EDX results. The nearest neighbor (NN) investigation examines the interatomic distances in the vicinity of each atom. [Figure 4.6](#) reveals the interatomic distances for Bi-Bi, Sb-Sb, and Te-Te pairs. The observed distributions closely resemble those expected for randomly arranged atoms within the alloy matrix, suggesting a statistically random distribution of Bi, Sb, and Te on the atomic scale.

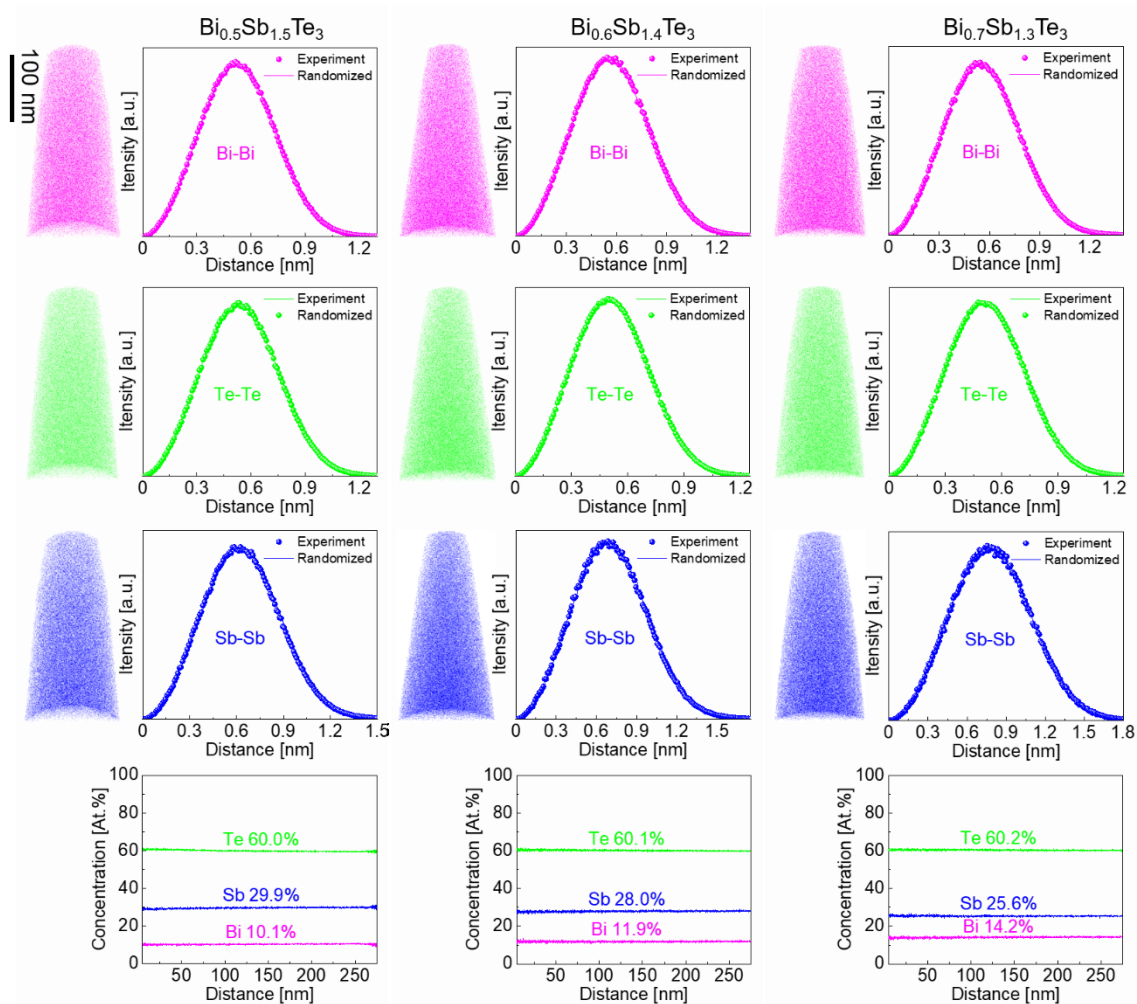


[Figure 4.6](#) | 3D elemental distribution of Ge and Se as well as the Nearest neighbor distribution of Ge and Se showing the homogeneous composition of $\text{Bi}_x\text{Sb}_{2-x}\text{Te}_3$ ($x = 0.5, 0.6, \text{ and } 0.7$).

4.2.2 Structure of Bismuth Telluride

As described in [Section 3.2.1](#), EBSD can be used to investigate the microstructure.

Figure 4.7 (a) illustrates the EBSD measurements of single crystals performed on the cleavage plane. The inverse pole figure (IPF) in Figures 4.7 (b) - (d) obtained from the post-processing software (OIM Analysis 7) shows the crystal orientation of the measured area, confirming that the regions have a single orientation (as evidenced by the inserted IPF color legend). Notably, all three detected surfaces exhibit crystal planes perpendicular to the (0 0 1) plane, indicating preferential growth along (0 0 1) crystal plane. This preferential growth aligns with the strong anisotropy of thermal conductivity discussed in Section 4.2, as layered BST materials possess a significantly higher thermal conductivity along the basal plane compared to directions perpendicular to it, so the crystals grow in the direction of higher thermal conductivity.

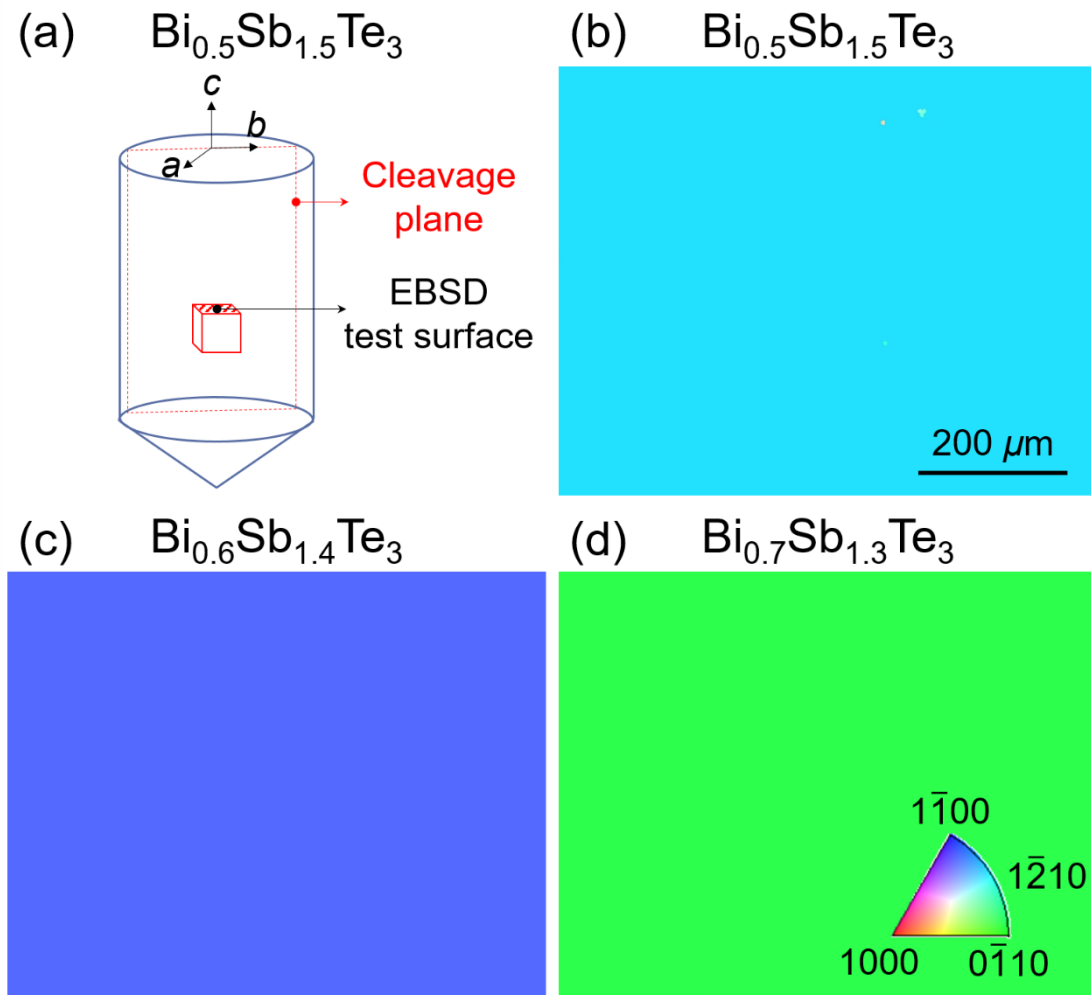


Figure 4.7 | Single crystals analysed via EBSD. (a) Illustration showing how the single crystals were cut for EBSD measurements. IPF of the region measured on the cleavage plane of (b) $\text{Bi}_{0.5}\text{Sb}_{1.5}\text{Te}_3$, (c) $\text{Bi}_{0.6}\text{Sb}_{1.4}\text{Te}_3$, and (d) $\text{Bi}_{0.7}\text{Sb}_{1.3}\text{Te}_3$.

4.3 Optical Properties and Unconventional Bond Breaking

4.3.1 Optical Reflection and Absorption of Bismuth Telluride

The vibrational spectrum refers to the absorption of light caused by the vibration of molecules or atomic groups of a substance due to the interaction with light. If the light source used is in the infrared spectral range, it is the infrared absorption spectrum (analysis of FTIR data will be presented in [Figure 4.9](#)). If an intense monochromatic light, such as a laser, is used, a laser Raman spectrum is produced. The measurements of the overall vibrational spectra of Bi_2Te_3 can be used to determine the values of some empirical parameters entering the pseudo-charge phonon model for identifying the characteristics and symmetries of the bulk phase and surface phonon dispersion of the crystal. FTIR and Raman spectroscopy are light scattering methods and therefore can only provide information about the BZ central optical phonon mode due to the low momentum transfer involved in the scattering process. The original rhombohedral cell of Bi_2Te_3 contains 5 different atoms, each with 3 degrees of freedom. Bi_2Te_3 bulk crystals show 15 lattice vibrational modes (phonon polarization branches). Of these, 3 are acoustic branches and 12 are optical phonons. The atomic displacements of these modes at the point Γ are shown in [Figure 4.8 \(a\)](#), showing the displacement of 5 atoms in the Bi_2Te_3 primitive unit cell for the optical phonon mode at the center of the bulk Brillouin zone. Non-degenerate A_g and doubly-degenerate E_g modes can be accessed by Raman scattering.

According to group theory, the 12 optical branches have $2A_{1g}$, $2E_g$, $2A_{1u}$, and $2E_u$ symmetries. Due to the inversion symmetry of the crystal, these phonon modes only exhibit Raman or infrared (IR) activity. [Figure 4.8 \(b\)](#) presents the Raman spectra of the Bi_2Te_3 bulk crystal and $\text{Bi}_x\text{Sb}_{2-x}\text{Te}_3$ ($x = 0.5$, 0.6 , and 0.7) samples, showing results for the Brillouin zone (BZ)-centered Raman active modes, i.e., E_g^1 (TO), A_{1g}^1 (LO), E_g^2 (TO) and A_{1g}^2 (LO), which are consistent with the literature.²¹⁴

In this nomenclature, TO and LO are transverse and longitudinal optical phonons, respectively. The E_g and A_{1g} modes are both doubly degenerate: in E_g , the atoms vibrate in the base plane, while in A_{1g} the atoms vibrate along c_H . The E_g^1 and A_{1g}^1 vibrations occur at lower frequencies than the E_g^2 and A_{1g}^2 . The latter mode, in which the external Bi and Te(1) atoms are in opposite phases, is mainly affected by the forces

between the Bi and Te(1) atoms (see Figure 4.8 (a)). In the E_g^1 and A_{1g}^1 modes, the more external Bi and Te(1) atomic pairs move in the same phase. Thus, these vibrations are primarily involved in the Bi-Te(2) bonding force. In crystals with inversion symmetry, the infrared activation mode (A_{1u}) must be odd-asymmetric when inverted, while the Raman activity modes (E_g and A_{1g}) must be even-asymmetric.

For maintaining the crystal symmetry, odd-union phonons (IR activity) would not appear in the Raman spectrum of a bulk sample, which is why A_{1u} mode is not displayed in all four bulk samples in Figure 4.8 (b), indicating good structural symmetry of the samples. Interestingly, as can be seen from Table 4.3, the ratio $I(A_{1g}^2)/I(E_g^2)$ in Figure 4.8 (b) evolves from bulk crystalline Bi_2Te_3 to $\text{Bi}_x\text{Sb}_{2-x}\text{Te}_3$ ($x = 0.5, 0.6$, and 0.7): the intensity of in-plane vibrations, $I(E_g^2)$, measured in the bulk crystalline Bi_2Te_3 is higher than that of the out-of-plane vibrations $I(A_{1g}^2)$. However, in $\text{Bi}_x\text{Sb}_{2-x}\text{Te}_3$ ($x = 0.5, 0.6$, and 0.7), the in-plane vibrational intensity $I(E_g^2)$ increases with increasing Sb content. Using $H = 4$ nm in $\text{Bi}_x\text{Sb}_{2-x}\text{Te}_3$, the ratio $I(A_{1g}^2)/I(E_g^2) > 1$.

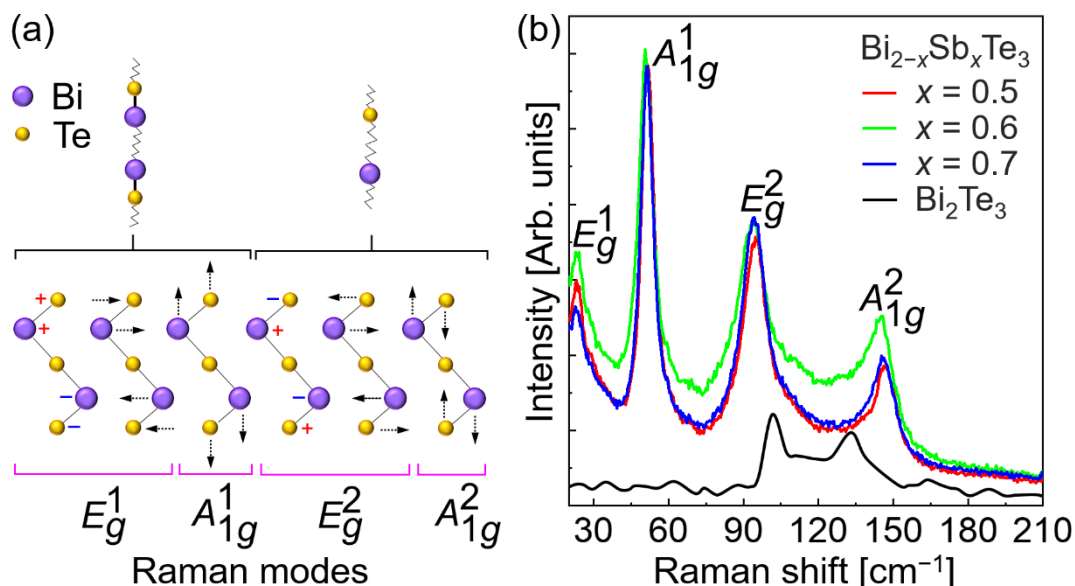


Figure 4.8 | (a) Schematic of the main lattice vibrations in $\{\text{-Te}(1)\text{-Bi}\text{-Te}(2)\text{-Bi}\text{-Te}(1)\}$ quintuples. Large circles are Bi atoms. A small circle in the middle is Te (2) atom, a center for the inversion symmetry. The “+” and “-” signs in the schematics indicate atomic motions toward and from the observer. In all panels, the letters “E” and “A” indicate the in-plane and out-of-plane (c axis) lattice vibrations, respectively. The subscript “g” denotes Raman active. (b) Raman spectra of reference bulk Bi_2Te_3 crystal²¹⁴ and $\text{Bi}_x\text{Sb}_{2-x}\text{Te}_3$ ($x = 0.5, 0.6$, and 0.7).

Table 4.3 | Comparison of experimental samples $\text{Bi}_{2-x}\text{Sb}_x\text{Te}_3$ ($x = 0.5, 0.6$, and 0.7) and phonon frequencies of Bi_2Te_3 at the Γ point.

Modes		Frequencies (cm^{-1})		
Symmetry	Number	$\text{Bi}_{2-x}\text{Sb}_x\text{Te}_3$		
		$x = 0.5$	$x = 0.6$	$x = 0.7$
A_{1g}	1	51.6	50.7	51.1
	2	146.3	145.8	145.3
E_g	1	23.2	24.2	22.7
	2	94.9	94.4	94.4
$I(A_{1g}^2)$		3085.15	3105.4	3083.1
$I(E_g^2)$		2856.7	2879.95	2882.95
$I(A_{1g}^2)/I(E_g^2)$		1.0799	1.0783	1.0694
				0.75

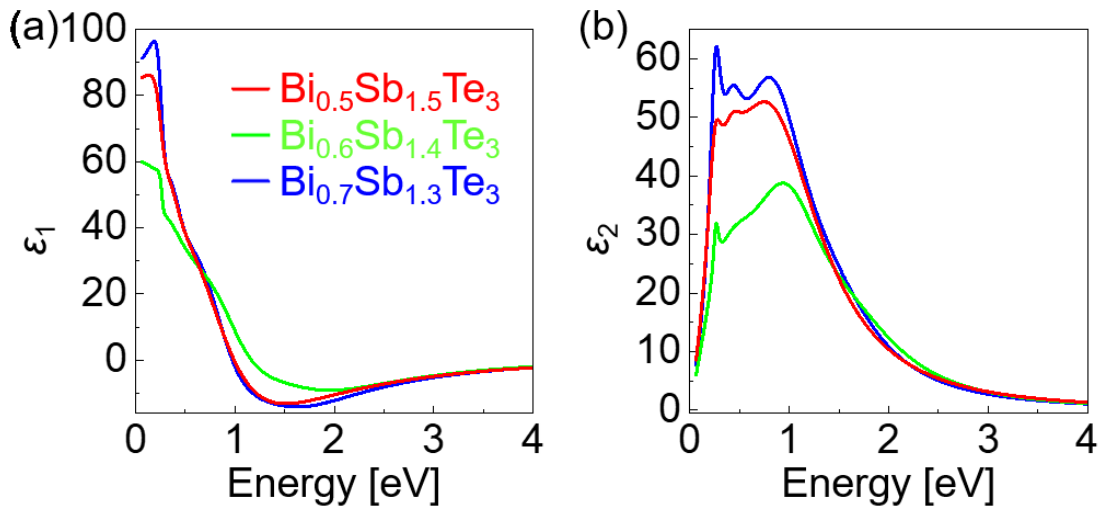


Figure 4.9 | Measured (a) real part and (b) imaginary part of the Bi-Sb-Te samples.

ε_2 is primarily influenced by two factors: density of states and matrix elements of the compounds. The matrix elements govern the ease of electron transitions between different states (interband transitions). Strong orbital overlap and band alignment facilitate electron transitions. While orbital alignment is influenced by chemical bonding, a more direct

factor is structural symmetry. Highly symmetric structures promote electron transitions, while distorted structures (e.g., staggered bonds) hinder them. Severely distorted structures (large Peierls distortion) are typical of covalent bonded materials, whereas minimal distortion in MVB compounds facilitates orbital overlap. FTIR analysis of the optical constants in [Figure 4.9](#) reveals that the energy ranges of optical absorption for the three samples are similar. The lower $\varepsilon_{2,\max}$ observed in $\text{Bi}_{0.6}\text{Sb}_{1.4}\text{Te}_3$ compared to the other two MVB counterparts likely originates from more structural defects that reduce orbital overlap and light absorption. This observation implies the changing pattern of TE performance of the three, which will be thoroughly analyzed in [Section 4.4](#).

Raman and FTIR revealed the light absorption characteristics of BST compounds, which are related to its chemical bonding. Further exploration into the specific bonding types responsible is necessary to comprehensively understand this behavior. Laser-assisted field evaporation in APT not only acquires three-dimensional atomic distributions of elements, but also elucidates bonding mechanisms in compounds through breaking chemical bonds.

4.3.2 Bond Breaking in Atom Probe Tomography of Bismuth Telluride

Bond-breaking measured by APT show systematic variations in compounds with different bonding mechanisms: metals and covalently bonded semiconductors display bond ruptures, with successful laser pulses predominantly dislodging single fragments. In bulk crystalline chalcogenides, there is a higher probability of observing multiple fragments. The high probability of multiple events (PME discussed in [Section 3.2.3](#)) per laser pulse offers compelling evidence for unique bonding in such chalcogenides. The 3D reconstruction using multiple events in [Figure 4.10](#) convincingly demonstrates the homogeneity of multi-event evaporation, which can be employed to explain the bonding mechanism. The PME profile along the APT reconstruction from top to bottom shows a stable value of about 78%-83% in the whole probed volume, providing evidence for the MVB bonding mechanism.

"Multiple events" exhibit a strong correlation in both the order of evaporation and their position on the sample surface. Studies have confirmed this correlation by comparing the ion evaporation sequence with a statistical Poisson distribution.²¹⁵ Spatial correlation within multiple events is evident through analysis of the distance distribution between ion pairs on the detector.²¹⁵ A powerful analytical tool called the "correlation histogram" has

been developed to reveal the chemical identity and associated correlations among fragments in these multiple events.²¹⁶ The correlation histogram captures multiple events from various mechanisms (normal evaporation, preferential evaporation, dissociation, etc.) observed during APT measurements, as illustrated in Figure 4.11 (a).²¹⁶ Ideally, laser-assisted APT should only trigger ion evaporation (single or multiple events) upon a laser pulse, as "normal multiple events", which contribute to the sharp peaks in the mass spectrum and appear at the intersection points in the correlation histogram.

The correlation histogram also offers valuable insights into dissociation and preferential evaporation processes. Dissociation refers to the phenomenon where a large ion fragments into smaller pieces due to the strong electric field. These dissociation events are visualized as curves with negative slopes in the correlation histogram, known as "dissociation tracks".²¹⁶ By analyzing these tracks, researchers can determine the dissociation formula, revealing the relationship between the parent ion and its fragment ions (daughter ions).²¹⁶ Notably, the smaller fragments produced by dissociation register as multiple events on the detector.

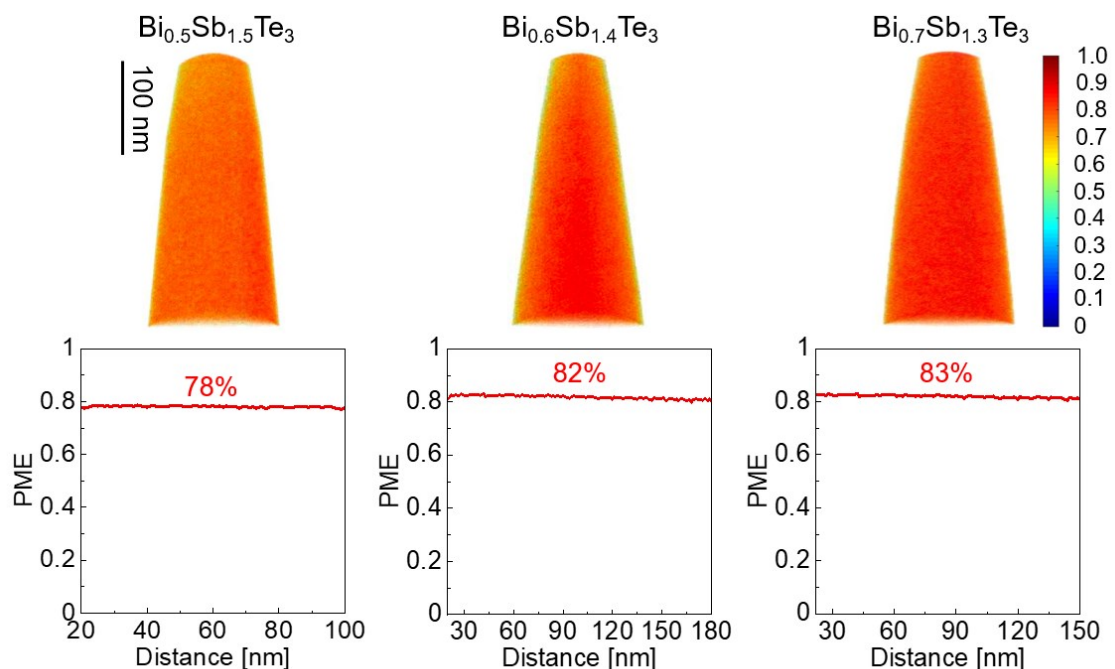


Figure 4.10 | 3D reconstruction using multiple events from APT measurement of $\text{Bi}_x\text{Sb}_{2-x}\text{Te}_3$ samples, and the corresponding PME values from top to bottom.

Preferential evaporation arises from non-ideal experimental parameters. If the applied base voltage exceeds the evaporation field of a particular element, that element will continuously evaporate even without a laser pulse. This unintended preferential evaporation can also occur when the laser pulse energy is insufficient. As preferential evaporation leads to a constant ion flow, it inevitably results in a higher frequency of multiple events. These multiple events manifest as positively sloped curves in the correlation histogram, starting at (0, 0) and extending towards infinity as illustrated in Figure 4.11 (a).

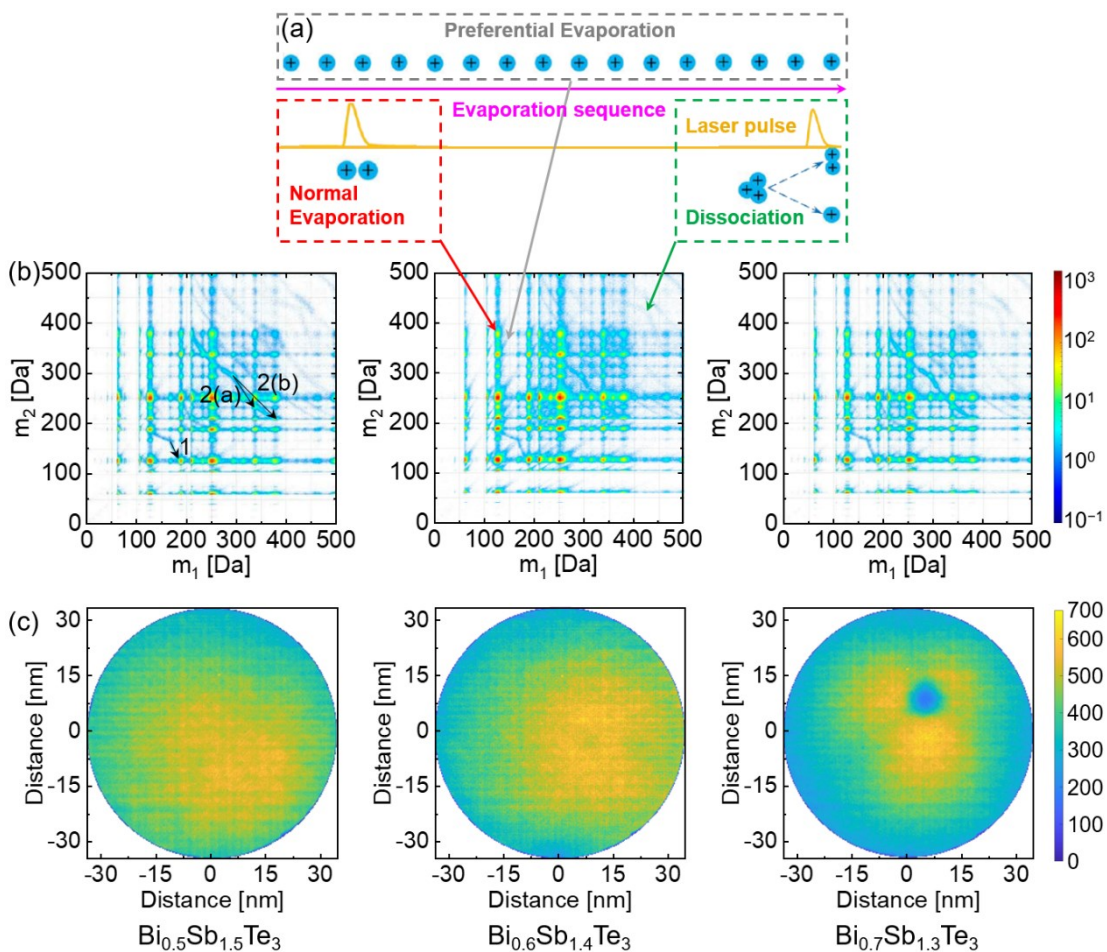


Figure 4.11 | (a) Illustration showing the three different mechanisms producing multiple events in the correlation histogram. (b) Correlation histograms of all materials studied. The dissociation tracks (marked by red arrows) represent the dissociation of a heavier molecule into two or more ions. A laser pulse energy of 10 pJ is used for all the measurements. (c) Spatial distributions of multiple events on the detector. Note the color scale is related to the total quantity of multiple events, which does not necessarily mean a high probability of multiple events since a longer testing time will also give rise to a denser detector histogram.

Figure 4.11 (b) shows the correlation histogram of the as-prepared compounds, and the tracks of line segments marked 1, 2 represent the dissociation process. The starting point of the arrow in track 1 represents the parent ion $\text{Sb}_2\text{Te}_2^{2+}$, and the end one represents the daughter ions after the dissociation process, Te^+ and Sb_2Te^+ . And in track 2 the parent ion BiSbTe_2^{2+} has two different dissociations, one is dissociated into SbTe^+ and BiTe^+ (track 2(a)), and the other is dissociated into Bi^+ and SbTe_2^+ (track 2(b)). Since the composition and structure of the three samples are very similar, the types of their field dissociation are also almost the same. Although field dissociation exists in BST materials, the multiple events due to this process only account for a small part of the total multiple events, which is not the root cause of the high PME of BST materials. The mechanism of correlated field evaporation is that after field evaporation of one atom setting at the surface of the needle sample, the nearest neighbors are evaporated subsequently. Although this mechanism is responsible for multiple events, the PME would not be higher than 10%-20%. Thus, correlated field evaporation is also not the reason for the high PME of BST materials. Note that all specimens in Figure 4.10 and Figure 4.11 were measured with the same 10 pJ laser pulse, since for all compounds the probability of multiple events increases with decreasing laser pulse energy. Therefore, the 10 pJ laser pulse is used to eliminate the factor of preferential evaporation caused by too low laser pulse energy, thereby increasing multi-event evaporation. Therefore, the stable evaporation process combined with the uniform distribution of multiple events in our study undoubtedly excludes the possibility of explosive evaporation as a possible source of multiple events.

Figure 4.11 (c) visually shows the spatial distribution of multiple events on a multi-channel detector (detector histogram), confirming measurement homogeneity across all compounds. The color intensity reflects the total number of events, where a denser histogram indicates either higher probability or longer testing time. All the $\text{Bi}_x\text{Sb}_{2-x}\text{Te}_3$ alloys show a high probability of multiple events, while $\text{Bi}_{0.7}\text{Sb}_{1.3}\text{Te}_3$ exhibits a distinct crystallographic pole. This can be attributed to atomic-scale discontinuities in the electric field near the tip apex caused by local curvature variations. Such discontinuities can lead to trajectory aberrations for ions, resulting in detector regions with abnormally high or low ion density. Crystallographic poles, as observed in previous studies for Bi_2Te_3 , Bi_2Se_3 and Sb_2Te_3 , typically align with the [100] direction, perpendicular to the quintuple layer and vacancy layer. These pole regions often exhibit high magnification.

4.4 Metavalent Bonding Empowers the High Thermoelectric Performance

4.4.1 Electric Transport Properties of Bismuth Telluride

The electrical conductivity and Seebeck coefficient versus temperature for the $\text{Bi}_x\text{Sb}_{2-x}\text{Te}_3$ samples ($x = 0.5$, 0.6, and 0.7) are shown in Figure 4.12 (a) and (b). The results reveal a significant influence of Sb doping on electrical conductivity: the conductivity increased with increasing Sb content. Bi_2Te_3 -based materials possess a high concentration of intrinsic lattice defects, making it sensitive to dopant effects on carrier concentration. Sb doping can manipulate these defects, promoting an increase in hole carriers and consequently enhancing electrical conductivity according to Equation (2.11). Table 4.4 includes the measured n_{H} and μ_{H} at room temperature, which confirms that $\text{Bi}_{0.5}\text{Sb}_{1.5}\text{Te}_3$ exhibits the highest n_{H} ($8.5 \times 10^{19} \text{ cm}^{-3}$) but the lowest μ_{H} ($182.3 \text{ cm}^2 \text{ V}^{-1} \text{ s}^{-1}$) among the studied compositions.

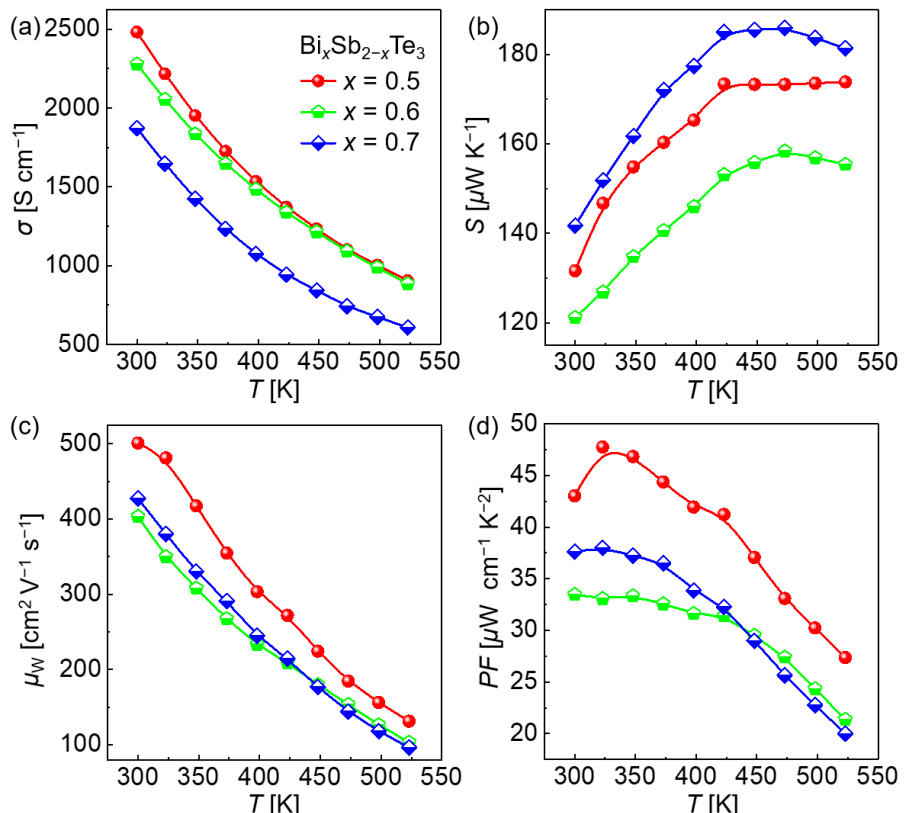


Figure 4.12 | Electrical transport properties of $\text{Bi}_x\text{Sb}_{2-x}\text{Te}_3$ ($x = 0.5$, 0.6, and 0.7). (a) electrical conductivity, (b) Seebeck coefficient, (c) weighted mobility (μ_w), and (d) power factor.

In Figure 4.12 (b), the addition of Sb also has a significant effect on the value and trend of the Seebeck coefficient, i.e., $\text{Bi}_{0.7}\text{Sb}_{1.3}\text{Te}_3$ with the least Sb content has the largest Seebeck coefficient. According to the Equation (2.17), S is inversely proportional to carrier concentration (n) and positively proportional to DOS effective mass of electrons (m_d^*). All three samples exhibit a similar trend in their Seebeck coefficients, with an initial rise followed by a decrease at higher temperatures. This decrease can be attributed to the bipolar effect. Interestingly, increasing Sb content elevates the peak temperature of S from 423 K to 473 K. Sb doping introduces additional charge carriers, which partially suppress and delay the onset of intrinsic excitation and the associated bipolar effect.

To analyze the effective mass and elucidate the origin of the enhanced Seebeck coefficient for $\text{Bi}_{0.7}\text{Sb}_{1.3}\text{Te}_3$, Pisarenko plots were constructed at room temperature (Figure 4.13). $\text{Bi}_{0.7}\text{Sb}_{1.3}\text{Te}_3$ with the highest Seebeck coefficient exhibits the lowest carrier concentration ($n_H = 4.5 \times 10^{19} \text{ cm}^{-3}$). Notably, the Seebeck coefficients, PF , and mobility of $\text{Bi}_{0.5}\text{Sb}_{1.5}\text{Te}_3$ and $\text{Bi}_{0.7}\text{Sb}_{1.3}\text{Te}_3$ are in accordance with the prediction of the SPB model. This suggests that Sb doping leads to an increase in the effective mass of Bi_2Te_3 , rising from 1.00 m_e to 1.38 m_e . While Hall carrier mobility decreases from a maximum of $\sim 259.7 \text{ cm}^2 \text{ V}^{-1} \text{ s}^{-1}$ at $x = 0.7$ with increasing Sb content.

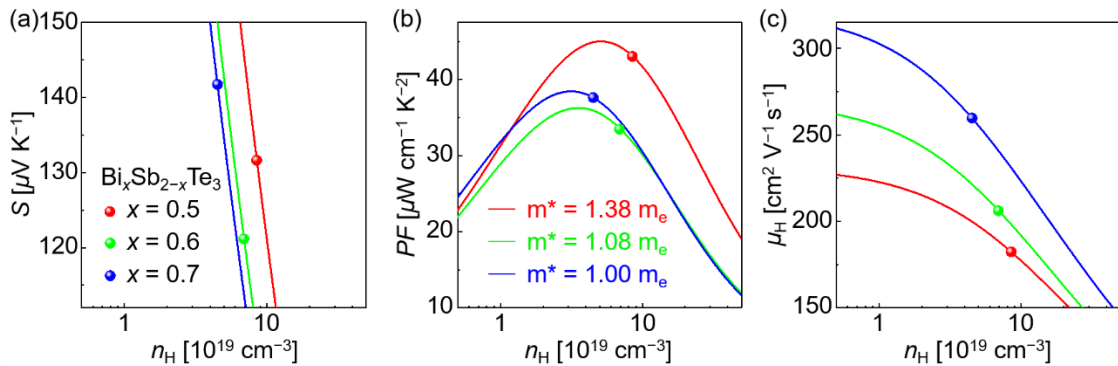


Figure 4.13 | The relationship between carrier concentration and (a) Seebeck coefficient, (b) power factor, and (c) carrier mobility of $\text{Bi}_x\text{Sb}_{2-x}\text{Te}_3$ samples, respectively.

To isolate the influence of carrier scattering mechanisms on transport properties, we employed the weighted mobility (μ_w) calculated from a simple function of the measured electrical conductivity (σ) and Seebeck coefficient (S), as μ_w is independent of the carrier concentration.²¹⁷

$$\mu_w = \frac{3h^3\sigma}{8\pi(2m_e k_B T)^2} \left[\frac{\exp[S_r-2]}{1+\exp[-5(S_r-1)]} + \frac{\frac{3}{\pi^2}S_r}{1+\exp[5(S_r-1)]} \right] \quad (4.3)$$

where $S_r = \frac{|S|}{\frac{k_B}{e}}$. Equation (4.6) provides a concise analytical expression for the weighted mobility. It approximates the exact Drude–Sommerfeld free electron model within 3% for absolute Seebeck coefficients exceeding $20 \mu\text{V K}^{-1}$. The largest weighted mobility over the entire measured temperature range supports that why $\text{Bi}_{0.5}\text{Sb}_{1.5}\text{Te}_3$ shows the highest electrical conductivity. Figure 4.12 (c) displays the temperature dependence of μ_w for the BST samples. All samples exhibit a decrease in μ_w with increasing temperature, consistent with the T^{-1} dependence for acoustic phonon scattering of charge carriers. Notably, the μ_w increases with increasing Sb content (295–525 K), particularly at low temperatures. The $\text{Bi}_{0.5}\text{Sb}_{1.5}\text{Te}_3$ sample demonstrates a significantly higher μ_w compared to the others, and its temperature dependence closely resembles that of single crystals dominated by acoustic phonon scattering. This enhancement in μ_w for $\text{Bi}_{0.5}\text{Sb}_{1.5}\text{Te}_3$ could be attributed to either an increase in Hall carrier mobility (μ_H) or a rise in the DOS effective mass.

Table 4.4 | Hall carrier concentration, mobility, heat capacity, and mass density of the as-alloyed samples measured at room temperature.

Composition of $\text{Bi}_x\text{Sb}_{2-x}\text{Te}_3$	$x = 0.5$	$x = 0.6$	$x = 0.7$
Hall concentration [$\times 10^{19} \text{ cm}^{-3}$]	8.5	6.9	4.5
Hall mobility [$\text{cm}^2 \text{ V}^{-1} \text{ s}^{-1}$]	182.29	206.15	259.65
Heat capacity [$\text{J g}^{-1} \text{ K}^{-1}$]	0.186	0.184	0.181
Mass density [g cm^{-3}]	6.83	6.77	6.83
DOS effective mass [m_e]	1.05	1.69	1.55
Bandgap [eV]	0.2	0.12	0.11
Mass density [g cm^{-3}]	6.772	6.827	6.834

Despite a notable decrease in the Seebeck coefficient upon Sb doping, the significant increase in electrical conductivity leads to an overall enhancement in PF , as shown in Figure 4.12 (d). Notably, $\text{Bi}_{0.5}\text{Sb}_{1.5}\text{Te}_3$ exhibits the highest PF within the measured temperature range (323 K - 523 K). The relationship between the band effective mass and

the PF can be derived as:

$$PF = S^2 \sigma \propto \frac{N_v}{m_b^*} \quad (4.4)$$

Accordingly, PF is directly related to the band degeneracy. Bi-Sb-Te materials exhibit high PF due to a combination of factors. Their highly symmetric crystal structure, despite a slight Peierls distortion from cubic towards rhombohedral (Figure 4.14 (a)), leads to a large band degeneracy ($N_v = 6$). This high degeneracy contributes to a significant Seebeck coefficient. Furthermore, spin-orbit coupling (SOC) effects significantly reduce the band effective mass (m_b^*) of single-crystal Bi_2Te_3 (Figure 4.14 (b)), as shown by calculations ($m_b^* = 0.15 m_e$ with SOC vs. $0.7 m_e$ without).²¹⁸ This small m_b^* , as described by Equation (4.7), further enhances the PF . Figures 4.14 (c) and (d) illustrate the contribution of atomic orbitals and the dominant role of p states near the Fermi energy, suggesting a limited influence of s-lone pairs on the bonding mechanism and resulting properties. In conclusion, the optimal carrier concentration, small band effective mass, and large band degeneracy arising from the complex band structure of Bi-Sb-Te materials work synergistically to achieve their excellent thermoelectric properties.

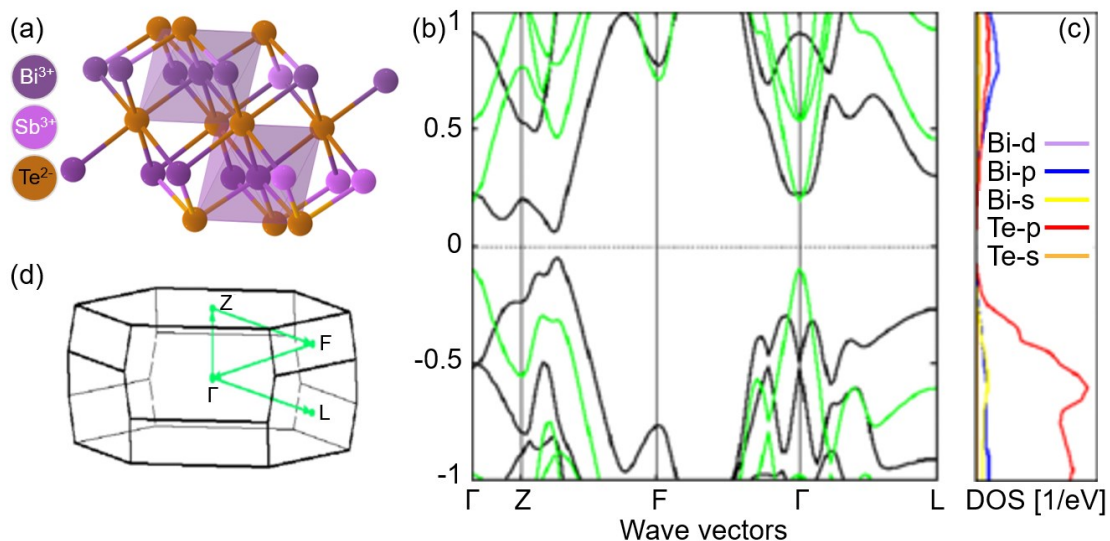


Figure 4.14 | (a) Highly symmetric rhombohedral structure of Bi-Sb-Te materials ($\text{Bi}(\text{SbTe}_2)_3$, mp-1227403). (b) Band structure of Bi_2Te_3 with (black) and without (green) SOC effect. The presence of SOC lowers the bandgap and Bi_2Te_3 turns to a narrow-gap semiconductor. (c) The projected density of states (DOS) including SOC shows that valence and conduction bands are mainly formed by Te and Bi p-orbitals, respectively. (d) The first Brillouin zone for Bi_2Te_3 crystal structure.²¹⁸

σ_{E_0} is the transport coefficient in units of conductivity, which characterizes the conductive performance of the material under a given η (that is, a given carrier concentration).²¹⁹ σ_{E_0} can be extracted by analyzing the measured electrical conductivity alongside the reduced chemical potential (η). η is calculated from the measured Seebeck coefficient using the equation $\eta = E_F/k_B T$. The analytical expressions become highly accurate (within 5% error) when $|S|$ exceeds $120 \mu\text{V K}^{-1}$:

$$\sigma_{E_0} = \sigma \cdot \exp \left[\frac{|S|}{\frac{k_B}{e}} - 2 \right] \quad (4.5)$$

where $S_r = \frac{|S|}{\frac{k_B}{e}}$. The calculated transport coefficients in Figure 4.15 reveal a material dependence, with $\text{Bi}_{0.5}\text{Sb}_{1.5}\text{Te}_3$ demonstrating the highest σ_{E_0} of $\approx 1.6 \times 10^5 \text{ S cm}^{-1}$. This superior σ_{E_0} likely stems from a combination of stronger band dispersion and a lower effective mass within the band structure.

S and σ are inherently coupled in the following aspects. High degeneracy can enhance the DOS near the Fermi level, potentially enhancing σ through higher carrier concentration, but also increase carrier-carrier scattering, reducing S . Similarly, lower effective mass generally improves σ by increasing carrier mobility, but can also lead to a lower S depending on the band structure. Scattering mechanisms also play a crucial role. Increased scattering reduces mobility and σ , while different scattering mechanisms can affect S and σ differently. For instance, phonon scattering can have a more significant impact on S by altering the energy distribution of carriers. Finally, the Fermi level position relative to the band edges influences carrier transport by determining available energy states. Doping can shift the Fermi level, affecting carrier concentration. This, in turn, affects σ and S through the mechanisms mentioned above. Elastic constants can indirectly affect S and σ through their influence on phonon scattering. Certain crystal structures with specific elastic properties may exhibit lower phonon scattering, leading to higher mobility and potentially improved S and σ . In summary, $S^2\sigma$ relies on various factors such as band structure, charge scattering, and doping level, constituting a multitude of parameters, encompassing band degeneracy, effective mass, scattering factor, Fermi level, and elastic constants. None of the above parameters are readily determinable or serve as comprehensive descriptors for PF . Moreover, since PF does not incorporate κ_{ele} , it fails to encompass all the electron transport effects impacting zT . While using a single set of

Seebeck coefficient and electrical conductivity data at any temperature, one can conveniently estimate the electronic quality factor (B_E) as per Equation (4.6).²²⁰

$$B_E = \frac{S^2 \sigma}{\left[\frac{S_r^2 \exp(2-S_r)}{1+\exp[-5(S_r-1)]} + \frac{S_r^2 \pi^2/3}{1+\exp[5(S_r-1)]} \right]} \quad (4.6)$$

where $S_r = \frac{|S|}{k_B/e}$. Equation (4.6) defines B_E for a simple thermoelectric semiconductor.

This temperature and doping-independent parameter allows to attribute variations in PF among different materials to differences in B_E or Fermi level (determined by S). B_E acts as a scaling factor for PF ²²⁰. B_E entirely captures the electronic contribution to the thermoelectric quality factor (B) through the equation below^{54,55,69,221–223}

$$B = \frac{B_E T}{\kappa_{\text{lat}}} = \left(\frac{k_B}{e} \right)^2 \frac{\sigma_{E0}}{\kappa_{\text{lat}}} T \quad (4.7)$$

The B factor is a property independent on the doping concentration (although still temperature-dependent).^{219,224} Analyzing B enables prediction of the maximum achievable zT (zT_{max}).⁶⁹

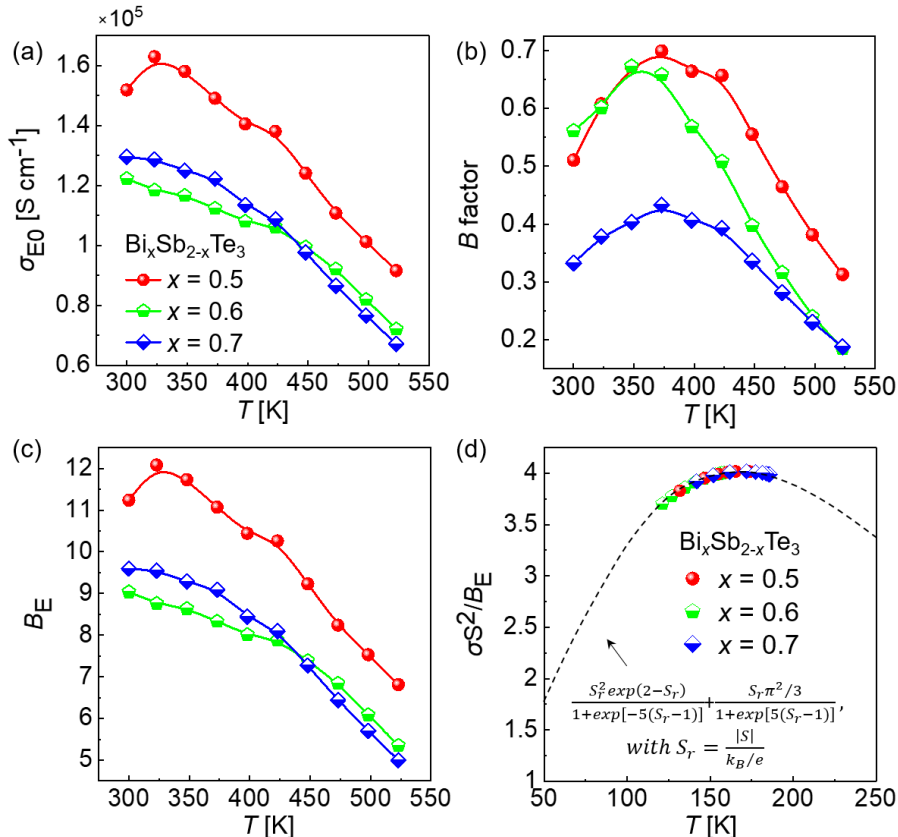


Figure 4.15 | (a) σ_{E0} . (b) B factor. (c) B_E . (d) $\sigma S^2 / B_E$ of the as-made samples.

4.4.2 Thermal Transport Properties of Bismuth Telluride

Figure 4.16 (a) shows κ_{tot} as a function of temperature: around room temperature, the total thermal conductivity of $\text{Bi}_{0.6}\text{Sb}_{1.4}\text{Te}_3$ is closer to that of $\text{Bi}_{0.7}\text{Sb}_{1.3}\text{Te}_3$, and lower than that of $\text{Bi}_{0.5}\text{Sb}_{1.5}\text{Te}_3$. As stated before, the thermal conductivity mainly consists of the electron thermal conductivity (κ_{ele} , shown in Figure 4.16 (c)) and lattice thermal conductivity (κ_{lat} , shown in Figure 4.16 (d)). The electron thermal conductivity is related to the electrical conductivity and Lorenz number (L) shown in Figure 4.16 (b) according to the Wiedemann Franz law as Equation (2.26). Thus, the phenomenon of the low κ_{tot} of $\text{Bi}_{0.6}\text{Sb}_{1.4}\text{Te}_3$ is closer to that of $\text{Bi}_{0.7}\text{Sb}_{1.3}\text{Te}_3$ around room temperature due to the large proportion of carrier thermal conductivity in κ_{tot} . The hole carrier concentration of Sb-doped samples increases significantly with the increase of Sb content, which leads to a significant increase in the carrier thermal conductivity κ_{ele} , therefore κ_{tot} increased with the increase of Sb content.

Compared with κ_{ele} , the contribution of κ_{lat} is smaller in the $\text{Bi}_x\text{Sb}_{2-x}\text{Te}_3$ compounds. Figure 4.16 (d) shows κ_{lat} versus temperature curves of Sb-doped samples. $\text{Bi}_{0.5}\text{Sb}_{1.5}\text{Te}_3$, which has the highest Sb content, has the lowest lattice thermal conductivity above 425 K. And the lattice thermal conductivity of all the $\text{Bi}_x\text{Sb}_{2-x}\text{Te}_3$ samples does not exceed $1.5 \text{ W m}^{-1} \text{ K}^{-1}$. κ_{lat} can be described by the phonon propagation expressed as Equation (2.36), where C_V is the specific heat determined by the Dulong-Petit law in Equation (3.34), v_{ph} is the phonon group velocity, and τ_p is the phonon relaxation time. Furthermore, v_g and the force constant between atoms exhibit a positive correlation, while τ_p and mean free path of phonons are directly proportional according to Eqs. (2.30) and (2.31). Therefore, a small bond strength and small mean free path of phonons contributes to the low κ_{lat} of Bi-Sb-Te samples. The small mean free path shows a strong phonon scattering, which can be further related to a large intrinsic anharmonicity. The anharmonicity can be expressed by the Grüneisen parameter (γ), describing the relationship between phonon frequency and crystal volume (V) change as Equation (2.36). For acoustic dominated phonon scattering system, the relationship between γ and κ_{lat} is expressed in Equation (2.38). Generally, the large anharmonicity causes small lattice thermal conductivity. This can also be confirmed in Figure 2.11 (c), showing that most of the MVB materials have high Grüneisen parameters and thus, small lattice thermal conductivity.

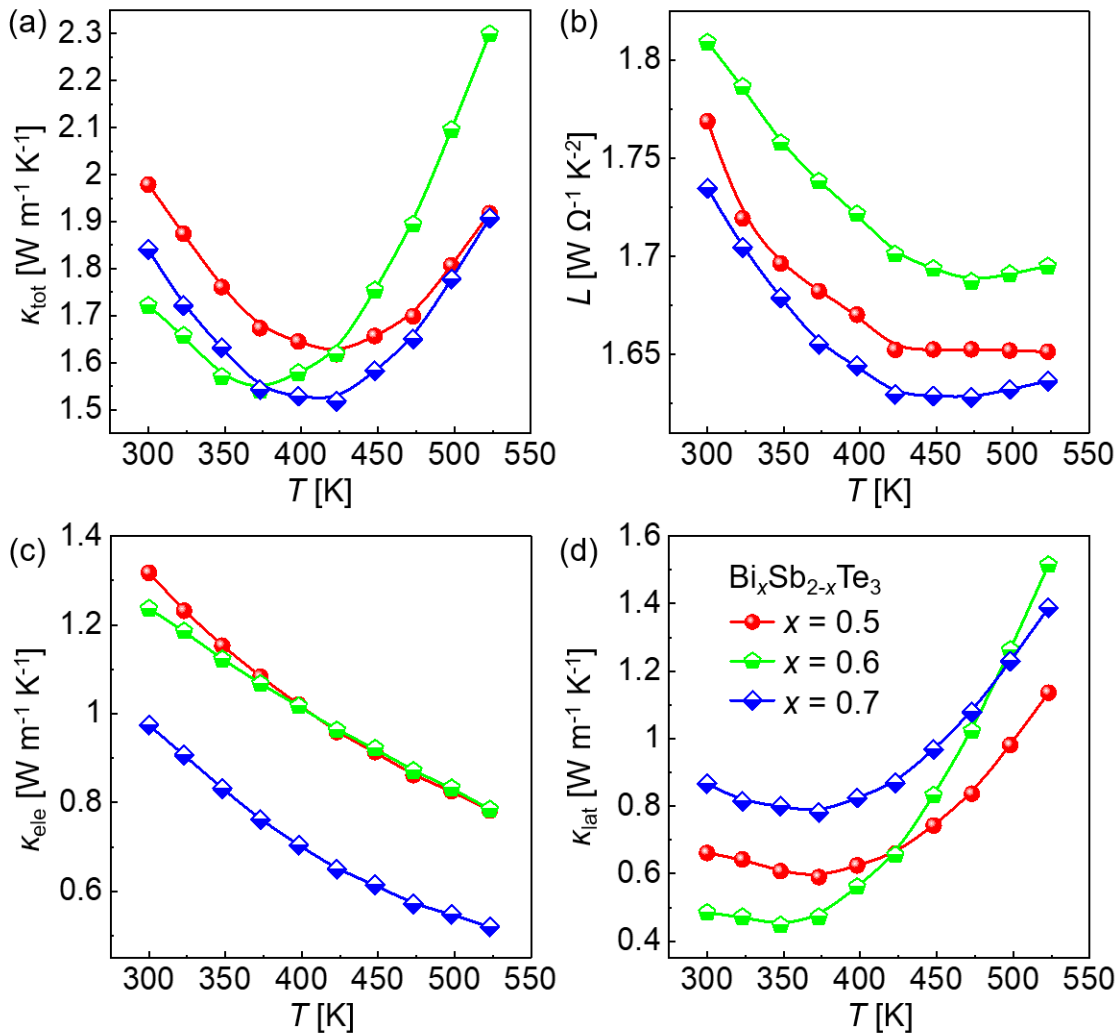


Figure 4.16 | (a) K_{tot} , (b) Lorenz number, (c) K_{ele} , and (d) K_{lat} of $\text{Bi}_x\text{Sb}_{2-x}\text{Te}_3$ ($x = 0.5, 0.6, \text{ and } 0.7$) samples.

The above phenomenon can be understood from the nature of the bond because the small bond strength indicates the soft chemical bond of the Bi-Sb-Te materials. The bond strength is closely related to the bulk modulus, the coordination number, the electron densities, and the bond length. As demonstrated in Figures 2.11 (a) and (b), all the metavalently bonded materials have low bulk modulus and low Debye temperature, which confirms the idea of the soft bonds for the MVB materials. Besides, there is only about 1 electron shared between two adjacent atoms in the MVB materials, which creates a small bond order and further supports the soft chemical bond of the MVB materials.

The potential maximum zT can be more effectively evaluated using the thermoelectric quality factor (B factor).^{16,217} Figure 4.15 (b) presents the calculated B as a function of temperature. Despite a slightly higher lattice thermal conductivity for $\text{Bi}_{0.5}\text{Sb}_{1.5}\text{Te}_3$

compared to $\text{Bi}_{0.6}\text{Sb}_{1.4}\text{Te}_3$ (Figure 4.16 (d)), the substantial improvement in μ_w for $\text{Bi}_{0.5}\text{Sb}_{1.5}\text{Te}_3$ outweighs the increase in lattice thermal conductivity, resulting in a higher B value for $\text{Bi}_{0.5}\text{Sb}_{1.5}\text{Te}_3$. This means that $\text{Bi}_{0.5}\text{Sb}_{1.5}\text{Te}_3$ will be expected to present the highest zT value, which will be verified in the following discussion.

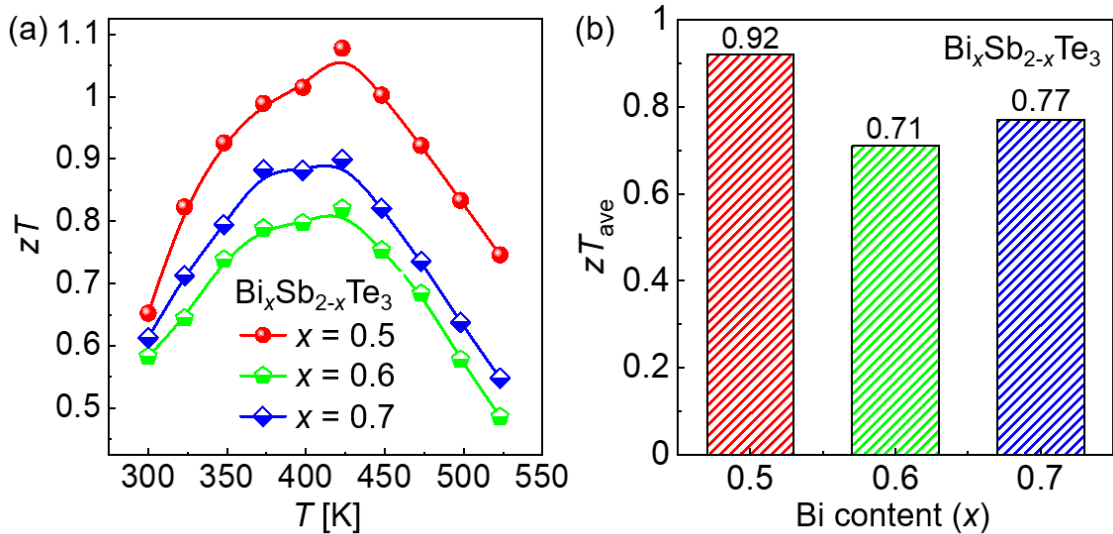


Figure 4.17 | (a) zT and (b) zT_{ave} of the $\text{Bi}_x\text{Sb}_{2-x}\text{Te}_3$ samples.

Figure 4.17 (a) shows the relationship between zT value as a function of temperature, and the measured zT values exceeding the predictions based on the B factor (Figure 4.16). The zT values of $\text{Bi}_{0.5}\text{Sb}_{1.5}\text{Te}_3$ are relatively close and higher than those of $\text{Bi}_{0.6}\text{Sb}_{1.4}\text{Te}_3$ and $\text{Bi}_{0.7}\text{Sb}_{1.3}\text{Te}_3$ samples. This may be attributed to the fact that with the further increase of the Sb content, the replacements of Bi^{3+} ions by Sb^{3+} ions introduce additional holes, which increases the carrier concentration and increases the electronic thermal conductivity, increasing zT . Among the studied materials, $\text{Bi}_{0.5}\text{Sb}_{1.5}\text{Te}_3$ reaches a peak value close to 1.1, exhibiting the highest average zT of nearly 1 over the entire temperature range measured (Figure 4.17 (b)).

Owing to the highly delocalized electron density distribution in the MVB system, the Born effective charge is quite large, which leads to the longitudinal optical (LO) and transverse optical (TO) phonon splitting. Under the impact of the highly delocalized p-electrons, the optical phonons couple with the electrons and result in the optical phonon softening. Because of the low group velocity, the optical phonons are inefficient for heat transport. However, the optical phonons can couple with the acoustic phonons by strong

anharmonic scattering and make low group velocity of the acoustic phonons and large phase space of Umklapp phonon scattering processes. In the end, the low κ_{lat} is generated. As a consequence of the high electrical conductivity, large Seebeck coefficient, and low thermal conductivity, the samples show high zT values.

4.5 Conclusions

Bi-Sb-Te single crystals were grown using a Bridgeman oven with slow cooling. Powder XRD confirmed the rhombohedral structure of the Bi-Sb-Te samples, while energy-dispersive X-ray spectroscopy (EDX) revealed homogeneous elemental distribution and stoichiometry close to the nominal composition. EBSD analysis identified preferential growth of the crystal ingots along the (001) plane. APT analysis of needle-shaped tips, fabricated using dual-beam SEM-FIB, revealed a high PME of $\sim 80\%$. This, along with the high absorption capacities observed by FTIR, suggests the presence of metavalent bonding (MVB) in Bi_2Te_3 -based alloys.

Thermoelectric properties were measured using PPMS, while Hall effect measurements determined carrier concentration and mobility. High carrier concentration and mobility lead to good electrical conductivity. A large band valley degeneracy and small band effective mass, which are inherent to MVB compounds, result in a high Seebeck coefficient and power factor. Strong anharmonicity and soft bonds due to MVB further suppress thermal conductivity, ultimately contributing to a high zT . The study highlights the role of metavalent bonding (MVB) in enhancing the thermoelectric properties of Bi_2Te_3 -based materials.

5 Doping by Design: Enhanced Thermoelectric Performance of SnSe Alloys over a Broad Temperature Range through Metavalent Bonding

5.1 Overview of Thermoelectric SnSe

Tin selenide exhibits promise across diverse fields including thermoelectrics,^{132,225–229} solar cells,²³⁰ photodetectors,²³¹ memory devices,²³² lithium and sodium-ion batteries,^{233,234} gas sensing,²³⁵ photocatalysis,²³⁶ supercapacitors,^{237,238} topological insulators,⁶⁴ and phase change memory.²³⁹ The two stable phases of SnSe, α -SnSe ($T < 800$ K) and β -SnSe ($T > 800$ K), possess a similar crystal structure (orthorhombic), but different lattice parameters and space groups.

The low-temperature α -SnSe belongs to the low symmetry *Pnma* space group (#62), and its lattice constants are respectively $a = 11.37$ Å, $b = 4.19$ Å, $c = 4.44$ Å,^{226,228} and it can be transformed into NaCl type rock-salt structure by simple space transformation,²⁴⁰ as illustrated in [Figure 5.1 \(a\)](#). It can be seen that *Pnma* SnSe has a layered structure and exhibits obvious anisotropy: the two-atom-thick SnSe layer is corrugated, which results in a zigzag arrangement of Sn and Se atoms along the *b*-axis and a spring-like arrangement along the *c*-axis. In a unit cell of *Pnma* SnSe, there are eight atoms joined with strong hetero-polar bonds, consisting of two planes of a zigzag-like chain. The adjacent layers are mainly bound by a combination of van der Waals forces and a long-range electrostatic attraction. Single crystal SnSe is easy to cleave along the (100) plane.

When the temperature is increased (~ 800 K $< T < 1134$ K), SnSe undergoes a reversible phase transition from the *Pnma* space group to the *Cmcm* space group (#63) with increased spatial symmetry and simultaneous change in the crystallographic axis, as shown in [Figure 5.1 \(b\)](#). Similar to α -SnSe, β -SnSe has a typical double-layered structure, and Sn and Se atoms are joined with strong heteropolar bonds.²²⁸ During the cooling process, a phase transition from β -SnSe to α -SnSe takes place at approximately 800 K,

accompanied by a transformation of crystallographic axes characterized by lattice constants $a = 4.31 \text{ \AA}$, $b = 11.71 \text{ \AA}$, and $c = 4.42 \text{ \AA}$.^{226,228}

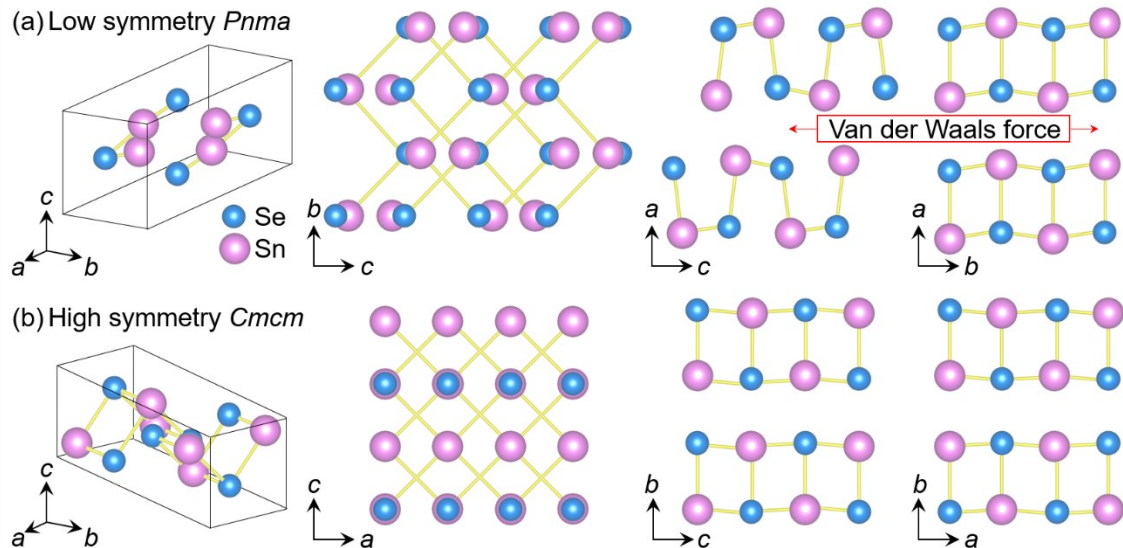


Figure 5.1 | (a) Unit cell of α -SnSe (*Pnma* space group) and crystal structures along the a -axis, b -axis, and c -axis. (b) Unit cell of β -SnSe (*Cmcm* space group) and crystal structures along the b -axis, a -axis, and c -axis.

These two structures show distinctive difference in transport properties.²²⁸ SnSe has garnered significant attention as a thermoelectric material following the 2014 report by Zhao et al.,²²⁶ which highlighted an exceptionally high zT of 2.6 at 923 K as illustrated in Figure 5.2 (a). Chemical doping with elements like Na,¹³² Br,²²⁷ Pb,²⁴¹ Cl,²⁴² and Cu²⁴³ significantly enhances the zT of SnSe single crystals. The layered structure of SnSe single crystals, however, presents challenges for practical applications due to its inherent brittleness and susceptibility to cleavage.²⁴⁴ In contrast, polycrystalline SnSe offers greater practicality for device applications due to lower costs, simpler processing, and enhanced mechanical properties.^{228,245} Despite the intrinsic low lattice thermal conductivity of single crystals, most polycrystalline SnSe suffers from higher κ_{lat} and lower σ values, limiting its thermoelectric performance as depicted in Figures 5.2 (b) and (c), respectively.^{126,226,246–250} This contradicts the expectation of phonon scattering at grain boundaries decreasing lattice thermal conductivity.²²⁹ Zhao et al.¹³² first proposed, and then Lee et al.²⁵¹ and Zhou et al.²⁵⁰ confirmed, that tin oxides at grain boundaries are

responsible for this unexpected increase. Polycrystalline SnSe achieves zT exceeding 2.0 through oxide removal²⁵⁰ or a combination of chemical synthesis and defect engineering.²⁵² However, high zT in polycrystalline SnSe is primarily observed above 600 K^{126,246,248–250,252,253,254} as shown in Figure 5.2 (d), limiting its overall energy conversion efficiency. It is particularly problematic for thermoelectric cooling, where monocrystalline SnSe shows promise at lower temperatures.^{243,255} For SnSe to be viable in cooling applications, enhancing its zT , particularly near room temperature, is critical.

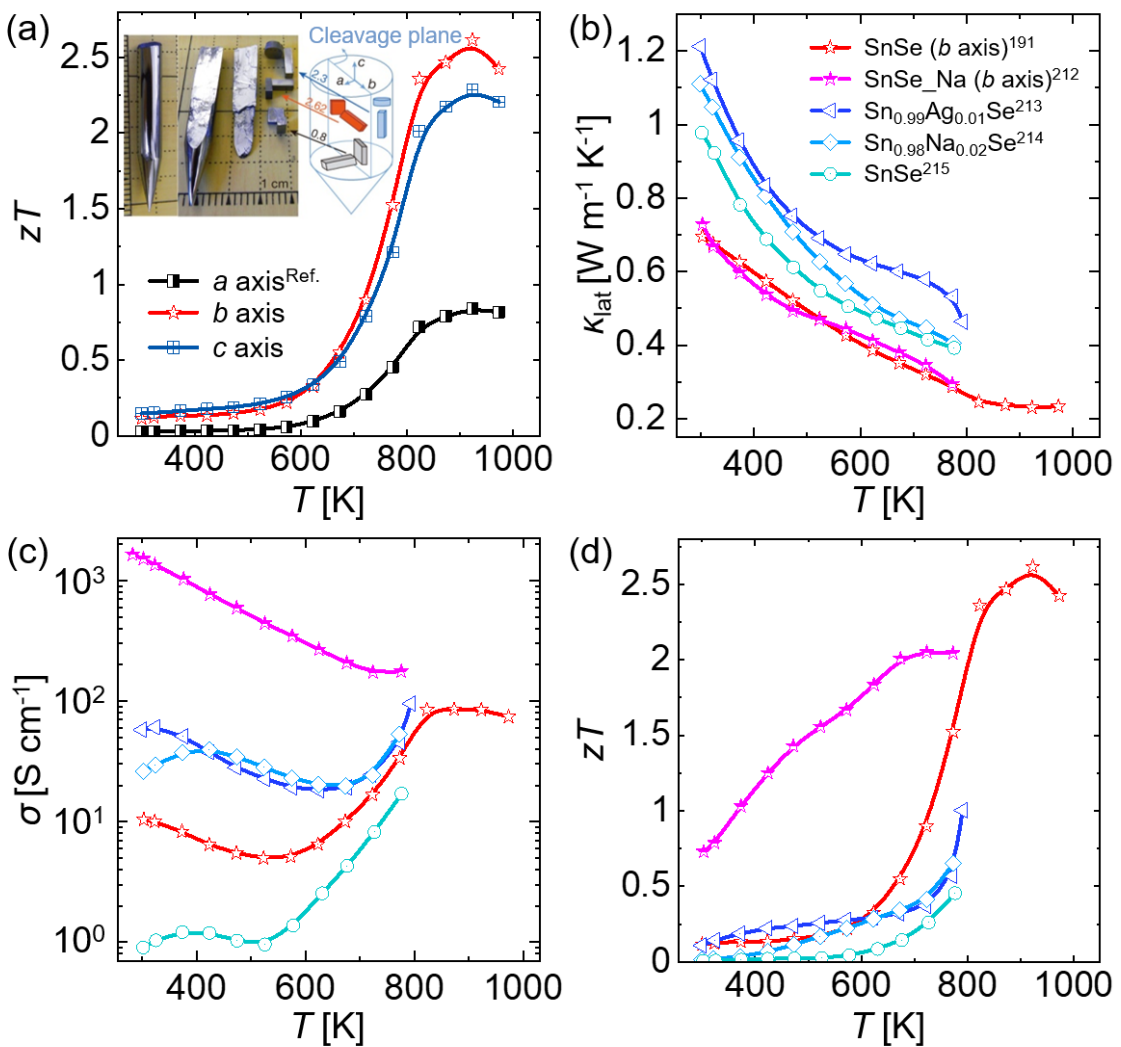


Figure 5.2 | (a) zT values for single-crystal SnSe measured along different axial.²²⁶ The inset image shows a typical single crystal alongside a cleaved (001) plane and specimens cut for directional measurements. Comparison of temperature-dependent thermoelectric properties of single-crystal SnSe and polycrystalline SnSe: (b) lattice thermal conductivity, (c) electrical conductivity, and (d) zT .^{226,247–250}

5.2 Obtaining Metavalyently Bonded SnSe

5.2.1 Motivation to Obtain High-symmetry SnSe

SnSe exhibits excellent thermoelectric properties at elevated temperatures, undergoing a phase transition from a low-symmetry *Pnma* phase to a high-symmetry *Cmcm* phase as temperature increases.^{226,250,252,256} High-symmetry chalcogenides like PbTe²⁵⁷ and GeTe²⁵⁸ exhibit thermoelectric performance comparable to *Cmcm* SnSe. Besides, the rock-salt SnSe with the space group of *Fm* $\bar{3}$ *m* formed by the distortion of orthorhombic SnSe leads to significant anharmonicity of Sn-Se bonds, with corresponding Grüneisen constants as high as 2.83, resulting in extremely low intrinsic thermal conductivity. Total energy calculations using DFT and GGA to examine the stability of the *Fm* $\bar{3}$ *m* rock salt cubic and *Pnma* orthorhombic phases of the SnSe compounds revealed that the energy differences between the cubic and orthorhombic phases were very small.^{64,240,259,260} For SnSe, the energy of the *Pnma* orthorhombic phase is only 74 meV/unit and 0.78 meV/unit lower than that of the *Fm* $\bar{3}$ *m* cubic phase. This result implies that the metastable *Fm* $\bar{3}$ *m* cubic phase is thermodynamically accessible. In 1967, Marino et al. pioneered the growth of a cubic SnSe film on the NaCl substrate using high-pressure epitaxial growth technology,²⁶¹ and its unit cell parameter is $a = b = c = 5.99$ Å. Theoretical study by Sun et al. in 2013 suggest the thermodynamic stability of cubic SnSe.⁶⁴ This prediction was validated by Wang et al. (2015) who successfully synthesized cubic SnSe with topological insulating properties on Bi₂Te₃ substrates by molecular beam epitaxy (MBE).²⁶² Cubic SnSe is proved to be driven by the SOC effect to decouple Seebeck coefficient and electrical conductivity,²⁶³ with a band gap of $E_{\text{gap}} \sim 0.2$ eV and a 4-fold degenerate band structure at point L. These studies, along with calculations by Zhao et al. (2015) indicating a potentially low κ_{lat} due to strong phonon anharmonicity and acoustic mode softening,²⁴⁰ highlight the promise of cubic SnSe for thermoelectric applications.

This raises intriguing questions: can we stabilize the high-symmetry *Cmcm* phase in SnSe at lower temperatures to improve its thermoelectric performance, and how can we achieve this structural manipulation? As seen in chalcogenides^{264,265} and even metals,²⁶⁶ differences in chemical bonding mechanisms often dictate crystal structures. Tailoring chemical bonds in GeSe alloys induces structural transitions,²⁶⁷⁻²⁷⁰ as exemplified by the room-temperature transformation of the *Pnma* phase to the higher-symmetry *R3m* and

$Fm\bar{3}m$ phases upon alloying with $AgSbTe_2$ ²⁷¹ and $AgSbSe_2$.²⁷² The $R3m$ and $Fm\bar{3}m$ phases exhibit a significant (>10 times) enhancement in zT compared to the $Pnma$ phase. The structural transitions in GeSe correlate with a shift from covalent bonding ($Pnma$) to metavalent bonding ($R3m$ and $Fm\bar{3}m$).^{268,270} SnSe's isoelectronic nature and similarity to GeSe in electronic properties suggest that manipulating its crystal structure via chemical bond tailoring might be achievable. Cubic SnSe alloys have been successfully produced in SnSe- $AgSbTe_2$,²⁵⁹ SnSe- $AgSbSe_2$,⁸ and SnSe- $AgBiSe_2$ systems.²⁷³ While increased entropy potentially provides a plausible explanation for the structural transition,^{8,274} clear design rules for selecting alloying compounds to enhance configuration entropy remain elusive. Intriguingly, only $AgVVI_2$ compounds have demonstrated effectiveness in inducing the structural transition of SnSe.^{8,259,273,275} This phenomenon cannot be solely ascribed to increased entropy, as many other ternary compounds should theoretically produce similar effects through entropy augmentation alone. Hence, the influence of chemical bonding on this phase transition warrants exploration.

5.2.2 Content of this Chapter

This study explores controlling the atomic arrangements of SnSe at room temperature and pressure through alloying with $AgVVI_2$ ($V = Sb, Bi$; $VI = Se, Te$) at specific atomic ratios: $(SnSe)_{0.67}(AgBiTe_2)_{0.33}$, $(SnSe)_{0.67}(AgBiSe_2)_{0.33}$, $(SnSe)_{0.67}(AgSbTe_2)_{0.33}$, and $(SnSe)_{0.5}(AgSbSe_2)_{0.5}$. Employing a combination of structural characterization, optical property measurements, bond-breaking analysis, and DFT calculations, we identify and elucidate the origin of the induced phase transitions in SnSe alloys with varying atomic arrangements. We further investigate the impact of these transitions on thermoelectric properties. Our findings reveal that tailoring the chemical bonding allows for the stabilization of a high-symmetry phase in polycrystalline SnSe, leading to improved low-temperature thermoelectric performance.

5.2.3 Confirmation of Metavalent Bonding in the As-synthesized Alloys

Figure 5.3 (a) confirms the orthorhombic ($Pnma$) structure of pristine SnSe at room temperature, while the alloyed samples exhibit a dominant cubic ($Fm\bar{3}m$) phase without obvious secondary phase. Raman spectroscopy in Figure 5.3 (b) corroborates this transition. Pristine SnSe shows Raman-active modes (23.5-160 cm^{-1}) consistent with

literature.²⁷⁶ The absence of Raman active modes in $Fm\bar{3}m$ phase aligns with the Raman selection rules for the NaCl-type structure, which forbids certain vibrational modes from Raman scattering. All samples were further characterized using ultrafast reflection-type pump-probe spectroscopy, a technique enabling quantification of coherent phonon modes via femtosecond real-time reflectivity measurements.^{172,277} Figure 5.3 (c) shows transient anisotropic reflectivity measured by electro-optical sampling (EO) for all samples. Only the pristine SnSe exhibits a clear coherent phononic response dominated by the A_g^1 and A_g^2 modes. Fitting with a two-damped harmonic oscillator model (Figure 5.3 (c)) reveals phonon frequencies (31.4 cm^{-1} , 69.4 cm^{-1}) and lifetimes (6.1 ps, 3.5 ps) consistent with literature⁸⁴ and Raman data, supporting the presence of high-symmetry phases.

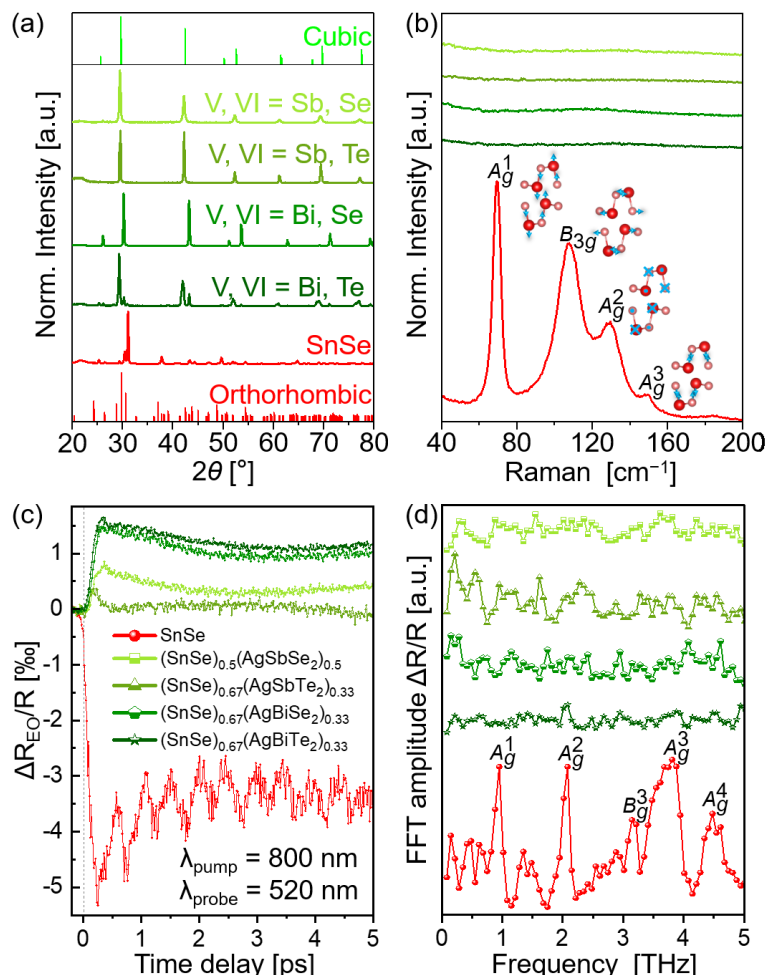


Figure 5.3 | (a) XRD patterns at room temperature, (b) Raman spectra for $Pnma$ SnSe and SnSe-Ag VVI_2 ($V = \text{Sb, Bi}$; $VI = \text{Se, Te}$) samples. (c) Transient reflectance data, obtained in the anisotropic (EO) scheme of the ultrafast pump-probe measurements. (d) Fourier spectra of transient reflectance data, after background subtraction. Both the A_g^1 and A_g^2 mode are easily identified.

The observed orthorhombic-to-cubic phase transition can be attributed to the suppression of Peierls-like distortions in the crystal lattice. This transition suggests a change in the preferred atomic arrangement, likely driven by a shift in the energetics of chemical bonding. To elucidate these bonding changes, we employed Fourier-Transform Infrared (FTIR) and Ultraviolet-Visible (UV-vis) spectroscopies. These techniques probe interband electronic transitions, which are sensitive to the nature of chemical bonds. Figure 5.4 displays the imaginary part of the dielectric constant (ε_2) versus photon energy. Pristine SnSe exhibits broad and weak absorption across a wide energy range, with a maximum ε_2 (ε_2^{\max}) of only 13. While all alloyed samples demonstrate significantly stronger absorption at lower energies, with a higher ε_2^{\max} compared to pristine SnSe. DFT calculations of the orbital-resolved ε_2 (Figures 5.4 (c) and (d)) for both *Pnma* and *Fm* $\bar{3}$ *m* SnSe phases confirm the experimental trends: the cubic phase exhibits a substantially larger and lower-energy ε_2^{\max} compared to the orthorhombic phase.

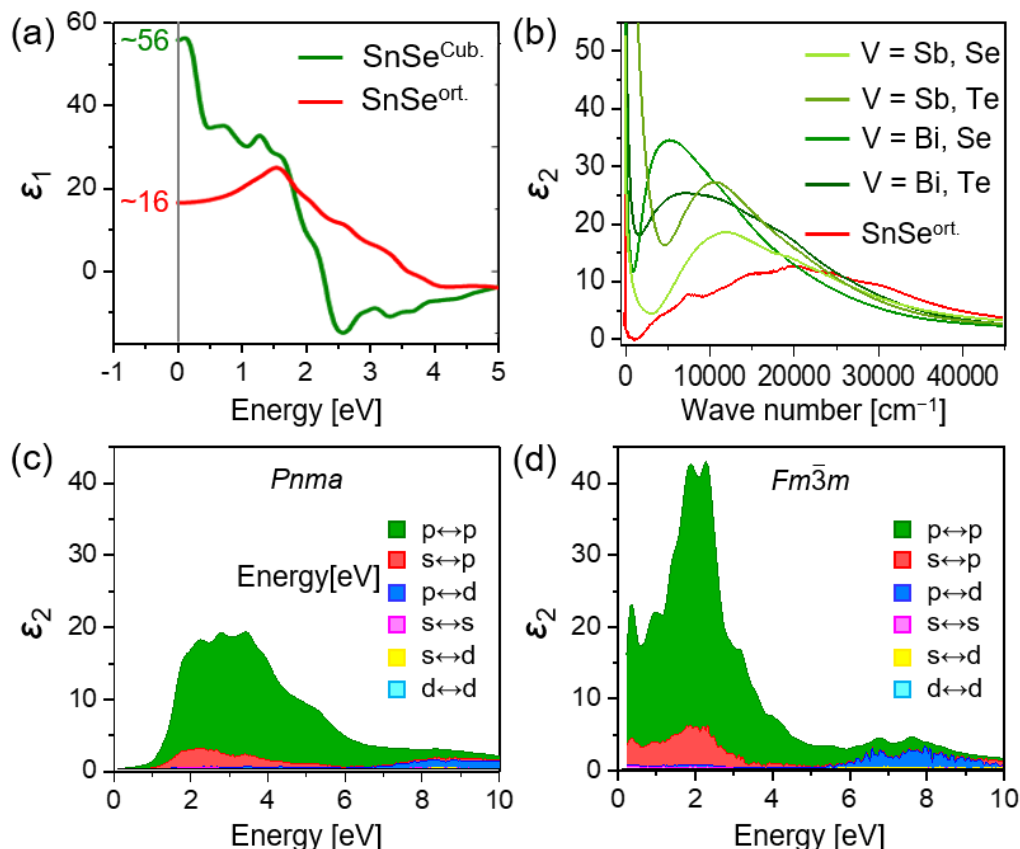


Figure 5.4 | (a) Calculated real part of the dielectric constant for *Pnma* SnSe and *Fm* $\bar{3}$ *m* SnSe. (b) Measured imaginary part of the as-made SnSe samples. Calculated imaginary part for (c) *Pnma* SnSe and (d) *Fm* $\bar{3}$ *m* SnSe.

The observed difference stems primarily from interband transitions involving Sn and Se p-orbitals. The contribution of Sn-s and Se-s orbital interactions is minimal in both phases.

Transitioning from the orthorhombic ($Pnma$) to the cubic ($Fm\bar{3}m$) phase results in a significant decrease in the energy of the ε_2^{\max} and an increase in its magnitude. This enhanced optical absorption in the cubic phase arises from the stronger p-p orbital overlap between Sn and Se. Alloying SnSe with cubic $AgVVI_2$ materials promotes this p-p interaction, ultimately driving the structural transition. The increased p-p bond alignment enhances electron delocalization, altering chemical bonding²⁶⁸ and consequently impacting transport properties (discussed next).

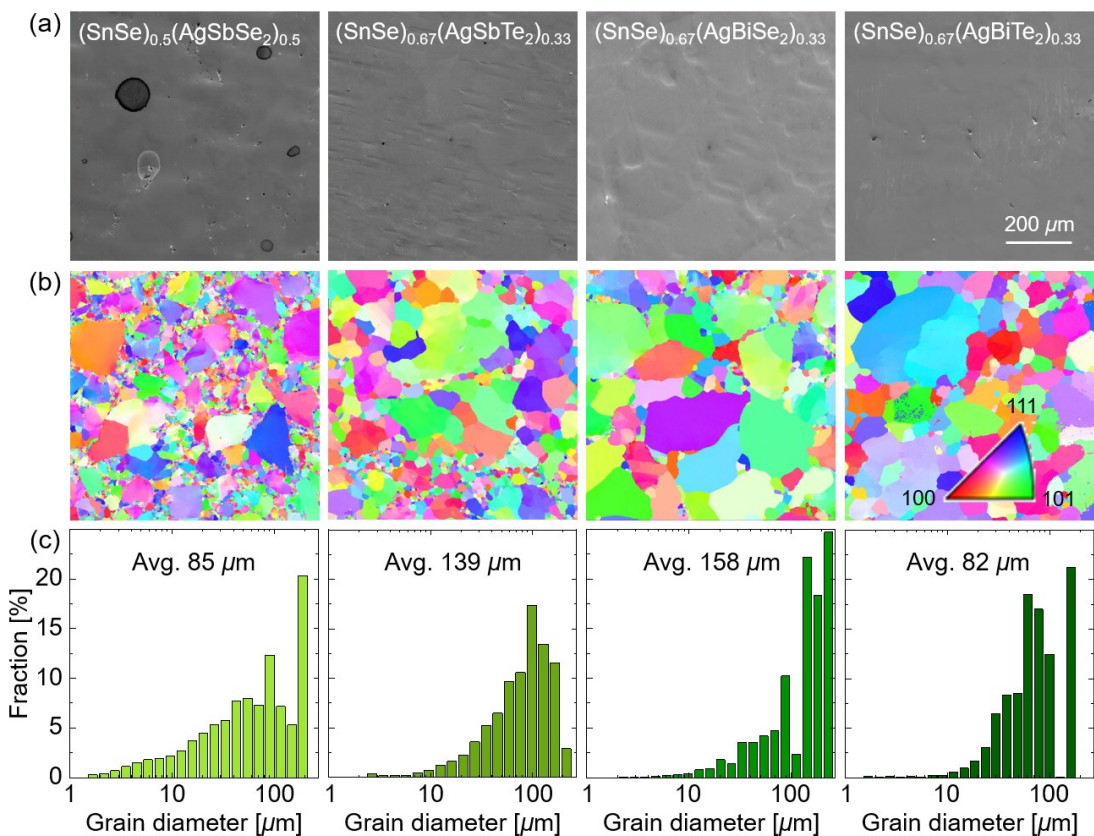


Figure 5.5 | (a) The SEM characterization for polycrystalline SnSe-AgVVI₂ ($V = Sb, Bi$; $VI = Se, Te$) samples. (b) IPF obtained from EBSD. (c) Corresponding grain size (diameter) distribution histogram.

Figure 5.5 (a) shows the secondary electron images of the individual samples, reflecting the well-polished condition for EBSD characterization, thereby minimizing the calibration noise and ensuring a high confidence index in the data. IPF images in Figure 5.5 (b) further validates the formation of high-symmetry phases and the homogeneous

cubic structure in these SnSe-Ag VVI_2 polycrystals. Despite small variations in grain size distribution, all samples possess an average grain size of approximately 100 μm as shown in [Figure 5.5 \(c\)](#). This dimension greatly exceeds the mean free path of electrons and phonons in SnSe alloys and other metavalently bonded chalcogenides like PbTe and PbSe. Hence, it is reasonable to infer that these differences in grain sizes likely have a negligible impact on the thermoelectric performance.

APT studies were conducted to characterize the accompanying bonding evolution upon the structural transition. As described before, a high electric field ionizes surface atoms on a needle-shaped sample, and laser pulses trigger their evaporation towards a position-sensitive detector. The evaporation process is sensitive to the sample's chemical bonding, as bond breaking leads to atom desorption. Usually, a single laser pulse dislodges only one ion ("single event"); and a small fraction of pulses can cause multiple ion evaporation ("multiple events"). While most materials exhibit a low probability of multiple events (PME) during APT measurements,²¹⁵ some solids display a unique bond-breaking process with unusually high PME values.^{83,278} These solids exhibit metavalent bonding (MVB), evidenced by their distinctive set of properties, including a large optical dielectric constant, a high Born effective charge (Z^*), and a substantial transverse optical mode Grüneisen parameter.^{77,80,279} Pristine SnSe displays a low PME value (~30%) ([Figure 5.6 \(a\)](#)), consistent with its covalent bonding nature. In contrast, all SnSe-Ag VVI_2 alloys exhibit high PME values ranging from 71% to 85% depending on composition. Notably, a PME value exceeding 60% is considered characteristic of MVB, a trait observed across approximately 100 different compounds.^{83,89,278,280} The high PME value is utilized as an additional identifier of metavalent bonding. 1D PME profiles ([Figure 5.6 \(b\)](#)) for these alloys show that PME values are consistent throughout all samples. Additionally, the correlation histogram offers valuable insights into studying dissociation and preferential evaporation processes, aiding in the determination of whether high PME values result from experimental artifacts or the nature of the chemical bonding. Preferential evaporation generates a continuous ion flow, leading to an increased occurrence of multiple events. This characteristic is discerned by curves exhibiting positive slopes extending from (0, 0) to infinity in the correlation histogram. The absence of such curves shown in [Figure 5.6 \(c\)](#) suggests that the elevated probabilities of multiple events observed during APT measurements are not attributable to experimental artifacts.

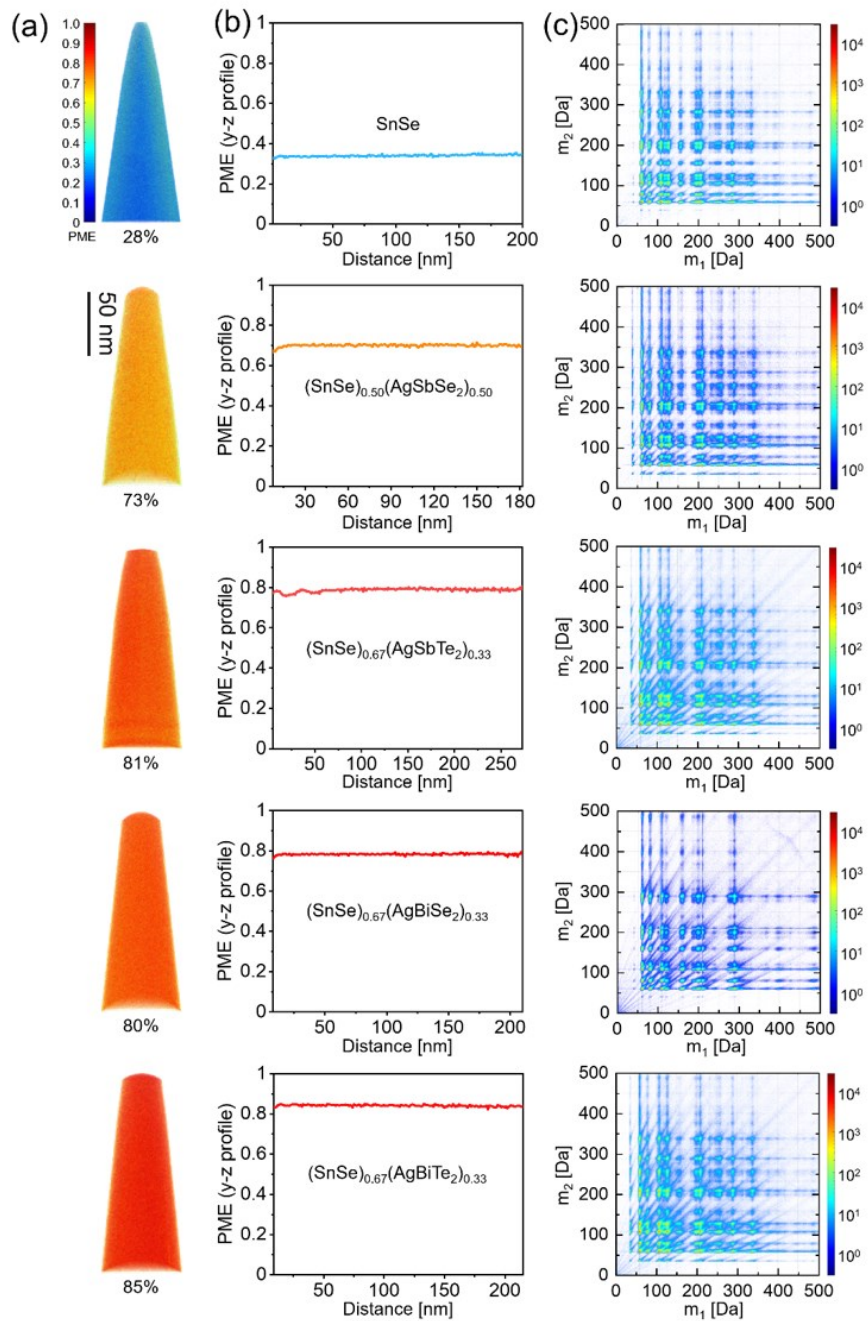


Figure 5.6 | (a) 2D version distribution of PME, (b) the related PME values, and (c) correlation histogram of pristine SnSe and SnSe- IVI_2 alloys.

5.2.4 Homogeneity in Various Scales of Cubic SnSe

EDX mapping in Figure 5.7 reveals micrometer-scale homogeneity with occasional Ag-rich or Sb-rich precipitates. Despite their presence, the significantly larger grain size (several hundred microns) compared to the mean free path of charge carriers minimizes their influence on electron and phonon scattering. The detected precipitates form during

the formation of metavalent bonds, similar to the Ge precipitates found in metavalently bonded GeTe.²⁸¹ This kind of precipitates create cation vacancies that stabilize the metavalently bonded structure by lowering the Fermi level and reducing the occupancy of antibonding states,⁹⁷ contributing to the increased hole carrier concentration.

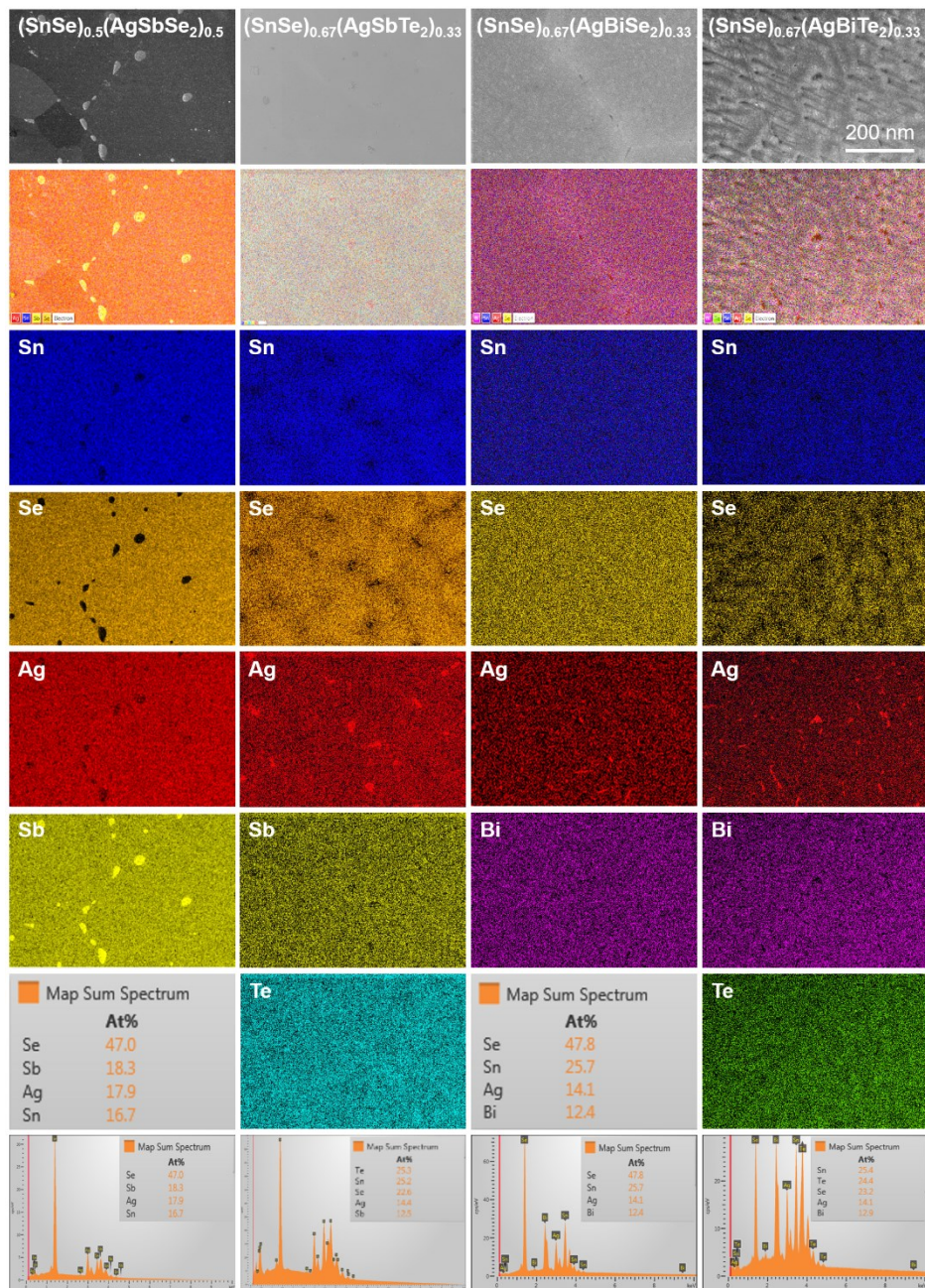


Figure 5.7 | SEM and EDX mapping patterns of the cubic phases. $(\text{SnSe})_{0.5}(\text{AgSbSe}_2)_{0.5}$ exhibits Sb-rich secondary phases primarily located at grain boundaries. While Ag-rich precipitates are observed in $(\text{SnSe})_{0.67}(\text{AgSbTe}_2)_{0.33}$ and $(\text{SnSe})_{0.67}(\text{AgBiSe}_2)_{0.33}$, but their low volume fraction limited their detection by laboratory XRD. The increased volume fraction of the Ag-rich phase in $(\text{SnSe})_{0.67}(\text{AgBiTe}_2)_{0.33}$ might correlate with a higher population of occupied antibonding states.

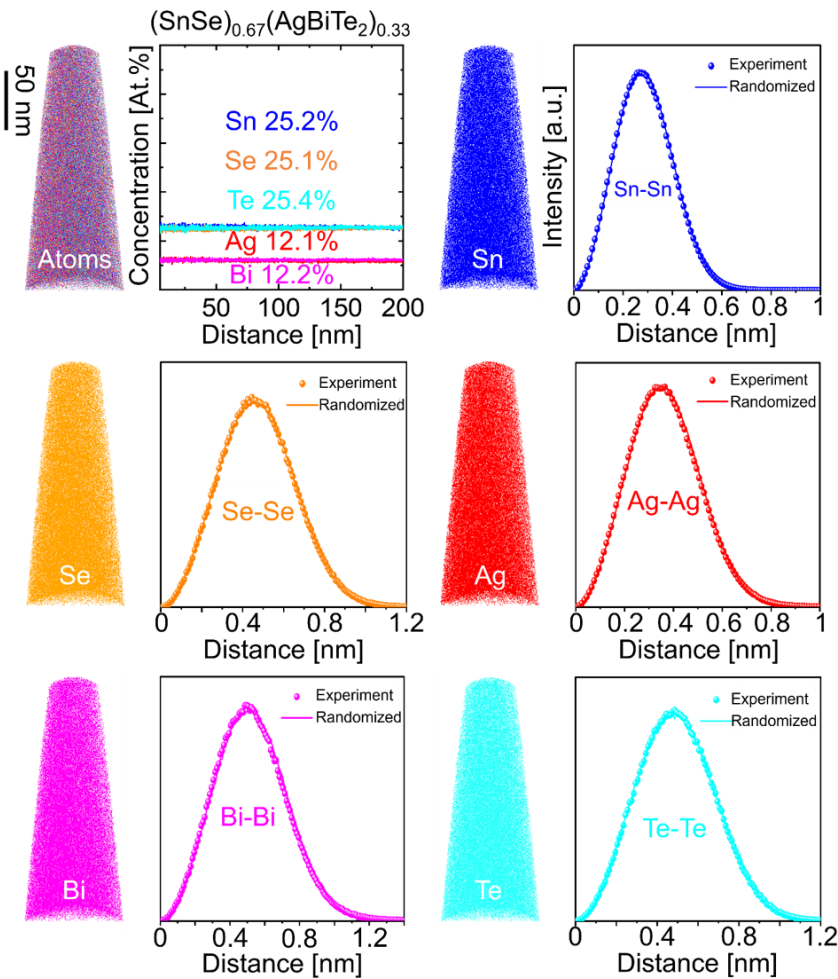


Figure 5.8 | 3D elemental distribution, and nearest neighbor distribution analyses for Sn, Se, Ag, Bi and Te of the sample $(\text{SnSe})_{0.67}(\text{AgBiTe}_2)_{0.33}$; the experimental data deviate from the randomized one indicating an inhomogeneous distribution.

The 3D distributions of constituting elements of APT measurements in Figure 5.8 reveal atomic-scale compositional homogeneity within the matrix of all samples. To analyze the bonding mechanism within the homogeneous cubic phase, advanced quantum-chemical tools that analyze electron transfer and electron sharing between bonded atoms can be utilized, as depicted in Figure 2.7. Ideal ionic bonds exhibit an ET value near 1 (renormalized by atomic oxidation states), while perfect covalent bonds have an ES value of 2, reflecting the model of electron-pair bonding suggested by Gilbert Newton Lewis.²⁸² Most materials lie along a continuum between ionic and covalent character, with the relative contributions reflected by the magnitudes of ES and ET. Metallic bonding occupies the lower-left region, exhibiting minimal ET and ES. This approach enables the quantification and visualization of various bonding types within a single framework,

which reveals a distinct region (green) encompassing compounds that deviate from conventional bonding mechanisms. These materials exhibit ES values ~ 1 and minimal ET values. Building upon the previously established properties (large ε_∞ , high Z^* , and pronounced anharmonicity) that deviate from conventional bonding,^{77,283} this distinct region identifies materials with a unique bonding mechanism termed MVB.^{77,80,83} To substantiate the presence of MVB in the cubic SnSe phase, **Table 5.1** summarizes various property-based bonding indicators for both the pristine orthorhombic and cubic phases. The two phases exhibit contrasting ES and ET values, which are further visualized in the bonding map. Notably, the *Pnma* SnSe phase resides in the covalent bonding region, while the *Fm\bar{3}m* SnSe phase is positioned within the MVB region. Furthermore, **Figure 2.7** emphasizes that all Ag VVI_2 compounds employed for alloying with SnSe also exhibit MVB characteristics. The orthorhombic SnSe structure arises from a Peierls distortion of the cubic phase, with the distortion degree correlating directly with the ES value. Materials on the dashed green line exhibit a perfect octahedral arrangement (no Peierls distortion), while those above possess a Peierls distortion that strengthens with increasing ES.¹⁰ This distortion induces electron redistribution, forming strong short bonds and weaker long bonds.²⁸³ As the bonding transitions from metavalent (green region) to covalent (red region), a pronounced Peierls distortion triggers a structural rearrangement,¹⁰ yielding the orthorhombic *Pnma* SnSe phase. Conversely, reducing the distortion lowers the ES value (red to green region) and can lead to metavalent bonding collapse for excessively large charge transfer (high ET values). Our design strategically alloys the strongly Peierls-distorted *Pnma* SnSe with distortion-free Ag VVI_2 compounds (minimal ET). This approach promotes p-p orbital overlap (confirmed by optical absorption in **Figure 5.4 (d)**) and reduces the Peierls distortion in SnSe. The resulting *Fm\bar{3}m* SnSe alloy exhibits a chemical bonding transition from covalent bonding to MVB.

Table 5.1 | Property-based chemical bonding indicators for orthorhombic and cubic SnSe phases obtained by DFT calculations. Due to the inability to stabilize the pure cubic SnSe phase at low temperatures, PME values measured by APT in cubic SnSe-Ag VVI_2 alloys are utilized.

Type	ε_∞	$\varepsilon_2^{\max} (E)$	Z^*	ET	ES	PME
SnSe ^{ortho.}	11.6	17.2	3.4	0.41	1.24	30%
SnSe ^{cubic}	35.3	37.4	6.4	0.43	0.79	71% - 85%

5.3 Thermoelectric Properties and their Chemical Bonding Origins

5.3.1 Thermoelectric Properties of Cubic SnSe

The impact of the metavalently bonded SnSe phase on thermoelectric properties is pronounced in Figure 5.9 (a), which compares the electrical conductivity of SnSe-Ag VVI_2 alloys with literature data for pristine polycrystalline SnSe.²⁵⁰ Pristine SnSe exhibits exceptionally low electrical conductivity (0.9 S cm^{-3} at room temperature) due to its intrinsically low carrier concentration ($\approx 2.0 \times 10^{17} \text{ cm}^{-3}$). Conversely, alloying with Ag VVI_2 significantly enhances conductivity by several orders of magnitude. Table 5.2 details the variations in carrier concentration and bandgap among these doped alloys, which primarily stem from their differing chemical compositions. The substantially higher n_H observed in cubic SnSe alloys likely originates, in part, from the significantly lower cation vacancy formation energy compared to the orthorhombic phase (Figure 5.10).

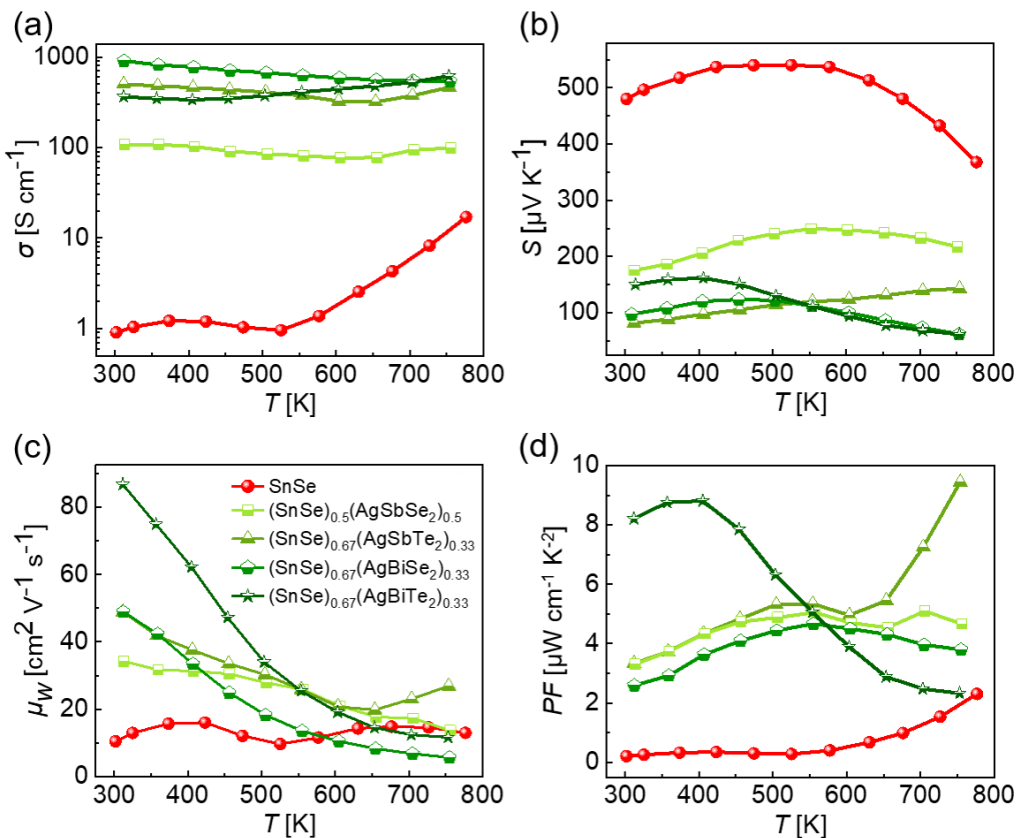


Figure 5.9 | The electrical transport characteristics of polycrystalline SnSe alloy with temperature variation. (a) σ . (b) S . (c) Weighted mobility (μ_w). (d) Power factor. Data for pristine SnSe are sourced from the literature,²⁵⁰ and are measured along the direction of the SPS pressure, i.e., the out-of-plane direction.

5 Doping by design: enhanced thermoelectric performance of SnSe alloys over a broad temperature range through metavalent bonding

Table 5.2 | Data measured at room temperature: Hall carrier concentration (n_H), Seebeck coefficient (S), DOS effective mass (m_d^*), Hall mobility (μ_H), heat capacity (C_p), mass density (ρ), and band gap (E_{gap}).

Composition	n_H [$\times 10^{19}$ cm $^{-3}$]	S [$\mu\text{V K}^{-1}$]	m_d^* [m_e]	μ_H [$\text{cm}^2 \text{V}^{-1} \text{s}^{-1}$]	C_p [$\text{J g}^{-1} \text{K}^{-1}$]	ρ [g cm^{-3}]	E_{gap} [eV]
SnSe	0.02	480.98	0.43	28.2	0.24	6.18	1.1
$V = \text{Sb}$, $VI = \text{Se}$	32.5	175.35	5.1	2.06	0.26	6.47	0.28
$V = \text{Sb}$, $VI = \text{Te}$	38.7	81.73	2.2	8.06	0.23	6.59	0.22
$V = \text{Bi}$, $VI = \text{Se}$	49.8	97.22	3.1	11.35	0.23	6.95	0.12
$V = \text{Bi}$, $VI = \text{Te}$	59	149.95	6.0	3.86	0.21	7.07	0.13

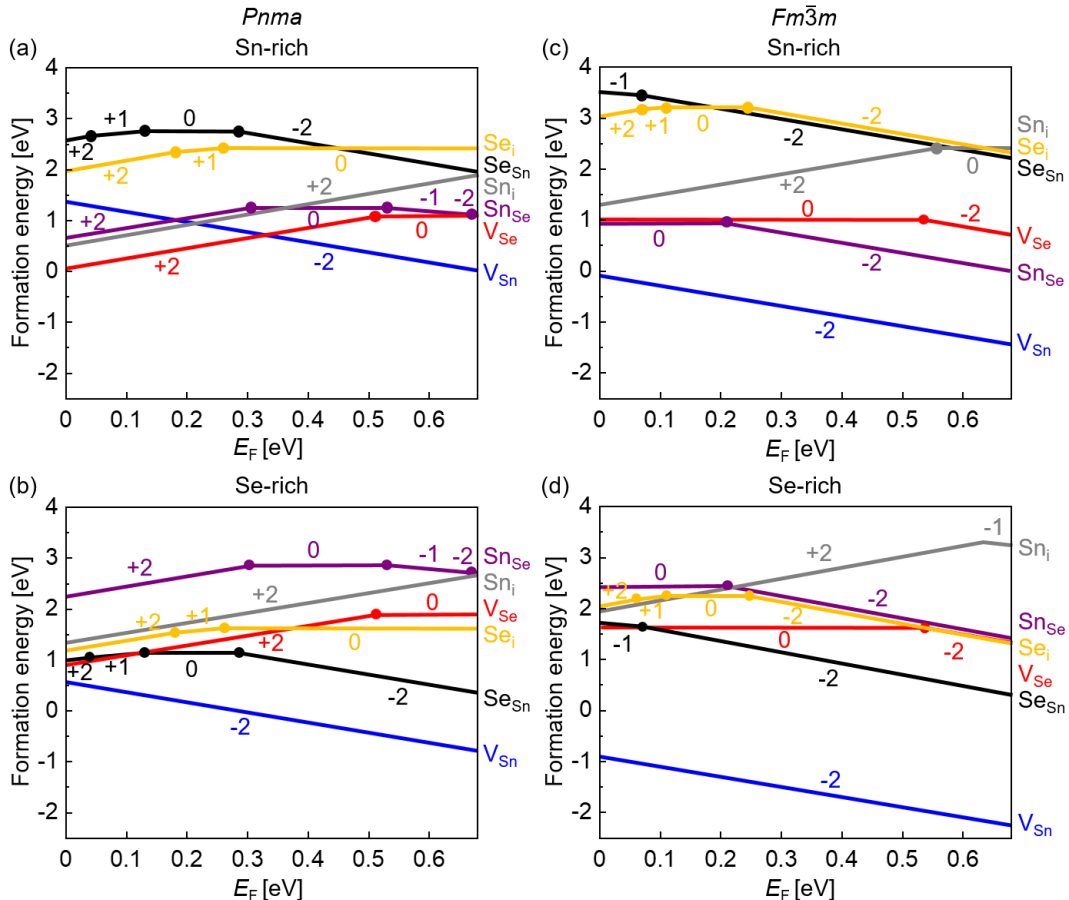


Figure 5.10 | Cation vacancy formation energy for $Pnma$ SnSe at (a) Sn-rich, (b) Se-rich and for $Fm\bar{3}m$ SnSe at (c) Sn-rich and (d) Se-rich conditions.

This finding aligns with the p -type semiconducting behavior of the cubic phase, as the negative formation energy of Sn vacancies in both Sn-rich and Se-rich conditions suggests the availability of positively charged holes for conduction. Limited

computational resources prevented this work from calculating defect formation energies in the complex cubic alloys. However, EDS analysis (Figure 5.7) revealed the presence of Sb-rich or Ag-rich precipitates in these materials. These precipitates likely create cation vacancies within the matrix, which can lower the Fermi energy level and depopulate antibonding states, ultimately stabilizing the structure.⁹⁷ This behavior aligns well with the inherent softness of MVB, characterized by a low bond order (around 0.5) and pronounced lattice anharmonicity.^{264,268} Consequently, the energy required to form vacancies in MVB solids is significantly lower compared to covalently bonded materials.

As predicted by the Pisarenko relationship, increased carrier concentration generally reduces the Seebeck coefficient. This trend is evident in Figure 5.9 (b), where pristine SnSe exhibits a high Seebeck coefficient due to its wide bandgap and low carrier concentration. Conversely, the Seebeck coefficients of cubic SnSe alloys fall within a desirable range for thermoelectrics.^{220,284,285} Notably, these alloys offer further optimization potential through precise carrier concentration tuning. However, the AgBiTe₂-alloyed sample exhibits a pronounced decrease in the Seebeck coefficient exceeding 400 K. This behavior likely stems from a strong bipolar effect, where intrinsic excitation of minority carriers partially cancels the majority carrier contribution to the Seebeck voltage. The temperature dependence of electrical conductivity in Figure 5.9 (a) also supports this interpretation. Despite high carrier concentrations ($\sim 10^{20} \text{ cm}^{-3}$), cubic SnSe alloys retain relatively large Seebeck coefficients. This suggests a high DOS effective mass for these doped alloys, as described in Equation 5.5 and Table 5.2. Pristine SnSe, with a calculated m_d^* of 0.43 m_e based on the single parabolic band model,²⁸⁶ aligns well with experimental values obtained via angle-resolved photoemission spectroscopy.²⁸⁷ Conversely, the cubic alloys possess significantly larger m_d^* values compared to pristine SnSe. However, a large effective mass can negatively impact carrier mobility, ultimately hindering electrical conductivity.³³ Therefore, the *PF* hinges on a delicate balance between DOS effective mass and carrier mobility for an optimized carrier concentration. This interplay can be captured by the weighted mobility,²⁸⁸ which represents the carrier mobility weighted by the DOS effective mass:

$$\mu_W \approx \mu \left(\frac{m_d^*}{m_e} \right)^{\frac{3}{2}} = \mu N_V \left(\frac{m_d^*}{m_e} \right)^{\frac{3}{2}} \quad (5.1)$$

Figure 5.9 (c) depicts the temperature dependence of the weighted mobility (μ_W)

calculated using experimental electrical conductivity and Seebeck coefficient data, following the method outlined by Snyder et al.²¹⁷ The pristine polycrystalline SnSe sample exhibits a distinct "up and down" trend in its μ_W curve. The initial rise up to 400 K aligns with a thermally-activated conduction process, attributed to charge carrier scattering at grain boundaries.^{213,252,289,290} Beyond 500 K, a second increase in μ_W is observed, coinciding with the well-established phase transition of SnSe from *Pnma* to *Cmcm* symmetry.

In contrast to pristine SnSe, all cubic SnSe alloys exhibit a decreasing trend in weighted mobility with increasing temperature, suggesting metal-like or degenerate semiconducting characteristics and indicating significantly weaker charge carrier scattering at grain boundaries compared to pristine SnSe. This difference can be attributed to the underlying bonding mechanisms: pristine SnSe utilizes on covalent bonding, while the cubic phases exhibit metavalent bonding. The Lyddane-Sachs-Teller relation predicts a larger static dielectric constant for the cubic samples.²¹³ Consequently, the stronger dielectric screening effect in cubic SnSe alloys weakens grain boundary scattering of charge carriers.²⁹¹ This enhanced μ_W across a broad temperature range translates to superior *PF* for the cubic alloys compared to pristine SnSe, as evident in Figure 5.9 (d).

The electronic quality factor (B_E)²²⁰ and intrinsic conductivity (σ_0)²⁸⁵ of these polycrystalline SnSe samples were further evaluated (Figure 5.11). The findings align perfectly with the weighted mobility analysis, further solidifying the superior electrical performance of cubic SnSe alloys (Figure 5.9). Notably, incorporating 33% AgBiTe₂ into SnSe yields a remarkable ninefold enhancement in power factor, from 0.9 $\mu\text{W cm}^{-1} \text{K}^{-2}$ for pristine SnSe to an impressive 8.0 $\mu\text{W cm}^{-1} \text{K}^{-2}$ for the alloy at room temperature (300 K). This value ranks among the highest reported for polycrystalline SnSe compounds near room temperature.^{250,252,254,256,259,290,292} A high room-temperature *PF* has also been achieved in the *p*-type cubic pure SnSe phase under high pressure conditions.²⁹³

A higher average power factor translates to improved power output.²⁹⁴ Conversely, the pristine polycrystalline SnSe sample exhibits a high power factor only at elevated temperatures, coinciding with the dominance of the high-symmetry *Cmcm* SnSe phase. The MVB mechanism, though identical in these cubic SnSe alloys, may not yield identical properties across all MVB materials. Figure 2.7 illustrates the distribution of various chemical bonding mechanisms across a map defined by two quantum-chemical

parameters. ET and ES serve as bonding descriptors and effective predictors of material properties due to the inherent link between bonding and material characteristics.²⁷⁹ The increasing iconicity along the PbTe-PbSe-PbS line is reflected by a rising ET value, which consequently leads to a declining trend in the maximum power factor.²⁶⁸ Computational limitations restricted the ES and ET calculations to pure SnSe phases. These values likely differ for SnSe-Ag VVI_2 alloys, explaining the variations in their thermoelectric properties. The MVB solids consistently demonstrate superior thermoelectric performance compared to covalently bonded SnSe.

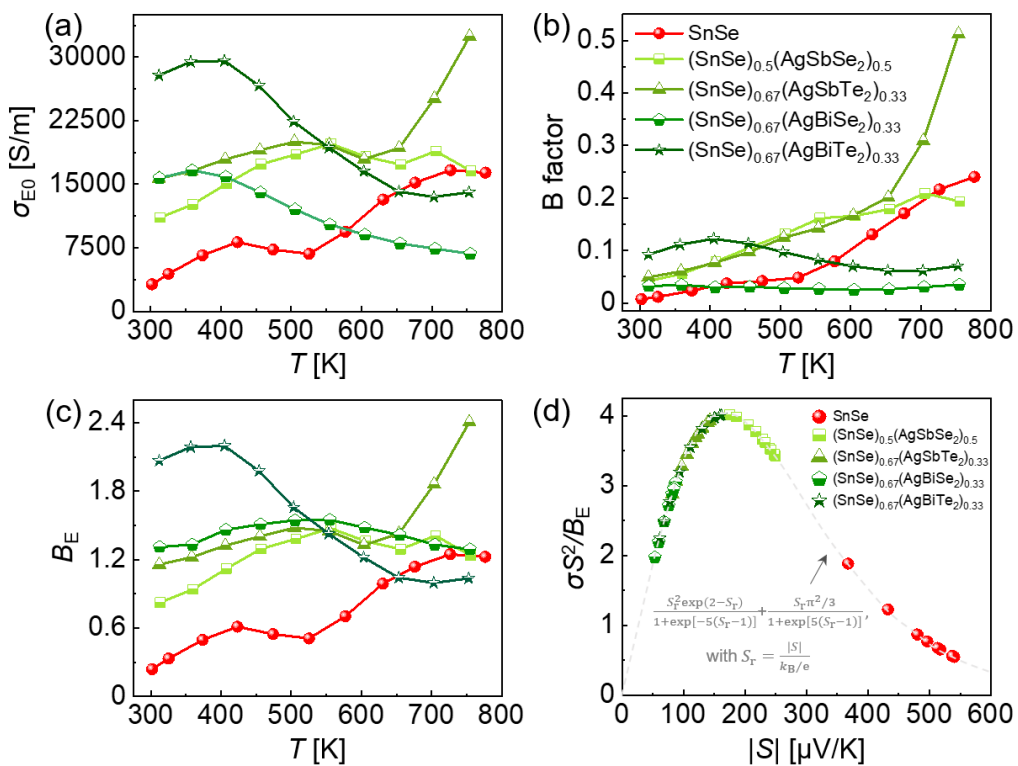


Figure 5.11 | (a) σ_{E0} ; (b) B factor; (c) B_{electron} (B_E). (d) Scaled power factor versus Seebeck coefficient of the pristine SnSe and the doped compounds.

5.3.2 Chemical Bonding Origins of Improved Thermoelectric Performance

DFT calculations with spin-orbital coupling effect reveal the orbital-resolved band structures of orthorhombic and cubic SnSe in Figures 5.12 (a) and (b). The dominance of Sn and Se p states in the conduction and valence bands near the Fermi energy suggests that the influence of s-lone pairs on electrical transport may be less significant than previously thought, as observed in PbTe, a $IV-VI$ compound.²⁹⁵ This aligns with the

optical absorption data in Figure 5.4, indicating that interband transitions predominantly involve p states. The *Pnma* phase exhibits a bandgap of 0.63 eV, consistent with experimental measurements and prior calculations.²²⁸ The *Fm $\bar{3}m$* SnSe phase displays a smaller bandgap of 0.24 eV, comparable to the experimentally observed range for cubic SnSe-Ag VVI_2 alloys (ranging from \sim 0.12 eV to 0.28 eV in Table 5.2) calculated using the Goldsmid-Sharp method²⁹⁶ according to Equation (5.2) and reported in DFT studies.²⁴⁰

$$E_{\text{gap}} = 2e \times |S|_{\text{max}} \times T_{\text{max}} \quad (5.2)$$

where T_{max} is the temperature corresponding to the $|S|_{\text{max}}$.

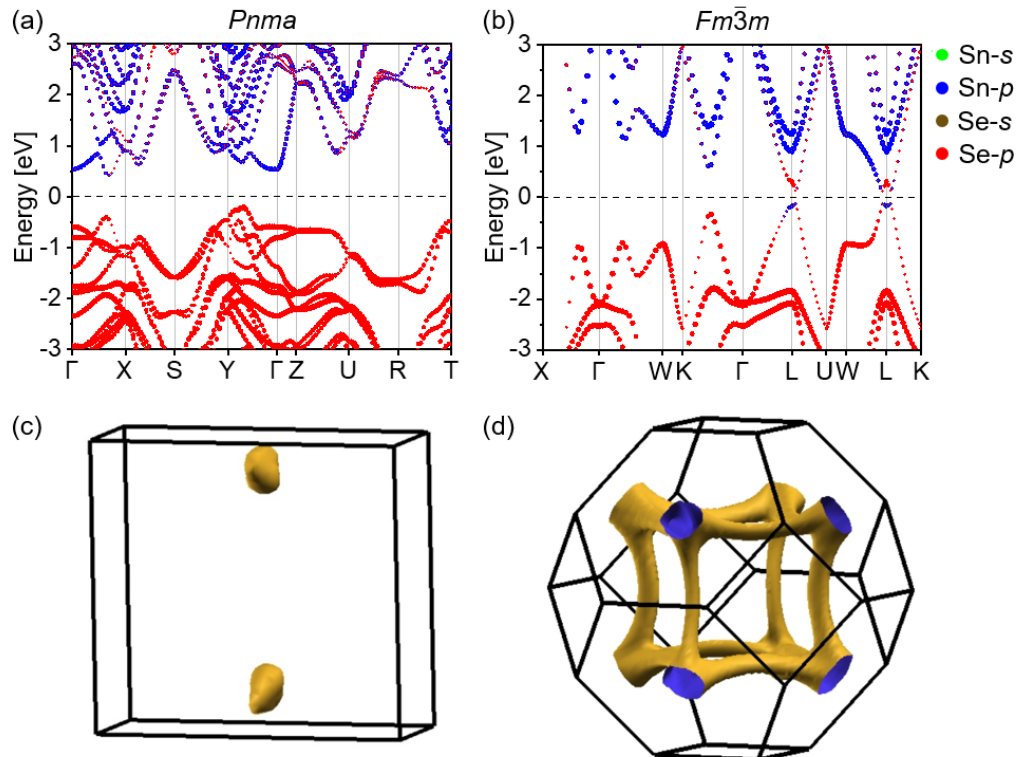


Figure 5.12 | Electronic band structures for various SnSe phases incorporating spin-orbit coupling effect: (a) *Pnma* SnSe; (b) *Fm $\bar{3}m$* SnSe. The constant energy surfaces at -0.3 eV and -0.4 eV relative to the Fermi energy in the first Brillouin zone for (c) *Pnma* SnSe and (d) *Fm $\bar{3}m$* SnSe phases, respectively.

Despite omitting the intricate compositions of the alloys in our DFT calculations, the electronic band structure of pure cubic SnSe likely captures key characteristics of the cubic alloys, including valley degeneracy and m_b^* . DFT calculations reveal a valence-band effective mass of $0.25 m_e$ and $0.09 m_e$ for the orthorhombic and cubic SnSe phases,

respectively, consistent with reported values.²⁹⁷ The lower m_b^* in the cubic phase stems from enhanced p-p orbital overlap, leading to increased band dispersion. In [Figure 5.12 \(c\)](#), constant energy surfaces at 0.3 eV below the Fermi energy in the first Brillouin zone for the *Pnma* SnSe phase are depicted, revealing a valley degeneracy (N_V) of 2. Conversely, the numerous high-symmetry points in the cubic phase's Brillouin zone led to a significantly higher N_V . The small energy difference (0.2 eV) between the L and Σ points enables Fermi level ([Figure 5.12 \(b\)](#)) tuning to achieve band convergence via doping. Consequently, the cubic phase exhibits a total N_V of 16 (4 from L and 12 from Σ point). Notably, [Figure 5.12 \(d\)](#) employs a value of 0.4 eV below the Fermi energy to enhance the visualization of constant energy surfaces. This high N_V value significantly enhances the weighted mobility and power factor in cubic SnSe alloys.

[Figure 5.13 \(a\)](#) illustrates the temperature-dependent total thermal conductivity (κ_{tot}). [Table 5.1](#) and [Figure 5.14](#) present relevant parameters, including sample density (ρ), specific heat (C_p), and thermal diffusivity (D). Considering that the total thermal conductivity comprises contributions from lattice vibration (κ_{lat}), heat-carrying charge carriers (κ_{ele}), and bipolar heat conduction, the increased κ_{tot} observed in cubic SnSe alloys primarily stems from the significantly enhanced electrical conductivity. Electronic thermal conductivity can be computed using Wiedemann Franz's law in Equation (2.26), $\kappa_{\text{ele}} = L\sigma T$, where the Lorenz number (L) is determined utilizing a SPB model (details regarding L and κ_{ele} can be found in [Figure 5.14](#)). Subtracting κ_{ele} from κ_{tot} yields the κ_{lat} depicted in [Figure 5.13 \(b\)](#). Notably, this value also incorporates the contribution of the bipolar effect. Near room temperature, the lattice thermal conductivity of all alloyed samples is lower than that of pristine SnSe, especially when the bipolar effect is not significant. The notable increase in κ_{lat} observed with temperature for samples SnSe-AgBiSe₂ and SnSe-AgBiTe₂ is attributed to bipolar heat conduction. The decrease in lattice thermal transport upon alloying with Ag₃V₂I₂ stems from various factors. Firstly, the presence of soft metavalent bonds leads to a reduced phonon group velocity.²⁶⁴ Secondly, the delocalized p-electrons in the MVB strongly interact with transverse optical phonons, resulting in lower phonon frequencies and increased anharmonicity.¹⁰⁰ Thirdly, the introduction of alloying elements complicates atomic arrangements, thereby enhancing the scattering strength of phonons by point defects.²⁹⁸ Collectively, these factors contribute to the reduction of lattice thermal conductivity.

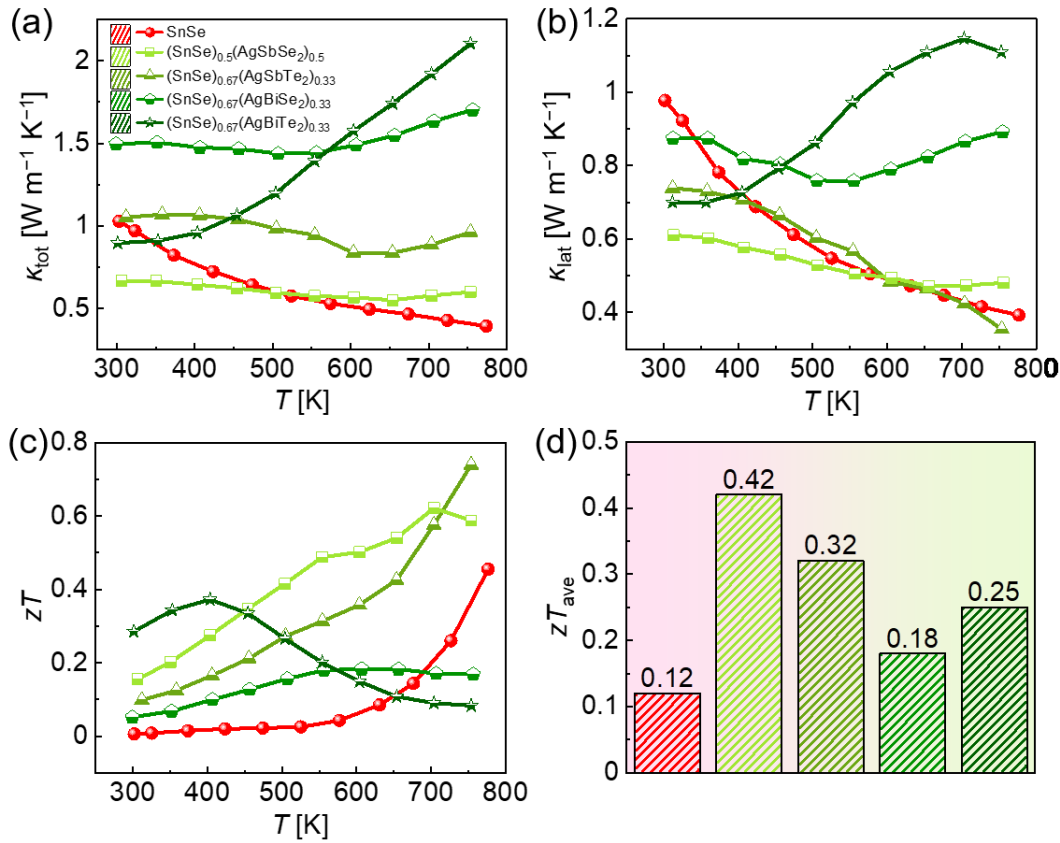


Figure 5.13 | (a) κ_{tot} , (b) κ_{lat} , (c) zT , and (d) zT_{ave} for *Pnma* SnSe and the as-alloyed SnSe. Due to the anisotropic nature of SnSe, the thermoelectric properties of pristine polycrystalline SnSe were measured along the direction of the SPS pressure (out-of-plane direction).

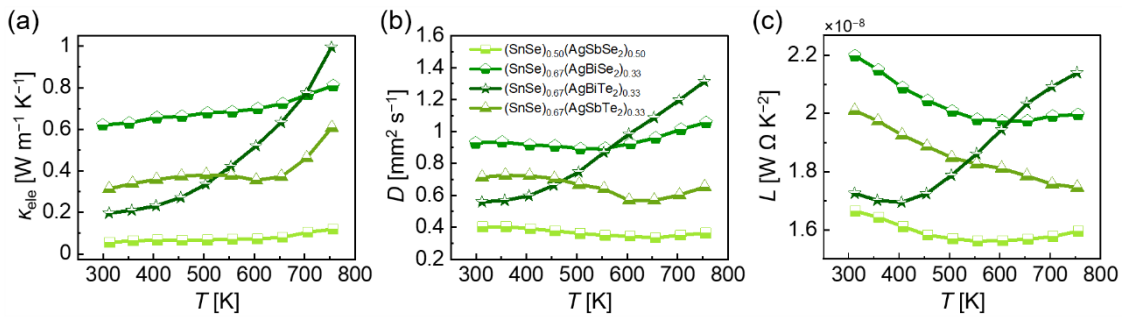


Figure 5.14 | (a) Electrical thermal conductivity calculated according to the Wiedemann-Franz law; (b) Thermal diffusivity (D) measured by the laser flash method. (c) Temperature-dependent Lorenz number.

Benefiting from both a broader range of high power factor and lower lattice thermal conductivity near room temperature, cubic SnSe alloys exhibit superior final zT values compared to pristine SnSe (see Figure 5.13 (c)). The higher temperature zT increase observed for pristine SnSe (>650 K) coincides with the dominance of the more

symmetrical *Cmcm* phase, for which DFT calculations suggest metavalent bonding^{299–301}. However, experimentally verifying the MVB mechanism in *Cmcm* SnSe hinges on its stabilization at ambient conditions, which is a significant challenge. Encouragingly, within the 300–750 K range, all MVB SnSe-Ag VVI_2 alloys outperform pristine SnSe in terms of average zT (zT_{ave}) (Figure 5.13 (d)). The zT values of our cubic SnSe-Ag VVI_2 alloys are consistent with literature data, considering the inherent $\pm 20\%$ measurement error for zT .^{259,263,275} Further zT improvement can be targeted through strategic dopant introduction (e.g., Pb²⁵⁹ or Ge²⁷⁵) in the cubic system for precise control of ES and ET values, alongside modulation of microstructural defects.

5.4 Improved Mechanical Properties of SnSe-Ag VVI_2 Alloys

As evident in Figure 5.15, the Vickers hardness exhibits a clear increase upon alloying SnSe with AgSbTe₂. Cubic SnSe-Ag VVI_2 alloys exhibit a notable increase in Vickers hardness, reaching an average of ~ 1.70 GPa, significantly higher than pristine SnSe (0.87 GPa). This enhanced hardness benefits both material processing and thermoelectric device applications. Alloying SnSe with elements like Ag, Sb, Bi, and Te effectively improve its hardness through modifications in the crystal structure, grain size refinement, and element interactions. These factors (lattice distortion, altered bonding, and secondary phase formation) refine the microstructure, leading to improved mechanical properties.

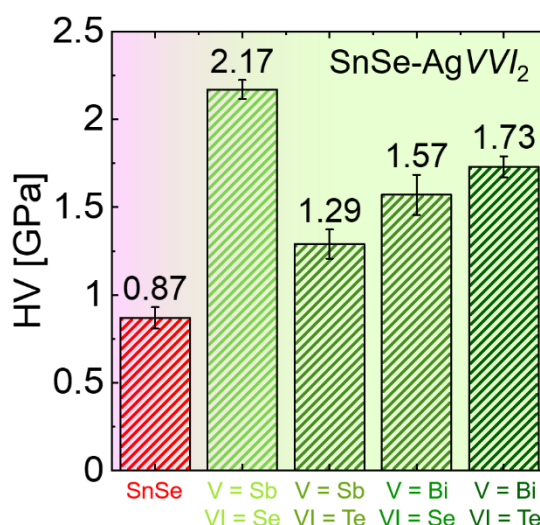


Figure 5.15 | Vickers hardness of SnSe and SnSe-Ag VVI_2 alloys (V = Sb, Bi; VI = Se, Te). The Vickers hardness was measured with a Verios G4 UC (Thermo Scientific). We are grateful to Dr. Marina Kemperle from Werkzeugmaschinenlabor WZL der RWTH Aachen for her assistance.

5.5 Conclusions

This study reveals superior thermoelectric performance in the high-symmetry cubic SnSe phase compared to its low-symmetry *Pnma* counterpart. This structural transition can be strategically controlled by manipulating the chemical bonding mechanism. Enhanced p-p orbital overlap in the cubic phases leads to stronger optical absorption. Additionally, these phases exhibit a large optical dielectric constant, a high Born effective charge, and unique bond-breaking behavior with a high "probability of multiple events". This confluence of properties strongly supports the presence of the metavalent bonding mechanism in cubic SnSe alloys, contrasting with the covalent bonding observed in pristine *Pnma* SnSe.

The formation of metavalent bonds in the cubic SnSe phase significantly enhances its power factor, primarily through increased carrier concentration and valley degeneracy. Additionally, the soft nature of these bonds, combined with the alloy scattering of phonons, contributes to the low thermal conductivity observed. Consequently, the zT of polycrystalline cubic SnSe solids surpasses that of pristine *Pnma* SnSe by a factor of over 10 at low temperatures. This approach of manipulating structural symmetry and thermoelectric performance through tailoring chemical bonds holds promise for other chalcogenides like SnS and GeS.

6 High-entropy Thermoelectrics: The Role of Metavalent Bonding

6.1 Introduction of High-entropy Thermoelectrics

Recently, high-entropy alloys (HEAs) have emerged as a promising class of materials due to their unique properties arising from the incorporation of multiple elements in near-equimolar ratios within a single-phase structure.^{302,303} Configurational entropy (ΔS_c) serves as a quantitative descriptor for the level of compositional disorder. ΔS_c reflects the number of microscopic arrangements (microstates) accessible to the atomic configuration. A higher degree of disorder translates to a greater number of microstates, which ΔS_c captures through the following equation derived from the Boltzmann hypothesis.^{304,305}

$$\Delta S_c = -R \left[\left(\sum_{i=1}^n x_i \ln x_i \right)_{\text{cation}} + \left(\sum_{j=1}^m x_j \ln x_j \right)_{\text{anion}} \right] \quad (6.1)$$

where R is the molar gas constant ($8.31 \text{ J mol}^{-1} \text{ K}^{-1}$), n and m are the species at the cation sites and anion sites respectively, x is the mole content and $\sum_{i=1}^n x_i = \sum_{j=1}^m x_j = 1$. When n is 5 and x is identical for all species, ΔS_c can reach $1.6 R$. ΔS_c can be adjusted by the number and content of each component in the material. Equation (6.1) illustrates that an increase in components number leads to a higher ΔS_c . Because the system becomes more disordered as the components approach equal amounts (multiple principal components). The solid solution's stability is governed by its Gibbs free energy (G) calculated as follows:

$$G = H - TS \quad (6.2)$$

where H , T , and S represent enthalpy, absolute temperature, and entropy, respectively. A large enough entropy change (ΔS) can compensate for an unfavorable enthalpy change (ΔH), resulting in $\Delta G < 0$. Equation (6.2) reveals that a decrease in Gibbs free energy upon doping, linked to higher entropy, favors the formation of stable, homogeneous solid solutions.^{306,307} HEAs leverage high ΔS_c from multiple principal elements to favor stable BCC or FCC solid solutions by suppressing intermetallic formation due to a larger decrease in G compared to the enthalpy change of intermetallic formation.

HEAs have demonstrated remarkable potential beyond traditional metal alloys, offering

not only superior mechanical properties like high strength and corrosion resistance,^{308–314} but also complex influences on various physical properties. This versatility has fueled the exploration of high entropy design principles in magnetic,^{315,316} dielectric,³¹⁷ and thermoelectric materials.^{318,319} Unlike conventional alloys where limited elemental solubility arises from decreasing enthalpy and atomic size mismatch-induced stresses, HEAs leverage their high configurational entropy to overcome these limitations. This allows for a significantly broader range of accessible compositions and diverse microstructural features, paving the way for a new generation of high-performance thermoelectric materials.

Materials with complex crystal structures can accommodate multiple elements in a single sublattice to induce configurational disorder, resulting in the formation of high-entropy oxides, tellurides, etc.³²⁰ Figure 6.1 (a) presents typical HEAs with NaCl (AB type) structure. High configurational entropy can be achieved even when only one sublattice is occupied by a mixture of elements in near-equimolar ratios, provided a sufficient number of alloying elements are incorporated. The undisturbed sublattice can then accommodate greater lattice distortion, further enhancing structural stability.³²¹

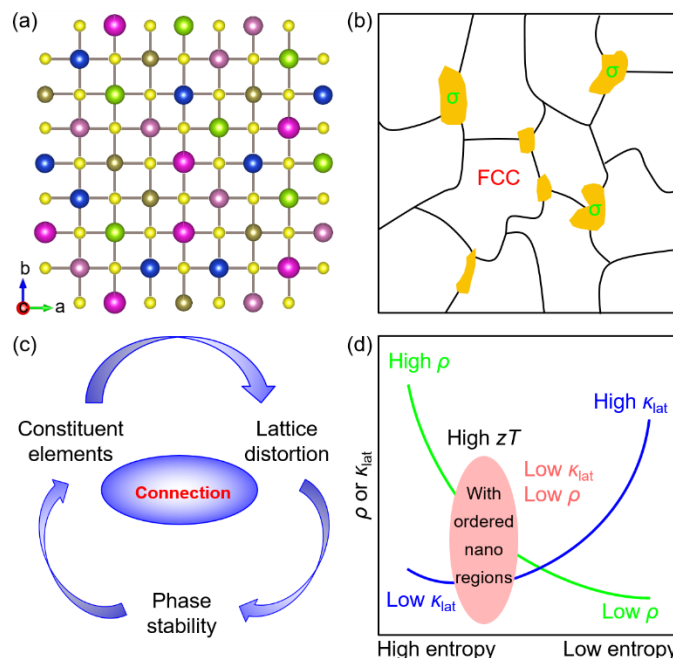


Figure 6.1 | (a) High-entropy compound with a typical $Fm\bar{3}m$ structure (AB, sublattice A is engineered with high-entropy). (b) Lattice distortion in stable FCC compounds. (c) The interplay between constituent elements, lattice distortion, and phase stability in multi-principal element alloys. (d) Schematic depicting the relationship between electrical resistivity, lattice thermal conductivity, and entropy.

Despite the effectiveness of lattice distortion in enhancing solid solution strengthening, data-driven studies employing machine learning and statistical methods have revealed that increasing distortion can lead to a decrease in phase stability.^{322,323} As illustrated in Figure 6.1 (b), there is a trade-off between lattice distortion and phase stability of HEAs. The addition of strengthening elements can increase the lattice distortion, but the FCC phase stability will decrease correspondingly as shown in Figure 6.1 (c). Studies show that maintaining the electrical conductivity with significantly suppressed thermal conductivity is key to realizing high-performance thermoelectric high-entropy compounds as depicted in Figure 6.1 (d).

Crystallographic order, defined by the periodic arrangement of atoms, is fundamental to most macroscopic properties, including heat transport in thermoelectric materials³²⁰. Here, the charged carrier transport and phonon propagation are highly sensitive to this atomic periodicity.³²⁴ Phonon dispersion, influenced by both atomic mass and bond strength, is significantly disrupted by deviations from periodicity, leading to phonon scattering.^{320,325,326} From the perspective of thermal performance, studies stated that the significant strains resulting from the severely distorted lattice in this high-entropy material induce strong scattering for heat-carrying phonons, thereby contributing to an ultralow κ_{lat} .³⁰⁴ This perspective can be corroborated by referring to Figures 6.2 (a) and (b): Due to the asymmetry of the probability distribution function, the equilibrium positions of the atoms in high-entropy materials should deviate from a uniform distribution. Some viewpoints suggest that entropy-induced disorder localizes phonons, impeding the propagation of transverse phonons, consequently increasing anharmonicity and significantly reducing lattice thermal conductivity.³²⁷ This opinion can be verified by Figure 6.2 (c): Within the octahedron formed by one Ge atom and six Te atoms, there are three shorter bonds and three longer bonds. The electrons exhibit high localization, resulting in the formation of shorter bonds due to symmetry breaking in the rhombohedral structure with a distorted lattice.³²⁷

As for electrical properties, certain studies propose that entropy increases in disordered systems can lead to higher crystal symmetry and delocalized electron distributions, thereby preserving favorable electrical transport properties.³²⁷ This perspective is elucidated in Figures 6.2 (c) and (d): By creating HEAs with a greater variety of element species, the charge density between Ge sites and surrounding Te sites becomes similar,

indicating a delocalized electron distribution. Upon incorporating alloying elements, localized electrons may transfer from shorter to longer bonds, leading to a delocalized electron distribution and similar bond characteristics in Figure 6.2 (d). Most studies prove that high-entropy materials tend to adopt highly symmetrical crystal structures to accommodate multiple elements and maximize configurational entropy.³²⁸ This structural characteristic promotes the formation of electronic bands with multivalley features, leading to an increased density of states and effective mass of charge carriers, ultimately contributing to a high Seebeck coefficient.^{329,330} Tailoring high-entropy structures by leveraging entropy-driven structural stabilization creates diverse materials that crucially maintain favorable electrical transport properties.^{331,332} This strategy of incorporating high entropy has been successfully applied in thermoelectric materials, such as Pb(S/Se/Te), Cu₂(S/Se/Te), and (Mn/Ge/Sn/Pb)Te.^{329,333} The concept has been extended to a wider range of material systems, including SnTe, SnSe, GeTe, and PbSe.^{8,304,327,330,334} Notably, (Pb/Sn)(Se/Te/S) and (Ge/Ag/Sb/Pb)Te demonstrate the promise of this approach, achieving high zT of 1.8 (900 K) and 2.7 (750 K) respectively.^{304,327}

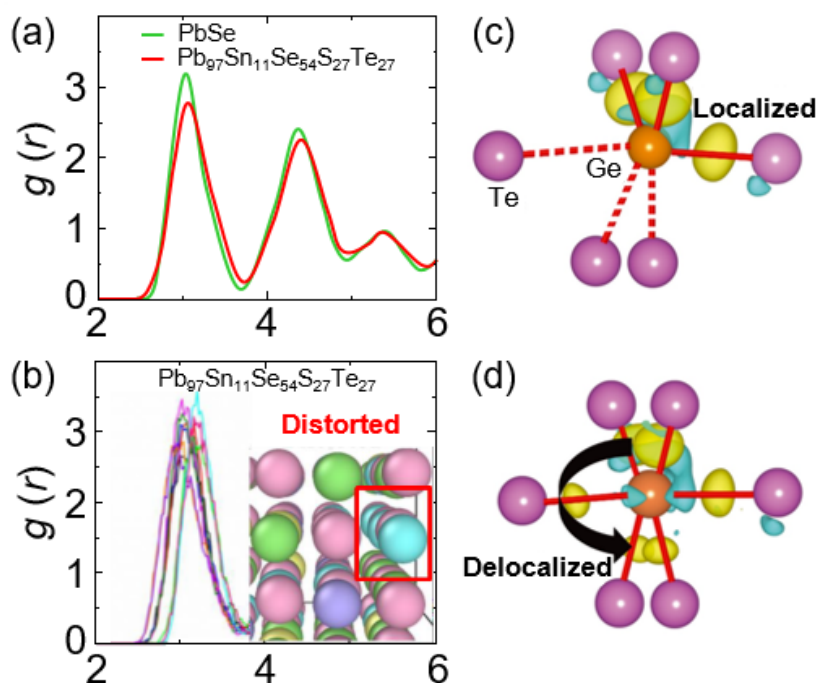


Figure 6.2 | (a) Total radial distribution functions $g(r)$ of pure PbSe and Pb₉₇Sn₁₁Se₅₄S₂₇Te₂₇ high-entropy sample.³⁰⁴ Partial radial distribution functions $g(r)$ of 10 atoms selected randomly in (b) Pb₉₇Sn₁₁Se₅₄S₂₇Te₂₇.³⁰⁴ Schematic electron distribution: (c) localized (solid red lines indicate short bonds) and (d) delocalized (dotted red lines indicate long bonds) states as determined by DFT calculations.³²⁷

Intrinsic limitations persist as disordered atoms may impede carrier transport, leading to reduced electrical conductivity,^{335,336} as illustrated in Figure 6.1 (d). Hence, achieving high-performance thermoelectric high-entropy compounds requires maintaining electrical conductivity while suppressing thermal conductivity. A strategy involves precisely tuning the arrangement patterns of multiple elements, some of which may form regularly clustered or structured nanofeatures spanning several nanometers.³³⁷ Matching the size of these nanoregions with the mean-free path of phonons can effectively decrease thermal conductivity (Figure 6.1 (d)). Sublattice engineering can mitigate the impact on carrier transport,³³⁸ while elements capable of optimizing carrier concentration and increasing density-of-states effective mass through band engineering show promise in counteracting potential reductions in carrier mobility. In summary, significant opportunities exist for further exploration of design principles for high-entropy materials, with the potential to discover novel high-performance thermoelectric compounds.

One potential exploration is to consider the fundamental principles underlying the constitution of high-entropy alloys: Why would the introduction of multiple elements, if randomly and disorderly occupying a single sublattice, lead to the disruption of local atom periodicity? In a conventional crystal structure, atoms are arranged in a repeating, periodic pattern. When multiple elements with different sizes and chemical properties are randomly distributed within a single sublattice, this periodicity order is disrupted. Classic binary thermoelectrics generally have two types of anionic and cationic atoms, A and B, with atoms arranged in a staggered manner, resulting in $\Delta S_c = 0$.³³⁹ If other atoms are introduced into binary thermoelectric materials through methods such as solid solution, doping, and alloying to become multi-component TE materials with three or more types of atoms, some of which are disorderly distributed in the lattice, resulting in a larger ΔS_c . Compared to binary thermoelectric materials, the ones with large ΔS_c have larger lattice distortions, larger cell volumes, and more pronounced mass fluctuations; but their macrostructural symmetry tends to be enhanced. The configurational entropies of $\text{Pb}_{0.89}\text{Sb}_{0.012}\text{Sn}_{0.1}\text{Se}_{0.5}\text{Te}_{0.25}\text{S}_{0.25}$ and $\text{Ge}_{0.61}\text{Ag}_{0.11}\text{Sb}_{0.13}\text{Pb}_{0.12}\text{Bi}_{0.01}\text{Te}$ mentioned in Figure 6.2 are $1.41R$ and $1.24R$ respectively. In both alloys, these elements form a single-phase solid solution and a highly symmetric structure without a significant precipitation phase. An alternative study investigating $(\text{GeTe})_{0.95}(\text{SnSe})_{0.025}(\text{SnS})_{0.025}$ ($\Delta S_c \approx 0.91R$) yielded different results. The performance improvement was attributed to the presence of abundant point defects and a complex microstructure, which effectively scattered

phonons and reduced κ_{lat} as shown in Figure 6.3. Notably, the researchers did not observe the classic "high-entropy effect" in this specific system.

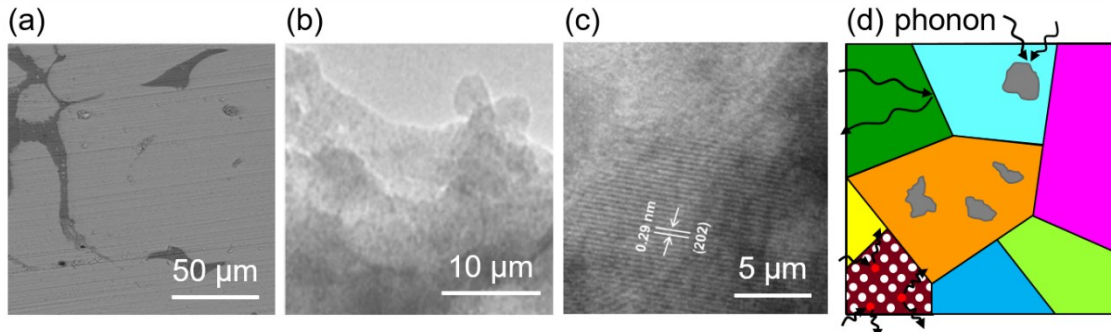


Figure 6.3 | (a) BSE-FESEM image, (b) TEM image, and (c) HRTEM image of $(\text{GeTe})_{0.95}(\text{SnSe})_{0.025}(\text{SnS})_{0.025}$, showing the presence of precipitates. (d) Schematic diagram of scattering of the heat-carrying phonon via the point defect mass fluctuations and microstructures.

This observation raises a critical question: why do some multi-component systems exhibit high-entropy characteristics and superior thermoelectric performance, while others with similar constituent elements do not? One potential factor lies in the chemical bonding. Studies suggest a correlation between high solid solubility and specific bonding types. For instance, materials like SnTe and AgSbTe_2 , which readily form high-entropy solid solutions, possess favorable chemical bonding that contributes to higher configurational entropy.

The high-entropy compositions, $\text{Pb}_{0.89}\text{Sb}_{0.012}\text{Sn}_{0.1}\text{Se}_{0.5}\text{Te}_{0.25}\text{S}_{0.25}$ (PbSe-chalcogenides) and $\text{Ge}_{0.61}\text{Ag}_{0.11}\text{Sb}_{0.13}\text{Pb}_{0.12}\text{Bi}_{0.01}\text{Te}$ (GeTe-based chalcogenides), can be conceptualized as a combination of various binary or ternary chalcogenides, i.e., $\text{PbTe} + \text{PbSe} + \text{PbS} + \text{Sb}_2\text{Te}_3 + \text{SnTe}$ and $\text{GeTe} + \text{AgSbTe}_2 + \text{PbTe} + \text{AgBiTe}_2$, due to their shared crystal structures and bonding characteristics. This mixing principle of elemental constituents facilitates high configurational flexibility, thereby contributing to the observed high ΔS_c . Hereby, high-entropy thermoelectric materials typically consist of metavalently bonded compounds, exemplified by chalcogenides and $\text{Ag}VI_2$ ($V = \text{Sb, Bi}$; $VI = \text{Se, Te}$). Conversely, $(\text{GeTe})_{0.95}(\text{SnSe})_{0.025}(\text{SnS})_{0.025}$, which exhibits favorable properties due to the presence of secondary phases rather than high entropy, comprises GeTe, SnSe, and SnS. Notably, both SnSe and SnS feature covalent bonding, implying that this material lacks the high-entropy characteristic and is instead dominated by covalent interactions.

Thus, is the formation of high-entropy alloys related to chemical bonding? Is doping or alloying of compounds with MVB characteristics necessary to constitute HEA? Is there a strong coincidence or correlation between high-entropy thermoelectrics and metavalent bonding? Is high configurational entropy a major factor contributing to materials with improved thermoelectric (TE) properties? Prerequisite conditions for forming high entropy materials rely on random, uniform distribution of constituent elements, and the formation of single-phase solid solutions. Despite the established link between high configurational entropy (ΔS_c) and solid solution formation, a clear design strategy for maximizing ΔS_c remains elusive. Notably, most successful high-entropy thermoelectrics reported to date are based on chalcogenides like PbTe and GeTe and their alloys, which interestingly exhibit unconventional metavalent bonding characteristics. To investigate the interplay between ΔS_c , metavalent bonding, and thermoelectric performance, we synthesized BiPbAg Q ($Q = S_3, Se_3, Te_3$, and TeSeS) samples and analyzed their microstructures, bonding mechanisms, and thermoelectric properties.

6.2 The Formation of Solid Solution

6.2.1 Homogeneity in Macro Scale of the Solid Solution

To investigate the relationship between the configurational entropy and the thermoelectric properties of the materials, Pb Q were alloyed with AgBi Q_2 systems to form BiPbAg Q ($Q = S_3, Se_3, Te_3$, and TeSeS). The configurational entropy varied with values of $1.24R$ for the first three samples, and a higher value of $1.79R$ for BiPbAgTeSeS. To visualize the concept of introducing Pb Q into the AgBi Q_2 lattice, [Figure 6.4 \(a\)](#) presents a schematic representation of the atomic structures of PbTe (undoped) and PbTe doped with AgBi Q_2 , suggesting that this doping strategy can lead to the formation of new compounds. The XRD pattern in [Figure 6.4 \(b\)](#) indicated that all synthesized samples exhibit a single-phase $Fm\bar{3}m$ structure without any detectable second phase, confirming the successful formation of BiPbAgS₃, BiPbAgSe₃, BiPbAgTe₃, and BiPbAgTeSeS. The stability of the $Fm\bar{3}m$ structure at room temperature can be attributed to the complex configuration of cations within the lattice and the kinetic processes of slow atomic diffusion during material formation. As shown in [Table 6.1](#), the calculated lattice constants obtained from XRD measurements are in close agreement with the theoretical values predicted by

Vegard's law. This observation supports the formation of solid solutions in the synthesized BiPbAgTeSeS . For the rest four-element samples, the diffraction peaks shifted to a lower angle with increasing atomic number of Q , and the calculated lattice parameters also increased linearly with increasing atomic number, in accordance with Vegard's law. The corresponding Rietveld refinement of the above XRD patterns shown in Figures 6.4 (c) - (f) reveals that Ag and Bi atoms preferentially occupy Pb sites upon incorporating $\text{AgBi}Q_2$ into the $\text{Pb}Q$ system, inducing disorder within the lattice. Furthermore, the absence of impurity peaks in the DSC data (Figure 6.5) suggests the absence of significant phase transitions, signifying the successful synthesis of high-purity phases.

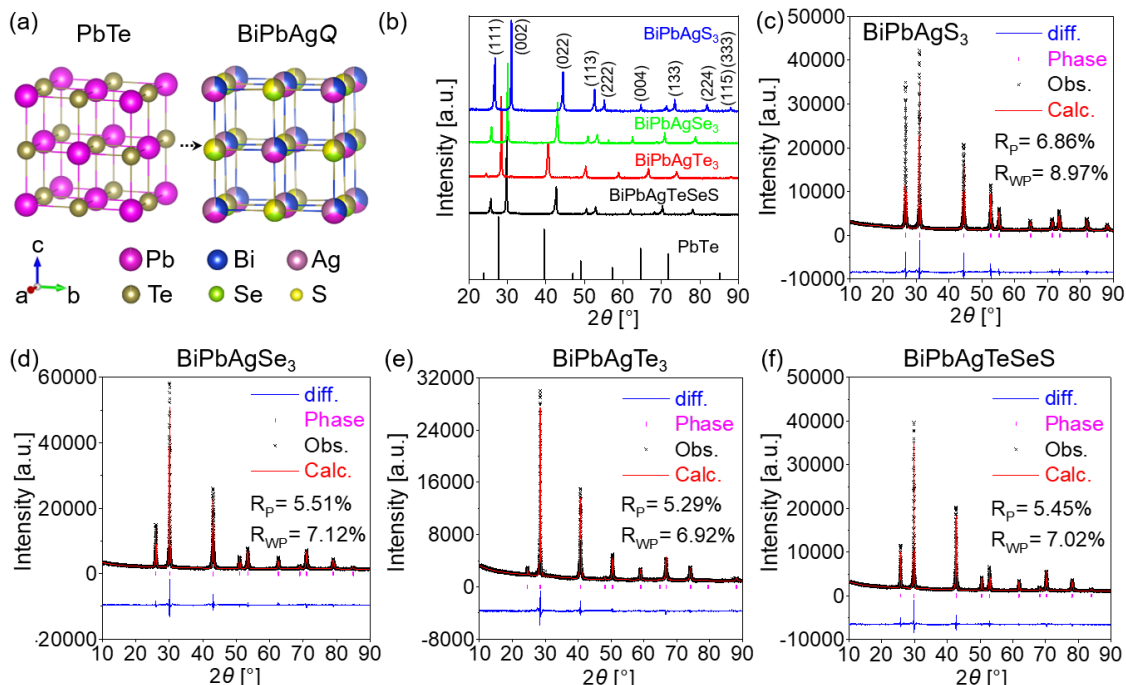


Figure 6.4 | (a) Structural transformation of PbTe upon $\text{AgBi}Q_2$ ($Q = \text{S, Se, Te}$) alloying. (b) XRD patterns at room temperature showing the pristine cubic PbTe and doped cubic phase. Rietveld refinement of XRD data of (c) BiPbAgS_3 , (d) BiPbAgSe_3 , (e) BiPbAgTe_3 , and (f) BiPbAgTeSeS .

Table 6.1 | Lattice parameters and Goldsmid-Sharp band gap of various high configurational entropy compounds with salt rock structure.

Compounds		BiPbAgS_3	BiPbAgSe_3	BiPbAgTe_3	BiPbAgTeSeS
Lattice parameter (\AA)	XRD measured	5.7545	5.9367	6.2640	5.9874
	Theoretical (Vegard's law)	5.752	5.98	6.3085	5.9851

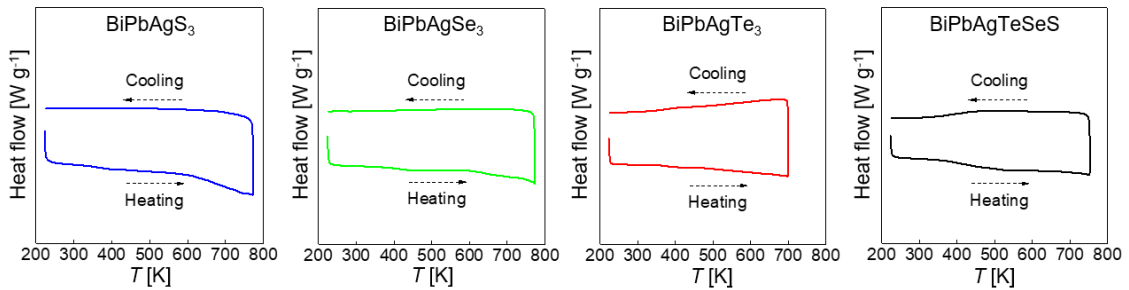


Figure 6.5 | DSC of the as-synthesized BiPbAgS_3 , BiPbAgSe_3 , BiPbAgTe_3 , and BiPbAgTeSeS samples.

Figure 6.6 (a) shows IPF obtained by post-processing the calibrated EBSD data, verifying the high purity of the rock-salt phase and illustrating that the grain orientation distributions of the samples are uniform and there is no obvious texture. Thus the influence of grain orientation on the thermoelectric properties can be excluded. Statistics of all the grain sizes in Figure 6.5 (b) indicate that the grain sizes of each sample are similar, with an average grain size of around $10\text{-}20\ \mu\text{m}$.

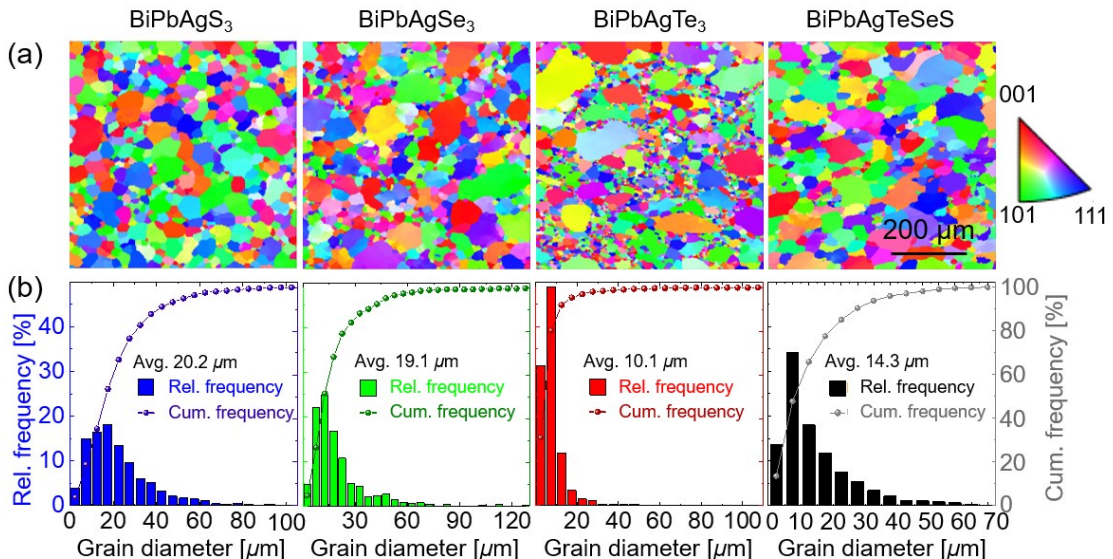


Figure 6.6 | (a) IPF from EBSD characterization, and (b) statistics of the grain sizes for the polycrystalline samples.

Backscattering Electron Images (BSI) of the fine-polished sample surface of the solid solutions in Figure 6.7 (a) also show no traces of a second phase. The corresponding elemental mapping images from EDS measurements are shown in Figure 6.6 (b). These images reveal a homogeneous distribution of all constituent elements (Ag, Bi, Pb, S, Se,

Te) across the analyzed area. The absence of elemental precipitation or enrichment indicates effective elemental mixing within the as-alloyed compounds. Figures 6.7 (c) and (d) present the weight percentages and atomic percentages of each element in all samples, respectively, both of which prove that the composition of the synthesized samples is close to the nominal composition, as further evidenced by the small deviation values from the nominal stoichiometry. This close match signifies successful synthesis with minimal compositional variation.

The above-analyzed XRD, BSI, EDX, and EBSD results successfully confirm the uniform distribution of the high-entropy solid solutions on the micrometer scale. However, these techniques primarily cannot probe structural features or resolve elemental distributions at the atomic scale. To achieve a higher level of precision for compositional uniformity, alternative characterization methods with finer detection capabilities are necessary.

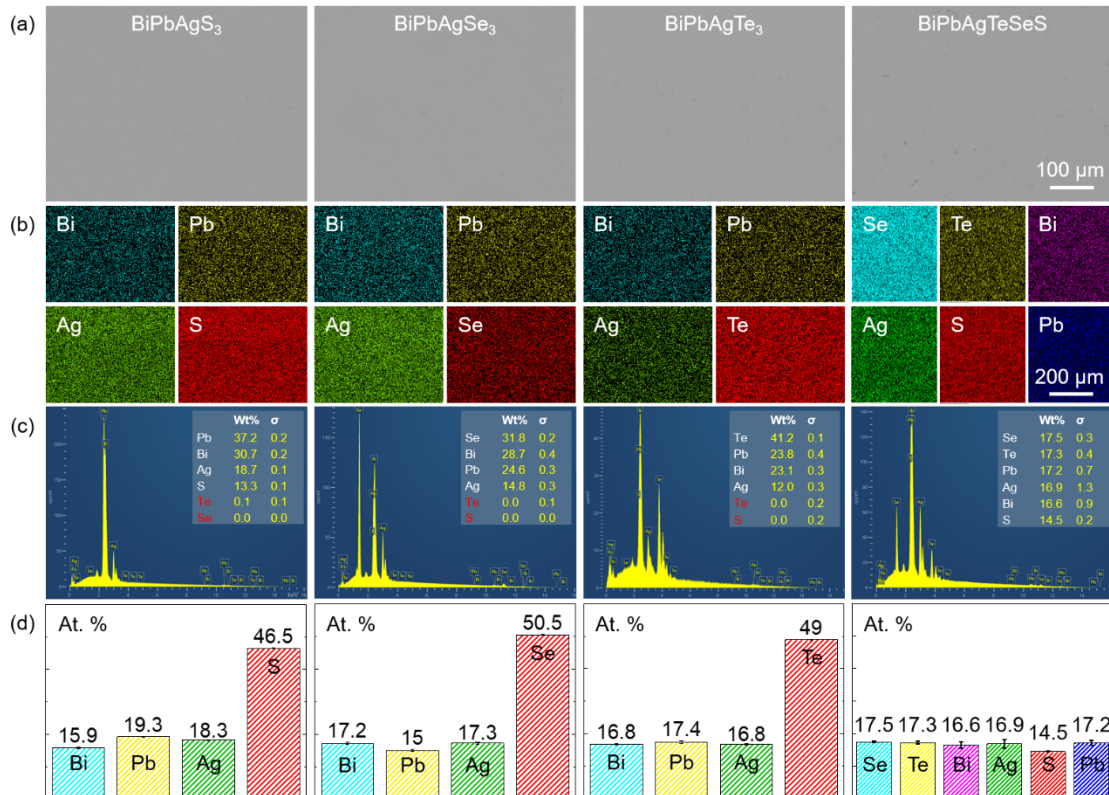


Figure 6.7 | (a) Structures obtained by backscattering electron image (BSI) of as-synthesized samples. (b) Elemental mapping of Bi, Pb, Ag, and S/Se/Te. (c) EDX spectra with values and standard deviations (σ) of weight percentages (wt. %) measured directly. (d) The atomic percentages (at. %) and standard deviations of individual samples transformed from weight percentages of (c).

6.2.2 Atomic Homogeneity of the Solid Solution

APT combining a point projection microscope and time-of-flight mass spectrometer is capable of providing 3D nanoscale insights into materials with sub-nanometer spatial resolution, demonstrating equal sensitivity for all elements. The elemental distributions were further analyzed at the nanoscale using laser-assist APT, shown in Figures 6.8 and 6.9. The quantitative data on the elemental distribution confirms that the composition of the samples closely matches the nominal composition at the atomic scale. Atomic distribution maps revealed that Bi, Pb, Ag, S, Se, and Te atoms are randomly and uniformly distributed at the atomic scale. To quantify this observation further, near-neighbor atomic distribution maps in 3D space were specifically constructed for Bi-Bi, Pb-Pb, Ag-Ag, S-S, Se-Se, and Te-Te pairs respectively. The experimental results closely match the randomized predictions and exhibit a Gaussian distribution profile.

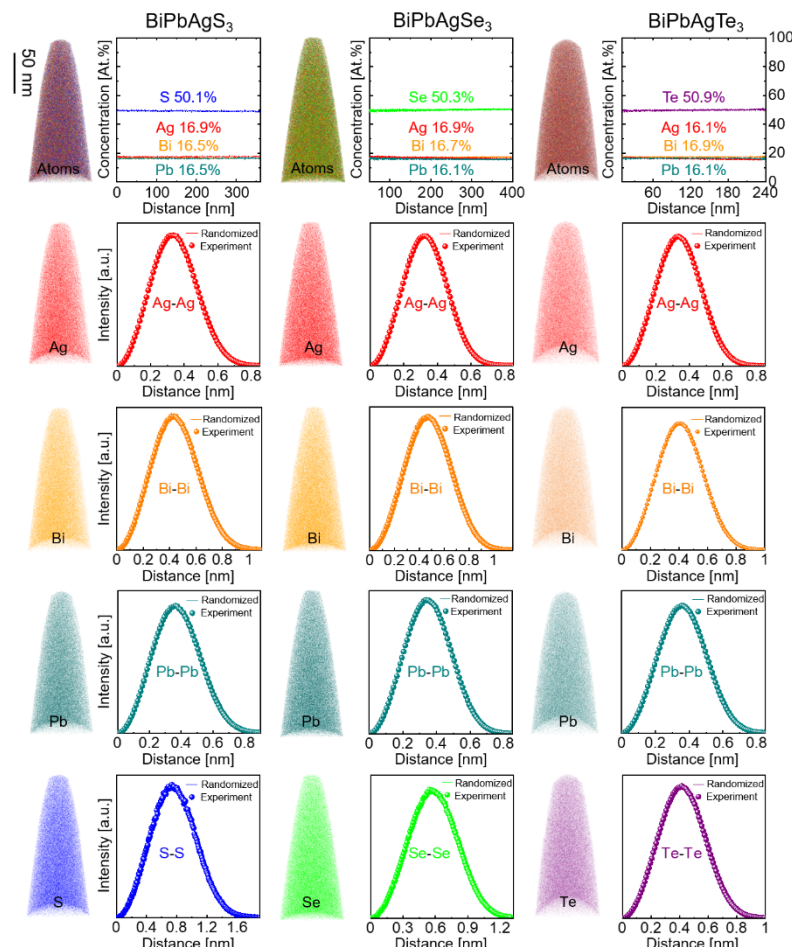


Figure 6.8 | 3D APT detection including ionic mass spectrum, 3D atomic maps, and nearest-neighbor atomic distribution histograms of the elements for BiPbAgS_3 , BiPbAgSe_3 , and BiPbAgTe_3 .

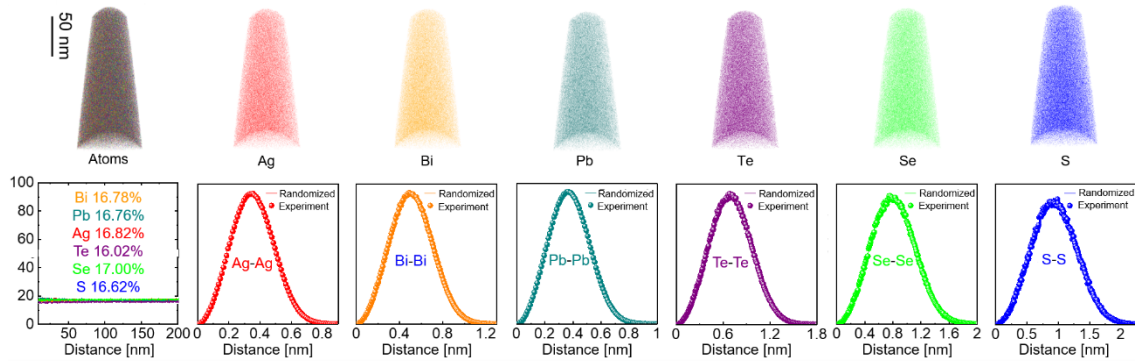


Figure 6.9 | 3D APT detection including ionic mass spectrum, 3D atomic maps, and nearest-neighbor atomic distribution histograms of the elements for BiPbAgTeSeS.

TEM was further employed to verify the atomic-level microstructural characteristics, and the corresponding high-resolution atomic image in Figure 6.10 reveals that all alloyed materials possess single-phase structures with random atomic distribution within the analyzed region. The selected area electron diffraction (SAED) pattern of BiPbAgTe₃ exhibits a significant difference compared to the others, suggesting an ordered arrangement and doubled unit cells. This is likely due to the larger lattice constant of BiPbAgTe₃ (~ 6.26 Å, Table 6.1). The increased spacing in the crystal lattice might allow Ag atoms to occupy interstitial sites, leading to a superlattice structure. Conversely, the smaller lattice constants of BiPbAgS₃ (~ 5.75 Å) and BiPbAgSe₃ (~ 5.94 Å) may make interstitial site occupation less energetically favorable, hindering superlattice formation.

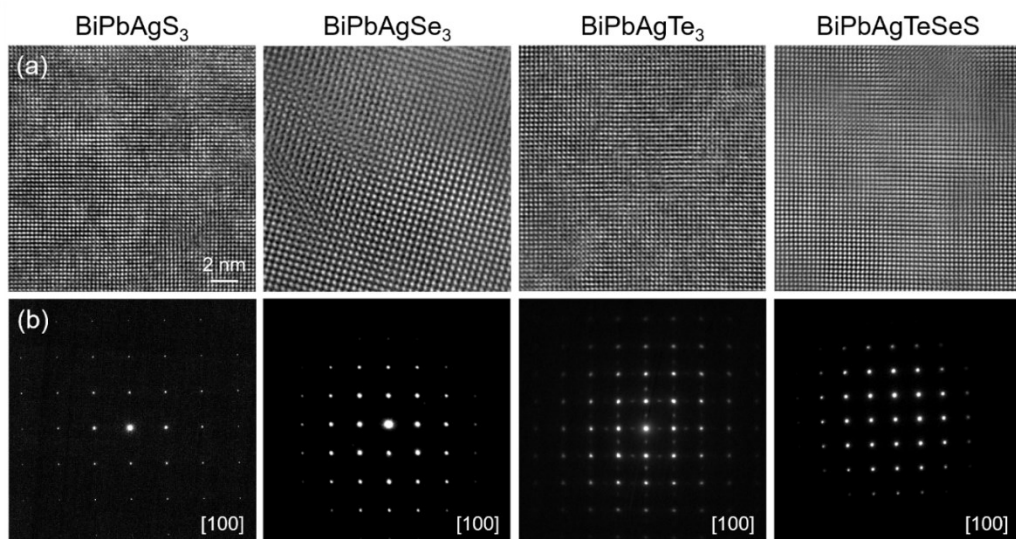


Figure 6.10 | (a) High-resolution TEM images. (b) Selected area electron diffraction patterns from [100] zone axes from (a) of the as-alloyed HEAs.

6.3 Chemical Bonding Mechanism of the Solid Solution

6.3.1 Confirmation of Metavalently Bonded Solid Solution

The above-mentioned analysis confirmed the formation of homogeneous HEAs across various length scales in $\text{BiPbAg}Q$ ($Q = \text{Te}_3, \text{Se}_3, \text{S}_3$, and TeSeS) samples. As discussed earlier, high solid solubility is a key requirement for constituting the high-entropy system. This section explores the potential reasons behind their high solid solubility in $\text{BiPbAg}Q$. Drawing on prior research and understanding of bonding types, we are now trying to prove that the ability of these systems to form HEAs is related to the dominant bonding character. Consistent with existing studies and the ET-ES map analysis, $\text{Pb}Q$ and $\text{AgBi}Q_2$ ($Q = \text{Te}, \text{Se}, \text{S}$) are identified as metavalently bonded compounds.^{78,84,84,212,213,279,300,340–343} Notably, phases with metavalent bonding have been shown to exhibit increased dopant solubility.²⁶⁷ This raises a crucial question: does the MVB character persist in the high-entropy solid solution formed by alloying $\text{Pb}Q$ and $\text{AgBi}Q_2$?

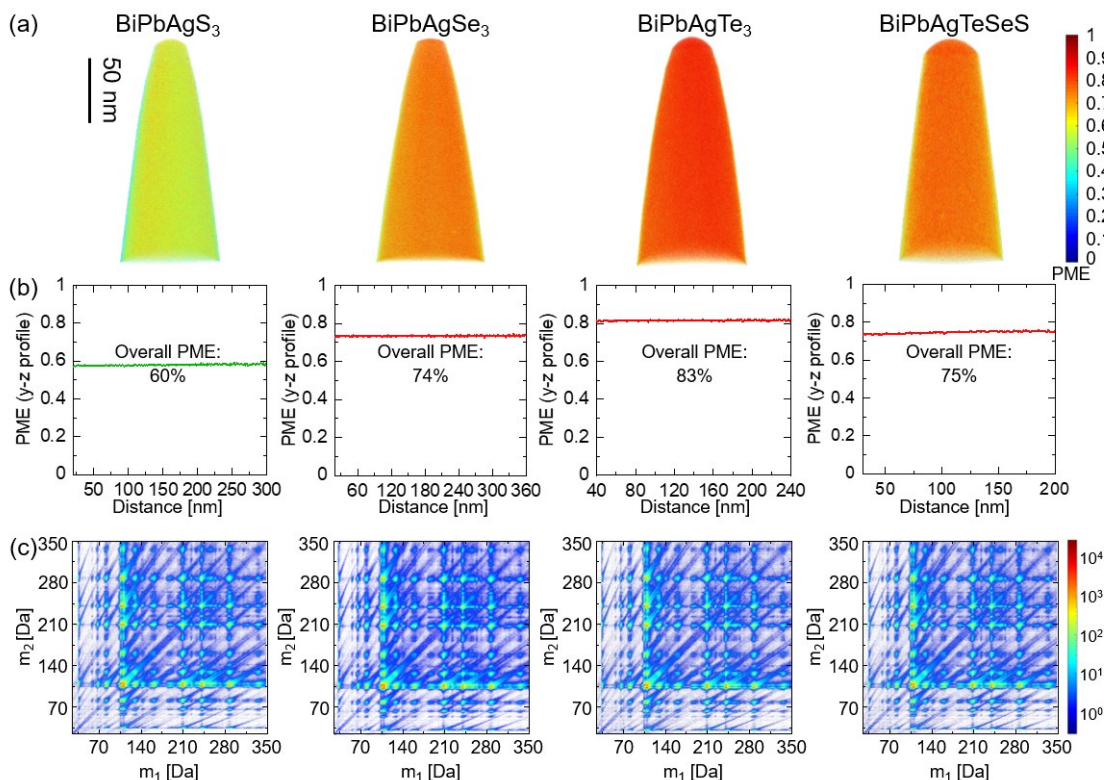


Figure 6.11 | (a) 3D PME distributions. (b) 2D PME along the y - z direction. (c) Correlation histogram of the as-synthesized HEAs samples.

To further investigate the bonding properties, APT was further analyzed in Figure 6.11 (a) and proved that all studied materials possess relatively high PME values of 60% ~ 83% as depicted in Figure 6.11 (b), which falls within the expected range for MVB materials. This observation strengthens the connection between the formation of high-entropy solid solutions with uniform composition and their dominant bonding character. Notably, all the constituent compounds, PbTe, PbSe, PbS, AgBiTe₂, AgBiSe₂, and AgBiS₂, are also recognized as MVB structures. Figure 6.11 (c) visualized the correlation histogram, illustrating that no obvious sign of preferential evaporation is observed for all compounds studied, although they show prominent thermal tails due to their low thermal conductivity.

6.3.2 Optical Properties of the Solid Solution

Raman spectroscopy is capable of reflecting distortions in a crystal structure. While a perfectly periodic cubic structure would not generate a Raman signal, otherwise Raman-active vibrational modes would be detectable. Based on the positions, shape and relative intensity of the Raman peaks in Figure 6.12, BiPbAgTe₃ has no clear measurable phonon mode and might therefore be expected to be almost perfectly cubic. All others seem to show comparatively weak modes at various wavenumbers, indicating that minor distortions are present. While the crystal structure of BiPbAgTeSeS exhibits less distortion compared to BiPbAgSe₃ and BiPbAgS₃, suggesting that BiPbAgTeSeS and BiPbAgTe₃ introduce less structural distortion within the lattice.

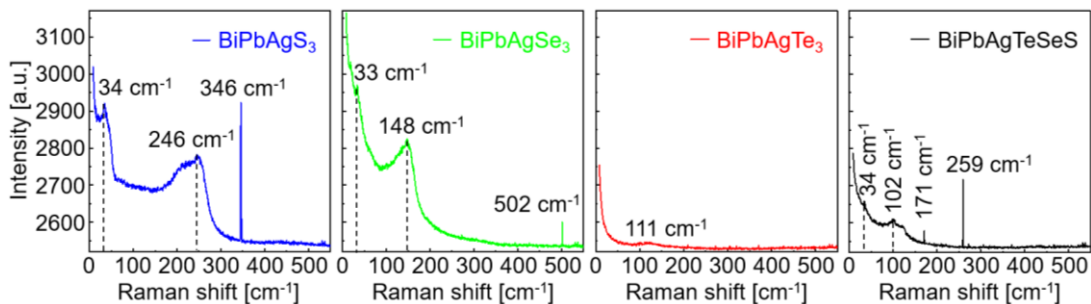


Figure 6.12 | Raman spectrum of the as-synthesized solid solutions.

Another effective method for studying bonding is FTIR, from which the optical dielectric constants can be extracted. Figure 6.13 presents ε_1 and ε_2 curves, with Figure 6.13 (b) highlighting the $\varepsilon_{2,\max}$ values. Since ε_1 and ε_2 are related by the Kramers-Kronig relations,

they provide equivalent information but with different emphases. $\varepsilon_{2,\max}$ increases with atomic number of Q for the samples $\text{BiPbAg}Q_3$ ($Q = \text{S, Se, and Te}$), coinciding with a gradual decrease in the charge transfer number estimated from the ET-ES map with 0.47 for $Q = \text{Se}$, 0.38 for $Q = \text{Se}$, and 0.26 for $Q = \text{Te}$. When the elements increase to six, the compounds exhibit the highest $\varepsilon_{2,\max}$ value, typically linked to small Peierls lattice distortion and charge transfer, for which a quantitative experimental technique is yet to be established. This limits a fully quantitative explanation for its exceptional light absorption coefficient.

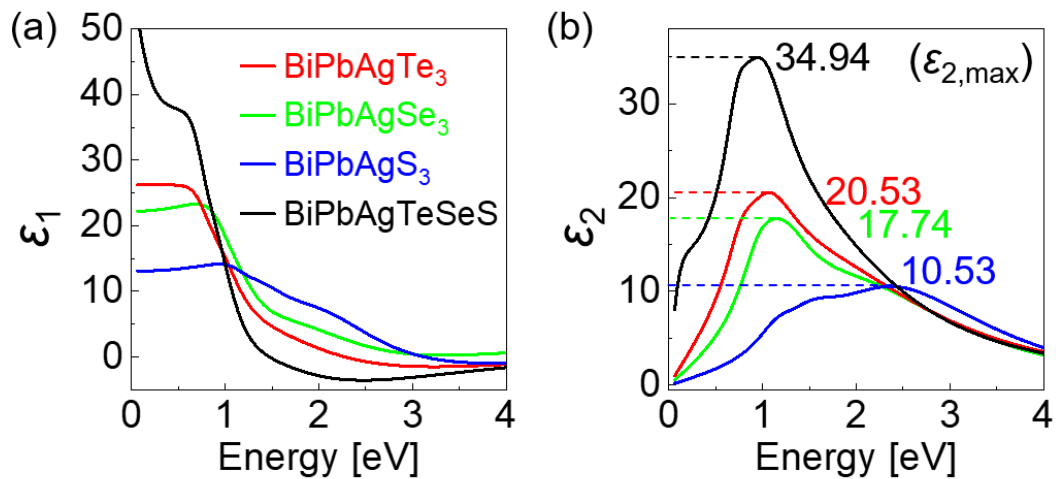


Figure 6.13 | Measured (a) real part and (b) imaginary part of the HE alloys.

6.4 Thermoelectric properties of $\text{BiPbAg}Q_3$

6.4.1 Electrical Transport and Band Structures of $\text{BiPbAg}Q_3$

BiPbAgTeSeS exhibits the highest electrical conductivity, while the conductivity of the remaining three samples gradually increases with the atomic number of element Q . The bipolar effect weakens from sulfide, selenide (onset around 670 K) to telluride (pronounced above 520 K), becoming negligible for BiPbAgTeSeS . BiPbAgS_3 exhibits increasing electrical conductivity with temperature in the range shown in Figure 6.14 (a). This behavior can be attributed to the bipolar effects due to the low carrier concentration ($8.1 \times 10^{18} \text{ cm}^{-3}$) and the small band gap ($\sim 0.21 \text{ eV}$) listed in Table 6.2, leading to a decrease in Seebeck coefficient with temperature. BiPbAgTe_3 demonstrates a similar trend of increasing σ with temperature. However, its exceptionally high carrier

concentration compared to other analogs minimizes the impact of thermally generated minority carriers on Seebeck coefficient at low temperatures. Consequently, the Seebeck coefficient initially increases with temperature. At approximately 600 K, intrinsic excitation becomes substantial, causing a decrease in S and a rapid, exponential rise in σ , which is also attributed to bipolar effect. BiPbAgSe_3 exhibits a larger band gap (~ 0.49 eV) and a higher carrier concentration ($6.08 \times 10^{19} \text{ cm}^{-3}$). Then intrinsic excitation plays a less prominent role at low temperatures. As temperature increases, phonon scattering intensifies, causing σ to decrease. However, at ~ 700 K, significant intrinsic excitation becomes evident, causing a rapid rise in σ accompanied by a decrease in S . BiPbAgTeSeS exhibits a non-monotonic temperature dependence in its electrical conductivity, marked by two inflection points. This behavior typically indicates a structural phase transition, but no obvious second phase was observed. This anomaly suggests a temperature-driven evolution in the compound's structure and atomic arrangement.

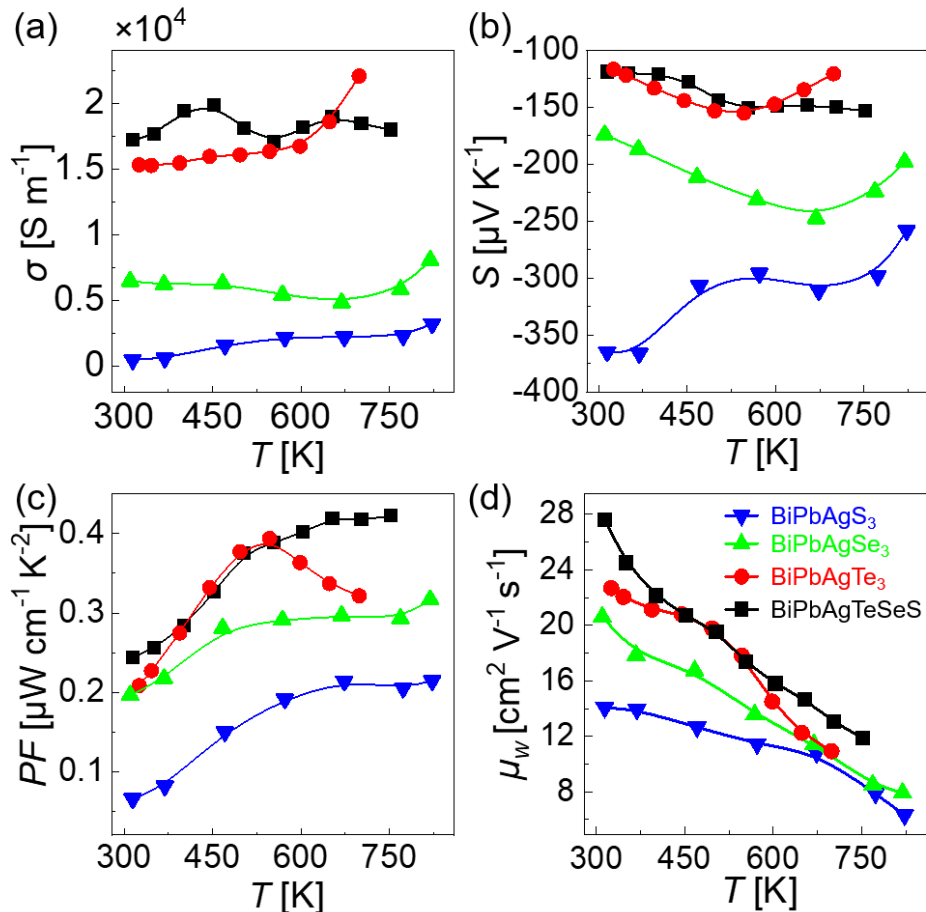


Figure 6.14 | Temperature-dependent electrical transport properties of the HE alloys. (a) Electrical conductivity (σ). (b) Seebeck coefficient (S). (c) Power factor (PF). (d) Weighted mobility (μ_w).

All samples exhibit negative Seebeck coefficients in Figure 6.14 (b), indicating that electrons are the majority carriers. BiPbAgS₃ exhibits a fluctuation *S* curve, potentially due to grain boundary scattering and intrinsic excitation within the material. The Seebeck coefficients of BiPbAgSe₃ and BiPbAgTe₃ witnessed sharp reduction near 670 K and 520 K respectively due to the bipolar effect, coinciding with the temperature range observed for the effect in Figure 6.14 (a). The *S* value of BiPbAgTeSeS is maintained around $-150 \mu\text{V K}^{-1}$ at 553 K \sim 752 K. The substantial enhancement in conductivity and the retained high Seebeck coefficient result in a *PF* of $0.4 \mu\text{W cm}^{-1} \text{K}^{-2}$ for BiPbAgTeSeS, compared to $0.2\text{--}0.3 \mu\text{W cm}^{-1} \text{K}^{-2}$ for the remaining three at this temperature point. Electrical performance is primarily governed by two key factors: carrier concentration and weighted mobility (μ_w). Hall measurements shown in Table 6.2 reveal that the BiPbAgTe₃ sample possesses the highest carrier concentration (n_h) at room temperature. However, μ_w incorporates the intrinsic capacity for carrier transport, reflected by the interplay between density-of-states effective mass and intrinsic mobility. With $\mu_w = \mu_0 \left(\frac{m_d^*}{m_e} \right)^{\frac{3}{2}}$, μ_w can well reflect the potential of materials to achieve high *PF*. BiPbAgTeSeS possesses the highest room-temperature weighted mobility (μ_w) exceeding $27 \text{ cm}^2 \text{ V}^{-1} \text{ s}^{-1}$, as listed in Table 6.2, whereas the μ_w values for the other three samples decrease as *Q* decreases. This superior performance stems from a favorable combination of BiPbAgTeSeS's intrinsically low density-of-states effective mass and exceptionally high Hall mobility, which together translate to superior electrical conductivity. As evident in Figure 6.15 (a), the power factors of the investigated compounds follow a universal curve consistent with the reference, when the Seebeck coefficient is varied. This suggests that the observed variations in *PF* among our four materials can be primarily attributed to differences in the electronic quality factor (*B_E*) or Fermi level (as indicated by *S*). And the measured *PF* of the other three samples, except for the BiPbAgS₃ sample, fall almost in the highest range. *B_E* which can be conveniently estimated from a single set of Seebeck coefficient and conductivity data, captures the combined influence of several parameters on $S^2\sigma$. These parameters include band structure (band degeneracy and effective mass), charge scattering mechanisms, and doping level (reflected by the Fermi level and influenced by elastic constants). Consistent with its high *B* factor observed in Figure 6.15 (b) across the measured temperature range, BiPbAgTeSeS exhibits superior electrical properties among the studied materials.

Table 6.2 | Hall carrier concentration, mobility, heat capacity, mass density and band gap of the HE samples measured or/and calculated at room temperature.

Composition	BiPbAgS ₃	BiPbAgSe ₃	BiPbAgTe ₃	BiPbAgTeSeS
Hall concentration [$\times 10^{19} \text{ cm}^{-3}$]	0.81	6.08	23.35	5.51
Hall mobility [$\text{cm}^2 \text{ V}^{-1} \text{ s}^{-1}$]	3.8	6.6	4.1	19.5
Weighted mobility [$\text{cm}^2 \text{ V}^{-1} \text{ s}^{-1}$]	14.07	20.62	22.68	27.58
$m_d^* (m_e)$	1.97	1.6	2.14	0.87
Heat capacity [$\text{J g}^{-1} \text{ K}^{-1}$]	0.241	0.197	0.165	0.196
Mass density [g cm^{-3}]	7.19	8.02	8.14	7.75
Goldsmid-Sharp	0.27	0.33	0.17	0.23
Band gap [eV]				
FTIR	0.212	0.489	0.114	0.283

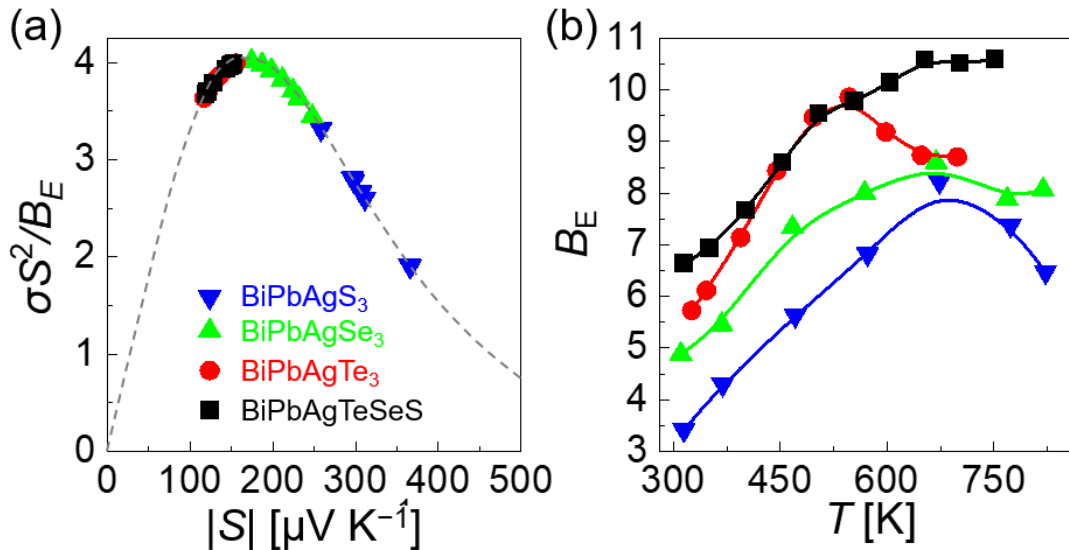


Figure 6.15 | (a) Scaled power factor versus Seebeck coefficient of the HE compounds. The source equation for the gray dashed curve in (a) is $\frac{S_r^2 \exp(2 \cdot S_r)}{1 + \exp[-5(S_r - 1)]} + \frac{S_r \pi^2 / 3}{1 + \exp[5(S_r - 1)]}$, with $S_r = \frac{|S|}{k_B/e}$.²¹⁷ (b) $B_{\text{electron}} (B_E)$.

The above analysis of electrical properties in BiPbAg Q_3 ($Q = \text{S, Se, and Te}$) reveals distinct trends for these materials compared to BiPbAgTeSeS. Despite sharing identical configurational entropy and compositional stoichiometry, the former three materials

exhibit a rule in their electrical properties likely influenced by variations in atomic number (Q). In contrast, BiPbAgTeSeS demonstrates a unique electrical behavior that deviates from the Q -dependent trend and exhibits superior performance. These observations suggest that high configurational entropy may not be the dominant factor governing electrical properties in this material system. To elucidate the underlying mechanisms, we can deconstruct these complex systems by analyzing the properties of their constituent binary analogs, PbTe, PbSe, and PbS. Figure 2.14 (b) reveals a clear trend: PbTe exhibits the highest PF , followed by PbSe and PbS. This aligns with the trend in Figure 6.13, where BiPbAgTe₃ demonstrates the smallest effective mass and narrowest band gap compared to BiPbAgSe₃ and BiPbAgS₃. Notably, the Fermi surface complexity factor, which encompasses the combined influence of band degeneracy, effective mass, and band gap, is also highest for PbTe. The electron transfer concept further supports the observed trends. According to the ET-ES map, PbTe exhibits the least charge transfer within the Pb Q (Q = Te, Se, and S) series. Similarly, AgBiTe₂ possesses the lowest ET value among AgBi Q ₂ (Q = Te, Se, and S) compounds. Combining them in pairs, ET should show a similar rule among BiPbAg Q ₃ (Q = S, Se, and Te), which is why as ET increases, the PF decreases with the decreased atomic number of Q in Figure 6.14 (d), and the corresponding $\varepsilon_{2,\max}$ values in Figure 6.13 are also getting smaller. It is worth noting that although the entropy of the BiPbAg Q ₃ (Q = S, Se, and Te) samples is exactly the same, the changes in electrical properties actually vary with the ET associated with their chemical bonding. As ET increases, enhanced charge transfer leads to a wider band gap and consequently, reduced mobility. This explains from the perspective of bonding why the telluride BiPbAgTe₃ exhibits a higher PF compared to the selenide and sulfide analogs, ultimately leading to its superior performance.

6.4.2 Thermal Conductivity and zT of BiPbAg Q ₃

Figure 6.16 presents the various thermal conductivity components (electrical, bipolar, lattice, and total) for the investigated samples. BiPbAgTeSeS exhibits the highest κ_{ele} (Figure 6.16 (a)) across 300 K to 670 K; the electrical conductivities of BiPbAgTe₃, BiPbAgSe₃, and BiPbAgS₃ progressively decrease. Notably, BiPbAgTeSeS also maintains a low lattice thermal conductivity (0.54 W m⁻¹ K⁻¹) at room temperature that further decreases to 0.28 W m⁻¹ K⁻¹ at 752 K, resulting in the lowest overall κ_{lat} among all samples shown in Figure 6.16 (b). BiPbAgTe₃ and BiPbAgSe₃ show comparable κ_{lat}

values. The highest κ_{lat} of BiPbAgS_3 can be attributed to the lighter mass of sulfur compared to the other elements (Se, Te). Despite the MVB-type bonding character shared by all samples, the sulfide exhibits a relatively stronger charge transfer, potentially contributing to its higher κ_{lat} .

Figure 6.16 (c) reveals a strong bipolar effect in BiPbAgTe_3 at temperatures exceeding 550 K, whereas the other three samples exhibit a weak bipolar effect only above 600 K. The sum of these three thermal conductivity components (electrical, lattice, and bipolar) constitutes the total thermal conductivity (κ_{tot}), presented in Figure 6.16 (d). BiPbAgTeSeS exhibits a room-temperature κ_{tot} of $\sim 0.64 \text{ W m}^{-1} \text{ K}^{-1}$, which steadily decreases to around $0.55 \text{ W m}^{-1} \text{ K}^{-1}$ at 750 K. The increase in κ_{tot} for BiPbAgTe_3 at 550 K is attributed to the bipolar effect, which is absent in the κ_{lat} curve. BiPbAgSe_3 possesses the lowest κ_{tot} across the entire temperature range investigated. BiPbAgS_3 displays a room-temperature κ_{tot} of $0.91 \text{ W m}^{-1} \text{ K}^{-1}$, decreasing to $0.63 \text{ W m}^{-1} \text{ K}^{-1}$ at 824 K.

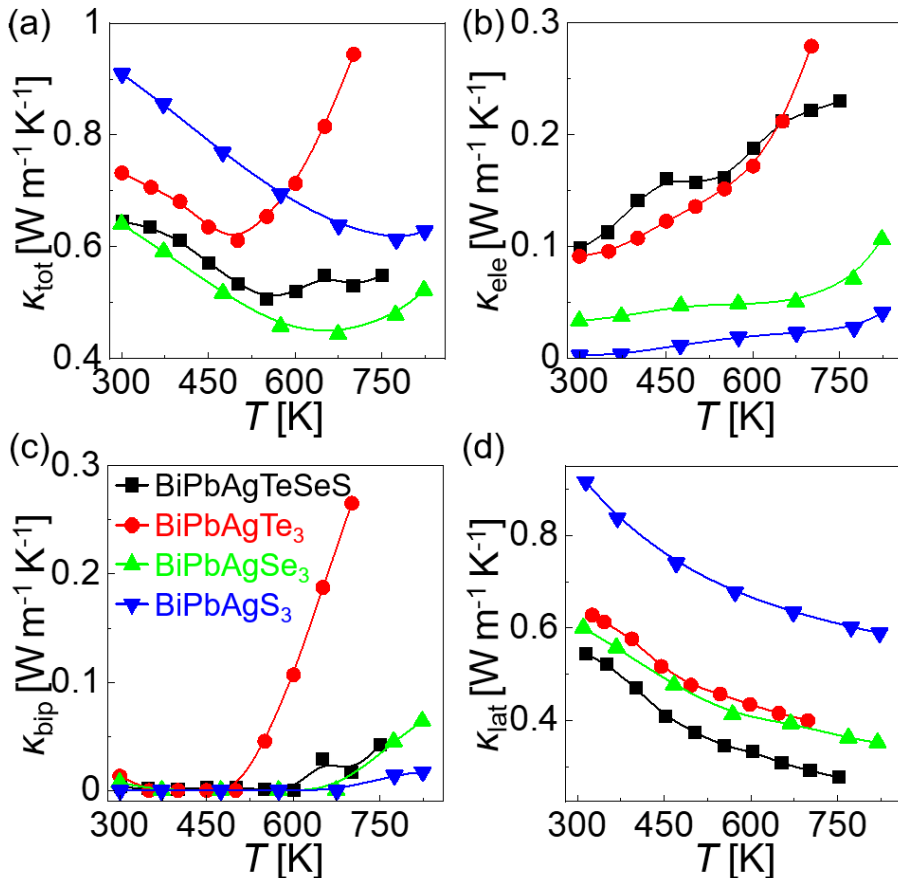


Figure 6.16 | (a) Total thermal conductivity (κ_{tot}), (b) Electrical thermal conductivity (κ_{ele}), (c) Bipolar thermal conductivity (κ_{bip}), and (d) Lattice thermal conductivity (κ_{lat}) of the as-made HE samples.

The soft chemical bonds and large anharmonicity can reduce κ_{lat} . According to Equation (2.30), the spring-ball model describes the phonon group velocity (v_{ph}) as approximately equal to $\frac{F}{M}$, where F is the force constant (characterizing chemical bond strength) and M is the atomic mass. Softer chemical bonds (smaller F) result in lower v_{ph} . In Figure 6.17 (a), as the chalcogenide element transitions from sulfur to selenium and tellurium, the $\text{BiPbAg}Q_3$ ($Q = \text{S, Se, and Te}$) series exhibits a trend of progressively softer chemical bonding, leading to decreasing v_{ph} . Furthermore, the mean free path of phonons ($l_{\text{ph}} = v_{\text{ph}}\tau_{\text{p}}$) as described in Equation (4.8) ranges from a few angstroms to hundreds of nanometers. In Figure 6.17 (b), BiPbAg has the lowest l_{ph} than the other three, which is consistent with the phenomenon that it has the lowest κ_{lat} .

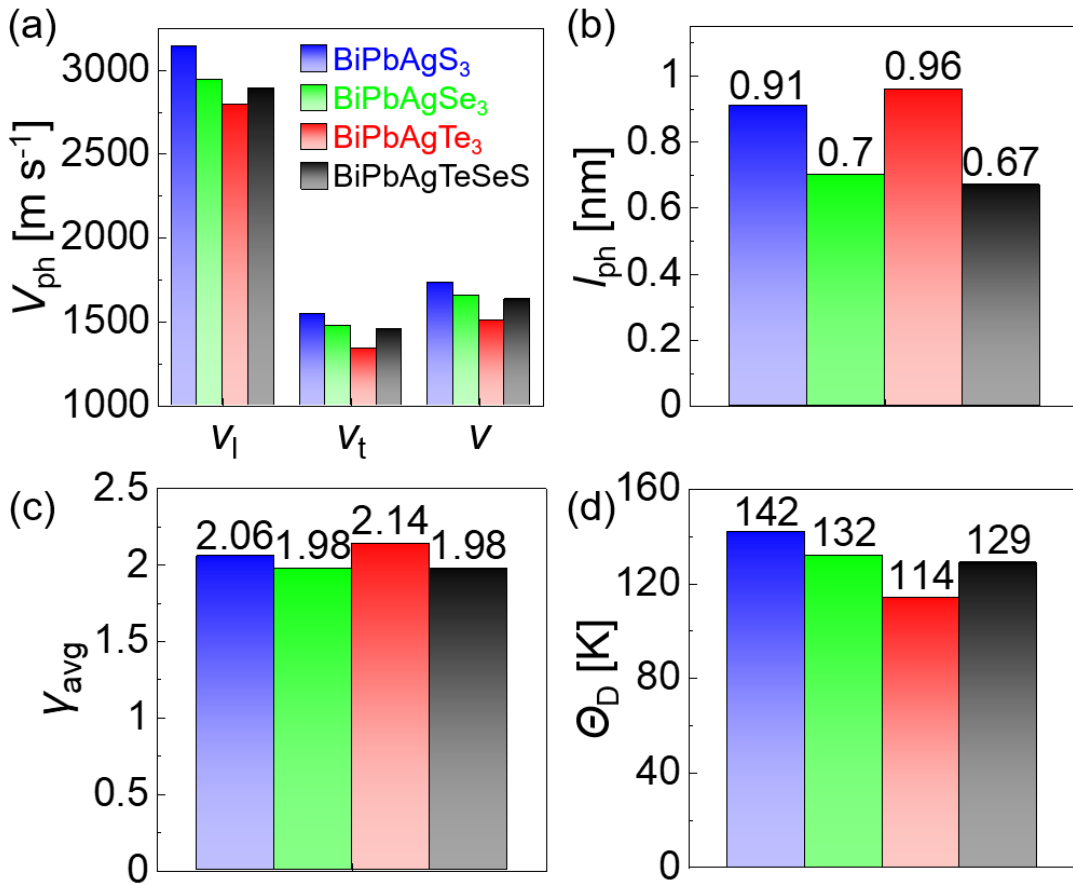


Figure 6.17 | (a) Sound velocities (v_{ph}), (b) Mean free path of phonons (l_{ph}), (c) Average Grüneisen parameter (γ_{avg}), and (d) Debye temperatures (Θ_{D}) of the HE samples.

Beyond extrinsic defects, the inherent material property of anharmonicity contributes to phonon-phonon scattering across the entire phonon spectrum. The Grüneisen parameter

serves as a common measure of anharmonicity, as explained in [Section 2.2](#). Notably, both the Debye temperature and the Grüneisen parameter are recognized as crucial factors in reducing thermal conductivity. [Figure 6.17 \(c\)](#) illustrates that the average Grüneisen parameter (γ_{avg}) for the investigated samples are all approximately 2, indicating a MVB-type bonding character due to the significant bonding anharmonicity. This large anharmonicity contributes to the inherently low κ_{lat} of metavalently bonded materials. Also the lowest κ_{lat} for the telluride sample due to its correspondingly lower Θ_D shown in [Figure 6.17 \(d\)](#) compared to the selenide and sulfide counterparts in the $\text{BiPbAg}Q_3$ ($Q = \text{S, Se, and Te}$) series.

[Figure 6.18 \(a\)](#) demonstrates that BiPbAgTeSeS exhibits superior thermoelectric performance due to its combined high power factor and low lattice thermal conductivity. BiPbAgTeSeS achieves a room-temperature zT value of 0.12, exceeding that of the other three investigated compounds, and it boasts a maximum zT of 0.58 at 752 K. This outstanding performance is corroborated by the highest average zT value (0.36) for BiPbAgTeSeS compared to the other samples in [Figure 6.18 \(b\)](#). Equation (4.10) establishes the quality factor (B factor) as a key metric to interpret the enhanced thermoelectric properties. B factor, proportional to the ratio of μ_w and κ_{lat} , serves as an indicator of the material's potential for achieving a high zT . Notably, the B factor is an intrinsic property with minimal dependence on doping concentration, although it does exhibit some temperature dependence.

[Figures 6.18 \(c~f\)](#) reveals a trend of increasing B factor with atomic number Q for the $\text{BiPbAg}Q_3$ samples: BiPbAgTe_3 exhibits a room-temperature B factor of 0.03, which is significantly higher than the 0.01 value observed for BiPbAgS_3 . Whereas BiPbAgTeSeS holds a higher value of 0.04. This trend aligns with the observed zT values. Telluride and selenide, with lower charge transfer compared to sulfide, generally achieve higher zT due to a more favorable balance between electrical conductivity and thermal conductivity. However, BiPbAgTe_3 's narrow band gap leads to a significant bipolar effect at higher temperatures (>550 K), causing its zT to decrease.

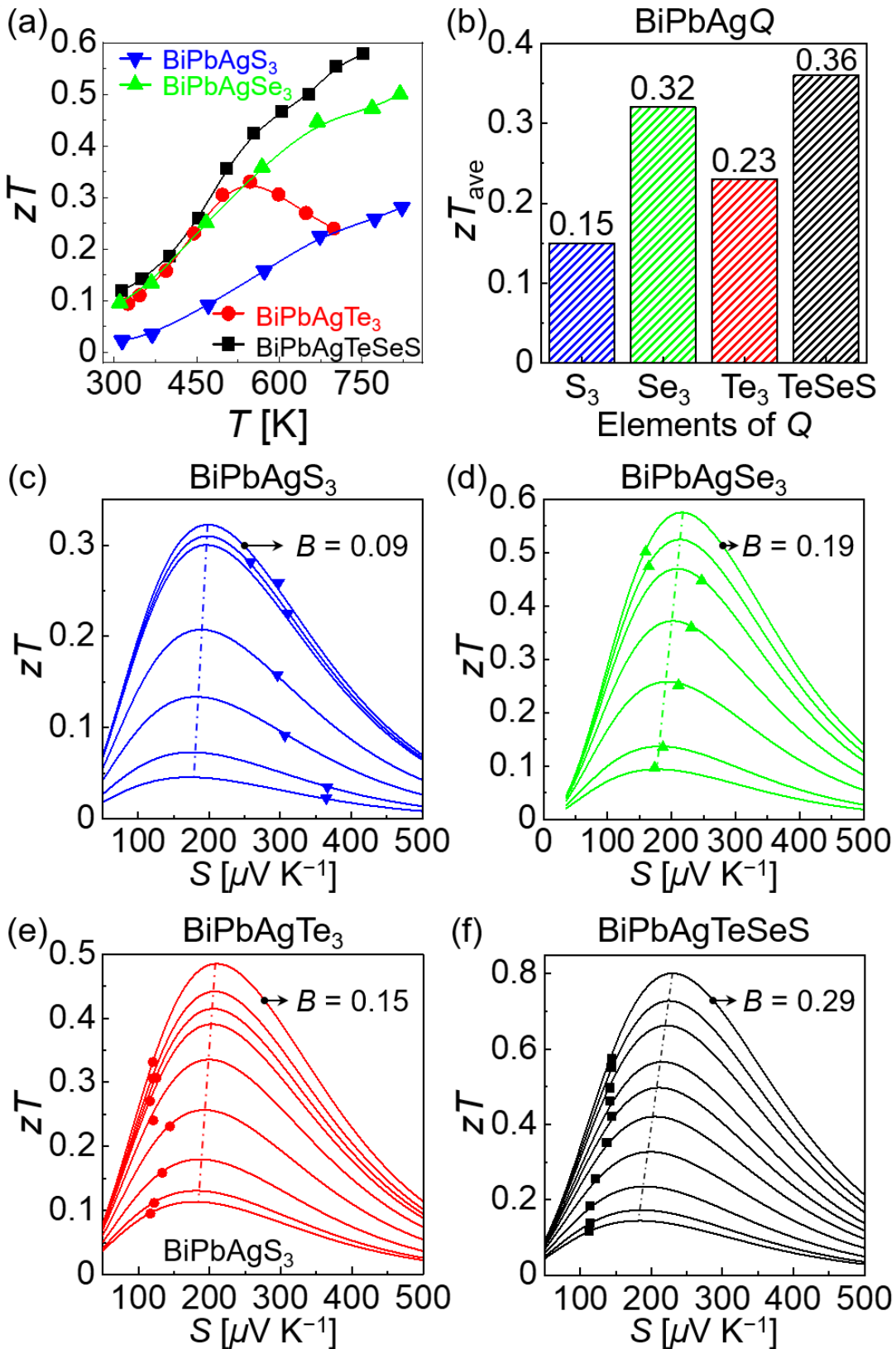


Figure 6.18 | (a) zT and (b) average zT of the HE samples. Maximum zT values as a function of the Fermi level (related to the Seebeck coefficient) and the quality factor (B) for (c) BiPbAgS_3 (d) BiPbAgSe_3 (e) BiPbAgTe_3 (f) BiPbAgTeSeS , respectively. The curve with the largest B factor is labeled in each figure.

6.5 Vickers Hardness of $\text{BiPbAg}Q_3$

Beyond thermoelectric performance, the mechanical properties of high-entropy alloys, including hardness, are crucial factors for practical applications. High entropy compounds generally exhibit high stiffness due to the solid-solution strengthening effect, which enhances device stability. In Figure 6.19, BiPbAgTeSeS possesses the highest Vickers hardness, approaching 159 HV. The remaining three samples display a sequential decrease in hardness: 156.1 HV for sulfide, 153.7 HV for selenide, and 138.5 HV for telluride.

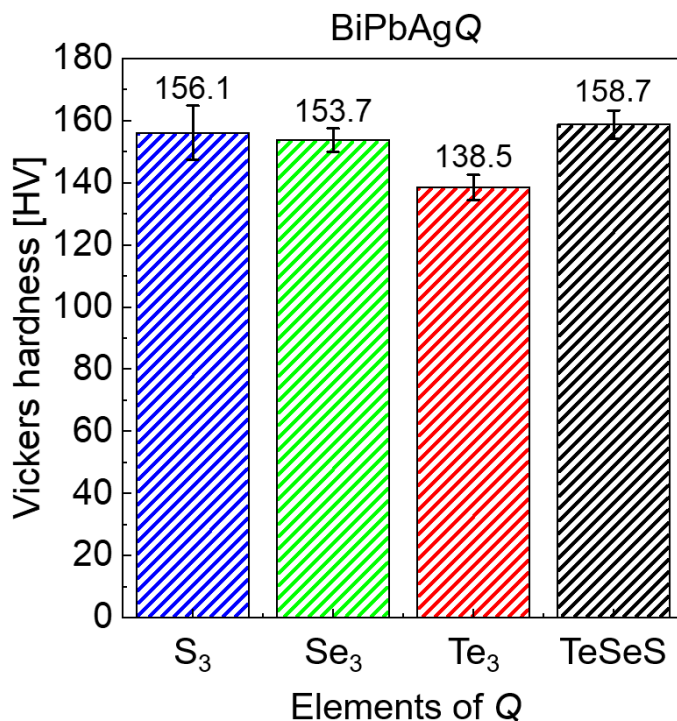


Figure 6.19 | Vickers hardness of the as-alloyed samples. The error bars indicate the standard deviation (STDEV) of the samples as 5.5, 2.2, 2.3 and 2.5, respectively.

6.6 Conclusions

This study explores how factors beyond the "high entropy effect," particularly chemical bonding, influence the thermoelectric properties of high-entropy alloys. *n*-type semiconductors $\text{BiPbAg}Q$ ($Q = \text{Te}_3, \text{Se}_3, \text{S}_3$, and TeSeS) with a rock salt structure were synthesized. XRD analysis and characterization techniques like EDX, EBSD, and APT confirmed the formation of a single cubic phase with a uniform elemental distribution.

Interestingly, BiPbAgTe_3 , BiPbAgSe_3 , and BiPbAgS_3 exhibit distinct electrical, thermal, and optical properties, yet these properties follow a systematic trend with variations in the atomic number of element Q . Notably, these property variations correlate with changes in the electron transferred parameter. BiPbAgTeSeS stands out from the other three by possessing superior electrical, thermal, and optical properties. Furthermore, BiPbAgTeSeS 's exceptionally high power factor and low lattice thermal conductivity translate to a remarkable zT value of approximately 0.6 at 752 K. This study establishes a crucial link between high entropy, chemical bonding (including the quantum parameter ET), and thermoelectric performance. Significantly, it demonstrates that high configuration entropy is not the sole determinant of thermoelectric efficiency, but rather the interplay between chemical bonding and electron transferred from one atom to its neighbors plays a critical role.

7 Conclusions and Outlooks

Inspired by the versatility of thermoelectirc materials and the metavalent bonding (MVB) mechanism employed, this thesis presents two research themes focusing on the exploration of MVB and its tailoring through disorder in a wider family of materials.

As a proof-of-principle study, we first demonstrated the relationship between MVB and classical Bi_2Te_3 -based thermoelectric properties. High-quality $\text{Bi}_x\text{Sb}_{2-x}\text{Te}_3$ ($x = 0.5, 0.6, 0.7$) single crystals were synthesized using the vertical Bridgman method to minimize defect-related effects on thermoelectric properties. Fourier-transform infrared spectroscopy and atom probe tomography confirmed the MVB character of the alloys, elucidating their optical properties and bond-breaking behavior, respectively. The interplay between metavalent bonding and the electronic band structure, characterized by large valley degeneracy, low band effective mass, and strong phonon anharmonicity, leads to favorable transport properties and finally high thermoelectric performance.

Building on the MVB-performance link in Bi_2Te_3 alloys, this work then explores strategies for navigating novel MVB-based thermoelectrics. SnSe, a budget-friendly thermoelectric material, shows high performance only in its high-symmetry phase for polycrystalline applications. This work tackles this challenge by stabilizing the high-symmetry rock-salt SnSe phase at lower temperatures using $\text{Ag}VVI_2$ ($V = \text{Sb}, \text{Bi}; VI = \text{Se}, \text{Te}$) dopants. Cubic SnSe exhibits MVB character, while the $Pnma$ phase relies on covalent bonding. Alloying-induced manipulation of the bonding mechanism (covalent to metavalent) stabilizes the high-symmetry cubic phase at lower temperatures. This approach leads to a tenfold enhancement in near-room-temperature zT for $Fm\bar{3}m$ SnSe alloys compared to pristine $Pnma$ SnSe. Notably, the cubic polycrystalline $(\text{SnSe})_{0.67}(\text{AgBiTe}_2)_{0.33}$ composition achieves a high zT of ~ 0.4 at 400 K, positioning SnSe-based alloys as promising candidates for near-room-temperature thermoelectrics.

High-entropy alloys are attracting interest as thermoelectrics, exemplified by the reported high-entropy-induced structural transformation in SnSe. This work finally investigates the interplay between MVB and the high-entropy effect in n -type polycrystalline $\text{BiPbAg}Q$ ($Q = \text{S}_3, \text{Se}_3, \text{Te}_3$, and TeSeS) alloys fabricated using spark plasma sintering.

Microstructure, bonding character, and thermoelectric properties were analyzed. Notably, the alloys exhibited no obvious phase separation, and atom probe tomography revealed unique bond-breaking behavior, indicative of MVB. Interestingly, maximum optical absorption decreased ($\text{BiPbAgTe}_3 > \text{BiPbAgSe}_3 > \text{BiPbAgS}_3$) with increasing charge transfer, implying a weakened MVB character. Consequently, thermoelectric properties also declined with increasing charge transfer (tellurides to sulfides). These findings underscore the potential of manipulating charge transfer for designing MVB-based high-entropy thermoelectrics.

Thus, it can be concluded here that unlike other bonding mechanisms (covalent, metallic, and ionic), metavalent bonding is a unique bonding mechanism that displays a distinct property portfolio. Such metavalent bonding is prevalent in a wide range of materials including chalcogenides. MVB is also sensitive to the degree of disorder, especially structural disorder. Understanding this novel bonding mechanism and its unique disorder dependence can open up new avenues for materials design. Since many properties are related to the strength of this bonding mechanism, disordered tailoring can provide recipes for applications as diverse as thermoelectric materials, phase change memories, and topological insulators.

References

1. Bahk, J.-H. & Shakouri, A. Enhancing the thermoelectric figure of merit through the reduction of bipolar thermal conductivity with heterostructure barriers. *Appl. Phys. Lett.* **105**, 052106 (2014).
2. Champier, D. Thermoelectric generators: A review of applications. *Energy Convers. Manag.* **140**, 167–181 (2017).
3. Jouhara, H. *et al.* Thermoelectric generator (TEG) technologies and applications. *Int. J. Thermofluids* **9**, 100063 (2021).
4. Mamur, H., Dilmaç, Ö. F., Begum, J. & Bhuiyan, M. R. A. Thermoelectric generators act as renewable energy sources. *Clean. Mater.* **2**, 100030 (2021).
5. Tohidi, F., Ghazanfari Holagh, S. & Chitsaz, A. Thermoelectric Generators: A comprehensive review of characteristics and applications. *Appl. Therm. Eng.* **201**, 117793 (2022).
6. Austin, I. G. The Optical Properties of Bismuth Telluride. *Proc. Phys. Soc.* **72**, 545 (1958).
7. Agarwal, A., Vashi, M. N., Lakshminarayana, D. & Batra, N. M. Electrical resistivity anisotropy in layered *p*-SnSe single crystals. *J. Mater. Sci. Mater. Electron.* **11**, 67–71 (2000).
8. Luo, Y. *et al.* High Thermoelectric Performance in the New Cubic Semiconductor AgSnSbSe_3 by High-Entropy Engineering. *J. Am. Chem. Soc.* **142**, 15187–15198 (2020).
9. Cagnoni, M., Führen, D. & Wuttig, M. Thermoelectric Performance of *IV–VI* Compounds with Octahedral-Like Coordination: A Chemical-Bonding Perspective.

Adv. Mater. **30**, 1801787 (2018).

10. Guarneri, L. *et al.* Metavalent Bonding in Crystalline Solids: How Does It Collapse? *Adv. Mater.* **33**, 2102356 (2021).

11. Dresselhaus, M. S. *et al.* New Directions for Low-Dimensional Thermoelectric Materials. *Adv. Mater.* **19**, 1043–1053 (2007).

12. Zhang, X. & Zhao, L.-D. Thermoelectric materials: Energy conversion between heat and electricity. *J. Materiomics* **1**, 92–105 (2015).

13. Bell, L. E. Cooling, Heating, Generating Power, and Recovering Waste Heat with Thermoelectric Systems. *Science* **321**, 1457–1461 (2008).

14. Ahsan, A. *Heat Analysis and Thermodynamic Effects*. (BoD – Books on Demand, 2011). doi:10.5772/1044.

15. Chen, R. *et al.* Towards the Carnot efficiency with a novel electrochemical heat engine based on the Carnot cycle: Thermodynamic considerations. *Energy* **284**, 128577 (2023).

16. He, J. & Tritt, T. M. Advances in thermoelectric materials research: Looking back and moving forward. *Science* **357**, eaak9997 (2017).

17. Vining, C. B. An inconvenient truth about thermoelectrics. *Nat. Mater.* **8**, 83–85 (2009).

18. Sommerfeld, A. Zur Elektronentheorie der Metalle auf Grund der Fermischen Statistik - I. Teil: Allgemeines, Strömungs- und Austrittsvorgänge. *Z. Für Phys.* **47**, 1–32 (1928).

19. Zannoni, A. & Fermi, E. On the Quantization of the Monoatomic Ideal Gas. (1999) doi:10.48550/arXiv.cond-mat/9912229.

20. Dirac, P. A. M. & Fowler, R. H. On the theory of quantum mechanics. *Proc. R. Soc. Lond. Ser. Contain. Pap. Math. Phys. Character* **112**, 661–677 (1997).

21. Liu, Y. *et al.* Large Enhancements of Thermopower and Carrier Mobility in Quantum Dot Engineered Bulk Semiconductors. *J. Am. Chem. Soc.* **135**, 7486–7495 (2013).
22. Yu, Y., Cagnoni, M., Cojocaru-Mirédin, O. & Wuttig, M. Chalcogenide Thermoelectrics Empowered by an Unconventional Bonding Mechanism. *Adv. Funct. Mater.* **30**, 1904862 (2020).
23. Zhang, Q. *et al.* Low effective mass and carrier concentration optimization for high performance *p*-type $Mg_{2(1-x)}Li_{2x}Si_{0.3}Sn_{0.7}$ solid solutions. *Phys. Chem. Chem. Phys.* **16**, 23576–23583 (2014).
24. Li, Y., Yi, Y., Coropceanu, V. & Brédas, J.-L. Optical conductivity and optical effective mass in a high-mobility organic semiconductor: Implications for the nature of charge transport. *Phys. Rev. B* **90**, 245112 (2014).
25. Yu, P. Y. & Cardona, M. Introduction. in *Fundamentals of Semiconductors: Physics and Materials Properties* (eds. Yu, P. Y. & Cardona, M.) 1–15 (Springer, Berlin, Heidelberg, 2010). doi:10.1007/978-3-642-00710-1_1.
26. May, A. F. & Snyder, G. J. Introduction to Modeling Thermoelectric Transport at High Temperatures. in *Materials, Preparation, and Characterization in Thermoelectrics* (CRC Press, 2012).
27. Snyder, G. J. & Toberer, E. S. Complex thermoelectric materials. in *Materials for Sustainable Energy* 101–110 (Co-Published with Macmillan Publishers Ltd, UK, 2010). doi:10.1142/9789814317665_0016.
28. Yuan, Z. *et al.* Entropy engineering enabled atomically dispersed Cu doping leading to an exceptionally high thermoelectric figure of merit in *n*-type lead chalcogenides. *Energy Environ. Sci.* **17**, 2921–2934 (2024).
29. Huang, Z.-Y. *et al.* Decorated dislocations lead to dynamically optimized thermoelectric performance in *n*-type PbTe. *Mater. Today Phys.* **37**, 101198 (2023).

30. Yu, Y. *et al.* Dynamic doping and Cottrell atmosphere optimize the thermoelectric performance of *n*-type PbTe over a broad temperature interval. *Nano Energy* **101**, 107576 (2022).
31. Goldsmid, H. J., Giutronich, J. E. & Kaila, M. M. Solar thermoelectric generation using bismuth telluride alloys. *Sol. Energy* **24**, 435–440 (1980).
32. Witting, I. T. *et al.* The Thermoelectric Properties of Bismuth Telluride. *Adv. Electron. Mater.* **5**, 1800904 (2019).
33. Zhu, T. *et al.* Compromise and Synergy in High-Efficiency Thermoelectric Materials. *Adv. Mater.* **29**, 1605884 (2017).
34. Rowe, D. M. & Min, G. An alpha-In sigma plot as a thermoelectric material performance indicator. *J. Mater. Sci. Lett.* **14**, 617–619 (1995).
35. Snyder, G. J., Pereyra, A. & Gurunathan, R. Effective Mass from Seebeck Coefficient. *Adv. Funct. Mater.* **32**, 2112772 (2022).
36. Dutta, M., Ghosh, T. & Biswas, K. Electronic structure modulation strategies in high-performance thermoelectrics. *APL Mater.* **8**, 040910 (2020).
37. Li, A. *et al.* Demonstration of valley anisotropy utilized to enhance the thermoelectric power factor. *Nat. Commun.* **12**, 5408 (2021).
38. Pei, Y., Lalonde, A., Wang, H. & Snyder, J. Low effective mass leading to high thermoelectric performance. *Energy Env. Sci* **5**, (2011).
39. Ravich, Iu. I. *Semiconducting Lead Chalcogenides*. (Springer Science & Business Media, 2013).
40. Zhao, L. *et al.* Improvement of thermoelectric properties and their correlations with electron effective mass in Cu_{1.98}S_xSe_{1-x}. *Sci. Rep.* **7**, 40436 (2017).
41. Kutorasinski, K., Wiendlocha, B., Kaprzyk, S. & Tobola, J. Electronic structure and thermoelectric properties of *n*- and *p*-type SnSe from first-principles calculations. *Phys.*

Rev. B Condens. Matter **91**, 205201 (2015).

42. Mehdizadeh Dehkordi, A., Zebarjadi, M., He, J. & Tritt, T. M. Thermoelectric power factor: Enhancement mechanisms and strategies for higher performance thermoelectric materials. *Mater. Sci. Eng. R Rep.* **97**, 1–22 (2015).

43. Gibbs, Z. M. Band Engineering in Thermoelectric Materials Using Optical, Electronic, and Ab-Initio Computed Properties. (California Institute of Technology, 2015). doi:10.7907/Z9XS5S9Z.

44. Fu, C. *et al.* High Band Degeneracy Contributes to High Thermoelectric Performance in *p*-Type Half-Heusler Compounds. *Adv. Energy Mater.* **4**, 1400600 (2014).

45. Feng, Z. *et al.* Thermoelectric optimization of AgBiSe₂ by defect engineering for room-temperature applications. *Phys. Rev. B* **99**, 155203 (2019).

46. Gibbs, Z. M. *et al.* Effective mass and Fermi surface complexity factor from ab initio band structure calculations. *Npj Comput. Mater.* **3**, 1–7 (2017).

47. Graziosi, P. & Neophytou, N. Ultra-High Thermoelectric Power Factors in Narrow Gap Materials with Asymmetric Bands. *J. Phys. Chem. C* **124**, 18462–18473 (2020).

48. F, I., A. *Semiconductor Thermoelements, and Thermoelectric Cooling*. (Infosearch, ltd., London, 1957).

49. Tan, G., Zhao, L.-D. & Kanatzidis, M. G. Rationally Designing High-Performance Bulk Thermoelectric Materials. *Chem. Rev.* **116**, 12123–12149 (2016).

50. Xiao, Y. *et al.* Rationally optimized carrier effective mass and carrier density leads to high average *ZT* value in *n*-type PbSe. *J. Mater. Chem. A* **9**, 23011–23018 (2021).

51. Lyden, H. A. Measurement of the Conductivity Effective Mass in Semiconductors Using Infrared Reflection. *Phys. Rev.* **134**, A1106–A1112 (1964).

52. Mahan, G. D. Good Thermoelectrics. in *Solid State Physics* (eds. Ehrenreich, H. & Spaepen, F.) vol. 51 81–157 (Academic Press, 1998).

53. Goldsmid, H. J. *Thermoelectric Refrigeration*. (Plenum Press, New York, 1964).
54. Rowe, D. M. *CRC Handbook of Thermoelectrics*. (CRC Press, 2018).
55. Pei, Y., Wang, H. & Snyder, G. J. Band Engineering of Thermoelectric Materials. *Adv. Mater.* **24**, 6125–6135 (2012).
56. Sun, Y., Liu, Y., Li, R., Li, Y. & Bai, S. Strategies to Improve the Thermoelectric Figure of Merit in Thermoelectric Functional Materials. *Front. Chem.* **10**, (2022).
57. Guo, L. *et al.* Manipulating the phase transformation temperature to achieve cubic $\text{Cu}_5\text{FeS}_{4-x}\text{Se}_x$ and enhanced thermoelectric performance. *J. Mater. Chem. C* **8**, 17222–17228 (2020).
58. Gui, Y., Ye, L., Jin, C., Zhang, J. & Wang, Y. The nature of the high thermoelectric properties of CuInX_2 ($X = \text{S, Se}$ and Te): First-principles study. *Appl. Surf. Sci.* **458**, 564–571 (2018).
59. Zhang, J. *et al.* High-Performance Pseudocubic Thermoelectric Materials from Non-cubic Chalcopyrite Compounds. *Adv. Mater.* **26**, 3848–3853 (2014).
60. Nagayama, T. *et al.* Direct observation of double valence-band extrema and anisotropic effective masses of the thermoelectric material SnSe . *Jpn. J. Appl. Phys.* **57**, 010301 (2017).
61. Guo, R., Wang, X., Kuang, Y. & Huang, B. First-principles study of anisotropic thermoelectric transport properties of IV-VI semiconductor compounds SnSe and SnS . *Phys. Rev. B* **92**, 115202 (2015).
62. Ul Haq, B. *et al.* Exploring single-layered SnSe honeycomb polymorphs for optoelectronic and photovoltaic applications. *Phys. Rev. B* **97**, 075438 (2018).
63. Li, F., Wang, H., Huang, R., Chen, W. & Zhang, H. Recent Advances in SnSe Nanostructures beyond Thermoelectricity. *Adv. Funct. Mater.* **32**, 2200516 (2022).
64. Sun, Y. *et al.* Rocksalt SnS and SnSe : Native topological crystalline insulators. *Phys.*

Rev. B **88**, 235122 (2013).

65. Zeier, W. G. *et al.* Thinking Like a Chemist: Intuition in Thermoelectric Materials. *Angew. Chem. Int. Ed Engl.* **55**, 6826–6841 (2016).

66. Pei, Y. *et al.* Convergence of electronic bands for high performance bulk thermoelectrics. *Nature* **473**, 66–69 (2011).

67. Su, L. *et al.* Realizing high doping efficiency and thermoelectric performance in *n*-type SnSe polycrystals via bandgap engineering and vacancy compensation. *Mater. Today Phys.* **20**, 100452 (2021).

68. Kim, H.-S., Gibbs, Z. M., Tang, Y., Wang, H. & Snyder, G. J. Characterization of Lorenz number with Seebeck coefficient measurement. *APL Mater.* **3**, 041506 (2015).

69. Goldsmid, H. J. *Introduction to Thermoelectricity*. (Springer, Berlin ; Heidelberg, 2016). doi:10.1007/978-3-662-49256-7.

70. Tian, Z., Lee, S. & Chen, G. Comprehensive Review of Heat Transfer in Thermoelectric Materials and Devices. *Annu. Rev. Heat Transf.* **17**, (2014).

71. Schreiber, E., Anderson, O. L., Soga, N. & Bell, J. F. Elastic Constants and Their Measurement. *J. Appl. Mech.* **42**, 747–748 (1975).

72. Anderson, O. L. A simplified method for calculating the Debye temperature from elastic constants. *J. Phys. Chem. Solids* **24**, 909–917 (1963).

73. Wachter, P., Filzmoser, M. & Rebizant, J. Electronic and elastic properties of the light actinide tellurides. *Phys. B Condens. Matter* **293**, 199–223 (2001).

74. Gusev, Yu. V. The field theory of specific heat. *Russ. J. Math. Phys.* **23**, 56–76 (2016).

75. Callaway, J. Model for Lattice Thermal Conductivity at Low Temperatures. *Phys. Rev.* **113**, 1046–1051 (1959).

76. Goldsmid, H. J. & Penn, A. W. Boundary scattering of phonons in solid solutions. *Phys. Lett. A* **27**, 523–524 (1968).

77. Wuttig, M., Deringer, V. L., Gonze, X., Bichara, C. & Raty, J.-Y. Incipient Metals: Functional Materials with a Unique Bonding Mechanism. *Adv. Mater.* **30**, 1803777 (2018).

78. Cheng, Y., Wahl, S. & Wuttig, M. Metavalent Bonding in Solids: Characteristic Representatives, Their Properties, and Design Options. *Phys. Status Solidi RRL – Rapid Res. Lett.* **15**, 2000482 (2021).

79. Baranov, A. I. & Kohout, M. Electron localization and delocalization indices for solids. *J. Comput. Chem.* **32**, 2064–2076 (2011).

80. Wuttig, M. *et al.* Revisiting the Nature of Chemical Bonding in Chalcogenides to Explain and Design their Properties. *Adv. Mater.* **35**, 2208485 (2023).

81. Zhu, T., Hu, L., Zhao, X. & He, J. New Insights into Intrinsic Point Defects in V_2VI_3 Thermoelectric Materials. *Adv. Sci.* **3**, 1600004 (2016).

82. Zhu, H. *et al.* Manipulating lattice distortion to promote average thermoelectric power factor in metavalently bonded $AgBiSe_2$. *Acta Mater.* **259**, 119260 (2023).

83. Zhu, M. *et al.* Unique Bond Breaking in Crystalline Phase Change Materials and the Quest for Metavalent Bonding. *Adv. Mater.* **30**, 1706735 (2018).

84. Arora, R., Waghmare, U. V. & Rao, C. N. R. Metavalent Bonding Origins of Unusual Properties of Group IV Chalcogenides. *Adv. Mater.* **35**, 2208724 (2023).

85. Castro, H., Galvis, J. & Castro, S. Automated Setup for Van Der Pauw Hall Measurements. *IEEE Trans. Instrum. Meas.* **60**, 198–205 (2011).

86. Sun, L., Wang, J. & Bonaccorso, E. Conductivity of individual particles measured by a microscopic four-point-probe method. *Sci. Rep.* **3**, 1991 (2013).

87. Chang, C. & Zhao, L.-D. Anharmonicity and low thermal conductivity in thermoelectrics. *Mater. Today Phys.* **4**, 50–57 (2018).

88. Zhang, W. *et al.* Metavalent Bonding in Layered Phase-Change Memory Materials.

Adv. Sci. **10**, 2300901 (2023).

89. Cheng, Y. *et al.* Understanding the Structure and Properties of Sesqui-Chalcogenides (i.e., V_2VI_3 or Pn_2Ch_3 (Pn = Pnictogen, Ch = Chalcogen) Compounds) from a Bonding Perspective. *Adv. Mater.* **31**, 1904316 (2019).

90. Matsunaga, T. *et al.* Phase-change materials: Vibrational softening upon crystallization and its impact on thermal properties. *Adv. Funct. Mater.* **21**, 2232–2239 (2011).

91. Raty, J. Y. *et al.* Aging mechanisms in amorphous phase-change materials. *Nat. Commun.* **6**, 7467 (2015).

92. Heremans, J. P. The anharmonicity blacksmith. *Nat. Phys.* **11**, 990–991 (2015).

93. Morelli, D. T., Jovovic, V. & Heremans, J. P. Intrinsically Minimal Thermal Conductivity in Cubic $I-VI_2$ Semiconductors. *Phys. Rev. Lett.* **101**, 035901 (2008).

94. Madelung, O. *Semiconductors — Basic Data*. (Springer Science & Business Media, 2012).

95. Zevalkink, A. *et al.* A practical field guide to thermoelectrics: Fundamentals, synthesis, and characterization. *Appl. Phys. Rev.* **5**, (2018).

96. Edwards, A. H. *et al.* Electronic structure of intrinsic defects in crystalline germanium telluride. *Phys. Rev. B* **73**, 045210 (2006).

97. Wuttig, M. *et al.* The role of vacancies and local distortions in the design of new phase-change materials. *Nat. Mater.* **6**, 122–128 (2007).

98. Liu, W. *et al.* Convergence of Conduction Bands as a Means of Enhancing Thermoelectric Performance of n -Type $Mg_2Si_{1-x}Sn_x$ Solid Solutions. *Phys. Rev. Lett.* **108**, 166601 (2012).

99. Shportko, K. *et al.* Resonant bonding in crystalline phase-change materials. *Nat. Mater.* **7**, 653–658 (2008).

100. Lee, S. *et al.* Resonant bonding leads to low lattice thermal conductivity. *Nat. Commun.* **5**, (2014).

101. Wang, H., Pei, Y., LaLonde, A. D. & Snyder, G. J. Heavily Doped *p*-Type PbSe with High Thermoelectric Performance: An Alternative for PbTe. *Adv. Mater. Deerfield Beach Fla* **23**, 1366–1370 (2011).

102. Zhang, Y., Ke, X., Kent, P. R. C., Yang, J. & Chen, C. Anomalous Lattice Dynamics near the Ferroelectric Instability in PbTe. *Phys. Rev. Lett.* **107**, 175503 (2011).

103. Tauber, R. N., Machonis, A. A. & Cadoff, I. B. Thermal and Optical Energy Gaps in PbTe. *J. Appl. Phys.* **37**, 4855–4860 (1966).

104. Božin, E. S. *et al.* Entropically Stabilized Local Dipole Formation in Lead Chalcogenides. *Science* **330**, 1660–1663 (2010).

105. Wei, S.-H. & Zunger, A. Electronic and structural anomalies in lead chalcogenides. *Phys. Rev. B* **55**, 13605–13610 (1997).

106. Tang, J. *et al.* Manipulation of Band Structure and Interstitial Defects for Improving Thermoelectric SnTe. *Adv. Funct. Mater.* **28**, 1803586 (2018).

107. Wu, H. *et al.* Synergistically optimized electrical and thermal transport properties of SnTe via alloying high-solubility MnTe. *Energy Environ. Sci.* **8**, 3298–3312 (2015).

108. Wu, D. *et al.* Origin of the High Performance in GeTe-Based Thermoelectric Materials upon Bi₂Te₃ Doping. *J. Am. Chem. Soc.* **136**, 11412–11419 (2014).

109. Tan, G. *et al.* Non-equilibrium processing leads to record high thermoelectric figure of merit in PbTe–SrTe. *Nat. Commun.* **7**, 12167 (2016).

110. Li, W. *et al.* Promoting SnTe as an Eco-Friendly Solution for *p*-PbTe Thermoelectric via Band Convergence and Interstitial Defects. *Adv. Mater.* **29**, 1605887 (2017).

111. Tan, G. *et al.* Extraordinary role of Hg in enhancing the thermoelectric performance of *p*-type SnTe. *Energy Environ. Sci.* **8**, 267–277 (2015).

112. Guo, F. *et al.* Thermoelectric SnTe with Band Convergence, Dense Dislocations, and Interstitials through Sn Self-Compensation and Mn Alloying. *Small* **14**, 1802615 (2018).

113. Tan, G. *et al.* Codoping in SnTe: Enhancement of Thermoelectric Performance through Synergy of Resonance Levels and Band Convergence. *J. Am. Chem. Soc.* **137**, 5100–5112 (2015).

114. Pei, Y. *et al.* Integrating Band Structure Engineering with All-Scale Hierarchical Structuring for High Thermoelectric Performance in PbTe System. *Adv. Energy Mater.* **7**, 1601450 (2017).

115. Zhang, Q. *et al.* Enhancement of thermoelectric figure-of-merit by resonant states of aluminium doping in lead selenide. *Energy Environ. Sci.* **5**, 5246–5251 (2012).

116. Wang, L. *et al.* Manipulating Band Convergence and Resonant State in Thermoelectric Material SnTe by Mn–In Codoping. *ACS Energy Lett.* **2**, 1203–1207 (2017).

117. Wu, L. *et al.* Resonant level-induced high thermoelectric response in indium-doped GeTe. *NPG Asia Mater.* **9**, e343–e343 (2017).

118. Jaworski, C. M., Kulbachinskii, V. & Heremans, J. P. Resonant level formed by tin in Bi₂Te₃ and the enhancement of room-temperature thermoelectric power. *Phys. Rev. B* **80**, 233201 (2009).

119. P. Heremans, J., Wiendlocha, B. & M. Chamoire, A. Resonant levels in bulk thermoelectric semiconductors. *Energy Environ. Sci.* **5**, 5510–5530 (2012).

120. Heremans, J. P. *et al.* Enhancement of Thermoelectric Efficiency in PbTe by Distortion of the Electronic Density of States. *Science* **321**, 554–557 (2008).

121. Xiao, Y. *et al.* Realizing high performance *n*-type PbTe by synergistically optimizing effective mass and carrier mobility and suppressing bipolar thermal conductivity. *Energy Environ. Sci.* **11**, 2486–2495 (2018).
122. Zhou, C. *et al.* High-Performance *n*-Type PbSe–Cu₂Se Thermoelectrics through Conduction Band Engineering and Phonon Softening. *J. Am. Chem. Soc.* **140**, 15535–15545 (2018).
123. Parker, D. S., May, A. F. & Singh, D. J. Benefits of Carrier-Pocket Anisotropy to Thermoelectric Performance: The Case of *p*-Type AgBiSe₂. *Phys. Rev. Appl.* **3**, 064003 (2015).
124. Xin, J. *et al.* Valleytronics in thermoelectric materials. *Npj Quantum Mater.* **3**, 1–10 (2018).
125. Hong, M., Zou, J. & Chen, Z.-G. 4 - Synthesis of thermoelectric materials. in *Thermoelectricity and Advanced Thermoelectric Materials* (eds. Kumar, R. & Singh, R.) 73–103 (Woodhead Publishing, 2021). doi:10.1016/B978-0-12-819984-8.00010-2.
126. Wei, T.-R. *et al.* Distinct Impact of Alkali-Ion Doping on Electrical Transport Properties of Thermoelectric *p*-Type Polycrystalline SnSe. *J. Am. Chem. Soc.* **138**, 8875–8882 (2016).
127. Ge, Z.-H. *et al.* Boosting the Thermoelectric Performance of (Na,K)-Codoped Polycrystalline SnSe by Synergistic Tailoring of the Band Structure and Atomic-Scale Defect Phonon Scattering. *J. Am. Chem. Soc.* **139**, 9714–9720 (2017).
128. Xiao, Y. *et al.* Remarkable Roles of Cu to Synergistically Optimize Phonon and Carrier Transport in *n*-Type PbTe-Cu₂Te. *J. Am. Chem. Soc.* **139**, 18732–18738 (2017).
129. Chen, Z. *et al.* Lattice Dislocations Enhancing Thermoelectric PbTe in Addition to Band Convergence. *Adv. Mater.* **29**, 1606768 (2017).
130. Chen, Z. *et al.* Vacancy-induced dislocations within grains for high-performance

PbSe thermoelectrics. *Nat. Commun.* **8**, (2017).

131. Wu, H.-J. & Yen, W.-T. High thermoelectric performance in Cu-doped Bi_2Te_3 with carrier-type transition. *Acta Mater.* **157**, 33–41 (2018).

132. Zhao, L.-D., Chang, C., Tan, G. & Kanatzidis, M. G. SnSe: a remarkable new thermoelectric material. *Energy Environ. Sci.* **9**, 3044–3060 (2016).

133. Poudel, B. *et al.* High-Thermoelectric Performance of Nanostructured Bismuth Antimony Telluride Bulk Alloys. *Science* **320**, 634–638 (2008).

134. Suryanarayana, C., Ivanov, E. & Boldyrev, V. V. The science and technology of mechanical alloying. *Mater. Sci. Eng. A* **304–306**, 151–158 (2001).

135. Liu, W. *et al.* New insight into the material parameter B to understand the enhanced thermoelectric performance of $\text{Mg}_2\text{Sn}_{1-x}\text{Ge}_x\text{Sb}_y$. *Energy Environ. Sci.* **9**, 530–539 (2016).

136. Chen, S. *et al.* Effect of Hf Concentration on Thermoelectric Properties of Nanostructured N-Type Half-Heusler Materials $\text{Hf}_x\text{Zr}_{1-x}\text{NiSn}_{0.99}\text{Sb}_{0.01}$. *Adv. Energy Mater.* **3**, 1210–1214 (2013).

137. Yang, L., Chen, Z.-G., Dargusch, M. S. & Zou, J. High Performance Thermoelectric Materials: Progress and Their Applications. *Adv. Energy Mater.* **8**, (2018).

138. Wang, X. W. *et al.* Enhanced thermoelectric figure of merit in nanostructured *n*-type silicon germanium bulk alloy. *Appl. Phys. Lett.* **93**, (2008).

139. Hong, M., Chen, Z.-G., Pei, Y., Yang, L. & Zou, J. Limit of zT enhancement in rocksalt structured chalcogenides by band convergence. *Phys. Rev. B* **94**, 161201 (2016).

140. Xu, B. *et al.* Highly Porous Thermoelectric Nanocomposites with Low Thermal Conductivity and High Figure of Merit from Large-Scale Solution-Synthesized

Bi₂Te_{2.5}Se_{0.5} Hollow Nanostructures. *Angew. Chem. Int. Ed.* **56**, 3546–3551 (2017).

141. Xu, B. *et al.* Manipulating Band Structure through Reconstruction of Binary Metal Sulfide for High-Performance Thermoelectrics in Solution-Synthesized Nanostructured Bi₁₃S₁₈I₂. *Angew. Chem.* **130**, 2437–2442 (2018).

142. Shi, X. *et al.* High Thermoelectric Performance in *p*-type Polycrystalline Cd-doped SnSe Achieved by a Combination of Cation Vacancies and Localized Lattice Engineering. *Adv. Energy Mater.* **9**, 1803242 (2019).

143. Nicolosi, V., Chhowalla, M., Kanatzidis, M. G., Strano, M. S. & Coleman, J. N. Liquid Exfoliation of Layered Materials. *Science* **340**, 1226419 (2013).

144. Cai, X., Luo, Y., Liu, B. & Cheng, H.-M. Preparation of 2D material dispersions and their applications. *Chem. Soc. Rev.* **47**, 6224–6266 (2018).

145. Brazhkin, V. V. High-pressure synthesized materials: treasures and hints. *High Press. Res.* **27**, 333–351 (2007).

146. Yang, M. *et al.* High-pressure synthesis and thermoelectric performance of tellurium doped with bismuth. *J. Mater. Sci.* **52**, 10526–10532 (2017).

147. Bae, S., Lee, S., Sohn, H.-S. & Lee, H. S. Synthesis and characteristics of PbTe_{1-x}Se_x thin films formed via electrodeposition. *Met. Mater. Int.* **23**, 1056–1061 (2017).

148. Li, L., Xu, S. & Li, G. Epitaxial Growth and Thermoelectric Measurement of Bi₂Te₃/Sb Superlattice Nanowires. *Chin. J. Chem. Phys.* **29**, 365–368 (2016).

149. Kumar, P. & Miller, B. N. Lyapunov Spectra of Coulombic and Gravitational Periodic Systems. *Entropy* **19**, 238 (2017).

150. Lee, J., Kim, J., Moon, W., Berger, A. & Lee, J. Enhanced Seebeck Coefficients of Thermoelectric Bi₂Te₃ Nanowires as a Result of an Optimized Annealing Process. *J. Phys. Chem. C* **116**, 19512–19516 (2012).

151. An, C. J. *et al.* Foldable Thermoelectric Materials: Improvement of the Thermoelectric Performance of Directly Spun CNT Webs by Individual Control of Electrical and Thermal Conductivity. *ACS Appl. Mater. Interfaces* **8**, 22142–22150 (2016).

152. Lee, E. K. *et al.* Large Thermoelectric Figure-of-Merits from SiGe Nanowires by Simultaneously Measuring Electrical and Thermal Transport Properties. *Nano Lett.* **12**, 2918–2923 (2012).

153. Jin, M. *et al.* Single crystal growth of $\text{Sn}_{0.97}\text{Ag}_{0.03}\text{Se}$ by a novel horizontal Bridgman method and its thermoelectric properties. *J. Cryst. Growth* **460**, 112–116 (2017).

154. Krishna, A., Vijayan, N., Singh, B., Thukral, K. & Maurya, K. K. Crystalline perfection and mechanical investigations on vertical Bridgman grown Bismuth telluride (Bi_2Te_3) single crystals for thermoelectric applications. *Mater. Sci. Eng. A* **657**, 33–37 (2016).

155. Kim, K. H., Shim, S. H., Shim, K. B., Niihara, K. & Hojo, J. Microstructural and Thermoelectric Characteristics of Zinc Oxide-Based Thermoelectric Materials Fabricated Using a Spark Plasma Sintering Process. *J. Am. Ceram. Soc.* **88**, 628–632 (2005).

156. Omori, M. Sintering, consolidation, reaction and crystal growth by the spark plasma system (SPS). *Mater. Sci. Eng. A* **287**, 183–188 (2000).

157. Schwarzer, R. A., Field, D. P., Adams, B. L., Kumar, M. & Schwartz, A. J. Present State of Electron Backscatter Diffraction and Prospective Developments. in *Electron Backscatter Diffraction in Materials Science* (eds. Schwartz, A. J., Kumar, M., Adams, B. L. & Field, D. P.) 1–20 (Springer US, Boston, MA, 2009).
doi:10.1007/978-0-387-88136-2_1.

158. Day, A. P. Spherical Kikuchi Maps and Other Rarities. in *Electron Backscatter Diffraction in Materials Science* (eds. Schwartz, A. J., Kumar, M., Adams, B. L. & Field, D. P.) 65–80 (Springer US, Boston, MA, 2009). doi:10.1007/978-0-387-88136-2_5.

159. Winkelmann, A., Aizel, K. & Vos, M. Electron energy loss and diffraction of backscattered electrons from silicon. *New J. Phys.* **12**, 053001 (2010).

160. Wells, O. C. Comparison of different models for the generation of electron backscattering patterns in the scanning electron microscope. *Scanning* **21**, 368–371 (1999).

161. Matsukawa, T., Shimizu, R. & Hashimoto, H. Measurements of the energy distribution of backscattered kilovolt electrons with a spherical retarding-field energy analyser. *J. Phys. Appl. Phys.* **7**, 695 (1974).

162. Lloyd, G. E. Atomic number and crystallographic contrast images with the SEM: a review of backscattered electron techniques. *Mineral. Mag.* **51**, 3–19 (1987).

163. Yubero, F., Pauly, N., Dubus, A. & Tougaard, S. Test of validity of the *V*-type approach for electron trajectories in reflection electron energy loss spectroscopy. *Phys. Rev. B* **77**, 245405 (2008).

164. Winkelmann, A., Salvat-Pujol, F. & Werner, W. Monte Carlo Simulations for Applications in Electron Backscatter Diffraction. *Microsc. Microanal.* **19**, 738–739 (2013).

165. Zaafferer, S. & Elhami, N.-N. Theory and application of electron channelling contrast imaging under controlled diffraction conditions. *Acta Mater.* **75**, 20–50 (2014).

166. Reyntjens, S. & Puers, R. A review of focused ion beam applications in microsystem technology. *J. Micromechanics Microengineering* **11**, 287 (2001).

167. Utke, I., Moshkalev, S. & Russell, P. *Nanofabrication Using Focused Ion and*

Electron Beams: Principles and Applications. (Oxford University Press, 2012).

168. Gault, B., Moody, M. P., Cairney, J. M. & Ringer, S. P. *Atom Probe Microscopy*. (Springer Science & Business Media, 2012).

169. Tanner, D. B. Use of x-ray scattering functions in Kramers-Kronig analysis of reflectance. *Phys. Rev. B* **91**, 035123 (2015).

170. Potts, W. J. *Chemical Infrared Spectroscopy*. (New York, NY : Wiley, 1963).

171. Schubert, M. Infrared ellipsometry on semiconductor layer structures phonons, plasmons, and polaritons. *Springer Tracts Mod. Phys.* **209**, 1–190 (2005).

172. Cho, G. C., Kütt, W. & Kurz, H. Subpicosecond time-resolved coherent-phonon oscillations in GaAs. *Phys. Rev. Lett.* **65**, 764–766 (1990).

173. Einstein, A. Die Plancksche Theorie der Strahlung und die Theorie der spezifischen Wärme. *Ann. Phys.* **327**, 180–190 (1907).

174. Blöchl, P. E. Projector augmented-wave method. *Phys. Rev. B* **50**, 17953–17979 (1994).

175. Otero-de-la-Roza, A., Johnson, E. R. & Lúaña, V. Critic2: A program for real-space analysis of quantum chemical interactions in solids. *Comput. Phys. Commun.* **185**, 1007–1018 (2014).

176. Bader, R. F. W. & Stephens, M. E. Spatial localization of the electronic pair and number distributions in molecules. *J. Am. Chem. Soc.* **97**, 7391–7399 (1975).

177. Kresse, G. & Furthmüller, J. Efficient iterative schemes for ab initio total-energy calculations using a plane-wave basis set. *Phys. Rev. B* **54**, 11169–11186 (1996).

178. Perdew, J. P., Burke, K. & Ernzerhof, M. Generalized Gradient Approximation Made Simple. *Phys. Rev. Lett.* **77**, 3865–3868 (1996).

179. Perdew, J. P., Burke, K. & Wang, Y. Generalized gradient approximation for the exchange-correlation hole of a many-electron system. *Phys. Rev. B* **54**, 16533–16539

(1996).

180. Setyawan, W. & Curtarolo, S. High-throughput electronic band structure calculations: Challenges and tools. *Comput. Mater. Sci.* **49**, 299–312 (2010).

181. Wang, V., Xu, N., Liu, J.-C., Tang, G. & Geng, W.-T. VASPKIT: A user-friendly interface facilitating high-throughput computing and analysis using VASP code. *Comput. Phys. Commun.* **267**, 108033 (2021).

182. Kokalj, A. XCrySDen—a new program for displaying crystalline structures and electron densities. *J. Mol. Graph. Model.* **17**, 176–179 (1999).

183. Le, P. S. Thermoelectric Properties of Bismuth Telluride and its Alloys. *Nature* (1958).

184. Goldsmid, H. J. Recent Studies of Bismuth Telluride and Its Alloys. *J. Appl. Phys.* **32**, 2198–2202 (1961).

185. Yim, W. M. & Rosi, F. D. Compound tellurides and their alloys for peltier cooling—A review. *Solid-State Electron.* **15**, 1121–1140 (1972).

186. Goldsmid, H. J. & Douglas, R. W. The use of semiconductors in thermoelectric refrigeration. *Br. J. Appl. Phys.* **5**, 386 (1954).

187. Huang, B.-L. & Kaviany, M. *Ab initio* and molecular dynamics predictions for electron and phonon transport in bismuth telluride. *Phys. Rev. B* **77**, 125209 (2008).

188. Tritt, T. M. & Subramanian, M. A. Thermoelectric Materials, Phenomena, and Applications: A Bird’s Eye View. *MRS Bull.* **31**, 188–198 (2006).

189. Goldsmid, H. J. The Thermal Conductivity of Bismuth Telluride. *Proc. Phys. Soc. Sect. B* **69**, 203 (1956).

190. Goldsmid, H. J. The Electrical Conductivity and Thermoelectric Power of Bismuth Telluride. *Proc. Phys. Soc.* **71**, 633 (1958).

191. Dennis, J. H. Anisotropy of the Seebeck coefficients of bismuth telluride. *Adv.*

Energy Convers. **1**, 99–105 (1961).

192. Champness, C. H., Muir, W. B. & Chiang, P. T. Thermoelectric properties of *n*-type Bi_2Te_3 - Bi_2Se_3 alloys. *Can. J. Phys.* **45**, 3611–3626 (1967).

193. Hyun, D. B., Hwang, G. S., You, B. C., Oh, T. S. & Hwang, C. W. Thermoelectric properties of the *n*-type 85% Bi_2Te_3 -15% Bi_2Se_3 alloys doped with SbI_3 and CuBr . *J. Mater. Sci.* **33**, 5595–5600 (1998).

194. Miller, G. R. & Li, C.-Y. Evidence for the existence of antistructure defects in bismuth telluride by density measurements. *J. Phys. Chem. Solids* **26**, 173–177 (1965).

195. Horák, J., Čermák, K. & Koudelka, L. Energy formation of antisite defects in doped Sb_2Te_3 and Bi_2Te_3 crystals. *J. Phys. Chem. Solids* **47**, 805–809 (1986).

196. Navrátil, J., Starý, Z. & Plecháček, T. Thermoelectric properties of *p*-type antimony bismuth telluride alloys prepared by cold pressing. *Mater. Res. Bull.* **31**, 1559–1566 (1996).

197. Mishra, S. K., Satpathy, S. & Jepsen, O. Electronic structure and thermoelectric properties of bismuth telluride and bismuth selenide. *J. Phys. Condens. Matter* **9**, 461 (1997).

198. Kutasov, V. A., Luk'yanova, L. N., Konstantinov, P. P. & Alekseeva, G. T. Carrier mobility in nonstoichiometric *n*- $\text{Bi}_2\text{Te}_{3-x}\text{Se}_x$ solid solutions. *Phys. Solid State* **39**, 419–422 (1997).

199. Hu, L.-P. *et al.* Shifting up the optimum figure of merit of *p*-type bismuth telluride-based thermoelectric materials for power generation by suppressing intrinsic conduction. *NPG Asia Mater.* **6**, e88–e88 (2014).

200. Thonhauser, T., Jeon, G. S., Mahan, G. D. & Sofo, J. O. Stress-induced defects in Sb_2Te_3 . *Phys. Rev. B* **68**, 205207 (2003).

201. Hu, L., Zhu, T., Liu, X. & Zhao, X. Point Defect Engineering of High-

Performance Bismuth-Telluride-Based Thermoelectric Materials. *Adv. Funct. Mater.* **24**, 5211–5218 (2014).

202. Suh, J. *et al.* Simultaneous Enhancement of Electrical Conductivity and Thermopower of Bi_2Te_3 by Multifunctionality of Native Defects. *Adv. Mater.* **27**, 3681–3686 (2015).

203. Hu, L. P. *et al.* Improving thermoelectric properties of *n*-type bismuth–telluride-based alloys by deformation-induced lattice defects and texture enhancement. *Acta Mater.* **60**, 4431–4437 (2012).

204. Puneet, P. *et al.* Preferential Scattering by Interfacial Charged Defects for Enhanced Thermoelectric Performance in Few-layered *n*-type Bi_2Te_3 . *Sci. Rep.* **3**, 3212 (2013).

205. Liu, Y., Zhou, M. & He, J. Towards higher thermoelectric performance of Bi_2Te_3 via defect engineering. *Scr. Mater.* **111**, 39–43 (2016).

206. Kim, S. I. *et al.* Dense dislocation arrays embedded in grain boundaries for high-performance bulk thermoelectrics. *Science* **348**, 109–114 (2015).

207. Zheng, Y. *et al.* Mechanically Robust BiSbTe Alloys with Superior Thermoelectric Performance: A Case Study of Stable Hierarchical Nanostructured Thermoelectric Materials. *Adv. Energy Mater.* **5**, 1401391 (2015).

208. Zhao, L. D., Zhang, B.-P., Li, J.-F., Zhang, H. L. & Liu, W. S. Enhanced thermoelectric and mechanical properties in textured *n*-type Bi_2Te_3 prepared by spark plasma sintering. *Solid State Sci.* **10**, 651–658 (2008).

209. Li, J. *et al.* BiSbTe-Based Nanocomposites with High *ZT*: The Effect of SiC Nanodispersion on Thermoelectric Properties. *Adv. Funct. Mater.* **23**, 4317–4323 (2013).

210. Li, Y. Y. *et al.* Enhanced thermoelectric performance of $\text{Cu}_2\text{Se}/\text{Bi}_{0.4}\text{Sb}_{1.6}\text{Te}_3$

nanocomposites at elevated temperatures. *Appl. Phys. Lett.* **108**, 062104 (2016).

211. Hao, F. *et al.* High efficiency Bi₂Te₃-based materials and devices for thermoelectric power generation between 100 and 300 °C. *Energy Environ. Sci.* **9**, 3120–3127 (2016).

212. Raty, J.-Y. & Wuttig, M. The interplay between Peierls distortions and metavalent bonding in *IV–VI* compounds: comparing GeTe with related monochalcogenides. *J. Phys. Appl. Phys.* **53**, 234002 (2020).

213. Wu, R. *et al.* Strong charge carrier scattering at grain boundaries of PbTe caused by the collapse of metavalent bonding. *Nat. Commun.* **14**, 719 (2023).

214. Shahil, K. M. F., Hossain, M. Z., Teweldebrhan, D. & Balandin, A. A. Crystal symmetry breaking in few-quintuple Bi₂Te₃ films: Applications in nanometrology of topological insulators. *Appl. Phys. Lett.* **96**, 153103 (2010).

215. Geuser, F., Gault, B., Bostel, A. & Vurpillot, F. Correlated field evaporation as seen by atom probe tomography. *Surf. Sci.* **601**, (2007).

216. Saxe, D. W. Correlated ion analysis and the interpretation of atom probe mass spectra. *Ultramicroscopy* **111**, 473–479 (2011).

217. Snyder, G. J. *et al.* Weighted Mobility. *Adv. Mater.* **32**, 2001537 (2020).

218. Akhanda, M. S. *et al.* Thermomagnetic properties of Bi₂Te₃ single crystal in the temperature range from 55 K to 380 K. *Phys. Rev. Mater.* **5**, 015403 (2021).

219. Kang, S. D. & Snyder, G. J. Transport property analysis method for thermoelectric materials: material quality factor and the effective mass model. (2018) doi:10.48550/arXiv.1710.06896.

220. Zhang, X. *et al.* Electronic quality factor for thermoelectrics. *Sci. Adv.* **6**, eabc0726 (2020).

221. Yan, J. *et al.* Material descriptors for predicting thermoelectric performance. *Energy Environ. Sci.* **8**, 983–994 (2015).

222. Wang, H., Pei, Y., LaLonde, A. D. & Jeffery Snyder, G. Material Design Considerations Based on Thermoelectric Quality Factor. in *Thermoelectric Nanomaterials: Materials Design and Applications* (eds. Koumoto, K. & Mori, T.) 3–32 (Springer, Berlin, Heidelberg, 2013). doi:10.1007/978-3-642-37537-8_1.

223. Xiao, Y. *et al.* Band Sharpening and Band Alignment Enable High Quality Factor to Enhance Thermoelectric Performance in *n*-Type PbS. *J. Am. Chem. Soc.* **142**, 4051–4060 (2020).

224. Kang, S. D. & Snyder, G. J. Charge-transport model for conducting polymers. *Nat. Mater.* **16**, 252–257 (2017).

225. Shi, W. *et al.* Tin Selenide (SnSe): Growth, Properties, and Applications. *Adv. Sci.* **5**, 1700602 (2018).

226. Zhao, L.-D. *et al.* Ultralow thermal conductivity and high thermoelectric figure of merit in SnSe crystals. *nature* **508**, 373–377 (2014).

227. Chang, C. *et al.* 3D charge and 2D phonon transports leading to high out-of-plane *ZT* in *n*-type SnSe crystals. *Science* **360**, 778–783 (2018).

228. Chen, Z.-G., Shi, X., Zhao, L.-D. & Zou, J. High-performance SnSe thermoelectric materials: Progress and future challenge. *Prog. Mater. Sci.* **97**, 283–346 (2018).

229. Wei, P.-C. *et al.* The intrinsic thermal conductivity of SnSe. *Nature* **539**, E1–E2 (2016).

230. Li, Z. *et al.* Effect of film thickness and evaporation rate on co-evaporated SnSe thin films for photovoltaic applications. *RSC Adv.* **10**, 16749–16755 (2020).

231. Kang, M. *et al.* Photodetector Based on Multilayer SnSe₂ Field Effect Transistor. *J. Nanosci. Nanotechnol.* **18**, 4243–4247 (2018).

232. Davitt, F. *et al.* Crystallographically Controlled Synthesis of SnSe Nanowires:

Potential in Resistive Memory Devices. *Adv. Mater. Interfaces* **7**, 2000474 (2020).

233. Li, Z., Ding, J. & Mitlin, D. Tin and Tin Compounds for Sodium Ion Battery Anodes: Phase Transformations and Performance. *Acc. Chem. Res.* **48**, 1657–1665 (2015).

234. Shaji, N. *et al.* Tin selenide/N-doped carbon composite as a conversion and alloying type anode for sodium-ion batteries. *J. Alloys Compd.* **834**, 154304 (2020).

235. Wang, X. *et al.* Solution-Processed *p*-SnSe/*n*-SnSe₂ Hetero-Structure Layers for Ultrasensitive NO₂ Detection. *Chem. – Eur. J.* **26**, 3870–3876 (2020).

236. Li, J., Zhao, H., Lei, Y., Yang, Q. & Zheng, Z. Synthesis and Photocatalytic Properties of SnSe₂/Se Heterojunction Films. *Nano* **13**, 1850045 (2018).

237. Harish, S. & Sathyakam, P. U. A review of tin selenide-based electrodes for rechargeable batteries and supercapacitors. *J. Energy Storage* **52**, 104966 (2022).

238. Zhang, C. *et al.* Two-Dimensional Tin Selenide Nanostructures for Flexible All-Solid-State Supercapacitors. *ACS Nano* **8**, 3761–3770 (2014).

239. Chung, K.-M., Wamwangi, D., Woda, M., Wuttig, M. & Bensch, W. Investigation of SnSe, SnSe₂, and Sn₂Se₃ alloys for phase change memory applications. *J. Appl. Phys.* **103**, 083523 (2008).

240. Wang, D. *et al.* Thermoelectric transport properties of rock-salt SnSe: first-principles investigation. *J. Mater. Chem. C* **6**, 12016–12022 (2018).

241. Qin, B. *et al.* Power generation and thermoelectric cooling enabled by momentum and energy multiband alignments. *Science* **373**, 556–561 (2021).

242. Su, L. *et al.* High thermoelectric performance realized through manipulating layered phonon-electron decoupling. *Science* **375**, 1385–1389 (2022).

243. Liu, D. *et al.* Lattice plainification advances highly effective SnSe crystalline thermoelectrics. *Science* **380**, 841–846 (2023).

244. Jin, M. *et al.* Mechanical Property of SnSe Single Crystal Prepared *via* Vertical Bridgman Method. *J. Inorg. Mater.* **36**, 313 (2021).

245. Feng, D., Chen, Y.-X., Fu, L.-W., Li, J. & He, J.-Q. SnSe + Ag₂Se composite engineering with ball milling for enhanced thermoelectric performance. *Rare Met.* **37**, 333–342 (2018).

246. Chere, E. K. *et al.* Studies on thermoelectric figure of merit of Na-doped *p*-type polycrystalline SnSe. *J. Mater. Chem. A* **4**, 1848–1854 (2016).

247. Zhao, L.-D. *et al.* Ultrahigh power factor and thermoelectric performance in hole-doped single-crystal SnSe. *Science* **351**, 141–144 (2016).

248. Zhao, Q., Qin, B., Wang, D., Qiu, Y. & Zhao, L.-D. Realizing High Thermoelectric Performance in Polycrystalline SnSe via Silver Doping and Germanium Alloying. *ACS Appl. Energy Mater.* **3**, 2049–2054 (2020).

249. Wang, Y.-P. *et al.* Realizing high thermoelectric properties in *p*-type polycrystalline SnSe by inducing DOS distortion. *Rare Met.* **40**, 2819–2828 (2021).

250. Zhou, C. *et al.* Polycrystalline SnSe with a thermoelectric figure of merit greater than the single crystal. *Nat. Mater.* **20**, 1378–1384 (2021).

251. Lee, Y. K., Luo, Z., Cho, S. P., Kanatzidis, M. G. & Chung, I. Surface Oxide Removal for Polycrystalline SnSe Reveals Near-Single-Crystal Thermoelectric Performance. *Joule* **3**, 719–731 (2019).

252. Liu, Y. *et al.* Defect Engineering in Solution-Processed Polycrystalline SnSe Leads to High Thermoelectric Performance. *ACS Nano* **16**, 78–88 (2022).

253. Chen, C.-L., Wang, H., Chen, Y.-Y., Day, T. & Jeffrey Snyder, G. Thermoelectric properties of *p*-type polycrystalline SnSe doped with Ag. *J. Mater. Chem. A* **2**, 11171–11176 (2014).

254. Chandra, S. *et al.* Modular Nanostructures Facilitate Low Thermal Conductivity

and Ultra-High Thermoelectric Performance in *n*-Type SnSe. *Adv. Mater.* **34**, 2203725 (2022).

255. Qin, Y. *et al.* Grid-plainification enables medium-temperature PbSe thermoelectrics to cool better than Bi₂Te₃. *Science* **383**, 1204–1209 (2024).

256. Wang, Y. *et al.* Modulating structures to decouple thermoelectric transport leads to high performance in polycrystalline SnSe. *J. Mater. Chem. A* **12**, 144–152 (2024).

257. Biswas, K. *et al.* High-performance bulk thermoelectrics with all-scale hierarchical architectures. *Nature* **489**, 414–418 (2012).

258. Hong, M., Li, M., Wang, Y., Shi, X.-L. & Chen, Z.-G. Advances in Versatile GeTe Thermoelectrics from Materials to Devices. *Adv. Mater.* **35**, 2208272 (2023).

259. Wang, Y. *et al.* Enhanced thermoelectric performance in cubic form of SnSe stabilized through engineering alloying AgSbTe₂. *Acta Mater.* **227**, 117681 (2022).

260. Rehman, S. U. *et al.* Pressure induced structural and optical properties of cubic phase SnSe: An investigation for the infrared/mid-infrared optoelectronic devices. *J. Alloys Compd.* **695**, 194–201 (2017).

261. Mariano, A. N. & Chopra, K. L. Polymorphism in some IV-VI compounds induced by high pressure and thin-film epitaxial growth. *Appl. Phys. Lett.* **10**, 282–284 (1967).

262. Wang, Z. *et al.* Molecular Beam Epitaxy-Grown SnSe in the Rock-Salt Structure: An Artificial Topological Crystalline Insulator Material. *Adv. Mater.* **27**, 4150–4154 (2015).

263. Wang, H.-X. *et al.* Nontrivial thermoelectric behavior in cubic SnSe driven by spin-orbit coupling. *Nano Energy* **51**, 649–655 (2018).

264. Yu, Y., Cagnoni, M., Cojocaru-Mirédin, O. & Wuttig, M. Chalcogenide Thermoelectrics Empowered by an Unconventional Bonding Mechanism. *Adv. Funct.*

Mater. **30**, 1904862 (2020).

265. Arora, R., Waghmare, U. V. & Rao, C. N. R. Metavalent Bonding Origins of Unusual Properties of Group IV Chalcogenides. *Adv. Mater.* **35**, 2208724 (2023).

266. Sun, Y. *et al.* Chemical interactions that govern the structures of metals. *Proc. Natl. Acad. Sci.* **120**, e2218405120 (2023).

267. Hu, L. *et al.* In Situ Design of High-Performance Dual-Phase GeSe Thermoelectrics by Tailoring Chemical Bonds. *Adv. Funct. Mater.* **33**, 2214854 (2023).

268. Yu, Y. *et al.* Doping by Design: Enhanced Thermoelectric Performance of GeSe Alloys Through Metavalent Bonding. *Adv. Mater.* **35**, 2300893 (2023).

269. Yao, W. *et al.* Two-step phase manipulation by tailoring chemical bonds results in high-performance GeSe thermoelectrics. *The Innovation* **4**, 100522 (2023).

270. Sarkar, D. *et al.* Metavalent Bonding in GeSe Leads to High Thermoelectric Performance. *Angew. Chem. Int. Ed.* **60**, 10350–10358 (2021).

271. Yan, M. *et al.* Synergetic optimization of electronic and thermal transport for high-performance thermoelectric GeSe–AgSbTe₂ alloy. *J. Mater. Chem. A* **6**, 8215–8220 (2018).

272. Huang, Z. *et al.* High Thermoelectric Performance of New Rhombohedral Phase of GeSe stabilized through Alloying with AgSbSe₂. *Angew. Chem. Int. Ed.* **56**, 14113–14118 (2017).

273. Chandra, S., Arora, R., V. Waghmare, U. & Biswas, K. Modulation of the electronic structure and thermoelectric properties of orthorhombic and cubic SnSe by AgBiSe₂ alloying. *Chem. Sci.* **12**, 13074–13082 (2021).

274. Roychowdhury, S., Ghosh, T., Arora, R., Waghmare, U. V. & Biswas, K. Stabilizing *n*-Type Cubic GeSe by Entropy-Driven Alloying of AgBiSe₂: Ultralow Thermal Conductivity and Promising Thermoelectric Performance. *Angew. Chem. Int.*

Ed. **57**, 15167–15171 (2018).

275. Dutta, M., Pal, K., Etter, M., Waghmare, U. V. & Biswas, K. Emphensis in Cubic $(\text{SnSe})_{0.5}(\text{AgSbSe}_2)_{0.5}$: Dynamical Off-Centering of Anion Leads to Low Thermal Conductivity and High Thermoelectric Performance. *J. Am. Chem. Soc.* **143**, 16839–16848 (2021).

276. Sriv, T. *et al.* Optical phonons of $\text{SnSe}_{(1-x)}\text{S}_x$ layered semiconductor alloys. *Sci. Rep.* **10**, 11761 (2020).

277. Zeiger, H. J. *et al.* Theory for displacive excitation of coherent phonons. *Phys. Rev. B* **45**, 768–778 (1992).

278. Yu, Y., Cojocaru-Mirédin, O. & Wuttig, M. Atom Probe Tomography Advances Chalcogenide Phase-Change and Thermoelectric Materials. *Phys. Status Solidi A* **n/a**, 2300425.

279. Kooi, B. J. & Wuttig, M. Chalcogenides by Design: Functionality through Metavalent Bonding and Confinement. *Adv. Mater.* **32**, 1908302 (2020).

280. Schön, C.-F. *et al.* Classification of properties and their relation to chemical bonding: Essential steps toward the inverse design of functional materials. *Sci. Adv.* **8**, eade0828 (2022).

281. Bai, G. *et al.* Boron Strengthened GeTe-Based Alloys for Robust Thermoelectric Devices with High Output Power Density. *Adv. Energy Mater.* **11**, 2102012 (2021).

282. Lewis, G. N. The atom and the molecule. *J. Am. Chem. Soc.* **38**, 762–785 (1916).

283. Raty, J.-Y. *et al.* A Quantum-Mechanical Map for Bonding and Properties in Solids. *Adv. Mater.* **31**, 1806280 (2019).

284. Hong, M., Lyu, W., Wang, Y., Zou, J. & Chen, Z.-G. Establishing the Golden Range of Seebeck Coefficient for Maximizing Thermoelectric Performance. *J. Am. Chem. Soc.* **142**, 2672–2681 (2020).

285. Hu, C. *et al.* Intrinsic conductivity as an indicator for better thermoelectrics. *Energy Environ. Sci.* **16**, 5381–5394 (2023).

286. Yu, Y. *et al.* Simultaneous optimization of electrical and thermal transport properties of $\text{Bi}_{0.5}\text{Sb}_{1.5}\text{Te}_3$ thermoelectric alloy by twin boundary engineering. *Nano Energy* **37**, 203–213 (2017).

287. Lu, Q. *et al.* Unexpected Large Hole Effective Masses in SnSe Revealed by Angle-Resolved Photoemission Spectroscopy. *Phys. Rev. Lett.* **119**, 116401 (2017).

288. Liu, Z. *et al.* Lattice expansion enables interstitial doping to achieve a high average ZT in *n*-type PbS. *Interdiscip. Mater.* **2**, 161–170 (2023).

289. Luo, T. *et al.* Nb-Mediated Grain Growth and Grain-Boundary Engineering in Mg_3Sb_2 -Based Thermoelectric Materials. *Adv. Funct. Mater.* **31**, 2100258 (2021).

290. Peng, K. *et al.* Grain size optimization for high-performance polycrystalline SnSe thermoelectrics. *J. Mater. Chem. A* **5**, 14053–14060 (2017).

291. Yu, Y. & Wuttig, M. Metavalent bonding impacts charge carrier transport across grain boundaries. *Nano Res. Energy* **2**, e9120057 (2023).

292. Liu, Y. *et al.* The Importance of Surface Adsorbates in Solution-Processed Thermoelectric Materials: The Case of SnSe. *Adv. Mater.* **33**, 2106858 (2021).

293. Morozova, N. V., Korobeynikov, I. V., Miyajima, N. & Ovsyannikov, S. V. Giant Room-Temperature Power Factor in *p*-Type Thermoelectric SnSe under High Pressure. *Adv. Sci.* **9**, 2103720 (2022).

294. Liu, W., Kim, H. S., Jie, Q. & Ren, Z. Importance of high power factor in thermoelectric materials for power generation application: A perspective. *Scr. Mater.* **111**, 3–9 (2016).

295. Brod, M. K., Toriyama, M. Y. & Snyder, G. J. Orbital Chemistry That Leads to High Valley Degeneracy in PbTe. *Chem. Mater.* **32**, 9771–9779 (2020).

296. Goldsmid, H. J. & Sharp, J. W. Estimation of the thermal band gap of a semiconductor from seebeck measurements. *J. Electron. Mater.* **28**, 869–872 (1999).

297. Bai, S., Zhang, X. & Zhao, L.-D. Rethinking SnSe Thermoelectrics from Computational Materials Science. *Acc. Chem. Res.* **56**, 3065–3075 (2023).

298. Gurunathan, R., Hanus, R., Dylla, M., Katre, A. & Snyder, G. J. Analytical Models of Phonon–Point-Defect Scattering. *Phys. Rev. Appl.* **13**, 034011 (2020).

299. Dargusch, M. *et al.* In-Situ Observation of the Continuous Phase Transition in Determining the High Thermoelectric Performance of Polycrystalline $\text{Sn}_{0.98}\text{Se}$. *J. Phys. Chem. Lett.* **10**, 6512–6517 (2019).

300. Arora, R., Waghmare, U. & Rao, C. N. R. Metavalent Bonding in 2D Chalcogenides: Structural Origin and Chemical Mechanisms. *Angew. Chem. Int. Ed.* **63**, e202313852 (2024).

301. Xu, M. *et al.* Impact of Pressure on the Resonant Bonding in Chalcogenides. *J. Phys. Chem. C* **121**, 25447–25454 (2017).

302. George, E. P., Raabe, D. & Ritchie, R. O. High-entropy alloys. *Nat. Rev. Mater.* **4**, 515–534 (2019).

303. Miracle, D. B. & Senkov, O. N. A critical review of high entropy alloys and related concepts. *Acta Mater.* **122**, 448–511 (2017).

304. Jiang, B. *et al.* High-entropy-stabilized chalcogenides with high thermoelectric performance. *Science* **371**, 830–834 (2021).

305. Qiu, Y. *et al.* Realizing high thermoelectric performance in GeTe through decreasing the phase transition temperature via entropy engineering. *J. Mater. Chem. A* **7**, 26393–26401 (2019).

306. Dragoe, N. & Bérardan, D. Order emerging from disorder. *Science* **366**, 573–574 (2019).

307. Rost, C. M. *et al.* Entropy-stabilized oxides. *Nat. Commun.* **6**, 8485 (2015).

308. Yeh, J.-W. *et al.* Nanostructured High-Entropy Alloys with Multiple Principal Elements: Novel Alloy Design Concepts and Outcomes. *Adv. Eng. Mater.* **6**, 299–303 (2004).

309. Gludovatz, B. *et al.* A fracture-resistant high-entropy alloy for cryogenic applications. *Science* **345**, 1153–1158 (2014).

310. Li, Z., Pradeep, K. G., Deng, Y., Raabe, D. & Tasan, C. C. Metastable high-entropy dual-phase alloys overcome the strength–ductility trade-off. *Nature* **534**, 227–230 (2016).

311. Youssef, K. M., Zaddach, A. J., Niu, C., Irving, D. L. & Koch, C. C. A Novel Low-Density, High-Hardness, High-entropy Alloy with Close-packed Single-phase Nanocrystalline Structures. *Mater. Res. Lett.* **3**, 95–99 (2015).

312. Zhang, Y. *et al.* Microstructures and properties of high-entropy alloys. *Prog. Mater. Sci.* **61**, 1–93 (2014).

313. Shi, Y., Yang, B. & Liaw, P. K. Corrosion-Resistant High-Entropy Alloys: A Review. *Metals* **7**, 43 (2017).

314. Senkov, O. N., Wilks, G. B., Miracle, D. B., Chuang, C. P. & Liaw, P. K. Refractory high-entropy alloys. *Intermetallics* **18**, 1758–1765 (2010).

315. Oikawa, K. *et al.* Effect of magnetic field on martensitic transition of Ni₄₆Mn₄₁In₁₃ Heusler alloy. *Appl. Phys. Lett.* **88**, 122507 (2006).

316. Zhang, Y., Zuo, T., Cheng, Y. & Liaw, P. K. High-entropy Alloys with High Saturation Magnetization, Electrical Resistivity and Malleability. *Sci. Rep.* **3**, 1455 (2013).

317. Bérardan, D., Franger, S., Dragoe, D., Meena, A. K. & Dragoe, N. Colossal dielectric constant in high entropy oxides. *Phys. Status Solidi RRL – Rapid Res. Lett.*

10, 328–333 (2016).

318. Shafeie, S. *et al.* High-entropy alloys as high-temperature thermoelectric materials. *J. Appl. Phys.* **118**, 184905 (2015).

319. Wei, P.-C. *et al.* Thermodynamic Routes to Ultralow Thermal Conductivity and High Thermoelectric Performance. *Adv. Mater.* **32**, 1906457 (2020).

320. Dong, J. & Yan, Q. High entropy strategy on thermoelectric materials. *Mater. Lab* **2**, (2023).

321. Oses, C., Toher, C. & Curtarolo, S. High-entropy ceramics. *Nat. Rev. Mater.* **5**, 295–309 (2020).

322. Huang, J. *et al.* Exploring the relationship between lattice distortion and phase stability in a multi-principal element alloy system based on machine learning method. *Comput. Mater. Sci.* **221**, 112089 (2023).

323. Rao, Z. *et al.* Machine learning-enabled high-entropy alloy discovery. *Science* **378**, 78–85 (2022).

324. Chen, Z., Zhang, X. & Pei, Y. Manipulation of Phonon Transport in Thermoelectrics. *Adv. Mater.* **30**, 1705617 (2018).

325. Chen, Z., Zhang, X., Lin, S., Chen, L. & Pei, Y. Rationalizing phonon dispersion for lattice thermal conductivity of solids. *Natl. Sci. Rev.* **5**, 888–894 (2018).

326. Toberer, E. S., Zevalkink, A. & Snyder, G. J. Phonon engineering through crystal chemistry. *J. Mater. Chem.* **21**, 15843–15852 (2011).

327. Jiang, B. *et al.* High figure-of-merit and power generation in high-entropy GeTe-based thermoelectrics. *Science* **377**, 208–213 (2022).

328. *High-Entropy Materials, Ultra-Strong Molecules, and Nanoelectronics: Emerging Capabilities and Research Objectives: Proceedings of a Workshop.* (National Academies Press, Washington, D.C., 2019). doi:10.17226/25106.

329. Liu, R. *et al.* Entropy as a Gene-Like Performance Indicator Promoting Thermoelectric Materials. *Adv. Mater.* **29**, 1702712 (2017).

330. Hu, L. *et al.* Entropy Engineering of SnTe: Multi-Principal-Element Alloying Leading to Ultralow Lattice Thermal Conductivity and State-of-the-Art Thermoelectric Performance. *Adv. Energy Mater.* **8**, 1802116 (2018).

331. Tsai, M.-H. Three Strategies for the Design of Advanced High-Entropy Alloys. *Entropy* **18**, 252 (2016).

332. Tsai, M.-H. & Yeh, J.-W. High-Entropy Alloys: A Critical Review. *Mater. Res. Lett.* **2**, 107–123 (2014).

333. Korkosz, R. J. *et al.* High ZT in p-type $(\text{PbTe})_{1-2x}(\text{PbSe})_x(\text{PbS})_x$ thermoelectric materials. *J. Am. Chem. Soc.* **136**, 3225–3237 (2014).

334. Wang, X. *et al.* Enhanced Thermoelectric Performance in High Entropy Alloys $\text{Sn}_{0.25}\text{Pb}_{0.25}\text{Mn}_{0.25}\text{Ge}_{0.25}\text{Te}$. *ACS Appl. Mater. Interfaces* **13**, 18638–18647 (2021).

335. Lannoo, M. & Bourgoin, J. *Point Defects in Semiconductors I*. vol. 22 (Springer, Berlin, Heidelberg, 1981).

336. Tan, X. Y. *et al.* Enhanced near-room-temperature thermoelectric performance in GeTe. *Rare Met.* **41**, 3027–3034 (2022).

337. Roychowdhury, S. *et al.* Enhanced atomic ordering leads to high thermoelectric performance in AgSbTe_2 . *Science* **371**, 722–727 (2021).

338. Wang, H., Cao, X., Takagiwa, Y. & Snyder, G. J. Higher mobility in bulk semiconductors by separating the dopants from the charge-conducting band – a case study of thermoelectric PbSe. *Mater. Horiz.* **2**, 323–329 (2015).

339. Terasaki, I. 13 - Introduction to thermoelectricity. in *Materials for Energy Conversion Devices* (eds. Sorrell, C. C., Sugihara, S. & Nowotny, J.) 339–357 (Woodhead Publishing, 2005). doi:10.1533/9781845690915.3.339.

340. An, D. *et al.* Metavalently bonded tellurides: the essence of improved thermoelectric performance in elemental Te. *Nat. Commun.* **15**, 3177 (2024).

341. Maier, S. *et al.* Discovering Electron-Transfer-Driven Changes in Chemical Bonding in Lead Chalcogenides (Pb X , where X = Te, Se, S, O). *Adv. Mater.* **32**, 2005533 (2020).

342. Hassan Osman, H. H. & Javier Manjón, F. Metavalent bonding in chalcogenides: DFT-chemical pressure approach. *Phys. Chem. Chem. Phys.* **24**, 9936–9942 (2022).

343. Guo, Z. *et al.* Design of High-Performance Cubic n -Type AgBiSe₂ Guided by Metavalent Bonding Mechanism. *Adv. Funct. Mater.* **n/a**, 2315546.

Acknowledgments

I am sincerely grateful to all those who have provided invaluable support throughout the past four years. Their contributions significantly aided the completion of this thesis.

I express my profound gratitude to Prof. Matthias Wuttig for his unwavering guidance, and deeply appreciate his patience, encouragement, and insightful academic guidance throughout my doctoral studies. Prof. Wuttig's exemplary approach to research, characterized by rigor, diligence, and thoroughness, has inspired my scientific development. His genuine kindness and accessibility further solidify his role as a true "Vorbild" for aspiring researchers. I extend my heartfelt appreciation to Prof. Joachim Mayer for serving as my advisor, providing valuable reports, and offering prompt and great support, particularly during challenging periods. I am deeply grateful to Prof. Sebastian Münstermann for being my PhD defense chair. His mentorship and encouragement have been invaluable to me, and I am truly fortunate to have had the opportunity to work with him.

Special appreciation is also extended to Dr. Yuan Yu for his continuous guidance and stimulating discussions, which have significantly advanced my research endeavors. Additionally, I am indebted to Prof. Tanmoy Ghosh for his invaluable assistance in optical measurements and his patient mentorship regarding experimental procedures, coupled with insightful discussions that have enriched the depth of this work.

I'm genuinely obliged to our APT team members: Dr. Oana Cojocaru-Mirédin, Dr. Mohit Raghuvanshi, Dr. Jens Keutgen, Dr. Jacques Perrin Toinin, Dr. Stefan Maier, and Jan Köttgen for their fruitful discussions. Additionally, I am deeply thankful to Dr. Carl-Friedrich Schön, Dr. Dasol Kim, and Prof. Jean-Yves Raty for their expertise in performing DFT calculations and providing crucial theoretical support. Special thanks are due to Jonathan Frank, Felix Hoff, Thomas Schmidt, Maria Häser for their assistance with various aspects of the experimental work, as also reflected in our published manuscript.

I'm incredibly grateful to Yiming Zhou, Christian Stanz, and Lisa Schäfer for their guidance in deepening my understanding of thermoelectrics, crystallography and transport measurement. The assistance provided by Dr. Pengfei Cao from Forschungszentrum Jülich in TEM analysis was particularly instrumental in advancing

my research. I extend my sincere gratitude to Dr. Peter Keeres and Christoph Ringkamp for their timely and perceptive comments on my research.

I extend special appreciation to Werkzeugmaschinenlabor (WZL), Institut für Werkstoffanwendungen im Maschinenbau (IWM), Institute of Crystallography, and Institut für Metallkunde und Materialphysik (IMM) in RWTH Aachen for their invaluable and prompt assistance in measuring sample hardness, cutting bulk samples, valuable suggestions for crystal growth, and determining sample density and Laue diffraction of single crystals, respectively.

Truly thankful to Prof. Shuai Wei, Dr. Yudong Chen, Prof. Jiangjing Wang, Huaide Zhang, Alexander Kiehn, Christian Tahirib, Guanmin Li, and Hao Luo for generously sharing their expertise. The technical support from Stephan Hermes, Patrick Thelen, Oliver Lehmann, Svitlana Taranenko, and Michael Wlochal, along with the administrative assistance of Dr. Ralf Detemple, Renate Breuers, Sarah Schlenter, Mara Kallweit from Physikzentrum (I A Institut), and Marion Köster from Institute of Metal Forming (IBF) was more than indispensable. I'm grateful to all colleagues for their enthusiasm and support, including Senhao Zhang, Minghao Shen, Ramon Pfeiffer, Julian Mertens, Sumayya Waheed, Azam Karami, Timo Veslin, Sophia Wahl, Haolong Li, Felix Meessen, Zhengchao Zhu, Lukas Conrads, etc. The constant kindness of Prof. Thomas Taubner and Prof. Gero von Plessen brightens each day here.

Furthermore, I heartily thank Dr. Dongwang Yang from Wuhan University of Technology China and Dr. Ran He from Leibniz-Institut für Festkörper- und Werkstoffsorschung (IFW) Dresden Germany, whose support and contributions on crystal preparation, property measurement, and microstructure characterization significantly aided the progress of this research. Yuke Zhu from Prof. Suijie He's team at Harbin Institute of Technology China made an invaluable contribution to measure thermoelectric properties.

This work acknowledges with gratitude the funding provided by the China Scholarship Council (CSC, 201906050145) and NeuroSys under the "Clusters4Future" initiative, supported by the Federal Ministry of Education and Research BMBF (03ZU1106BA).

Lastly, I dedicate this thesis to my parents, sister, and husband Dr. Yixu Wang, as beacons in my life.

Personal Details

First Name:	Nan	
Family Name:	Lin	
Date of Birth:	23/10/1992	
English proficiency:	IELTS score 6.5	
E-mail:	lin@physik.rwth-aachen.de; nan.lin0928@gmail.com	
Education:	Doctoral study in in I. Physikalisches Institut (IA), RWTH Aachen	07.2024 - 05.2020
	Master Degree of Materials Engineering, Chongqing University	06.2019 - 09.2016
	Bachelor Degree of Engineering, Henan Univeristy of Science and Technology	06.2015 - 09.2011
Awards	2024 Deutscher Akademischer Austauschdienst Dienst (DAAD) Scholarship for Doctoral Candidates	
	2019 Ph.D. Scholarship funded by China Scholarship Council (CSC, China)	
	2018 Postgraduate National Scholarship awarded by Ministry of Education (MOE, China)	

List of Publications during Doctoral Studies

1. **Nan Lin**, Shuai Han, Tanmoy Ghosh, Carl-Friedrich Schön, Dasol Kim, Jonathan Frank, Felix Hoff, Thomas Schmidt, Pingjun Ying, Yuke Zhu, Maria Häser, Minghao Shen, Ming Liu, Chongjian Zhou, Jiehe Sui, Oana Cojocaru-Mirédin, Ran He, Matthias Wuttig, and Yuan Yu. “Metavalent bonding in cubic SnSe alloys improves thermoelectric properties over a broad temperature range.” *Advanced Functional Materials* (2024) 2315652.

2. Zhang Qi, Yangjian Lin, Nan Lin, Yuan Yu, Feng Liu, Chenguang Fu, Binghui Ge, Oana Cojocaru-Mirédin, Tiejun Zhu, and Xinbing Zhao. “Enhancing the room temperature thermoelectric performance of *n*-type Bismuth-telluride-based polycrystalline materials by low-angle grain boundaries.” *Materials Today Physics* 22 (2022): 100573.
3. Yuan Yu, Guodong Tang, Yuqi Liu, Xiaoyu Yang, Yongsheng Zhang, Pengfei Nan, Pan Ying, Yaru Gong, Xuemei Zhang, Binghui Ge, Nan Lin, Xuefei Miao, Kun Song, Carl-Friedrich Schön, Matteo Cagnoni, Dasol Kim, and Matthias Wuttig. “Interplay between metavalent bonds and dopant orbitals enables the design of SnTe thermoelectrics.” *Nature Communications* (2024) (Accepted Decision)
4. Lipeng Hu, Bingcai Duan, Tu Lyu, Nan Lin, Chaohua Zhang, Fusheng Liu, Junqin Li, Matthias Wuttig, and Yuan Yu. “In Situ Design of High-Performance Dual-Phase GeSe Thermoelectrics by Tailoring Chemical Bonds.” *Advanced Functional Materials* 33, no. 17 (2023): 2214854.
5. Yu-Zheng Li, Qi Zhang, Kai Liu, Yang-Jian Lin, Nan Lin, Yuan Yu, Feng Liu, Xin-Bing Zhao, Bing-Hui Ge, Oana Cojocaru-Mirédin, Chenguang Fu, Tie-Jun Zhu. “Multi-scale hierarchical microstructure modulation towards high room temperature thermoelectric performance in *n*-type Bi₂Te₃-based alloys.” *Materials Today Nano* 22 (2023): 100340.
6. Yingcai Zhu, Yuan Yu, Huaide Zhang, Yongxin Qin, Zi-Yuan Wang, Shaoping Zhan, Dongrui Liu, Nan Lin, Yinghao Tao, Tao Hong, Siqi Wang, Zhen-Hua Ge, Matthias Wuttig, Li-Dong Zhao. “Large Mobility Enables Higher Thermoelectric Cooling and Power Generation Performance in n-type AgPb_{18+x}SbTe₂₀ Crystals.” *Journal of the American Chemical Society* 145, no. 45, (2023): 24931-24939.
7. Huaide Zhang, Minghao Shen, Christian Stenz, Christian Teichrib, Riga Wu, Lisa Schäfer, Nan Lin, Yiming Zhou, Oana Cojocaru-Mirédin, Matthias Wuttig, and Yuan Yu. “Improved charge carrier transport across grain boundaries in *n*-type PbSe by dopant segregation.” *Small Science* (2024) 2300299.

Declaration of Authorship

I, Nan Lin declare that this thesis and the work presented herein are my own and have been generated by me as a result of my original research.

I do solemnly affirm that:

1. This work was conducted entirely or primarily during my doctoral candidacy at this faculty and university;
2. If any portion of this thesis has been previously submitted for a degree or any other qualification, whether at this university or elsewhere, it has been explicitly disclosed;
3. Whenever I have referenced the published work of others or myself, proper attribution has consistently been provided;
4. Whenever I have quoted from the works of others or from my own previous publications, proper attribution has been provided. This thesis represents solely my own efforts, except for these cited quotations.
5. I have properly acknowledged all significant sources of assistance;
6. If the thesis is founded on collaborative work between myself and others, I have distinctly delineated the contributions of each party, specifying what was conducted by others and what I have personally contributed;
7. Portions of this work have been previously published as:

Nan Lin, Shuai Han, Tanmoy Ghosh, Carl-Friedrich Schön, Dasol Kim, Jonathan Frank, Felix Hoff, Thomas Schmidt, Pingjun Ying, Yuke Zhu, Maria Häser, Minghao Shen, Ming Liu, Chongjian Zhou, Jiehe Sui, Oana Cojocaru-Mirédin, Ran He, Matthias Wuttig, and Yuan Yu. “Metavalent bonding in cubic SnSe alloys improves thermoelectric properties over a broad temperature range.” (2024) *Advanced Functional Materials* 2315652.